PSL UNIVERSITÉ PARIS

THÈSE DE DOCTORAT
DE L'UNIVERSITÉ PSL

Préparée à Observatoire de Paris

Relativistic effects on the orbits of the closest stars to the black hole at the center of the Galaxy

Soutenue par
Karim ABD EL DAYEM
Le 08 Décembre 2025

École doctorale n°127
École Doctorale Astronomie et Astrophysique d'Ile de France

Spécialité
Astronomie et Astrophysique

Préparée au
LIRA

Composition du jury :

Marie-Christine ANGONIN Astronome, Observatoire de Paris (LTE)	*Président du jury*
Natalie WEBB Astronome, IRAP	*Rapporteur*
Christos CHARMOUSIS Directeur de recherche, IJCLab	*Rapporteur*
Delphine PORQUET Directrice de recherche, LAM	*Examinateur*
Frédéric VINCENT Chargé de recherche, Observatoire de Paris (LIRA)	*CoDirecteur de thèse*
Thibaut PAUMARD Chargé de recherche, Observatoire de Paris (LIRA)	*CoDirecteur de thèse*
Guy PERRIN Astronome, Observatoire de Paris (LIRA)	*Invité*

LIRA Observatoire de Paris | PSL

Acknowledgments

I would first like to express my deepest gratitude to my supervisors, Frédéric Vincent, Thibaut Paumard and Guy Perrin. Their constant guidance, insightful advice, and unwavering support have been vital to the success of this work. Their knowledge and experience have been a great source of inspiration, and I am truly grateful for their patience, trust, and encouragement, without which starting a career in astronomy would not have been possible.

I warmly thank the jury members — Marie-Christine Angonin, Natalie Webb, Christos Charmousis, and Delphine Porquet — for taking the time to read my thesis, for their thoughtful feedback, and for participating in my defense. I am also grateful to the École Doctorale d'Astronomie et d'Astrophysique d'Île-de-France for funding my three years of research and allowing me to embark on this journey.

I wish to express my sincere appreciation to Gernot Heißel and Nicolas Aimar for many enlightening discussions and for their help throughout the PhD. My thanks also go to the team at the Max-Planck-Institut für Extraterrestrische Physik (MPE) for their willingness to collaborate and share their expertise, which greatly broadened my understanding and improved my results.

In the framework of my part-time teaching at the Paris Observatory, I am thankful to Jérémie Vaubaillon and Cédric Leyrat for their guidance in helping me become a better teacher. I also thank the engineers, technicians, and administrative staff — in particular Denis Savaris, Goran Greblo, Jacqueline Plancy, and Géraldine Gaillant — as well as all the personnel of Building 5 at the Observatory for their warm welcome and for creating a joyful work environment in which we all get along very well.

Finally, I am deeply grateful to my parents, my sister, Isis the dog, and my friends for their unfailing support, encouragement, and belief in me from the very beginning.

Abstract

Context. Measuring the astrometric and spectroscopic data of stars orbiting the central black hole in our galaxy (Sgr A*) offers a promising way to detect relativistic effects and test the "no-hair" theorem through the monitoring of orbital precession induced by the spin and quadrupole moment of the black hole. Closer-in stars, more strongly affected by spin-related effects, may be detectable in the near future with GRAVITY+.

Aims. We analytically and numerically characterize the orbital reorientations induced by spin-related effects of Sgr A* up to second post-Newtonian (2PN) order, and assess the observational requirements to detect them. We also quantify the impact of coordinate system choice on the interpretation of orbital parameters, and explore strategies to improve spin constraints by combining multiple stellar orbits.

Methods. Using the two-timescale method, we derive 2PN analytical expressions for the secular evolution of orbital parameters relevant to the observer. I implement and extend existing dynamical models—from Keplerian and Schwarzschild up to 2PN order—to include 1.5PN and 2.5 spin terms, 2PN quadrupole-moment effects, 3PN Schwarzschild precession, and the spin contribution to the redshift factor in the GR model. These models are compared to each other and to full GR ray tracing to determine which relativistic effects and PN orders are necessary for different orbital configurations. I simulate both the star S2 and a hypothetical S2/10 (same orbital parameters as S2 but with a ten times smaller semi-major axis) to probe the strong-field regime. I also compute the differences in right ascension, declination, and radial velocity when using different coordinate systems for the same osculating orbital elements. Finally, I investigate the combined-fitting potential of currently known S stars and the newly discovered S301 to constrain spin magnitude and orientation.

Results. We identify three orbital-timescale precession rates encoding the in-plane pericenter shift and out-of-plane redirection of the osculating ellipse, and provide their 2PN expressions together with the associated integrated angular shifts. Coordinate-system choices introduce discrepancies in RA, DEC, and RV that can reach the level of current instrumental precision, underscoring the need to explicitly state both the osculation time and coordinate system when reporting orbital elements. Among known stars, S301 shows spin sensitivity comparable to S2/10; jointly fitting it with other stars of diverse orientations mitigates degeneracies, potentially reducing the observational time needed to constrain the spin parameters. Furthermore, quantitative forecasts show that, when only fitting the spin magnitude, the latter can be recovered with 1σ uncertainties of $\sim$0.1 by 2032, $\sim$0.05 by 2034, and $\sim$0.03 by 2036. Comparable results are obtained when fitting all spin parameters. Astrometry provides the primary leverage on these constraints, while spectroscopy becomes highly complementary if radial-velocity precision reaches the $\sim$2 km/s level expected with MICADO. Overall, spin detectability is robust provided sufficient monitoring, with orientation emerging as the key factor, and combined astrometric and spectroscopic datasets from multiple stars offering the most powerful path forward.

Résumé

Contexte. L'observation astrométrique et spectroscopique des étoiles en orbite autour du trou noir supermassif au centre de notre Galaxie (Sgr A*) constitue une voie privilégiée pour mettre en évidence les effets relativistes et tester le théorème de «calvitie» des trous noirs. Cette étude peut être réalisé à travers le suivi de la précession orbitale induite par le taux de rotation (ou *spin*) et le moment quadrupolaire du trou noir. Des étoiles plus proches, plus fortement affectées par les effets liés au spin, pourraient être détectées dans un avenir proche grâce à l'interféromètre GRAVITY+.

Objectifs. Nous caractérisons, par une approche analytique et numérique, les réorientations orbitales induites par le spin de Sgr A* jusqu'au deuxième ordre post-newtonien (2PN), et évaluons les conditions d'observation nécessaires pour les mettre en évidence. Nous étudions également l'impact du choix du système de coordonnées sur l'interprétation des paramètres orbitaux, et explorons des stratégies pour améliorer les contraintes sur le spin en combinant les données de plusieurs orbites.

Méthodes. En appliquant la méthode aux deux échelles de temps, nous obtenons des expressions analytiques à l'ordre 2PN décrivant l'évolution séculaire des paramètres orbitaux pertinents pour l'observateur. J'ai étendu les modèles dynamiques existants — du képlérien et du Schwarzschild jusqu'au 2PN — pour inclure les termes de spin à 1.5PN et 2.5PN, les effets du moment quadrupolaire à 2PN, la précession de Schwarzschild à 3PN, ainsi que la contribution du spin au facteur de décalage spectral dans le modèle relativiste complet. Ces modèles sont comparés entre eux et à un tracé de rayons en relativité générale afin de déterminer les effets et ordres PN nécessaires selon les configurations orbitales. Je simule l'étoile S2 ainsi qu'une étoile hypothétique S2/10 (mêmes paramètres orbitaux que S2 mais avec un demi-grand axe dix fois plus petit) pour sonder le régime en champ fort. Je calcule également les différences d'ascension droite, de déclinaison et de vitesse radiale obtenues avec différents systèmes de coordonnées pour un même jeu d'éléments orbitaux osculateurs. Enfin, j'évalue le potentiel d'un ajustement combiné des orbites d'étoiles S connues et de la nouvelle étoile S301 pour contraindre l'amplitude et l'orientation du spin.

Résultats. Nous identifions trois vitesses de précession à l'échelle orbitale, traduisant le déplacement du périastre dans le plan et la réorientation hors du plan de l'ellipse osculatrice, et donnons leurs expressions à l'ordre 2PN ainsi que les décalages angulaires intégrés correspondants. Le choix du système de coordonnées peut induire des écarts en RA, DEC et RV comparables à la précision instrumentale actuelle, ce qui impose de préciser la temps d'osculation et le système de coordonnée utilisé avec les éléments orbitaux. Parmi les étoiles connues, S301 présente une sensibilité au spin comparable à S2/10 ; un ajustement conjoint avec d'autres étoiles aux orientations variées permet de réduire les dégénérescences et pourrait raccourcir le temps d'observation nécessaire pour contraindre les paramètres du spin de Sgr A*. En outre, nos prévisions indiquent que, si l'on ajuste uniquement la magnitude du spin, celle-ci pourra être contrainte avec une précision de l'ordre de $1\sigma \simeq 0{,}1$ d'ici 2032, 0,05 d'ici 2034 et 0,03 d'ici 2036. Des performances simi-

laires sont obtenues lorsqu'on ajuste simultanément l'ensemble des paramètres du spin. L'astrométrie reste la source principale de contraintes, mais la spectroscopie devient un atout majeur si la précision en vitesse radiale atteint le niveau de $\sim$2 km/s, comme attendu avec MICADO. Dans l'ensemble, la détection du spin apparaît robuste pour peu que l'on dispose d'un suivi observationnel suffisant, l'orientation du spin jouant un rôle déterminant. La combinaison de données astrométriques et spectroscopiques issues de plusieurs étoiles constitue ainsi la stratégie la plus prometteuse.

Contents

1 Context **10**

I Astrophysical context **11**

I.1 Interests of our study 12

I.1.1 The importance of probing strong-field gravity 12

I.1.2 Why study Sgr A*? 14

I.2 The Galactic Center 15

I.2.1 Main structures and stellar population of Sagittarius A 15

I.2.2 Sgr A* and its accretion disk 17

I.2.3 Relativistic effects in the vicinity of Sgr A* 21

I.3 Detectability of the spin related effects in the literature 23

I.3.1 Testing the General Relativistic "no-hair" theorem Using the Galactic Center Black Hole Sagittarius A* (Will et. al. 2008) 24

I.3.2 Toward Relativistic Orbit Fitting of Galactic Center Stars and Pulsars (Angélil et. al. 2010) 28

I.3.3 Prospects for Constraining the Spin of the Massive Black Hole at the Galactic Center via the Relativistic Motion of a Surrounding Star (Yu et. al. 2016) 32

I.3.4 General Relativistic Effects on the Orbit of S2 with GRAVITY (Grould et al. (2017)) 35

I.3.5 What stellar orbit is needed to measure the spin of the Galactic

Center black hole from astrometric data? (Waisberg et al. (2018)) 37
I.3.6 Constraining the spin using other methods 42

II Theoretical context **46**

II.1 General relativistic framework and coordinate systems 46

II.1.1 Schwarzschild Metric and Harmonic Coordinates 47

II.1.2 Kerr Metric: Boyer–Lindquist and Kerr–Schild Coordinates 48

II.2 Lagrange planetary equations 50

II.3 Post-Newtonian formalism 51

II.3.1 Post-Newtonian acceleration 52

III Instrumental context **56**

III.1 Interferometry: From Principles to GRAVITY+ 57

III.1.1 Introduction to Optical Interferometry 57

III.1.2 The GRAVITY Instrument 62

III.1.3 The GRAVITY+ Upgrade 64

III.2 Spectroscopy: ERIS and MICADO 65

III.2.1 Basics of Spectroscopy 65

III.2.2 The ERIS Instrument 65

III.2.3 The MICADO Instrument 66

2 Presenting the framework and modeling the simulation tools **70**

IV Relativistic orbits **71**

IV.1 Reference frames 72

IV.1.1 Observer frame 72
IV.1.2 Orbit frame 74
IV.1.3 Black hole frame 75
IV.1.4 Gaussian frame 77
IV.2 Orbit parametrization 79
IV.2.1 Newtonian orbits 79
IV.2.2 Relativistic orbits and osculating orbital parameters 80
IV.3 Differences between coordinate systems in orbit simulations 81
IV.3.1 Non-uniqueness of relativistic orbital parameterizations 82
IV.3.2 Estimating the coordinate system discrepancy 83

V Extending our palette of relativistic models 88

V.1 Codes for relativistic simulations 88
V.1.1 `GYOTO` 89
V.1.2 `OOGRE` 89
V.1.3 Orbit models 90
V.2 Development of the spin aspects in the `GR_proj` model 92
V.2.1 Detailed derivation of the redshift formula in curved spacetime . . 92
V.2.2 Approximate expression without ray tracing 95
V.3 Extending `OOGRE` to higher order effects 98

VI Evaluating the detectability of various effects 101

VI.1 Which model for which orbit? 101
VI.1.1 Code Verification with S2 102
VI.1.2 Comparing the Various Relativistic Effects 104

VI.1.3 Assessing the required model for accuracy and efficiency 108
VI.2 Evaluating the detectability of the spin using orbit fitting 111
VI.2.1 Methodology 112
VI.2.2 Fitting Kerr Data with a Zero-Spin Model 114

3 Spin-induced dynamics and observational prospects 116

VII The effects of the spin and quadrupole moment on the star orbits 117

VII.1 Post-Newtonian expressions of the secular shifts 118
VII.1.1 Analytical integration at the dominant order 119
VII.1.2 Secular evolution in the PN formalism and two-timescale analysis 122
VII.2 Spin impact on the orientation of the orbit 133
VII.2.1 Instantaneous orientation change 133
VII.2.2 Secular shifts for S2 and S2/10 137
VII.2.3 Time-averaged orientation change 140
VII.2.4 Numerical illustration 141

VIII Detecting the spin parameters using multiple S stars 151

VIII.1 Fitting the spin orientation 152
VIII.1.1 Special orientations for sky-projected apocenter shifts 154
VIII.1.2 Curve-fitting the spin angles using a single star at a time 157
VIII.1.3 Multi-star fitting of the spin angles 159
VIII.1.4 Exploring three-dimensional spin parameter space 160
VIII.2 Detectability of the spin parameters using multi-star fitting 163

VIII.2.1 Only fitting the spin magnitude 163
VIII.2.2 Fitting all spin parameters 170

Appendix **191**

A Numerical illustration: mid-inclined orbits 191

B Estimating characteristic spin orientations in the observer's frame 195

B.1 Relation between (θ, ψ) and $(i_\bullet, \Omega_\bullet)$ 195

B.2 Projected apocenter displacement vector as a function of (θ, ψ) . . 196

Part 1

Context

Chapter I

Astrophysical context

Contents

I.1 Interests of our study 12

I.1.1 The importance of probing strong-field gravity 12

I.1.2 Why study Sgr A*? 14

I.2 The Galactic Center 15

I.2.1 Main structures and stellar population of Sagittarius A 15

I.2.2 Sgr A* and its accretion disk 17

I.2.3 Relativistic effects in the vicinity of Sgr A* 21

I.3 Detectability of the spin related effects in the literature . . 23

I.3.1 Testing the General Relativistic "no-hair" theorem Using the Galactic Center Black Hole Sagittarius A* (Will et. al. 2008) . 24

I.3.2 Toward Relativistic Orbit Fitting of Galactic Center Stars and Pulsars (Angélil et. al. 2010) 28

I.3.3 Prospects for Constraining the Spin of the Massive Black Hole at the Galactic Center via the Relativistic Motion of a Surrounding Star (Yu et. al. 2016) 32

I.3.4 General Relativistic Effects on the Orbit of S2 with GRAVITY (Grould et al. (2017)) 35

I.3.5 What stellar orbit is needed to measure the spin of the Galactic Center black hole from astrometric data? (Waisberg et al. (2018)) 37
I.3.6 Constraining the spin using other methods 42

In this first chapter, we set the stage for the work presented in this thesis. We begin in Section I.1 by discussing the scientific motivations behind our study, starting with the broader importance of probing the strong-field regime of gravity, before narrowing our focus to the specific case of Sgr A*, the supermassive black hole at the center of our Galaxy.

In Section I.2, we describe the Galactic Center environment. We introduce the main structures within the central 10 parsecs and their stellar populations, then focus on Sgr A* and its accretion disk, and finally review the various relativistic effects expected in its vicinity.

Section I.3 addresses the state of the art of the detectability of spin-related effects. We first discuss how the Lense–Thirring and quadrupole moment effects might be measured using S-stars, then review existing literature on their detectability from Galactic Center stellar orbits, and conclude with other complementary methods for constraining the spin.

This chapter draws inspiration from [130], [72], [129], [55], and [48].

I.1 Interests of our study

I.1.1 The importance of probing strong-field gravity

Since the emergence of "modern science"[1], humanity has been driven by a powerful question: can the astonishing complexity of the natural world be explained by a smaller number of universal principles? From the very beginnings of abstract reasoning, Greek philosophers such as Thales and Anaximander speculated that the diversity of natural phenomena — trees, rivers, animals, stars — could be traced back to a single, fundamental substance or idea. Whether this principle was conceived as water (Thales) or a more abstract and indefinite "apeiron" (Anaximander), the underlying motivation was the same: to find unity beneath multiplicity.

[1]The Egyptian science is much older than that, as the Great Pyramid of Giza — built millennia earlier — can overwhelmingly illustrate. However, we believe that this science was closer to what we would now call a technique, i.e., a practical set of knowledge enabling outstanding feats, but lacking an abstract theoretical foundation (there are, for instance, no records of Egyptian abstract geometry). Here, I use the term "modern science" to refer to a form of abstract, general reasoning about natural phenomena, developed in Greece in the 6th century BCE, where the quest for unity quickly became a dominant intellectual pursuit.

This philosophical desire to understand nature through unifying principles did not remain a speculative curiosity. Over centuries, it matured into what we now recognize as the scientific method. Newton's law of universal gravitation, for instance, showed that the same force pulling apples to the ground also governs the orbits of the Moon and planets. Later, the 20th century brought a deeper revolution: Einstein's general theory of relativity, which replaced Newton's idea of gravitational force with the curvature of spacetime itself [27], and quantum mechanics, which radically reshaped our view of matter and energy at microscopic scales.

By the 1970s, this quest for unity had achieved one of its greatest triumphs: the Standard Model of particle physics [103], a remarkably successful theory combining quantum field theory and special relativity to describe three of the four known fundamental forces — electromagnetic, weak, and strong — within a common framework. But gravity, the very first force to be described mathematically, still stands apart. Despite the elegance and predictive power of general relativity, it remains stubbornly incompatible with quantum theory. The dream of unifying all the fundamental interactions — the ultimate goal that has guided theoretical physics for several millennia — remains incomplete.

So why study gravity today? And why in the context of astrophysics?

While general relativity has passed every observational test in the weak-field regime [82, 141] — including exquisite measurements in the Solar System and binary pulsars — we know that it must eventually break down. It predicts its own limits in the form of singularities inside black holes [106] and at the origin of the universe. Moreover, unlike the other fundamental interactions, gravity becomes strongest precisely in regions we cannot easily access: near compact objects like black holes and neutron stars, or in the very early universe. This makes astrophysical observations an indispensable tool to test general relativity in its most extreme predictions.

At the heart of our own galaxy lies one of the most promising natural laboratories for strong-field gravity: Sagittarius A* (Sgr A*), the supermassive black hole candidate at the Galactic Center. Over the past three decades, high-resolution infrared observations have revealed the presence of stars — the so-called S-stars — orbiting [51, 52] within a few thousand Schwarzschild radii of this object. Some of these stars, follow highly elliptical trajectories that bring them extremely close to the black hole, where relativistic effects become significant and observable.

The study of these stellar orbits allows us to do something remarkable: test general relativity not in theoretical thought experiments or computer simulations, but in the real world, using actual stars moving under the influence of a real compact object. This opens the possibility of probing phenomena such as gravitational redshift [59], orbital precession [70], frame-dragging due to the spin of the black hole (Lense-Thirring effect) [91], and possibly even the influence of the black hole's mass quadrupole moment — a signature of its spacetime geometry, and a test of the no-hair theorem [83].

These observations are not just a curiosity. They provide one of the only avenues we currently have to test gravity in the strong-field regime and to look for deviations that might hint at new physics. If general relativity would fail near Sgr A*, it would signal the breakdown of our current understanding of spacetime and point toward the deeper

theory that so many physicists have sought.

In this thesis, I explore in detail the relativistic effects acting on the orbits of the S-stars, focusing in particular on how the spin and quadrupole moment of Sgr A* modify their dynamics. Using both post-Newtonian formalism and numerical simulations, I aim to provide a clear and testable description of how strong-field gravity manifests itself in this exceptional astrophysical setting.

I.1.2 Why study Sgr A*?

As mentioned in subsection I.1.1, a precise understanding of the environment of supermassive black holes (SMBHs) is essential for probing strong-field gravity. SMBHs are also key actors in many other areas of astrophysics, influencing phenomena across a vast range of spatial and temporal scales. Their study has major implications in the following domains:

- **Galaxies:** Observations reveal a correlation between the velocity dispersion of galactic bulges and the mass of their central SMBH [41, 46]. This relation likely arises from the interplay between the SMBH's energy output—in the form of intense radiation and outflows, possibly powered by black hole spin [38]—and the large-scale galactic environment (up to ten orders of magnitude larger in scale). This injected energy can heat the interstellar gas, inhibit cooling, and suppress star formation. Conversely, inflowing gas and stellar winds can feed the SMBH. Intriguingly, some models suggest that SMBHs may also enhance star formation under certain conditions, making their role in galactic evolution even more complex.

- **Cosmology:** Since most galaxies likely host an SMBH at their center, understanding how small black hole seeds grow to reach millions or billions of solar masses is a fundamental challenge [133, 134]. It is tightly linked to our understanding of the accretion and ejection mechanisms in the strong-field regions around these compact objects. Furthermore, some studies have suggested the possibility that SMBH would have started out as overdensities in the early universe that progressively created the potential well in which galaxies would later have taken form. If confirmed, this would place SMBHs at the heart of cosmological structure formation.

- **Gravitational waves:** Multi-messenger astronomy, combining electromagnetic and gravitational-wave observations, will be a cornerstone of 21st-century astrophysics. The strongest gravitational wave sources originate in strong-field gravity regimes, making their study highly relevant. The upcoming space-based interferometer *LISA*, designed to detect low-frequency gravitational waves, will benefit greatly from a detailed prior understanding of these sources to maximize its scientific return [2].

Beyond these domains, SMBHs are also connected to topics such as massive star and binary evolution, supernova explosions, and neutron star physics.

Given these motivations, Sagittarius A* (Sgr A*) is an ideal target for such investigations. Located at the center of the Milky Way, it is a compact radio source with a mass of $\sim 4.3 \times 10^6\,M_\odot$ [57](see subsection I.2.2). An additional and crucial advantage of Sgr A* is its exceptionally low level of accretion activity. Unlike active galactic nuclei, where luminous accretion disks, radiation pressure, and strong outflows can significantly perturb stellar dynamics, Sgr A* is presently in a quiescent state with an extremely low accretion rate [48]. Its bolometric luminosity is many orders of magnitude below its Eddington luminosity [5, 100], implying that non-gravitational forces acting on the S-stars are negligible. As a result, the stellar orbits provide a remarkably clean probe of the gravitational potential, making the Galactic Center one of the most pristine laboratories for testing strong-field gravity. This SMBH has the remarkable advantage of being only $\sim 8\,$kpc from the Solar System—roughly 100 times closer than the nearest comparably observable spiral galaxy (Andromeda). Furthermore, because the Milky Way is a typical spiral galaxy, insights gained from Sgr A* can be generalized to a broad class of galactic nuclei.

I.2 The Galactic Center

Having outlined the motivations for studying the close vicinity of Sgr A*, we now present its environment, beginning with the main structures and stellar populations within the central 10 parsecs. This section is largely inspired by [48], which provides a comprehensive overview and detailed references.

I.2.1 Main structures and stellar population of Sagittarius A

In addition to Sgr A* itself, the inner few parsecs of our Galaxy contain a complex interplay of neutral, ionized, and extremely hot gas, as well as a dense and luminous Nuclear Star Cluster. As illustrated in Figure I.1, the central 10 parsecs comprise several distinct structures:

- **Sgr A*:** the compact radio source at the dynamical center of the Galaxy (see subsection I.2.2).
- **Circumnuclear disk (CND):** a torus-like structure of 10–20 dense molecular clouds, each with a characteristic size of $\sim$0.5 pc and a mass of $\sim$1000 $M_\odot$. Its pronounced asymmetry suggests it is an unstable structure, possibly due to interactions with Sgr A East.
- **Sgr A East:** an expanding 7×9 pc bubble, likely the remnant of a supernova, encompassing the other three substructures.

- **Sgr A West ("mini-spiral"):** a three-armed spiral-like feature within the central ∼2 pc, dominated by dust and ionized gas emission from the surrounding H II region. In reality, it is a complex 3D structure unrelated to the large-scale spirals of disk galaxies.

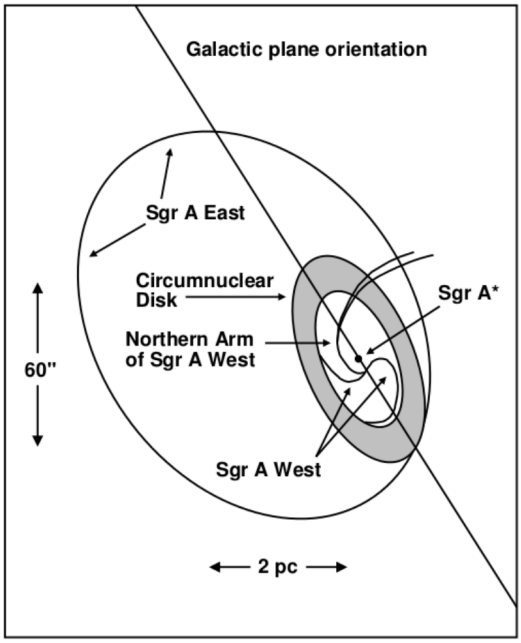

Figure I.1: Schematic view of the Sgr A complex and its main components (adapted from [6]).

The Nuclear Star Cluster in this region is dominated by cool, low-mass, old late-type giant stars with largely random and isotropic orbits. Surprisingly, many hot, massive, young early-type O, B, and Wolf–Rayet (WR) stars have also been detected, concentrated in a warped, clockwise-rotating stellar disk within the central 0.5 pc. This so-called *"Paradox of Youth"* arises because the strong tidal field of the central black hole should hinder star formation so close to it. Possible explanations include in-situ formation via fragmentation of a massive accretion disk [102], or migration of a massive star cluster from further out, subsequently disrupted by tidal forces [49].

Within the innermost arcsecond lies the *S-star cluster*, composed mainly of faint ($m_K \lesssim 15$) B-type stars with isotropically distributed orbits. Years of astrometric and spectroscopic monitoring have enabled precise orbital solutions for many of these stars (Figure I.2), yielding tight constraints on fundamental parameters such as the distance to the Galactic Center ($R_0 = 8275.9 \pm 8.6$ pc) and the black hole mass ($M_\bullet = (4.2996 \pm 0.0118) \times 10^6$ $M_\odot$) [57].

Among these stars, S2 stands out with a pericenter distance of ∼1400 Schwarzschild radii ($\sim 700\, GM_\bullet/c^2$; see subsection II.1.1) and a semi-major axis of 0.123 arcsec, making

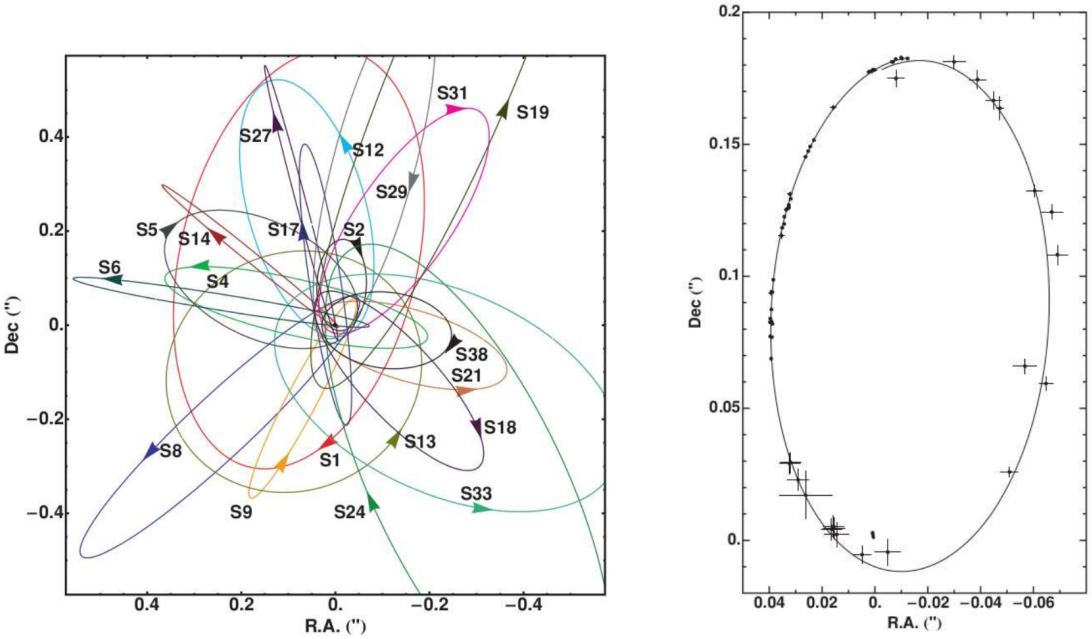

Figure I.2: Orbits of S stars as obtained in [52] (left), and a zoom on the orbit of S2 (right)

it one of the closest known stars to Sgr A* with a magnitude in the K-band under $m_K < 15$.

The isotropic distribution of S-stars may be explained by several scenarios. One is the *Hills mechanism* [80], in which tidal disruption of a binary by the SMBH ejects one star at high velocity while capturing the other into a tight, random orbit. Another possibility is migration of massive stars from the ∼0.1–1 pc stellar disk inward via interactions with intermediate-mass black holes [92].

These two massive-star populations (Figure I.3) make the Galactic Center one of the regions with the highest rates of massive-star formation in the Milky Way.

I.2.2 Sgr A* and its accretion disk

Sgr A*, the compact radio source

In order to explain the radio emissions detected in the 1950s, Lynden-Bell & Rees hypothesized for the first time in 1971 that Sgr A* could be a black hole [95]. Soon after, Balick & Brown discovered a compact, point-like radio source within the Sgr A complex, which they named Sgr A* [7]. Using radial velocity measurements of ionized gas in the Galactic nucleus and applying the virial theorem, Wollman et al. inferred in [144] the presence of a 2–4 $\times$ 10^6 $M_\odot$

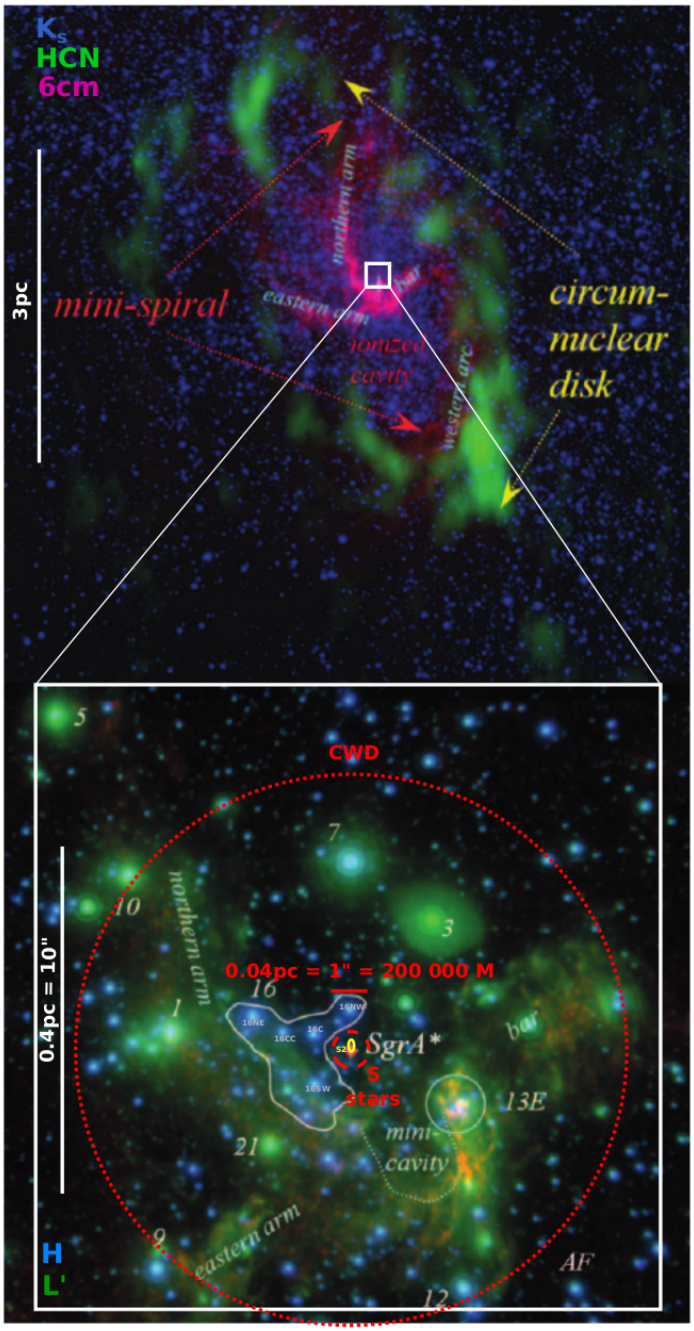

Figure I.3: 10pc-scale multiwavelengths image of the Galactic center with the 2.2µm K_S band in blue (stars), HCN emission in green (dense molecular clouds, forming the circum-nuclear disk), and radio emission in pink (ionized HII region, the mini-spiral). In the bottom we have the 1pc-scale image of the surrounding of Sgr A* with the 1.6µm H band in blue and L' band (3.8µm) in green.The dotted red circle encompasses the clockwise disk (CWD) of young stars. The dashed red circle shows the central arcsecond occupied by the S-star cluster. The tiny yellow orbit at the center of the image represents approximately to scale the orbit of S2 (extracted from [48])

mass within the central parsec. However, because ionized gas is strongly affected by non-gravitational forces, these measurements alone were insufficient to confirm the compactness of the source.

Over the following decades, increasingly precise astrometric and spectroscopic monitoring of stars in the so-called S-star cluster—most notably S2—provided the strongest constraints on the mass and compactness of Sgr A* [23, 50]. These results have established Sgr A* as a $\sim 4.3\times10^6\,M_\odot$ object located at the dynamical center of the Galaxy. It should be noted, however, that current stellar observations do not probe the gravitational field inside $\sim$ 1400 Schwarzschild radii. In principle, future observations of closer-in stars could reveal deviations from the black hole hypothesis in favor of alternative compact object scenarios.

Emission spectrum

Sgr A* exhibits both a *quiescent* (steady) and a *flaring* (variable) state. In its steady state, it has a sub-Eddington bolometric luminosity of $L_{\mathrm{SgrA*}} \approx 10^{36}\,\mathrm{erg\,s^{-1}} \approx 10^{-8.5} L_{\mathrm{Edd}}$, where L_{Edd} is the Eddington luminosity — the maximum luminosity at which outward radiation pressure balances inward gravitational attraction for spherical accretion [24] — indicating that radiation pressure is negligible compared to gravity. As shown in Figure I.4, the spectral energy distribution rises with frequency, peaking at $\sim 5\times10^{35}\,\mathrm{erg\,s^{-1}}$ in the submillimeter regime (the "submillimeter bump"), before dropping sharply at mid-infrared wavelengths. Detections in the near-infrared and X-ray bands correspond to luminosities of $\sim 3\times10^{34}$ and $\sim 2\times10^{33}\,\mathrm{erg\,s^{-1}}$, respectively. At higher frequencies the angular resolution of the observations are too weak to distinguish Sgr A* from its surroundings.

Sgr A* also undergoes bright flares at submillimeter, near-infrared, and X-ray wavelengths (Figure I.5). These events typically last one to two hours and show quasi-periodic oscillations with a period of $\sim$ 20 minutes. The flux variations are frequency-dependent; in the near-infrared, for example, the flux can increase by a factor of $\sim$ 40 [48]. Such flares provide valuable probes of the strong-field regime.

Several models have been proposed to explain these flares:

- **Hot spot model:** the bursts would stem from electron clumps that were heated by magnetic reconnection in the accretion disk surrounding the black hole [see 127].
- **Red noise model:** the bursts would be due to random flux intensity fluctuations in the accretion disk [see 21].
- **Jet model:** the bursts would originate from hot-spots inside jets of matter ejected from the accretion structure around Sgr A* [39]. This model is capable of reproducing both the quiescent and flaring states.

Accretion disk

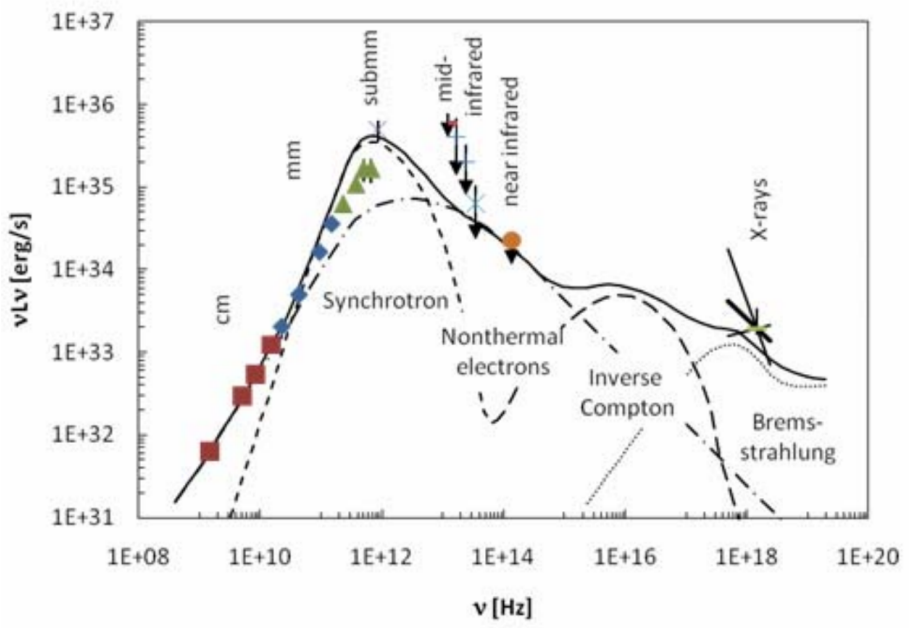

Figure I.4: : Spectral energy distribution of Sgr A* in its steady state. The coloured data points originate from multiple authors of which the references will be found in [48] and the model of the quiescent emission is the one from [146]: synchrotron emission of thermal electrons (short dashed line); emission from a non-thermal power-law distribution of electrons (dashed-dotted line); thermal Bremsstrahlung from the outer parts of the accretion flow (dotted line); inverse Compton up-scattering of the synchrotron spectrum by the thermal electrons (long-dashed line). Source: [48]

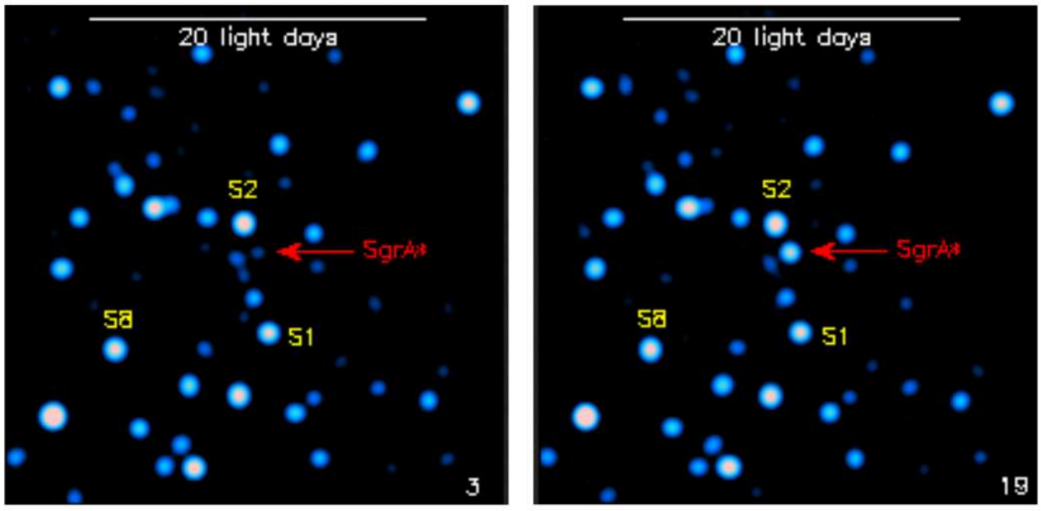

Figure I.5: : Observation of a bright burst appearing in the K-band with a few minutes interval and coming from the center of the Galaxy. Source: [47]

After five years of calculations and analysis, the international collaboration of the Event Horizon Telescope (EHT) delivered on May 12, 2022 the image of Sagittarius A* in Figure I.6, and what could seem to be its accretion disk or photon rings. Whether this constitutes a direct observation of the accretion disk or not, it is natural to suppose that the quiescent emission of Sgr A* is technically that of its accretion disk.



(a) **(b)**

Figure I.6: This is the first-ever image of the Milky Way's central black hole, Sgr A* (left) and some of the EHT telescopes that made the image possible (right). Left image credit: EHT Collaboration. Right image credit: ESO/B. Tafreshi

The low luminosity of Sgr A* is best explained by a radiatively inefficient accretion flow (RIAF; [146]), a geometrically thick, optically thin flow in which a large fraction of dissipated energy is stored rather than radiated. RIAFs can reach near-virial temperatures in the inner regions. In contrast, the classical thin-disk model of [122]—geometrically thin and optically thick—cannot reproduce the observed low radiative efficiency of Sgr A*.

I.2.3 Relativistic effects in the vicinity of Sgr A*

The observable phenomena in the strong gravitational field near Sgr A* can be broadly classified into three categories: (1) *Keplerian* effects, which are purely Newtonian and contain no general relativistic corrections; (2) *Schwarzschild* effects, which account for the spacetime curvature due to a non-rotating central mass; and (3) *Kerr* effects, which additionally include the influence of the black hole's spin. The main effects relevant to our study are:

- **(Kepler/Minkowski) Rømer time delay:** This effect is due to the finite

speed of light propagating in a Newtonian spacetime [74, 118]. Depending on where the star is located along its orbit, the time needed by photons to reach the observer (following Euclidian straight lines) will differ. This affects both the astrometry and the spectroscopy.

- **(Minkowski) Special relativistic redshift:** The *transverse Doppler shift* from special relativity is due to the relative motion between the emitter and the observer, and modifies the observed radial velocity [25].
- **(Schwarzschild) Pericenter advance:** The curvature of spacetime causes the orbit to precess, shifting the pericenter and apocenter positions from one revolution to the next [120, 136]. This relativistic precession modifies both the astrometric track and the radial velocity curve.
- **(Schwarzschild or Kerr) Shapiro time delay:** This effect is due to the slowdown of the proper time of the photon with respect to the proper time of the observer when the photon crosses a gravitational field [124]. This affects both the astrometry and the spectroscopy.
- **(Schwarzschild or Kerr) General relativistic redshift:** The *gravitational redshift* from general relativity is caused by the climb of the photon out of the gravitational well, and modifies the observed radial velocity [26].
- **(Schwarzschild or Kerr) Gravitational lensing:** The bending of photon trajectories by spacetime curvature (including spin-induced deflections) alters the apparent position of the star in the sky plane, with secondary impacts on spectroscopy via path-dependent time delays [28].
- **(Kerr) Lense–Thirring effect:** Also known as frame dragging, this gravitomagnetic effect is caused by the rotation of the black hole, dragging the local spacetime itself along with its rotation [91, 138]. It leads to a precession of the star's orbital plane around the black hole's spin axis, including a pericenter advance as in Schwarzschild. The effect depends on both the magnitude and orientation of the spin, and influences the stellar orbital motion and photon propagation, thereby impacting astrometric and spectroscopic signals.
- **(Kerr) Mass multipole moments:** The mass multipole moments introduce additional precession of the orbital plane and pericenter beyond the Lense–Thirring effect, once more, including a pericenter advance as in Schwarzschild [75, 85]. This effect impacts both astrometry and spectroscopy for sufficiently close-in orbits.

The Lense-Thirring effect and the dominant contribution of the mass multipole moments, the quadrupole moment effect, will be detailed in sections I.3 below and II.3.

The GRAVITY instrument enables precise astrometric and spectroscopic measurements near the Galactic Center, allowing robust detections of effects such as Schwarzschild precession and both types of relativistic redshifts in S2's orbit [36, 59]. The Roemer time delay is well above GRAVITY's sensitivity threshold [74, 148] and, of course, included in the data fitting. At the time being, there still is still no detection of the Shapiro delay, gravitational lensing, frame dragging, and Kerr multipole effects, which remain around or below detection limits for S2 [114]. However, they can be included the modeling and data fitting when needed.

I.3 Detectability of the spin related effects in the literature

We summarize the current understanding from the literature on the detectability of the spin and quadrupole moment of Sgr A* using the orbits of S-stars. These higher-order relativistic effects, predicted by general relativity, are much weaker than the dominant Schwarzschild terms but carry direct information about the black hole's angular momentum and multipole structure.

In the context of general relativity, the spacetime around a rotating black hole is described by the Kerr metric (see subsection II.1.2). Beyond the dominant Schwarzschild (non-rotating) effects, the black hole's angular momentum introduces two primary higher-order phenomena that perturb stellar orbits as mentioned in subsection I.2.3 above. The Lense-Thirring (LT) effect scales with the black hole's dimensionless spin parameter, denoted as a or χ. The latter is linked to the norm of the angular momentum J of a black hole of mass $M_\bullet$ by:

$$\chi = J\frac{c}{GM_\bullet^2}. \tag{I.1}$$

The spin parameter χ of a black hole is positive and has a maximum value of 1. The values $\chi > 1$ correspond to naked singularities rather than black holes. Although cosmic censorship conjectures and numerical simulations suggest that astrophysical black holes cannot exceed this bound, this remains a conjecture rather than a rigorous theorem. Other conventions allow the spin to be negative such that a configuration where the spin is negative and the orbit is prograde with respect to the black hole is equivalent to the configuration where the spin is positive and the orbit is retrograde with respect to the black hole (see subsection IV.1.3 for more details about the black hole frame).

As for the Quadrupole Moment Effect, it scales with the quadrupole moment parameter Q, i.e the mass quadrupole moment of the central object:

$$Q = -\frac{1}{c^2}\frac{J^2}{M_\bullet} = -\frac{G^2M_\bullet^3}{c^4}\chi^2, \tag{I.2}$$

where the fact that Q depends only on $M_\bullet$ and χ is a consequence of the no-hair theorem [89, 111]. Both effects fall off faster with distance than Schwarzschild precession, making them detectable primarily for very close-in orbits.

I.3.1 Testing the General Relativistic "no-hair" theorem Using the Galactic Center Black Hole Sagittarius A* (Will et. al. 2008)

The work by Clifford M. Will in [142] focuses on the potential for testing the general relativistic "no-hair" theorem using observations of stars orbiting Sgr A*. The paper highlights the significance of high-precision adaptive infrared optics instruments, like GRAVITY, in making such fundamental tests possible.

The "No-Hair" Theorem and Black Hole Properties A central tenet of general relativity concerning black holes is the "no-hair" theorem, which states that an electrically neutral black hole is completely characterized by its mass and angular momentum. Consequently, all the multipole moments of its external spacetime are uniquely determined as functions of these two parameters. Specifically, the quadrupole moment of a black hole is linked to its angular momentum by the relation in Eq. (I.2). If a black hole is non-rotating, its external metric is described by the Schwarzschild solution, and the primary relativistic effect is the advance of the pericenter.

Orbital Perturbations and Precession Rates The paper provides a rough analysis in the post-Newtonian limit to describe the equation of motion for a body of negligible mass in the field of a rotating black hole with mass, angular momentum, and quadrupole moment. This equation includes terms for the Schwarzschild part, the frame-dragging effect, and the quadrupole moment effect.

Using standard orbital perturbation theory (see subsection II.3), the precessions per orbit of the orientation variables (see section IV.2 for more details on the orbital parameters) are given by:

- Pericenter Precession ($\Delta\omega$):

$$\Delta\omega = A_S - 2A_J \cos\alpha - \frac{1}{2}A_{Q2}(1 - 3\cos^2\alpha). \tag{I.3}$$

  This represents the precession of the pericenter relative to a fixed reference direction.

- Node Precession ($\Delta\Omega$) and Inclination Precession (Δi):

$$\sin i\,\Delta\Omega = \sin\alpha\,\sin\beta\,(A_J - A_{Q_2}\cos\alpha)\,, \tag{I.4}$$

$$\Delta i = \sin\alpha\,\cos\beta\,(A_J - A_{Q_2}\cos\alpha)\,. \tag{I.5}$$

These describe the precession of the orbital plane.

The amplitudes for these precessions are given by:

- $A_S = 6\pi GM_\bullet/(c^2 p)$ (Schwarzschild)
- $A_J = 4\pi(GM_\bullet/(c^2 p))^{3/2}\chi$ (Frame-dragging)
- $A_{Q2} = -3\pi Q/(M_\bullet p^2) = 3\pi(GM_\bullet/(c^2 p))^2\chi^2$ (Quadrupole)

where $p = a_{\text{sma}}(1-e^2)$ is the semilatus rectum, a_{sma} is the semi-major axis, and e is the eccentricity. α and β are polar angles of the black hole's angular momentum vector relative to the star's orbital plane. I noticed that in the expression of A_{Q2} a minus sign was missing, and confirmed it by writing to the author of [142]. The expression in this work is the correct one.

The precession of the orbital plane is deemed the "most important effect" for testing the no-hair theorem because it depends only on J and Q, while the Schwarzschild part of the metric only affects pericenter advance.

To understand the astrometric size of these precessions, the paper defines angular precession rate amplitudes (in µas/yr) for a Galactic Center distance of 8 kpc and a black hole mass of $M_\bullet = 3.6 \times 10^6 M_\odot$:

- Schwarzschild: $\dot{\Theta}_S \approx 13.3 P^{-1}(1-e^2)^{-1/2}$
- Frame-Dragging: $\dot{\Theta}_J \approx 0.847\chi P^{-4/3}(1-e^2)^{-3/2}$
- Quadrupole: $\dot{\Theta}_{Q2} \approx 9.68 \times 10^{-3}\chi^2 P^{-2}(1-e^2)^{-5/2}$

where P is the orbital period in years.

Requirements for Detection and Challenges For the quadrupole precessions to be observable, the black hole must have a significant angular momentum ($\chi \geq 0.5$) and the star must be in a short-period, high-eccentricity orbit. The paper illustrates that if stars were found with orbital periods of fractions of a year and sufficiently high eccentricities ($e \gtrsim 0.95$), the quadrupole-induced precessions could be as large as 10 µas/yr. For example, Figure I.7a extracted from [142] indicates the orbital period required as a function of eccentricity for Schwarzschild, frame-dragging, and quadrupole precessions to reach specific magnitudes (10, 5, and 1 µas/yr, respectively).

The pericenter advance, despite being the largest relativistic orbital effect, is less suitable for testing the no-hair theorem. This is because:

- It is a small correction to the dominant Schwarzschild pericenter precession, requiring very accurate knowledge of $M_\bullet$, a_{sma}, and e to subtract the main term.
- It can be affected by second post-Newtonian (2PN) order corrections.

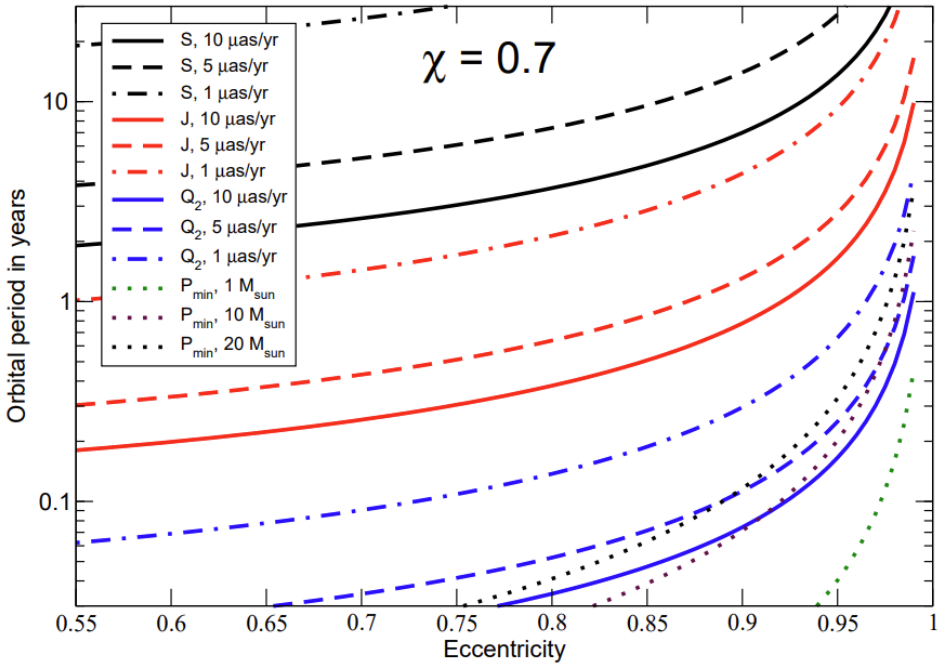

(a) Orbital periods vs. eccentricity required to give measurable relativistic precession rates. Dotted curves show minimum periods vs. e that avoid tidal disruption, for various stellar masses.

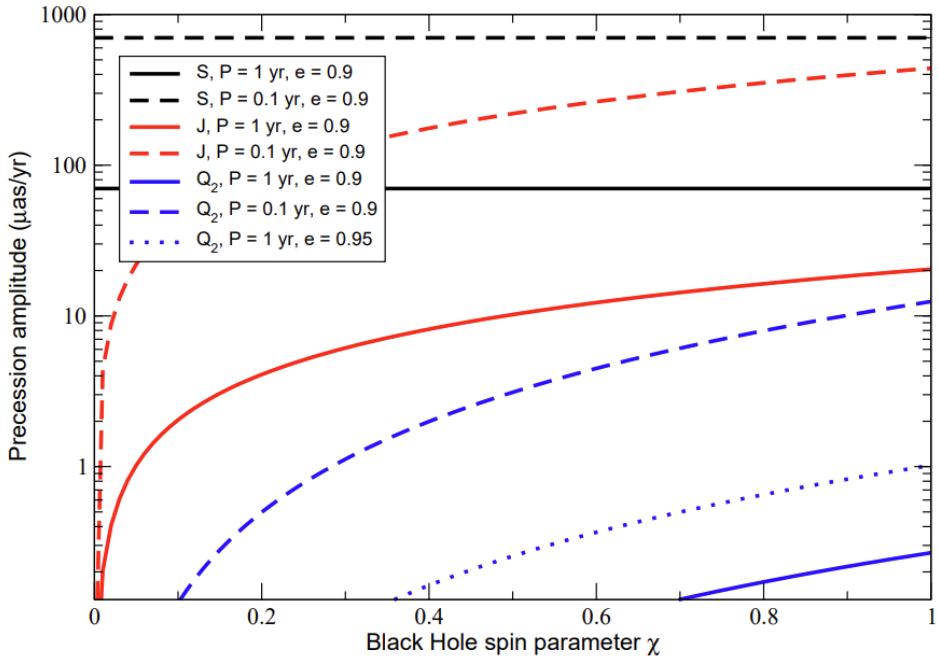

(b) Relativistic precession amplitudes vs. black hole spin parameter χ.

Figure I.7: Requirements for detecting the Schwarzschild precession and the spin related effects (extracted from [142])

- Any spherically symmetric distribution of mass (e.g., dark matter, gas) within the orbit can contribute to the pericenter advance.
- Tidal distortions of the stars near pericenter in highly eccentric orbits can also lead to additional pericenter advance.

Furthermore, a star getting too close to the black hole could be tidally disrupted, setting a lower bound on the orbital period.

In contrast, the precessions of the node and inclination are relatively immune to these complicating effects:

- Spherically symmetric mass distributions have no effect on these orbital elements.
- Tidal distortions of the star (if quasi-equilibrium with negligible tidal lag) produce purely radial perturbing forces, thus not affecting the node or inclination.

Testing the no-hair theorem To test the no-hair theorem, one must determine five parameters: the black hole's mass ($M_\bullet$), the magnitude and two angles of its spin (J), and the value of its quadrupole moment (Q). While the "Kepler-measured" mass can be derived from stellar orbital periods, it might require data from multiple stars to separate it from any extended mass distribution.

The key strategy proposed is to measure the rates of change of the node and inclination for at least two stars in non-degenerate orbits.

- Using the measured orbital elements and their drifts for a single star, the geometric relation:
$$\frac{\sin i \, \frac{d\Omega}{dt}}{\frac{di}{dt}} = \tan \beta,$$
allows for the determination of the angle β. This measurement constraints the black hole's spin axis to lie on a plane perpendicular to the star's orbital plane that makes an angle β relative to the line of nodes.
- A second stellar orbit measurement provides another such plane. The intersection of these two planes determines the direction of the spin axis (modulo a reflection).
- With the spin axis direction determined, the magnitudes of J, and Q can then be solved for using the measured quantities.

The analysis of astrometric data would involve a sophisticated multiparameter least-squares fit, similar to those used in solar system celestial mechanics, treating $M_\bullet$, J, and Q as parameters to be fitted alongside the orbital elements of each

star. This model can be extended to include additional matter distributions, tidal effects, and other phenomena.

The study also notes the need for future work to account for complicating effects such as:

- Second post-Newtonian (2PN) corrections to Schwarzschild pericenter advance.
- Tidal effects.
- Effects of unseen mass distributions within the stellar orbits (e.g., a massive torus of matter could induce fractional changes in apparent angular momentum and quadrupole moment).
- Light deflection and Shapiro time delay effects.

I.3.2 Toward Relativistic Orbit Fitting of Galactic Center Stars and Pulsars (Angélil et. al. 2010)

The work by Angélil, Saha and Merritt in [3] develops a technique for fitting nearly Keplerian orbits with general relativistic perturbations to observations of stars or pulsars orbiting the Galactic Center black hole. The authors emphasize that stars like S2, during their pericenter passage, reach speeds making them significantly more relativistic than known binary pulsars, thus offering new avenues for testing general relativity. The long orbital periods of S stars (e.g., S2 at ~ 16 years) compared to binary pulsars (e.g., ~ 1 day or less) mean that a different strategy is needed, focusing on detailed observation of one or a few orbits, particularly around pericenter passage where relativistic effects are strongest.

Relativistic Effects and Observables The study considers various physical effects influencing the observed apparent frequency (spectral lines for stars, pulses for pulsars):

- **Time Dilation**: This is the strongest relativistic perturbation, a consequence of the equivalence principle. For S stars, spectroscopic detection is expected around pericenter passage (detected for for S2 [59]). In pulsar timing, this is known as the Einstein time delay.
- **Orbit Perturbations**:
  - *Pericenter Advance*: The Schwarzschild precession is well-measured in binary pulsars [as well as for S2 since the writing of this work [70]].

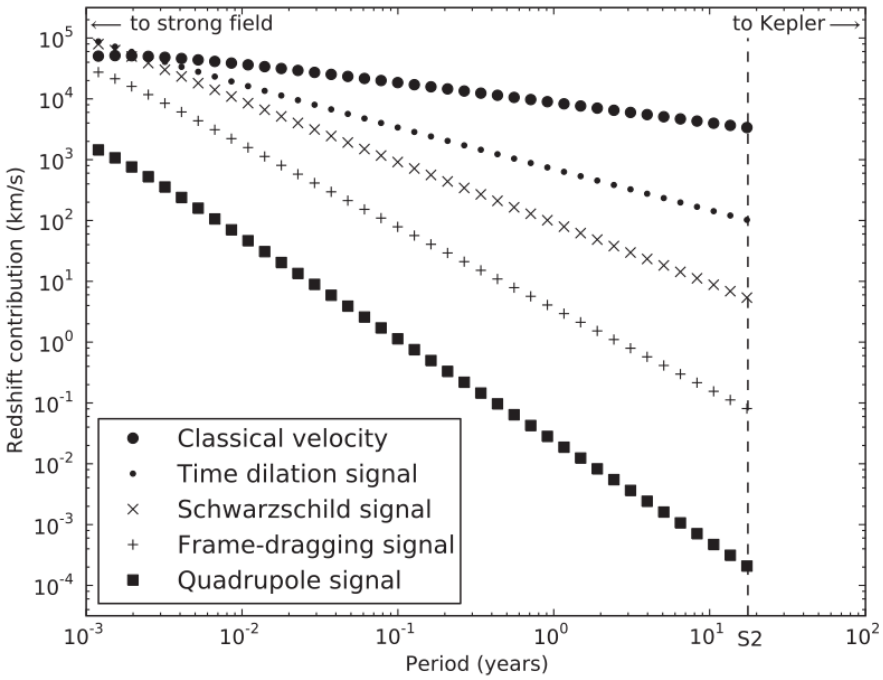

(a) Redshift contributions of different orbital effects

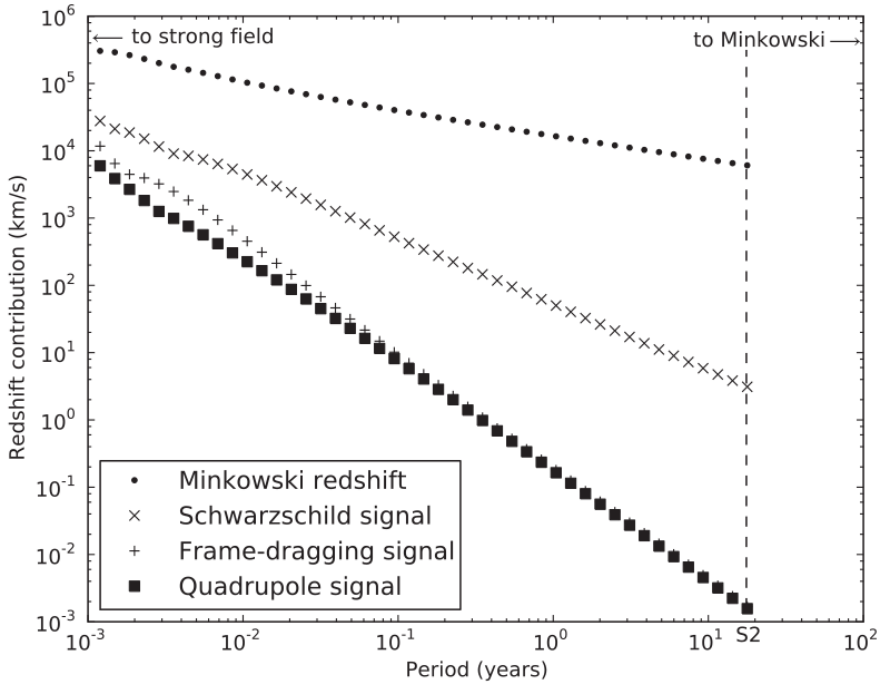

(b) Same as I.8a but for photon propagation delays

Figure I.8: GR effects affecting the radial velocity (extracted from [3])

However, long orbital period of S stars and potential Newtonian precession from distributed mass present difficulties for measuring higher order precessions. Nevertheless, for stars significantly closer to the black hole, precession of orbital planes due to higher-order spin and quadrupole effects becomes accessible.

- *Orbital Decay*: This effect, due to gravitational radiation, is not considered measurable for S stars due to long timescales and extreme mass ratios.
- *Velocity Perturbations*: GR-induced velocity perturbations vary along the orbit and are larger and more concentrated around pericenter for S stars, making them potentially easier to isolate from Newtonian effects. They include frame dragging, and torquing-like effects induced by the black hole's quadrupole moment.

- **Light Paths and Travel Times**:
  - *Strong Deflection (Lensing)*: While spectacular, this would be a rare event.
  - *Small Perturbations (Shapiro Delay)*: These can produce detectable changes in light travel time, leading to a time-dependent redshift contribution that for a star like S2 is comparable to velocity perturbations.

The observable chosen is the apparent frequency, ν. The paper defines "redshift" as $c\ln(\nu_0/\nu)$, where ν_0 is the source frequency. This approach treats stellar spectroscopy and pulsar timing in a unified way.

Modeling and Methodology The core of the paper's method assumes that both star (or pulsar) and photon trajectories are geodesics in a pure Kerr metric. The authors of [3] use a perturbative Hamiltonian formulation derived from the Kerr metric, where each relativistic effect corresponds to a specific Hamiltonian term that can be "toggled on and off" for analysis.

In Figure I.8 extracted from [3], we see that while Schwarzschild effects are comparable between photon and orbit perturbations, the frame-dragging effect is considerably weaker on photons than on the star, suggesting that the orbital manifestation is what matters for measuring black hole spin in the post-Newtonian regime. The study uses numerical integration of Hamilton's equations for calculations, and an algorithm to solve the boundary value problem of finding photons that reach the observer. This is computationally intensive but parallelized for efficiency.

A significant caveat noted is the *neglect of Newtonian perturbations* due to other mass distributions (stars, stellar remnants, dark matter) in the Galactic Center region. While these can introduce "Newtonian foreground" effects, the specific time-dependence of relativistic effects may allow them to be extracted.

Fitting and Signal-to-Noise Ratio (S/N) The redshift curve is dependent on eight essential parameters, plus additional ones for secondary effects. The nine parameters considered are:

- Black hole mass ($M_{\rm BH}$), setting the overall timescale.
- Intrinsic emission frequency (ν_0), corresponding to the pulsar spin frequency, treated as an additive constant.
- Keplerian orbital elements: semimajor axis (a), eccentricity (e), argument of pericenter (ω), orbital inclination (I), and epoch (ϵ_0). The longitude of the ascending node (Ω) is fixed to 0 as it does not affect redshift in their chosen coordinate system.
- Pulsar spin-down rate ($\dot{\nu}$) for pulsar cases.

The black hole spin is assumed to be maximal and perpendicular to the line of sight for simplicity. A quasi-Newton limited memory Broyden–Fletcher–Goldfarb–Shanno optimization routine is used for the fitting [101].

To quantify detectability, the paper defines a Signal-to-Noise Ratio (S/N) as $\sqrt{\chi^2_{\rm red}}$. This is calculated by generating a full redshift curve with all relevant Hamiltonian terms, adding Gaussian noise, and then fitting the data with a model *lacking* a specific Hamiltonian contribution. A higher $\chi^2_{\rm red}$ indicates a stronger detection of the missing effect.

Results on Detectability The paper presents results in two ways:

1. **Redshift Accuracy Demands for S2**:
   - With current spectroscopic precision of approximately 10 km/s, *time dilation is comfortably feasible to detect* [and done ever since the detection of the source [59]].
   - *Space curvature* requires a modest improvement in redshift resolution.
   - *Frame dragging and quadrupole effects* are "far below" current capabilities for S2.
   - If a pulsar on an S2-like orbit were discovered, timing precision of 3 μs over 1 hour (equivalent to 30 cm/s redshift precision) could, in principle, bring frame dragging and even quadrupole effects within reach.
2. **Orbit-Size Demands for Given Redshift Precision**:
   - If stars with orbital periods of order of a month are discovered, *frame dragging and the quadrupole moment could be measured with stellar spectroscopy from the European Extremely Large Telescope (E-ELT) at the level of 1 km/s.*

Effect	Required Redshift Rccuracy for S2	Required Orbital Period (yr) for Given Redshift Accuracy		
		$10\,\mathrm{km\ s^{-1}}$	$1\ \mathrm{km\ s^{-1}}$	$30\,\mathrm{cm\ s^{-1}}$
Time dilation	$\sim 60\ \mathrm{km\ s^{-1}}$	~ 50	$\gg P_{S2}$	$\gg P_{S2}$
Schwarzschild	$\sim 3\ \mathrm{km\ s^{-1}}$	~ 13	~ 30	$\gg P_{S2}$
Frame dragging	$\sim 10\,\mathrm{m\ s^{-1}}$	~ 0.5	~ 0.8	$> P_{S2}$
Quadrupole	$\sim 50\,\mathrm{cm\ s^{-1}}$	~ 0.04	~ 0.1	$\sim P_{S2}$

Table I.1: Summary of the Observational Thresholds at which Different Relativistic Effects are Exposed, Assuming a Source of Negligible Mass in a Pure Kerr Spacetime (extracted from [3]). Time dilation and Schwarzschild precession have been detected [59, 70]

.

- Relativistic effects become stronger closer to the black hole, and Newtonian perturbations are likely to weaken.

Table I.1 (extracted from [3]) summarizes the observational thresholds for various effects based on the required redshift precision and orbital period for S2 or scaled S2-like orbits.

The paper concludes that observing redshift variations over one or a few orbits, particularly around the pericenter passage, is a viable strategy for testing relativity using Galactic Center stars or pulsars. Incorporating astrometric information into the fitting procedure would enhance detection prospects, especially for constraining angular Keplerian elements. Detecting additional stars or pulsars with periods shorter than one year would significantly boost the chances of observing cumulative effects, such as precession.

I.3.3 Prospects for Constraining the Spin of the Massive Black Hole at the Galactic Center via the Relativistic Motion of a Surrounding Star (Yu et. al. 2016)

The work by Yu, Zhang, and Lu in [145] also investigates the feasibility and quality of constraining the spin of Sgr A*, through the detailed observation of the relativistic motion of surrounding stars. It addresses critical questions regarding the required observational precision and the orbital parameters of target stars necessary for obtaining tight constraints on the SMBH spin and metric. The authors aim to advance this research by using a full GR numerical method, arguing that an accurate constraint on the spin direction can also offer insights into the SMBH's assembly history.

Methodology

The study employs a full GR numerical method to simulate both the stellar motion around Sgr A* and the photon propagation from the star to a distant observer.

- **Kerr Metric and Geodesics**: The motion of a particle (star or photon) is described by equations derived from the Boyer–Lindquist coordinates of the Kerr metric (see subsection II.1.2) accounting for the particle's rest mass, energy at infinity, azimuthal angular momentum, and Carter's constant. Numerical integration of these equations is performed using an explicit fifth (fourth)-order Runge–Kutta method with high relative accuracies to precisely capture spin-induced effects.
- **System Geometry**: Two pseudo-Cartesian coordinate systems are defined: one in the SMBH frame (with the z-axis along the spin direction) and another in the observer's rest frame. The transformation between these frames is defined by the SMBH's spin angles (inclination i and position angle Ω). Stellar orbits are initially approximated as Newtonian ellipses, and their parameters are converted into the Boyer–Lindquist coordinates for GR calculations.
- **Ray-tracing**: For photons, a ray-tracing technique is used to determine the trajectories and energy shifts (redshifts) as they propagate from the star to the observer. This connects the star's apparent position on the sky plane to its relativistic orbital motion. The numerical accuracies for positions and redshifts are set to 10^{-4} µas and 10^{-6} km/s, respectively.
- **Mock Observations and Fitting**: Mock observations are generated for various stellar orbital parameters and assumed astrometric and velocity precisions. These mock data are then used to reconstruct the star's orbital elements and the SMBH's intrinsic properties (mass, spin, spin direction, and distance to the Sun) using a Markov Chain Monte Carlo (MCMC) fitting technique.

Key Findings and Results

The study presents detailed results on the sensitivity of spin-induced signals to the SMBH's spin direction and the quality of spin constraints achievable with future observational facilities. The leading spin effect is the Lense–Thirring (LT) precession of the star's orbital plane. The quadrupole (Q) term also contributes, but its contribution is typically only about 1% to a few percent of the total spin-induced effects for stars with semi-major axes of $\sim 300\text{˘}1000$ AU and eccentricities $\gtrsim 0.88$, significantly smaller than the LT precession.

Spin-Induced Signals and Spin Direction Dependence:

- **S2 Star**: For S2, the spin-induced position displacement at apoapsis can be close to the detection limit (up to ~ 13 µas for $\chi = 0.99$) or very small (~ 0.2 µas), depending on the spin direction. Similarly, the maximum spin-induced redshift difference over one orbit varies significantly (up to ~ 0.56 km s^{-1} or as low as 10^{-2} km s^{-1}) with spin direction.
- **Hypothetical Closer Star**: For a hypothetical star with a semimajor axis of 300 AU and eccentricity of 0.95 (orbital period ~ 2.6 years), the spin-induced signals are significantly stronger: up to ~ 84.9 µas for position displacement and ~ 38.9 km s^{-1} for redshift difference.

Comparison with Analytical Approximations: The study highlights the critical importance of including photon propagation effects (light bending and energy shifts) in the full GR numerical calculations. While analytical approximations for position displacement at apoapsis show a relatively good consistency with numerical results (residuals of 1% and 10% for S2 and the hypothetical star, respectively), analytical redshift differences often deviate significantly. This is because the analytical models usually omit photon propagation effects and the effect of the "slight difference between the true anomalies" ($\delta v'$ term[2]). The authors show that these effects, while smaller than the position shift, cannot be neglected for accurate SMBH spin constraints or quadrupole moment measurements.

Quality of Spin Constraint (MCMC Fitting):

- **Dependence on Precision**: For SMBH spin $\chi = 0.99$ and a favorable spin direction, the spin can be constrained to an accuracy of $\delta\chi \sim 0.1$ over ~ 45 years for S2 with position/velocity precisions of (10 μas, 1 km/s). For the hypothetical star, an accuracy of $\delta\chi \leq 0.02$ is achievable over ~ 10 years with the same precision.
- **Astrometric vs. Velocity Precision**: The paper finds that within the range of 1–30 μas for astrometric precision and 0.1–10 km/s for velocity precision, an improvement in astrometric precision is generally more effective at enhancing the quality of spin constraint than an improvement in velocity precision.

[2]When evaluating the effect of the spin on the redshift, we consider two orbits, one for a star with given initial orbital elements rotating around a non-spinning SMBH, and the other for a star with the same initial orbital elements but rotating around a rapidly rotating SMBH. Therefore, if one wants to be precise, we need to consider a redshift contribution due to the slight difference between the true anomalies (v') of these two stars at a given time t caused by the difference of the spin values. This contribution can only be calculated numerically and is thus neglected in analytical work.

- **Single Star vs. Multiple Stars**: Contrary to previous arguments that at least two stars might be needed to disentangle spin and quadrupole moment (e.g., [142]), the authors suggest that even a single star can achieve this if measurement precisions are sufficiently high and the observational period is long enough. They argue that this is because the star's orbital configuration evolves over time, thus having a different orientation after each revolution, replacing the need to have at least two orbits.

The study concludes that future facilities like GRAVITY, TMT, and E-ELT, offer promising prospects for constraining the GC SMBH spin. The spin direction's influence on signal strength is crucial, and monitoring stellar motion can help test its alignment with the young stellar disk, revealing aspects of the SMBH's assembly history. For optimal results, stars with semi-major axes $\leq$ 300 AU and eccentricities $\geq$ 0.95, observed over $\sim$ 10 years, are ideal for high-precision spin and potentially quadrupole moment constraints. The authors acknowledge that their results are optimistic, as they simplify by neglecting complications such as perturbations from background stars and tidal dissipation. While tidal dissipation is deemed negligible for the studied parameter space, background stellar perturbations could be a significant challenge. However, they note that the distinct evolutionary patterns of spin-induced effects versus Newtonian perturbations might allow for their separation. The study emphasizes the necessity of utilizing full GR numerical methods that account for photon propagation effects for high-precision constraints.

I.3.4 General Relativistic Effects on the Orbit of S2 with GRAVITY (Grould et al. (2017))

The study of [74] once again investigates the detectability of various general relativistic (GR) effects on the orbit of the S2 star around Sgr A*. The primary goal was to determine the minimum observational timescales needed to detect specific relativistic signatures such as the transverse Doppler shift, gravitational redshift, pericenter advance, gravitational lensing, Shapiro delay, and spin-related effects like the Lense–Thirring precession.

Methodology. The authors generated mock astrometric and spectroscopic observations of S2 using a fully general relativistic model (Model G), computed with the ray-tracing code `GYOTO` (see subsection V.1.1) in the Kerr metric (see subsection II.1.2). This model incorporates both star and photon geodesics, accounting for all relevant effects. Gaussian noise was added according to assumed measurement precisions: astrometric (σ_A = 10–100 μas) and spectroscopic (σ_V = 1–100 km s^{-1}), with denser sampling near pericenter passages.

Seven stellar-orbit models of increasing complexity (A to G) were compared:

- *Keplerian models* (A–C) — from pure Keplerian motion to inclusion of Roemer delay, transverse Doppler shift, and gravitational redshift.
- *Relativistic models* (D–F) — Schwarzschild and Kerr orbits, including Lense–Thirring effects, weak-field lensing, and (for Model F) approximations to photon curvature.
- *Full GR model* (G) — Kerr metric with full photon curvature and Shapiro delay, computed via ray tracing.

Detection thresholds were determined by fitting simplified models (A–F) to the mock Model G data and testing goodness-of-fit via χ^2 statistics (Levenberg–Marquardt for Keplerian models; MCMC for relativistic models).

Key results:

- *Roemer delay*[3]*:* detectable within 4 months (10 μas, 100 $\mathrm{km\,s^{-1}}$).
- *Relativistic redshifts*[4]*:* detectable within 2 months (10 μas, 10 $\mathrm{km\,s^{-1}}$).
- *Pericenter advance*[5]*:* detectable within $\sim$8 years (10 μas, 1-10 $\mathrm{km\,s^{-1}}$).
- *Gravitational lensing*[6]*:* detectable within $\sim$4 years (10 μas, 10 $\mathrm{km\,s^{-1}}$).
- *High-order photon curvature / Shapiro delay*[7]*:* detectable within 6–10 months (10 μas, 1 $\mathrm{km\,s^{-1}}$).
- *Lense–Thirring effect*[8]*:* not detectable for S2 within $\leq$30 years at the assumed precisions. The LT effect on photon paths is negligible ($<$ 1 μas, $\approx 10^{-2}$ $\mathrm{km\,s^{-1}}$).

[3]Its impact is necessary for exact orbit determination due to GRAVITY's precision, but it has not been distinctly detected or published as an independent empirical confirmation; its contribution is smaller than other relativistic effects and mainly enters as a correction term.

[4]These (gravitational redshift + transverse Doppler shift) were robustly detected with GRAVITY during S2's 2018 pericenter passage [59], matching GR's predictions—just as Grould et al. anticipated.

[5]GRAVITY confirmed this effect with S2, detected as predicted, with the first robust measurement published in [70]

[6]As of now, gravitational lensing's astrometric deflection has not been distinctly detected for S2—the signal is smaller than current systematic and random errors, so Grould et al. predicted timeline was optimistic for current data quality.

[7]These higher-order effects are modeled, and their cumulative contribution is at or lower than the detectability threshold, but they remain below robust detection significance for S2 so far (their very small signature is within noise and systematic floors).

[8]Not detected for S2 as of 2025. As Grould et al. forecast, this effect is too small for S2 under current measurement precision and timescales.

Detailed illustration: spin-induced shifts. Figure I.9 (adapted from [74]) shows the astrometric (upper panels) and spectroscopic (lower panels) residuals due to the spin effect, computed as the difference between Kerr ($a = 0.99$) and Schwarzschild ($a = 0$) predictions:

$$\begin{aligned} \Delta A_{\rm LT}|_{\rm rt} &= \sqrt{(RA_{a=0.99} - RA_{a=0})^2 + (DEC_{a=0.99} - DEC_{a=0})^2}, \\ \Delta RV_{\rm LT}|_{\rm rt} &= RV_{a=0.99} - RV_{a=0}. \end{aligned} \tag{I.6}$$

Astrometric differences are largest near apoapsis (lever-arm effect), while spectroscopic differences peak near pericenter. For certain (i', Ω') configurations, LT-induced astrometric shifts reach $\sim$40 μas; for others, they remain below 10 μas over three orbits. With $(\sigma_A, \sigma_{RV}) = (10\ \mu\text{as}, 10\ \text{km s}^{-1})$, $(a, i', \Omega') = (0.99, 45°, 160°)$, projected 1σ uncertainties on a are $\sim$0.4, 0.2, and 0.1 after 16, 30, and 47 years, respectively, with $\sigma_{i'} \sim 15°$, and $\sigma_{\Omega'} \sim 30°$ after three orbits (47 years). Comparable uncertainties were found for $a = 0.7$.

These constraints are similar to those obtained by Yu et al. (2016), who used a full ray-tracing model, supporting the sufficiency of Model F for these parameters.

I.3.5 What stellar orbit is needed to measure the spin of the Galactic Center black hole from astrometric data? (Waisberg et al. (2018))

Waisberg et al. investigated in [135] the requirements for stellar orbits to enable detection of black hole spin, focusing on what can be achieved with the GRAVITY instrument at the VLTI. While low-order GR effects (e.g., gravitational redshift, pericenter advance) are within reach for the S2 star, spin-related effects require closer stars to overcome Newtonian perturbations from other masses in the Galactic Center.

Methodology

Waisberg et al. (2018) employed a semi-analytic approach for their simulations:

- **Spacetime Approximation and Stellar Orbits:** The potential near the black hole is approximated as a Kerr spacetime, and stars are treated as test particles. The study uses the public YNOGKM code to trace time-like geodesics in the Kerr metric, which semi-analytically solves the geodesic equations. This method is efficient for irregular, sparse observing epochs as each sample is independent. Stellar orbits are parameterized in terms of Keplerian orbital elements relative to the sky plane, then rotated to the black hole coordinate frame, allowing for arbitrary spin axis orientation.

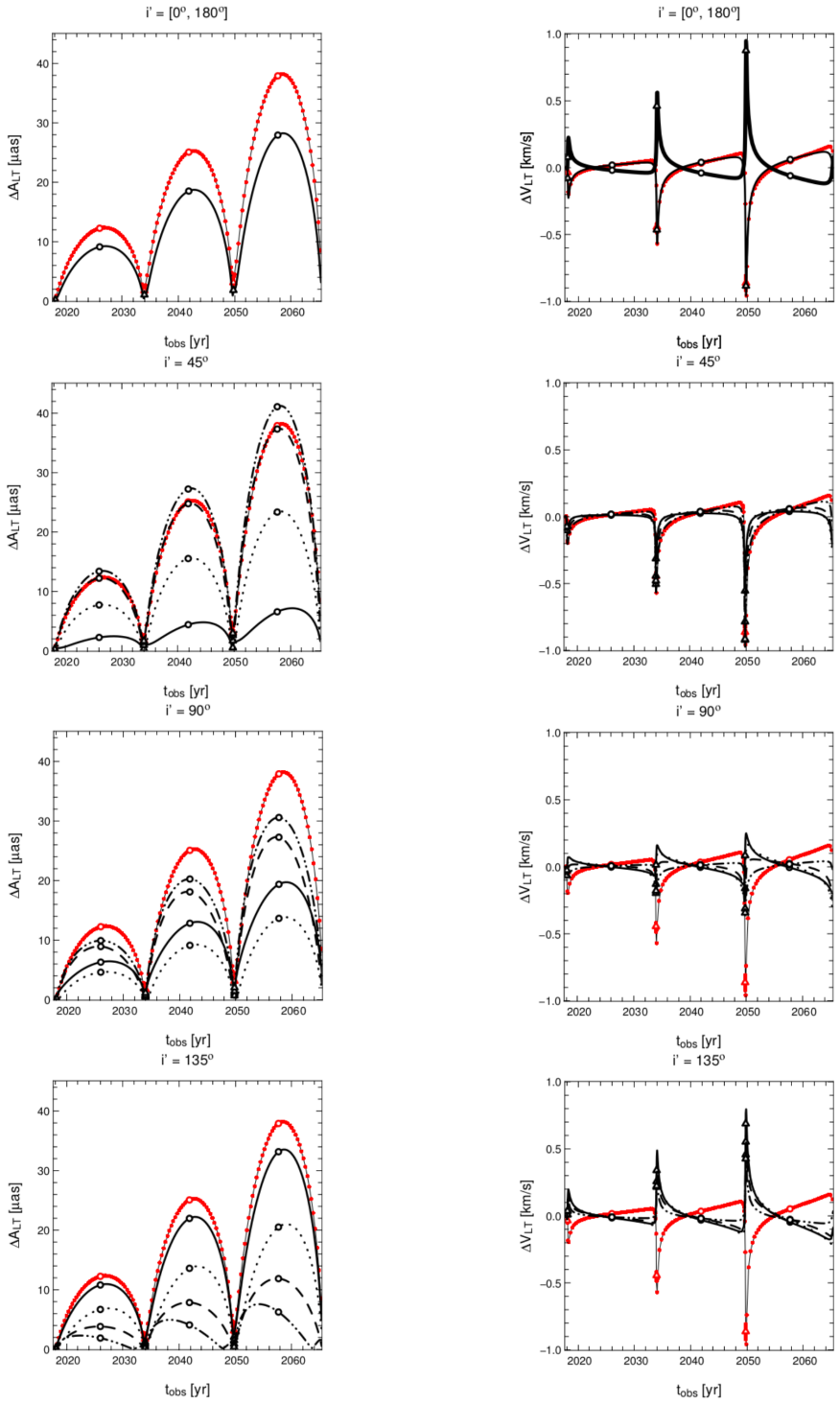

Figure I.9: Astrometric (left) and spectroscopic (right) residuals induced by black hole spin for S2, in KerrKS coordinates, for $a = 0.99$ and various (i', Ω') values [74]. Curve styles correspond to different Ω'; see text for details. Red circles indicate the fiducial case $(i' = 45°, \Omega' = 160°)$; open triangles mark pericenters; open circles mark apocenters.

- **Redshift Calculation:** The redshift (Z) of the received starlight is computed based on the photon energies measured by an observer co-moving with the star and at infinity, and the star's four-velocity and the photon's four-momentum at emission and reception.
- **Photon Orbit Simplification:** The effect of black hole spin on the photon orbit is considered negligible for the stars of interest (with semi-major axis $a_{orb} \gtrsim 100R_S$), inducing shifts of less than 1 μas astrometrically and less than 3 km/s spectroscopically. Therefore, the photon orbit is computed using the Schwarzschild metric in the weak-field approximation. This approximation is valid except for stars with extremely high inclinations ($i_{orb} \gtrsim 78°$) passing behind the black hole, which are rare but could offer significant light bending effects for probing spin.
- **Simulated Campaigns and Fitting:**
  - Mock observations are simulated across a grid of stellar orbital parameters (a_{orb}, e), with a_{orb} ranging from 200 R_S to 5000 R_S and eccentricity e from 0.1 to 0.9. Other Keplerian parameters are set similar to S2, and the black hole spin is assumed to be $\chi = 0.9$ with specific spin angles ($i_{spin} = \epsilon_{spin} = 0°$).
  - Observing campaigns are set for a total duration of $T = 4$ years, with 120 observations (3 consecutive months per year, 10 consecutive days per month). Gaussian errors are added with astrometric accuracies (σ_x) of 10 μas and 100 μas.
  - To estimate spin error, a null hypothesis test is used, rather than Bayesian Markov Chain Monte Carlo (MCMC), due to challenges in spin parameter convergence. This involves finding the best-fit zero-spin orbit to the simulated data and assessing the probability that the data were generated by such a model based on the residuals. The χ^2 value is converted to a p-value, then to a significance σ. A downhill simplex algorithm is employed for fitting, with 10 initial simplexes to avoid local minima.

Required Orbital Parameters for Black Hole Spin Measurement

A key result of the study is an analytic criterion for the detectability of black hole spin in terms of the orbital semi-major axis $a_{\rm sma}$ and eccentricity e:

$$a_{\rm sma}(1-e^2)^{3/4} \leq 300R_S\sqrt{\frac{T}{4\text{ years}}}\left(\frac{N_{\rm obs}}{120}\right)^{0.25}\sqrt{\frac{10\,\mu\text{as}}{\sigma_x}}\sqrt{\frac{a}{0.9}}. \tag{I.7}$$

When fitting all orbital parameters simultaneously, spin effects are partially masked, tightening this requirement by a factor of $\sim$ 2–3 compared to the pure effect-size estimate.

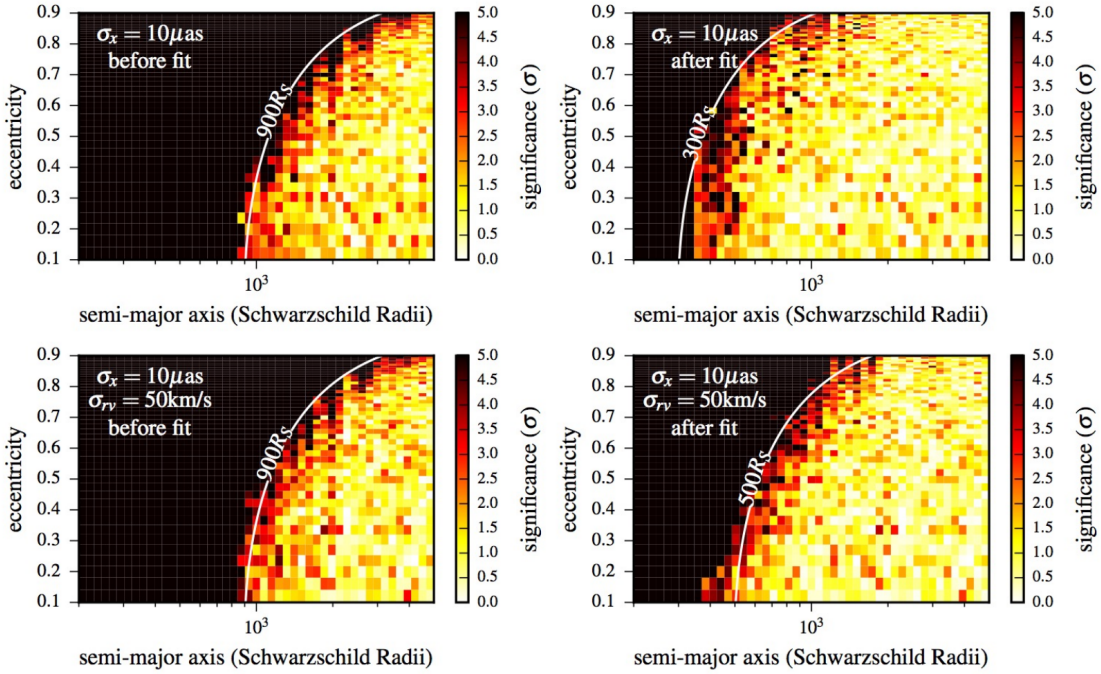

Figure I.10: Significance σ of a black hole spin detection from stellar orbit monitoring as a function of $(a_{\rm sma}, e)$ for a 4-year campaign with $N = 120$ observations [135]. Panels and curves are described in the text.

As shown in Figure I.10, the white contours correspond to constant $a_{\rm sma}(1 - e^2)^{3/4}$ and separate regions of low and high detection significance. For an astrometric precision $\sigma_x = 100\,\mu$as, a star would need $a_{\rm sma}(1 - e^2)^{3/4} \lesssim 100\,R_S$ to allow a high-significance spin measurement.

Expected Number of Stars

Based on known stellar distributions in the GC (thermal eccentricity distribution $n(e)de = 2ede$, semi-major axis distribution $n(a_{orb}) \propto a_{orb}^{0.7}$, and K-band Luminosity Function $\beta \approx 0.20$), the study estimated the number of detectable stars.

- Stars that would undergo tidal disruption (periastron distance $R_p < R_t \sim 30R_S$) are excluded.
- For GRAVITY, stars with K < 19 are considered detectable.
- For a canonical observing campaign of 4 years with 120 observations and $\sigma_x = 10\mu$as, the expected number of stars that would allow a significant detection of black hole spin is approximately 0.035. The median orbital parameters for such stars are $\approx (1200R_S, 0.95)$.

- When other orbital parameters must be fitted simultaneously, degeneracies between parameters can partially absorb the relativistic signal, thereby reducing the number of stars for which relativistic effects can be robustly detected.
- Extending the observing campaign to 10 years with 300 observations increases the expected number of stars to 0.12.
- These estimates should be regarded as cautious, as they rely on extrapolations into the innermost region of the Galactic Center (GC), which has so far remained beyond current angular resolution limits. In particular, they depend on assumptions about the K-band luminosity function (KLF), i.e., the distribution of stars as a function of their near-infrared brightness. If the KLF continues rising toward fainter magnitudes, the number of detectable stars suitable for relativistic studies could increase. Conversely, a break or flattening of the KLF in the inner region would reduce the expected number of observable targets. In addition, the possible presence of a cusp of massive stars or stellar-mass black holes could further enhance the number of suitable objects. Some recent studies suggest that current estimates may in fact be pessimistic by a factor of ~ 2.

Effect of Radial Velocities

The paper also explores the potential contribution of radial velocity measurements:

- Direct detection of spin through radial velocity alone requires very high precision (e.g., 0.3 km/s for S2/10), which is not currently achievable with existing instruments ($\sim$ 30 km/s for S2).
- A potential method using spectral differential interferometry with GRAVITY in medium resolution is proposed, which could achieve a radial velocity precision (σ_V) of approximately 50 km/s.
- While this precision might not be sufficient to measure spin directly, adding radial velocity measurements can improve the constraints on other orbital parameters, thereby preventing the masking of spin effects. This effect is more pronounced for more eccentric orbits.
- Including radial velocity measurements with $\sigma_V = 50$ km/s, while maintaining astrometric precision at $\sigma_x = 10\mu$as, increases the expected number of stars by a factor of two, to 0.07 for a 4-year campaign, and to 0.23 for a 10-year campaign.

Conclusions and Discussions

Waisberg et al. (2018) conclude that while GRAVITY will be instrumental in detecting GR effects, closer stars are essential for measuring black hole spin due to the dominance of Newtonian perturbations for currently known stars like S2.

- The semi-analytical Kerr geodesics code used proved efficient for simulating orbits with sparse sampling.
- Light bending can enhance the pericenter advance signature for S2, potentially leading to earlier detection.
- The need to fit simultaneously for non-spin parameters makes the requirements for spin detection more stringent than theoretical predictions based purely on effect size.
- Radial velocity measurements at $\sim$ 50 km/s precision can significantly aid spin detection by improving constraints on other orbital parameters.
- The study assumes the black hole is at the origin; however, GRAVITY may reference stellar positions directly to Sgr A*, potentially simplifying the reference frame. This approach is enabled by GRAVITY's phase-referenced interferometry: the instrument tracks both Sgr A* and nearby stars simultaneously, so stellar positions are defined relative to the observed Sgr A* centroid in the same visibility data set [58].
- Crucially, the study acknowledges the simplification of neglecting extended mass distributions. Newtonian perturbations from stars and stellar remnants could mask the spin precession, although their different temporal evolution patterns might allow for separation over long observation periods. Existing estimates of stellar mass in the inner region are low, but a theoretical cusp of stellar-mass black holes could pose a significant challenge if their total mass exceeds $\sim 100 M_{\odot}$ within 25 mas.
- Other complementary methods for constraining Sgr A*'s spin include pulsar timing, direct imaging of the "black hole shadow," and monitoring of NIR flares.

I.3.6 Constraining the spin using other methods

Apart from analyzing the orbits of S stars there exist several other complementary methods to constrain the spin of Sagittarius A*. These alternative approaches exploit distinct observational signatures and physical processes associated

with the black hole's strong gravitational field and its surrounding environment. In the following, we present these methods, which include direct imaging and polarimetry with the Event Horizon Telescope, pulsar timing in the Galactic Center region, variability studies of the accretion flow leveraging quasi-periodic oscillations, modeling of relativistic outflows and jets linked to spin energy extraction, and prospective gravitational wave observations. Each technique provides unique insights and constraints on the spin parameter, contributing to a comprehensive multi-modal understanding of this complex and pivotal astrophysical object.

Event Horizon Telescope Imaging and Polarimetry

The Event Horizon Telescope (EHT) has revolutionized the study of Sagittarius A* by providing horizon-scale imaging through very long baseline interferometry (VLBI). This method constraints the spin by resolving the black hole's shadow and its surrounding photon ring, whose size, shape, and asymmetry directly depend on the spacetime metric governed by the spin parameter [34, 37]. In particular, the shadow diameter scales with mass, while deviations from circularity can reflect spin-induced frame dragging effects. Polarimetric measurements from the EHT enhance understanding by revealing magnetic field geometry and dynamics of the accretion flow at the event horizon, which are themselves influenced by spin through magnetohydrodynamic (MHD) processes [20, 33]. Although current spin constraints derived from EHT data rely on detailed MHD modeling and radiative transfer assumptions, improvements in array sensitivity, frequency coverage, and imaging algorithms continue to reduce systematic uncertainties. Thus, EHT imaging remains one of the most direct methods for probing the black hole's spin-related strong gravity effects in situ [37].

Radio Pulsars Orbiting Sagittarius A*

Pulsar timing offers a uniquely precise probe of the spin of Sgr A* through general relativistic effects on pulsar orbits. Pulsars orbiting near the black hole experience relativistic frame-dragging causing characteristic modulations in their pulse arrival times dependent on the spin magnitude and orientation [81, 94]. Precision timing facilitates measurements of spin-induced orbital precession to accuracies approaching one percent or better, especially when timing multiple pulsars with varied orbital parameters [81, 113, 115]. Current observational challenges include the non-discovery of pulsars within milliparsec-scale orbits around Sgr A*, limited by scattering and sensitivity constraints, but upcoming surveys with the Square Kilometre Array (SKA) are expected to vastly improve this capability [22, 88]. Simulation studies underscore that combining data from multiple orbiting pulsars can break degeneracies with mass and distance parameters and mitigate systematics from perturbations due to stellar environment in the Galactic Center [81].

Accretion Flow Variability and Quasi-Periodic Oscillations

Variability in Sgr A*'s accretion flow, including quasi-periodic oscillations (QPOs), provides an indirect channel to infer its spin by linking observed flux modulations to orbital dynamics near the innermost stable circular orbit (ISCO) [113, 115, 147]. QPO frequencies correspond to general relativistic orbital frequencies or resonances within the accretion disk, which shift with the spin parameter altering the ISCO radius [9]. Temporal and spectral analyses across radio, submillimeter, and X-ray bands have identified candidate oscillations whose properties can be modeled using relativistic hydrodynamic simulations and diskoseismology frameworks [117]. Nonetheless, interpretation remains challenging due to the complexity of the accretion environment, magnetic turbulence, and uncertainties in the emission mechanisms [132]. Despite these challenges, the QPO approach offers valuable spin constraints complementary to imaging and timing, especially when used alongside multiwavelength observations [113, 115].

Outflow and Jet Modeling

The spin of Sagittarius A* can also be indirectly inferred by modeling relativistic jets or outflows powered by spin energy extraction mechanisms such as the Blandford-Znajek process [12, 126]. Observations in radio and X-ray bands characterize jet power, collimation, and variability, which can then be matched to theoretical models linking jet luminosity and efficiency to the black hole's spin [96, 99]. However, these methods are inherently model-dependent due to uncertainties in accretion physics, magnetic field topology, and environmental factors influencing jet formation and propagation [19]. Consequently, while outflow modeling provides useful supplementary constraints and insight into energetics related to spin, it is best employed combined with more direct probes like stellar dynamics, imaging or pulsar timing [40].

Gravitational Wave Observations

Detecting gravitational waves (GWs) from compact objects orbiting Sgr A* offers a fundamentally direct probe of the black hole spin through its imprint on orbital dynamics and GW waveforms. Spin modifies the orbital frequencies and precession of inspiraling stellar-mass black holes, neutron stars, or white dwarfs, affecting the multipolar structure of the emitted continuous gravitational waves [4, 54]. Although no continuous GW signals from the Galactic Center have yet been observed, proposed next-generation detectors such as the Einstein Telescope and LISA are expected to have sensitivity in relevant frequency bands to detect these sources [2, 116]. Analyses of GW signals will allow disentangling spin magnitude and orientation effects via frame dragging-induced waveform modulations, yielding model-independent spin determinations complementary to electromagnetic meth-

ods [4]. The feasibility depends strongly on the presence of suitably compact and close orbiting bodies and future advances in GW data analysis techniques.

Chapter II

Theoretical context

Contents

II.1 General relativistic framework and coordinate systems . . . 46

II.1.1 Schwarzschild Metric and Harmonic Coordinates 47

II.1.2 Kerr Metric: Boyer–Lindquist and Kerr–Schild Coordinates . . 48

II.2 Lagrange planetary equations 50

II.3 Post-Newtonian formalism 51

II.3.1 Post-Newtonian acceleration 52

II.1 General relativistic framework and coordinate systems

In this section, inspired by [56] and [77], we present the theoretical framework of general relativity (GR) relevant to the study of stellar orbits around Sgr A*. We first recall the Schwarzschild solution for a non-rotating spacetime, then extend it to the Kerr solution describing rotating black holes. The different coordinate systems commonly used in these contexts are also introduced.

II.1.1 Schwarzschild Metric and Harmonic Coordinates

The Schwarzschild solution describes the geometry of spacetime around a static, spherically symmetric mass M (e.g., a non-rotating star, planet, or black hole). In Schwarzschild coordinates (ct, r, θ, ϕ) and using the metric signature $(-,+,+,+)$, the spacetime interval reads:

$$ds^2 = g_{\alpha\beta}dx^\alpha dx^\beta = g_{tt}c^2dt^2 + g_{rr}dr^2 + g_{\theta\theta}d\theta^2 + g_{\phi\phi}d\phi^2 \tag{II.1}$$

with metric components:

$$\begin{aligned} &g_{tt} = -\left(1 - \frac{2GM}{rc^2}\right), \quad g_{rr} = \left(1 - \frac{2GM}{rc^2}\right)^{-1}, \\ &g_{\theta\theta} = r^2, \quad g_{\phi\phi} = r^2\sin^2\theta. \end{aligned} \tag{II.2}$$

Here G is the gravitational constant and c the speed of light.

The metric tensor $g_{\alpha\beta}$ is called the Schwarzschild metric. It should also be noted that far enough from the central mass, i.e. when $2GM/(rc^2) \to 0$, the Schwarzschild metric converges to the Minkowski metric and the spacetime is said to be asymptotically flat.

The Schwarzschild solution also exhibits two singularities:

- at $r = 0$, corresponding to a genuine physical singularity where curvature invariants diverge,
- at $r = R_S = \frac{2GM}{c^2}$, the so-called Schwarzschild radius, which is only a coordinate singularity in these coordinates (removable by a suitable change of variables).

The quantity R_S provides a natural length scale for the geometry around the central mass. In particular, for $r \gg R_S$, the Schwarzschild metric approaches the flat Minkowski metric.

Harmonic coordinates. It is sometimes useful to express the Schwarzschild metric in harmonic coordinates (ct, r_H, θ, ϕ), which are related to the Schwarzschild coordinates by

$$r_H = r - \frac{GM}{c^2}. \tag{II.3}$$

These coordinates satisfy the harmonic gauge condition

$$\Box x^\mu = \frac{1}{\sqrt{-g}}\partial_\nu\left(\sqrt{-g}\, g^{\mu\nu}\right) = 0.$$

In these coordinates the metric becomes [11, 137]:

$$ds^2 = -\frac{1-\frac{GM}{2c^2 r_H}}{1+\frac{GM}{2c^2 r_H}}\, c^2 dt^2 + \left(1+\frac{GM}{2c^2 r_H}\right)^4 \left(dr_H^2 + r_H^2 d\Omega^2\right), \tag{II.4}$$

where $d\Omega^2 = d\theta^2 + \sin^2\theta\, d\phi^2$. This form is asymptotically Cartesian and particularly convenient for post-Newtonian expansions.

II.1.2 Kerr Metric: Boyer–Lindquist and Kerr–Schild Coordinates

In reality, black holes — like any astrophysical body — are expected to be rotating. The Schwarzschild solution presented above is static and thus only offers an approximate description: while it correctly describes the exterior spacetime of any non-rotating, spherically symmetric body (whether a star, planet, or black hole), it does not apply once angular momentum is present. In 1963, Roy Kerr found the exact vacuum solution of Einstein's equations corresponding to a stationary, axisymmetric spacetime: the Kerr metric. Unlike the Schwarzschild case, this solution is restricted to describing the spacetime of a rotating black hole. The exterior geometry of a rotating star is never exactly Kerr, since it contains higher multipole moments that depend on the star's internal structure (e.g. mass distribution, equation of state). Because accretion processes are expected to spin up black holes efficiently, we generally expect astrophysical black holes to be rapidly rotating, which makes the Kerr metric the relevant exact solution for their description.

In a coordinate system (ct, r, θ, ϕ), called Boyer-Lindquist coordinates, the Kerr metric takes the form:

$$ds^2 = g_{\alpha\beta} dx^\alpha dx^\beta = g_{tt} dt^2 + g_{t\phi} dt\, d\phi + g_{rr} dr^2 + g_{\theta\theta} d\theta^2 + g_{\phi\phi} d\phi^2, \tag{II.5}$$

where

$$\begin{aligned}
\epsilon_\chi &= \frac{2GMr}{c^2(r^2 + \chi'^2\cos^2\theta)},\\
g_{tt} &= -(1-\epsilon_\chi), \quad g_{t\phi} = -2\chi'\epsilon_\chi \sin^2\theta,\\
g_{rr} &= \frac{r^2 + \chi'^2\cos^2\theta}{r^2 - \frac{2GM}{c^2}r + \chi'^2},\\
g_{\theta\theta} &= r^2 + \chi'^2\cos^2\theta,\\
g_{\phi\phi} &= \left[r^2 + \chi'^2(1+\epsilon_\chi\sin^2\theta)\right]\sin^2\theta.
\end{aligned} \tag{II.6}$$

where χ' is related to the angular momentum J or spin parameter χ of the black hole by:

$$\chi' = \frac{J}{cM} = \frac{GM}{c^2}\chi \tag{II.7}$$

When $\chi = 0$, the Kerr space-time becomes equivalent to the Schwarzschild one. The Boyer-Lindquist coordinates can thus be seen as a generalization of the Schwarzschild coordinates to the case with $\chi \neq 0$. As with Schwarzschild, the Kerr metric is asymptotically flat.

Singularities. Two singularities appear in the Kerr metric:

- $\rho^2 = r^2 + \chi'^2 \cos^2\theta = 0$, which corresponds to $r = 0$ and $\theta = \pi/2$: a physical *ring singularity* that appears regardless of the coordinate system.
- $\Delta = r^2 - \frac{2GM}{c^2} r + \chi'^2 = 0$, which admits two solutions:

$$r_\pm = \frac{GM}{c^2} \pm \sqrt{\left(\frac{GM}{c^2}\right)^2 - \chi'^2}.$$

These correspond to the *inner (Cauchy) horizon* at r_- and the *outer (event) horizon* at r_+. These are coordinate singularities specific to Boyer–Lindquist coordinates.

Kerr–Schild coordinates. To reveal the geometry of the ring singularity, one can transform to Kerr–Schild Cartesian coordinates $(c\tilde{t}, \tilde{x}, \tilde{y}, \tilde{z})$, where the metric becomes:

$$\begin{aligned} d\tilde{s}^2 = &-c^2 d\tilde{t}^2 + d\tilde{x}^2 + d\tilde{y}^2 + d\tilde{z}^2 \\ &+ \frac{R_S \tilde{r}^3}{\tilde{r}^4 + \chi'^2 \tilde{z}^2} \left[d\tilde{t} + \frac{\tilde{r}(\tilde{x}d\tilde{x} + \tilde{y}d\tilde{y})}{\chi'^2 + \tilde{r}^2} + \frac{\chi'(\tilde{y}d\tilde{x} - \tilde{x}d\tilde{y})}{\chi'^2 + \tilde{r}^2} + \frac{\tilde{z}}{\tilde{r}d\tilde{z}} \right]^2, \end{aligned} \tag{II.8}$$

with $\tilde{r}$ defined by

$$\tilde{r} = \sqrt{\frac{1}{2}\left(\tilde{x}^2 + \tilde{y}^2 + \tilde{z}^2 - \chi'^2 + \sqrt{(\tilde{x}^2 + \tilde{y}^2 + \tilde{z}^2 - \chi'^2)^2 + 4\chi'^2\tilde{z}^2}\right)}. \tag{II.9}$$

These coordinates are related to the Kerr-Schild spherical coordinates $(\tilde{r}, \tilde{\theta}, \tilde{\phi})$ by:

$$\begin{aligned} \tilde{x} &= \sqrt{\tilde{r}^2 + \chi'^2} \sin\tilde{\theta} \cos\left[\tilde{\phi} - \arctan\left(\frac{\chi'}{\tilde{r}}\right)\right] \\ \tilde{y} &= \sqrt{\tilde{r}^2 + \chi'^2} \sin\tilde{\theta} \sin\left[\tilde{\phi} - \arctan\left(\frac{\chi'}{\tilde{r}}\right)\right] \\ \tilde{z} &= \tilde{r}\cos\tilde{\theta} \end{aligned} \tag{II.10}$$

The Kerr-Schild spherical coordinates are related to the Boyer-Lindquist ones by the expressions:

$$\begin{aligned} c d\tilde{t} &= c dt + \frac{2r}{\Delta} dr \\ d\tilde{r} &= dr \\ d\tilde{\theta} &= d\theta \\ d\tilde{\phi} &= d\phi + \frac{\chi'}{\Delta} dr \end{aligned} \tag{II.11}$$

and we note that the BL r and θ are respectively equal to the spherical Kerr-Schild coordinates $\tilde{r}$ and $\tilde{\theta}$ respectively.

At $r = 0$, $\theta = \pi/2$ ($\tilde{z} = 0$), we find $\tilde{x}^2 + \tilde{y}^2 = \chi'^2$, a ring of radius χ'—hence the term *ring singularity*.

In the following, we refer to Boyer–Lindquist coordinates as "KerrBL" and Kerr–Schild Cartesian coordinates as "KerrKS".

II.2 Lagrange planetary equations

As will be presented in subsections V.1.2, we can use the orbital perturbation theory [97, 142] to write the derivative of each, time-varying, osculating orbital parameter with respect to time, as a function of the various $\mathcal{R}$, $\mathcal{S}$ and $\mathcal{W}$ terms, the perturbative accelerations expressed in the Gaussian frame (see subsection

IV.1.4). They are called the Lagrange planetary equations[1] and are expressed as:

$$\frac{\mathrm{d}p}{\mathrm{d}t} = 2\sqrt{\frac{p^3}{Gm}}\frac{1}{1+e\cos f}\mathcal{S}; \tag{II.12}$$

$$\frac{\mathrm{d}e}{\mathrm{d}t} = \sqrt{\frac{p}{Gm}}\left[\sin f\mathcal{R} + \frac{2\cos f + e(1+\cos^2 f)}{1+e\cos f}\mathcal{S}\right]; \tag{II.13}$$

$$\frac{\mathrm{d}\iota}{\mathrm{d}t} = \sqrt{\frac{p}{Gm}}\frac{\cos(\omega+f)}{1+e\cos f}\mathcal{W}; \tag{II.14}$$

$$\sin\iota\frac{\mathrm{d}\Omega}{\mathrm{d}t} = \sqrt{\frac{p}{Gm}}\frac{\sin(\omega+f)}{1+e\cos f}\mathcal{W}; \tag{II.15}$$

$$\begin{aligned}\frac{\mathrm{d}\omega}{\mathrm{d}t} = \frac{1}{e}\sqrt{\frac{p}{Gm}}\Bigg[&-\cos f\mathcal{R} + \frac{2+e\cos f}{1+e\cos f}\sin f\mathcal{S} \\ &-e\cot\iota\frac{\sin(\omega+f)}{1+e\cos f}\mathcal{W}\Bigg].\end{aligned} \tag{II.16}$$

No approximations are done to obtain Eqs. (II.12) to (II.16) from Eqs. (II.19).

Finally,

$$\begin{aligned}\frac{\mathrm{d}f}{\mathrm{d}t} &= \left(\frac{\mathrm{d}f}{\mathrm{d}t}\right)_{\text{Kepler}} - \left(\frac{\mathrm{d}\omega}{\mathrm{d}t} + \cos\iota\frac{\mathrm{d}\Omega}{\mathrm{d}t}\right) \\ &= \sqrt{\frac{Gm}{p^3}}(1+e\cos f)^2 \\ &\quad + \frac{1}{e}\sqrt{\frac{p}{Gm}}\left[\cos f\mathcal{R} - \frac{2+e\cos f}{1+e\cos f}\sin f\mathcal{S}\right],\end{aligned} \tag{II.17}$$

which reminds that f is the angle between the *varying* pericenter and the position vector of the star $\mathbf{r}$ (see Figure IV.3).

II.3 Post-Newtonian formalism

As will be seen in parts 2 and 3 of this manuscript, the post-Newtonian (PN) formalism is particularly well-suited for modeling the motion of stars near Sgr A*, as it provides a perturbative expansion in powers of a small parameter $\epsilon \propto v/c$ that

[1] If one want to study circular orbits where $e = 0$, it is advised to use an alternative set of variables to avoid the null denominator in Eq. (II.16). This is done in [139]. Here we consider realistic orbits where $e \neq 0$.

cleanly separates different relativistic effects—Schwarzschild precession, Lense–Thirring frame dragging, and quadrupole moment—according to their PN order [112].

Post-Newtonian orders. The PN formalism consists of expanding the metric, and hence the equations of motion, in powers of the dimensionless parameter $v/c \sim (Gm/rc^2)^{1/2}$, where v is the characteristic orbital velocity and r a typical orbital separation. The Newtonian dynamics corresponds to the zeroth order, denoted 0PN. The successive corrections scale as $(v/c)^{2n}$ and are referred to as nPN orders. For example, 1PN terms are of order $(v/c)^2$ relative to Newtonian gravity, 2PN terms are of order $(v/c)^4$, and so on. Half-integer orders, such as 1.5PN $\sim (v/c)^3$, appear when spin couplings are included. In this work, we will use the PN expansion of the orbital dynamics up to the 2PN order, as will be justified in subsection VI.1.3.

This separation is crucial when fitting astrometric and spectroscopic data, as it allows the contributions of each effect to be identified and measured independently, a key requirement for testing the no-hair theorem. The PN approach is also compatible with the osculating elements method used in orbital mechanics, enabling observational data to be interpreted in terms of time-varying Keplerian elements while retaining relativistic corrections. Moreover, the framework naturally accommodates additional Newtonian perturbations from extended mass distributions or stellar encounters, and because the relativistic parameter

$$\epsilon = \frac{Gm}{c^2 p}, \tag{II.18}$$

is small for S-star orbits ($\epsilon \sim 10^{-4} - 10^{-3}$, even for S2/10), the PN series converges quickly, providing accurate results without integrating the full Kerr geodesics. Finally, the PN framework is flexible enough to allow the quadrupole moment Q to be treated as independent from the spin χ, which is essential when testing deviations from the Kerr prediction $Q \propto -\chi^2$.

II.3.1 Post-Newtonian acceleration

In the PN approximation, the equation of motion of a star of negligible mass $m_{\rm star}$ compared to the mass of the black hole $M_\bullet$ written in harmonic coordinates [112] is given by:

$$\ddot{\mathbf{r}} = -\frac{Gm}{r^2}\mathbf{n}_{\rm orb} + \mathbf{a}_{\rm PN}, \tag{II.19}$$

where $m = M_\bullet + m_{star} \approx M_\bullet$. This approximation will be referred to as ❶ and can be justified by the fact that the small PN parameter ϵ defined in Eq. (VII.1) is

at least one or two orders of magnitude greater than $\eta = m_{star}/M_\bullet \sim 10^{-6} - 10^{-5}$ for any hypothetical star relevant for our study ($m_{star} \sim 1 - 10 M_\odot$ and with $p \leq p^{\mathrm{S2}}$). The separation vector from the black hole to the star is denoted by $\mathbf{r}$, and $\mathbf{n}_{\mathrm{orb}} = \mathbf{r}/r$ with:

$$r = |\mathbf{r}| = \frac{p}{1 + e\cos f}, \tag{II.20}$$

where $p = a_{\mathrm{sma}}(1-e^2)$ is the semi-latus rectum. It is important to emphasize that the above definitions of p, e, r_{peri}, and r_{apo} refer to the instantaneous osculating Newtonian ellipse used in the PN formalism. These quantities evolve secularly under relativistic perturbations such as pericenter precession. This is in contrast with the case of exact geodesic motion in a Kerr (or Schwarzschild) spacetime, where bound timelike geodesics possess well-defined pericenter and apocenter radii r_p and r_a that remain constant. One can then define

$$p = \frac{2 r_a r_p}{r_a + r_p}, \qquad e = \frac{r_a - r_p}{r_a + r_p},$$

which are constants of the geodesic motion and will yield a different definition of the pericenter advance compared to $p = a_{\mathrm{sma}}(1-e^2)$, [see 128]. These "relativistic" orbital elements should thus not be confused with the osculating ones employed here.

A dot in (II.19) denotes derivation with respect to the harmonic-coordinate time t and the PN acceleration $\mathbf{a}_{\mathrm{PN}}$ accounts for deviations from Keplerian motion due to GR. Thanks to the use of the osculating orbital elements method, we are able to use the Newtonian relation of Eq. (II.20) at each date, while keeping in mind that the involved parameters are time-varying, and that we use the weak-field and small-velocity approximation when working with the PN formalism.

If one wants to understand, at leading order, how the Schwarzschild precession and the spin-related effects impact the orbit of S-stars, it is sufficient to look at the dominant order of the analytical expressions of the secular shifts of orbital elements [142]. In practice, however, since the PN formalism appears to be the most suitable for the process of fitting the data of S stars[2], one will have to choose one specific PN order for all effects to be consistent in the fitting process. As will be seen in this section, the dominant order of the Lense-Thirring and quadrupole moment effects are at the 1.5PN (corresponding to $(v/c)^3$) and 2PN orders (corresponding to $(v/c)^4$), respectively. Therefore, we need to obtain the analytical expressions up to the 2PN order.

Considering the second-order PN approximation (2PN) corresponding to $(v/c)^4$, the PN acceleration can be decomposed into 3 parts:

$$\mathbf{a}_{\mathrm{PN}} \approx \mathbf{a}_{\mathrm{2PN}} = \mathbf{a}^{\mathrm{2PN}}_{\mathrm{Sch}} + \mathbf{a}^{\mathrm{1.5PN}}_{\mathrm{LT}} + \mathbf{a}^{\mathrm{2PN}}_{Q}, \tag{II.21}$$

[2]Because it allows to disentangle the Lense-Thirring from the quadrupole moment effects.

with $\mathbf{a}_{\rm Sch}^{\rm 2PN}$, $\mathbf{a}_{\rm LT}^{\rm 1.5PN}$, $\mathbf{a}_{Q}^{\rm 2PN}$ corresponding to the 2PN acceleration of the star due to the Schwarzschild precession, the spin and the quadrupole moment, respectively. The kPN notation indicates the PN order up to which the various effects enter the equation of motion. For instance $\mathbf{a}_{\rm Sch}^{\rm 2PN}$ contains both the 1PN and 2PN Schwarzschild contributions. By considering approximation $m = M_\bullet + m_{\rm star} \approx M_\bullet$, the accelerations can be expressed in terms of ϵ as [10, 97, 142]:

$$\begin{aligned}\mathbf{a}_{\rm Sch}^{\rm 2PN} = &\frac{\epsilon}{p}(1+e\cos f)^2\left[\left(4\frac{Gm}{r}-v^2\right)\mathbf{n}_{\rm orb}+4v_r\mathbf{v}\right]\\ &+\frac{\epsilon^2}{p}(1+e\cos f)^3\left[\left(2v_r^2-9\frac{Gm}{r}\right)\mathbf{n}_{\rm orb}-2v_r\mathbf{v}\right],\end{aligned} \tag{II.22}$$

$$\begin{aligned}\mathbf{a}_{\rm LT}^{\rm 1.5PN} = &-2\epsilon^{3/2}\sqrt{\frac{Gm}{p^3}}(1+e\cos f)^3\chi\\ &\times\left[2\mathbf{v}\times\mathbf{z}_{\rm bh}-3\left(\mathbf{n}_{\rm orb}\cdot\mathbf{v}\right)\mathbf{n}_{\rm orb}\times\mathbf{z}_{\rm bh}-3\mathbf{n}_{\rm orb}\left(\mathbf{n}_{\rm orb}\times\mathbf{v}\right)\cdot\mathbf{z}_{\rm bh}\right],\end{aligned} \tag{II.23}$$

$$\begin{aligned}\mathbf{a}_{Q}^{\rm 2PN} = &\frac{3}{2}\epsilon^2\frac{Gm}{p^2}(1+e\cos f)^4\chi^2\\ &\times\left[5\mathbf{n}_{\rm orb}\big(\mathbf{n}_{\rm orb}\cdot\mathbf{z}_{\rm bh}\big)^2-2\big(\mathbf{n}_{\rm orb}\cdot\mathbf{z}_{\rm bh}\big)\mathbf{z}_{\rm bh}-\mathbf{n}_{\rm orb}\right],\end{aligned} \tag{II.24}$$

with $v^2 = v_r^2 + v_t^2$. The dimensionless spin parameter χ and quadrupole moment parameter Q are defined in section I.3 by Eqs. (IV.1) and (I.2), respectively.

Finally, it is worth elaborating on the physical meaning of the quadrupole moment in the context of a Kerr black hole. The fact that the dimensionless quadrupole moment is negative implies, from a Newtonian analogy, that the Kerr black hole behaves as an *oblate* body—i.e., flattened along the spin axis. This interpretation holds when working in harmonic coordinates, where the effective gravitational potential takes a form resembling the classical Newtonian potential of an extended mass distribution. Hence, this analogy is inherently *coordinate-dependent*, as the concept of "oblateness" presupposes a spatial slicing and a Newtonian-like potential structure.[3]

It is also noteworthy that the acceleration associated with the quadrupole moment, which we will encounter explicitly in Section II.3.1, does not arise from the standard post-Newtonian expansion, at any order. This is because such expansions usually model all gravitating bodies as point masses, thereby excluding internal structure effects like multipole moments. Instead, the quadrupole term must be

[3]The quadrupole moment defined in harmonic coordinates does not have the same interpretation in other coordinate systems such as Boyer-Lindquist or Kerr-Schild.

added separately as a Newtonian perturbation due to an axisymmetric mass distribution. Specifically, the quadrupole acceleration is the lowest-order correction to a departure from spherical symmetry and takes the generic Newtonian form

$$\mathbf{a}_Q \propto \frac{GQ}{r^4} \propto \frac{G^3M^3}{r^4c^4}\chi^2 \propto \epsilon^2\frac{GM}{r^2}\chi^2,$$

as shown in Eq. (II.24). This means it effectively contributes at the 2PN order in the motion of a test particle. However, it is important to emphasize that this is a *Newtonian* term in form—introduced as a classical potential correction rather than derived from the post-Newtonian expansion—despite entering the dynamics at the same order as true 2PN terms.

We note that the Schwarzschild acceleration is composed of first and second terms of the RHS in Eq. (II.22), respectively of 1PN and 2PN orders. The Lense-Thirring and quadrupole moment accelerations are composed of only one term (see Eqs. (II.23) and (II.24)), of order 1.5PN and 2PN, respectively. The leading order of the various effects is thus 1PN, 1.5PN, 2PN, for Schwarzschild, Lense-Thirring, and quadrupole moment effects, respectively. We need to consider the subleading order only for the Schwarzschild term. Lense-Thirring and quadrupole moment subleading terms appear at order above 2PN. In this paper, we consider only the Kerr spacetime, and thus plug the expression of Q given by Eq. (I.2) into our equations. However, if we want to test the no-hair theorem, we should not assume Eq. (I.2) when generating the expression of the secular shifts[4], since Q would need to be measured independently from χ.

[4]One can thus replace χ by its expression as a function of Q in the analytical expressions of subsection VII.2.1 to retrieve he analytical expressions as a function of quadrupole moment.

Chapter III

Instrumental context

Contents

III.1 Interferometry: From Principles to GRAVITY+ 57

III.1.1 Introduction to Optical Interferometry 57

III.1.2 The GRAVITY Instrument 62

III.1.3 The GRAVITY+ Upgrade 64

III.2 Spectroscopy: ERIS and MICADO 65

III.2.1 Basics of Spectroscopy 65

III.2.2 The ERIS Instrument 65

III.2.3 The MICADO Instrument 66

This chapter provides an overview of the principles of interferometry, leading to a presentation of the Very Large Telescope Interferometer (VLTI) instrument GRAVITY and its ongoing upgrade, GRAVITY+.

As mentioned previously, the use of the interferometric instrument GRAVITY, composed of the 4 Unit Telescopes of the VLT was at the center of the study of the Sgr A* environment. This instrument, coupled with the spectrograph SINFONI, which was also located at Paranal, allowed us to study not only the movement of flares but also the orbits of several stars in the vicinity of the black hole. Most importantly, by accurately following the motion of the star S2, the precise deter-

mination of the mass of Sgr A* was finally made possible.

In table III.1 we present the instruments with the best astrometric and spectroscopic precisions in the near infrared. Note that the values given in this table are only indicative and depend on the flux received by the instrument, which depend on the observation conditions. GRAVITY+ involves adaptive optics improvements that will allow the instrument to get up to a 20-fold increase of the number of photons that can be captured by this new generation. This implies a better temporal coverage and the reduction of systematic errors as well as photon noise. In other words, GRAVITY+ will allow us to detect stars in the galactic center region with a magnitude in the K-band up to $m_K = 22$ [62], as opposed to $m_K \leq 19$ with GRAVITY. This will thus have the potential to track fainter stars that could be closer to the black hole than S2, such as the putative S2/10 star considered in our work.

Table III.1: Astrometric and spectroscopic precisions of various past, current and future instruments, capable of observing in the near infrared.

Maximal precision	Astrometric (µas)	Spectroscopic (km/s)	State
SINFONI (VLT)	–	$\approx 10 - 100$	Decommissioned
NIRSPEC (Keck)	–	$\approx 10 - 100$	Operational
GRAVITY (VLT)	$\approx 50 - 100$	–	Operational
ERIS (VLT)	–	$\approx 10 - 100$	Operational
GRAVITY+ (VLT)	$\approx 10 - 50$	–	Under development
MICADO (ELT)	$\approx 50 - 100$	$\approx 1 - 10$	Operational in 2028+

III.1 Interferometry: From Principles to GRAVITY+

III.1.1 Introduction to Optical Interferometry

Optical interferometry is one of the most powerful observational techniques in modern astronomy, allowing angular resolutions far beyond those of any single telescope. Its principle relies on correlating the light waves collected at spatially separated apertures, whose correlations are mathematically linked to the source brightness distribution through the Zernike–van Cittert theorem [110] (see below).

This connection between spatial coherence and imaging forms the theoretical foundation of long-baseline interferometric astronomy.

Historically, long-baseline interferometry was pioneered in the 19th century. Fizeau's 1868 idea of double-slit experiment provided the first conceptual framework [43], quickly followed by Stephan's attempt to measure stellar diameters in 1874 [125]. In 1921, Michelson and Pease famously measured the angular diameter of Betelgeuse [98], proving the principle of very high-angular-resolution observations. Nearly half a century later, Labeyrie's demonstration of interference between two independent telescopes in 1975 laid the foundations for modern optical long-baseline interferometry [90].

During the same decades, radio interferometry advanced rapidly, producing landmark results such as the imaging of Cygnus A and observations of apparent superluminal motion in 3C273 [76, 105]. By contrast, optical interferometry progressed more slowly because of several fundamental challenges intrinsic to shorter wavelengths [8, 29]:

- **Heterodyne detection inefficiency:** In the radio regime, phase-sensitive amplifiers allow the measurement of complex visibilities across many baselines simultaneously. At optical wavelengths, direct detection must be used. As a consequence, beams must be physically recombined, introducing significant photon losses [61].
- **Atmospheric turbulence:** Short wavelengths are far more affected by atmospheric seeing. Two consequences arise:
  - *Partial coherence across telescope apertures.* Incoming stellar wavefronts are distorted by turbulence. The introduction of single-mode fibers (the FLUOR instrument demonstrated by V. Coudé du Foresto [17] and G. Perrin [108] in the 1990s) largely solved this by spatially filtering the wavefronts. On large telescopes, adaptive optics (AO) became essential, with systems like MACAO at the VLTI enabling efficient fiber injection [61].
  - *Short coherence times between telescopes.* In the near-infrared K-band, the coherence time is typically below 100 ms. This necessitated the development of fringe tracking, i.e. real-time stabilization of the relative phase between telescopes. Introduced by **(author?)** [123], fringe tracking is critical for long coherent integrations, high spectral resolution, and phase-referenced astrometry.
  - *Atmospheric coherence length (Fried parameter).* In the optical/infrared, the Fried parameter r_0 is typically much smaller than large telescope apertures, meaning the wavefront is not coherent across the mirror. Unless AO is used, this severely limits single-dish imaging resolution and makes interferometry the only path forward [8].

- **Free-space propagation through multiple mirrors:** Complex optical trains in large interferometers reduce throughput compared to radio arrays [29].

Despite these difficulties, continuous technological progress in optics, detectors, methods, and control systems has made possible the current generation of long-baseline interferometers such as CHARA and the ESO Very Large Telescope Interferometer (VLTI).

Basic Quantities [110]

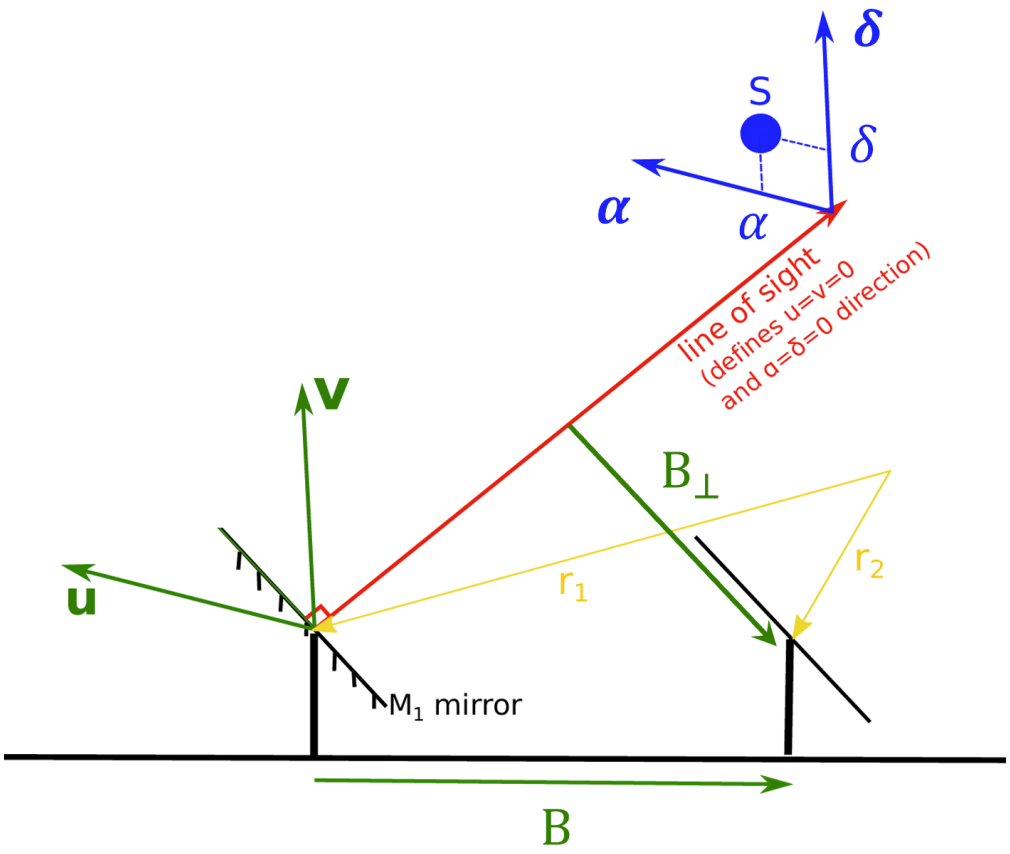

Figure III.1: Basic geometry in interferometry: line of sight, sky plane with angular coordinates (α, δ), and aperture plane with (u, v) coordinates. The baseline $\mathbf{B}$ between two telescopes is projected orthogonally to the line of sight as $\mathbf{B}_\perp$. Adapted from [110].

An extended source, located at angular coordinates (α, δ), emits an electric field measured at two points, $\mathbf{r}_1$ and $\mathbf{r}_2$, and times t_1 and t_2, within the aperture

plane of a telescope array as illustrated in Figure III.1. The recombined flux, F, is given by:

$$F = \iint_{\text{fov}} \left\langle |E(\alpha,\delta,\mathbf{r}_1,t_1) + E(\alpha,\delta,\mathbf{r}_2,t_2)| \right\rangle^2 d\alpha\, d\delta. \tag{III.1}$$

Here, $E(\alpha,\delta,\mathbf{r},t)$ denotes the complex electric field amplitude emitted by a source element located at angular coordinates (α,δ) and measured at position $\mathbf{r}$ and time t. The angular brackets $\langle\cdot\rangle$ indicate a time average performed over an interval long compared to the coherence time of the radiation. This expands to include the coherent flux (F_{coh}), which is the primary quantity of interest for interferometry:

$$F_{\text{coh}} = 2 \iint_{\text{fov}} \left\langle \text{Re}[E(\alpha,\delta,\mathbf{r}_1,t_1)\, E^*(\alpha,\delta,\mathbf{r}_2,t_2)] \right\rangle d\alpha\, d\delta. \tag{III.2}$$

The symbol E^* represents the complex conjugate of the electric field, and Re[$\cdot$] denotes the real part of a complex quantity.

The mutual coherence function, $\Gamma(\mathbf{r}_1,\mathbf{r}_2,t_1,t_2)$, is the time-averaged cross product of the electric field:

$$\Gamma(\mathbf{r}_1,\mathbf{r}_2,t_1,t_2) = \iint_{\text{fov}} \langle E(\alpha,\delta,\mathbf{r}_1,t_1) E^*(\alpha,\delta,\mathbf{r}_2,t_2)\rangle\, d\alpha\, d\delta \tag{III.3}$$

which is often simplified to its stationary counterpart

$$\Gamma(\mathbf{r}_1,\mathbf{r}_2,\tau) = \iint_{\text{fov}} \langle E(\alpha,\delta,\mathbf{r}_1,t) E^*(\alpha,\delta,\mathbf{r}_2,t+\tau)\rangle\, d\alpha\, d\delta, \tag{III.4}$$

assuming that the value of t does not matter (time-translation symmetry).

The *mutual degree of coherence* or visibility V is simply the normalized mutual coherence function at $\tau = 0$

$$V(\mathbf{r}_1,\mathbf{r}_2) = \frac{\iint_{\text{fov}} \langle E(\alpha,\delta,\mathbf{r}_1,t) E^*(\alpha,\delta,\mathbf{r}_2,t)\rangle\, d\alpha\, d\delta}{\sqrt{F_1 F_2}} \tag{III.5}$$

where F_i is I_i integrated over the field of view (fov), given by:

$$F_i = \iint_{\text{fov}} \left\langle |E_i| \right\rangle^2 d\alpha\, d\delta. \tag{III.6}$$

.

The contrast of the fringes, C, is defined by the flux contrast:

$$C = \frac{F_{\max} - F_{\min}}{F_{\max} + F_{\min}}. \tag{III.7}$$

This can be expressed using the modulus of the visibility:

$$V \;=\; 2\,\frac{\sqrt{F_1 F_2}}{F_1 + F_2}\,|V|\,, \tag{III.8}$$

which simplifies to $|V|$ if $F_1 = F_2$.

The phase information, $\arg V$, is related to the path difference between the rays and the intrinsic phase difference of the source:

$$\arg V \;=\; \frac{2\pi}{\lambda}\,\mathbf{B}\cdot\mathbf{s} \;+\; \delta\phi_{\rm intr}, \tag{III.9}$$

where $\mathbf{s}$ is the unit vector pointing to the source, and $\mathbf{B} = \mathbf{r}_2 - \mathbf{r}_1$ is the baseline connecting the two measurement points, and $\delta\phi_{\rm intr}$ is the intrinsic phase difference between the two waves. This leads to the standard form of the interferogram:

$$F \;=\; F_{\rm tot}\left(1 + |V|\cos\left(\frac{2\pi}{\lambda}\,\mathbf{B}\cdot\mathbf{s} + \delta\phi_{\rm intr}\right)\right). \tag{III.10}$$

Assuming there are delay lines that can vary the optical path x between the two paths of the rays, the interferogram reads

$$F = F_{\rm tot}\left(1 + C\cos\left(\frac{2\pi}{\lambda}\,\mathbf{B}_\perp\cdot\mathbf{s} + \frac{2\pi}{\lambda}x + \delta\phi_{\rm intr}\right)\right). \tag{III.11}$$

It is necessary to adjust the value of x (i.e. the differential lengths of the delay lines) such that $x + \mathbf{B}\cdot\mathbf{s}_0 = 0$ at some particular position $\mathbf{s}_0$ defined as the center of the field of view to center the fringes in the beam combination lab. Then for some other location $\mathbf{s} = \mathbf{s}_0 + \delta\mathbf{s}$ the interferogram reads

$$F = F_{\rm tot}\left(1 + |V|\cos\left(\frac{2\pi}{\lambda}\,\mathbf{B}_\perp\cdot\delta\mathbf{s} + \delta\phi_{\rm intr}\right)\right) \tag{III.12}$$

where $\mathbf{B}_\perp$ is the baseline projected orthogonally to the line of sight (note that $\delta\mathbf{s}$ is normal to the line of sight for a small enough source on sky).

The vector $\mathbf{B}_\perp/\lambda$ projected orthogonally to the line of sight and normalized by the wavelength, shows up as the important quantity for imaging. The two orthogonal directions in this plane normal to the line of sight are called (u, v), respectively pointing towards the East and the North. Thus the spatial coherence function or visibility becomes

$$\mathcal{V}(\mathbf{B}) \;\to\; \mathcal{V}\left(\frac{\mathbf{B}_\perp}{\lambda}\right) = \mathcal{V}(u, v). \tag{III.13}$$

The next section shows why these (u, v) coordinates are a good choice: they are the Fourier conjugates of the sky coordinates (α, δ).

Zernike–van Cittert Theorem [110]

The Zernike–van Cittert theorem establishes a direct relationship between the spatial coherence function, $V(u, v)$, and the intensity distribution on the sky, $I(l, m)$, where l and m are direction cosines (equivalent to angular coordinates α, δ for a small source). The theorem states that $V(u, v)$ and the normalized intensity distribution $I(\alpha, \delta)/F$ form a Fourier pair:

$$V(u,v) \;=\; \frac{\iint I(\alpha,\delta)\, e^{-2\pi i(u\alpha+v\delta)}\, d\alpha\, d\delta}{\iint I(\alpha,\delta)\, d\alpha\, d\delta}, \tag{III.14}$$

where $F = \iint I(\alpha, \delta)\, d\alpha\, d\delta$ is the total flux.

III.1.2 The GRAVITY Instrument

The GRAVITY instrument at the VLTI represents a major leap in optical interferometry, designed to overcome the historical limitations outlined above and to push faint-object science into a new regime [61]. It coherently combines the light from the four 8.2-m Unit Telescopes (UTs), delivering the angular resolution of a 140-m telescope with a collecting area of 200 m^2. Additionally, the four Auxiliary Telescopes (ATs) with 1.8-m diameters provide baselines up to 200 m.

GRAVITY's architecture integrates several key subsystems:

- **Adaptive optics:** the CIAO infrared wavefront sensors, working with the UT deformable mirrors, stabilize atmospheric turbulence in H+K bands, maximizing coupling into the single-mode fibers [119].
- **Fiber-fed beam combination:** single-mode fibers filter atmospheric corrugations and provide nm-precision differential Optical Path Delay (dOPD) control [109].
- **Integrated optics beam combiners:** two IO chips (for science and reference beams) implement an ABCD beam-combination scheme, providing instantaneous fringe sampling across all six baselines [107].
- **Fringe tracker:** real-time stabilization using SAPHIRA detectors, which achieve sub-electron read noise at kHz frame rates [42].
- **Laser metrology:** back-propagated laser light measures internal dOPDs with nanometer accuracy, enabling astrometric precision at the μas level.

The instrument reached science operations in 2016, demonstrating phase-tracking sensitivity to $m_K \approx 10$ and coherent science exposures down to $m_K \approx 17$, with visibility accuracies up to 0.3% and astrometric precision of a few 10 μas [61].

GRAVITY has already produced landmark results: detection of gravitational redshift and orbital precession in stars near Sgr A* [59, 64, 69], measurement of the Galactic Center distance to 0.3% precision [68], spatially resolving the BLR of quasar 3C 273 [66], direct spectroscopy of exoplanets such as HR 8799e and β Pic b [67, 71], and resolved studies of young stellar accretion and massive star multiplicity [63, 65].

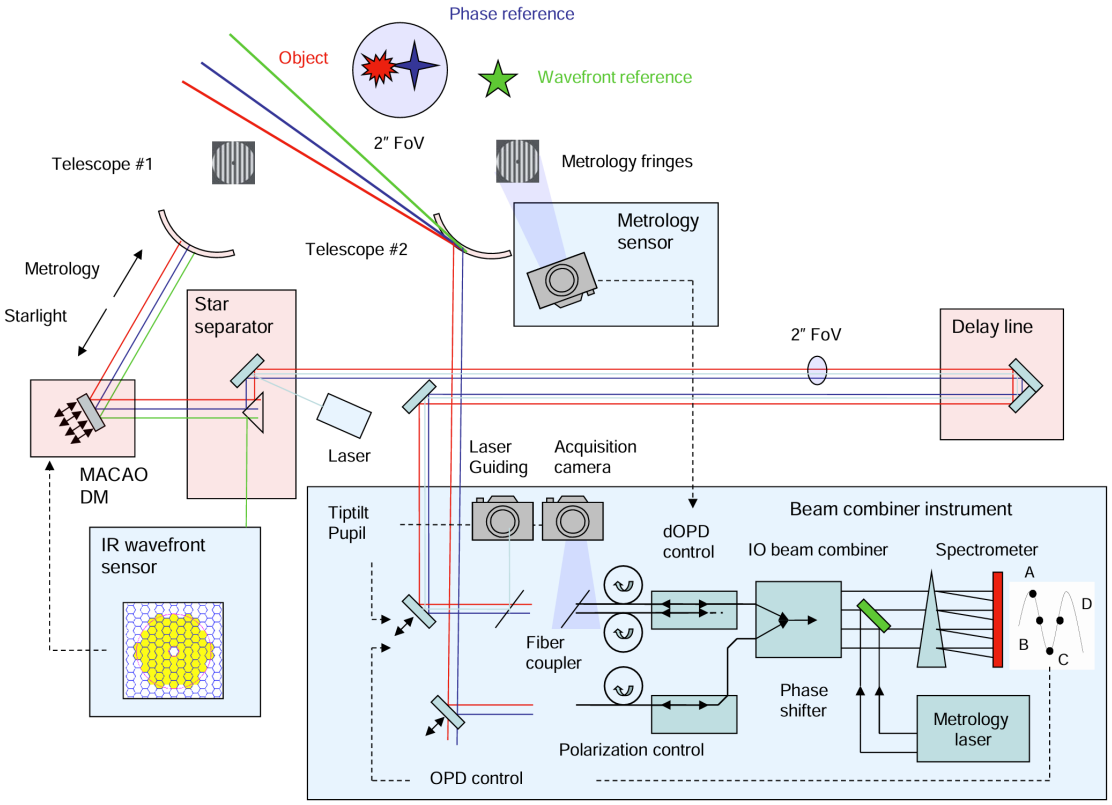

Figure III.2: Overview of the GRAVITY instrument. It combines adaptive optics, fiber-fed beam combiners, integrated optics chips, fringe tracking, and laser metrology to achieve unprecedented sensitivity and astrometric precision. (Adapted from [61, Figure 1])

III.1.3 The GRAVITY+ Upgrade

Despite its revolutionary capabilities, GRAVITY's sensitivity remains limited by AO performance and vibration-induced phase noise. The GRAVITY+ project, approved by ESO in 2021, introduces upgrades to both the instrument and VLTI infrastructure to extend sensitivity by 4–5 magnitudes and enable imaging down to $m_K \approx 22$ [29, 62]. The main upgrades include:

1. **Wide-field fringe tracking (GRAVITY-Wide):** off-axis phase referencing up to 30 arcseconds, dramatically increasing sky coverage.
2. **New AO systems:** high-order deformable mirrors (40×40 actuators) and improved wavefront sensors will boost Strehl ratios above 80% in K-band.
3. **Laser guide stars (LGS):** providing AO correction independent of natural guide star brightness, crucial for extragalactic targets.
4. **Instrumental improvements:** higher-throughput grisms, advanced vibration control, and reduced metrology noise.

With these upgrades, GRAVITY+ will expand science cases to fainter stars near Sgr A*, extragalactic AGN at $z \gtrsim 4$, cooler exoplanets, embedded young stars, microlensing events, and searches for intermediate-mass black holes in globular clusters. It will thus transform the VLTI into a facility capable of probing astrophysical processes across the Universe at unprecedented angular resolution.

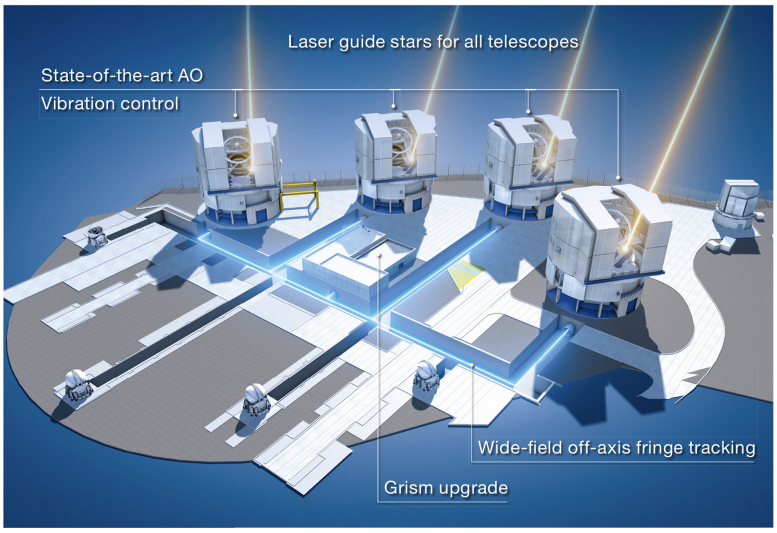

Figure III.3: The GRAVITY+ upgrade introduces wide-field fringe tracking, advanced AO with LGS, vibration suppression, and higher throughput optics, enabling a ∼5 mag sensitivity boost. (Adapted from [62])

III.2 Spectroscopy: ERIS and MICADO

III.2.1 Basics of Spectroscopy

Spectroscopy is a powerful analytical technique used to study the interaction between matter and electromagnetic radiation. Fundamentally, it involves the measurement of the intensity of light as a function of wavelength or frequency and can reveal a wealth of information about the physical and chemical properties of astronomical objects. At its core, spectroscopy relies on the quantum mechanical principle that atoms and molecules absorb and emit electromagnetic radiation at discrete energy levels corresponding to electronic, vibrational, and rotational transitions.

The principal quantities measured in spectroscopy are the position (wavelength or frequency) of spectral lines, their intensity, and their shape or width. These parameters encode critical information such as elemental composition, temperature, density, velocity, and magnetic fields of the source.

A spectrum can be continuous, line, or band in nature, reflecting the complexity of the source and the physical conditions present.

In astronomical contexts, spectroscopy enables the determination of radial velocities through Doppler shifts, chemical abundances, and physical conditions of stellar atmospheres, nebulae, and galaxies. It forms the backbone of modern astrophysics, providing direct measurements complementing photometric observations.

Understanding spectroscopy's fundamentals requires familiarity with quantum mechanics, electromagnetic theory, and statistical mechanics, linking microscopic processes to macroscopic observations. For a comprehensive introduction, readers can refer to resources such as [93] and [14].

III.2.2 The ERIS Instrument

The Enhanced Resolution Imager and Spectrograph (ERIS) is a state-of-the-art near-infrared instrument installed on the Very Large Telescope (VLT) Unit Telescope 4 (UT4). Designed to replace and advance the capabilities of earlier instruments such as SINFONI and NACO, ERIS combines high spatial resolution imaging with integral field and long-slit spectroscopy, optimized for diffraction-limited observations aided by advanced adaptive optics.

As shown in Figure III.4, ERIS is composed of two main subsystems: SPIFFIER, an integral-field spectrograph delivering spatially resolved spectra, and NIX, a near-infrared camera optimized for high-contrast and diffraction-limited imaging. Together, these modules cover the 1–2.5 µm range, enabling both detailed spec-

troscopy and sharp imaging across the near-infrared atmospheric windows. This spectral coverage is particularly well suited to probing heavily obscured regions such as the Galactic Center.

A key strength of ERIS is the synergy between its adaptive optics system and various modules: it provides the sharpness and sensitivity required to investigate crowded stellar fields and trace the kinematics of ionized and molecular gas in the immediate environment of Sgr A*. Beyond Galactic Center science, the combination of imaging and spectroscopy in a single instrument also makes ERIS a versatile tool for exoplanet characterization and extragalactic studies.

The commissioning and first results of ERIS, including its performance at the VLT are reported in recent publications from ESO [30, 31] and the Max Planck Institute for Extraterrestrial Physics [44].

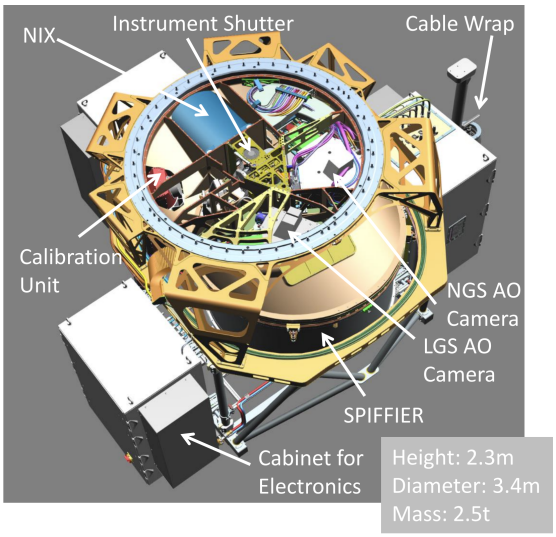

Figure III.4: Overview of the ERIS instrument major subsystems and installation at VLT UT4. CAD drawing (left) and telescope-mounted instrument (right). Adapted from Eisenhauer et al. (2023) Figure 1 [35].

III.2.3 The MICADO Instrument

MICADO is the Multi-AO Imaging Camera for Deep Observations, designed as the first-light near-infrared camera and spectrograph for the Extremely Large Telescope (ELT). With a primary mirror diameter of 39 meters, the ELT will be the world's largest optical telescope, and MICADO will exploit its extraordinary light-gathering power and angular resolution.

Optimized for imaging and long-slit spectroscopy in the 0.8 to 2.45 micron range, MICADO works in conjunction with advanced adaptive optics modules,

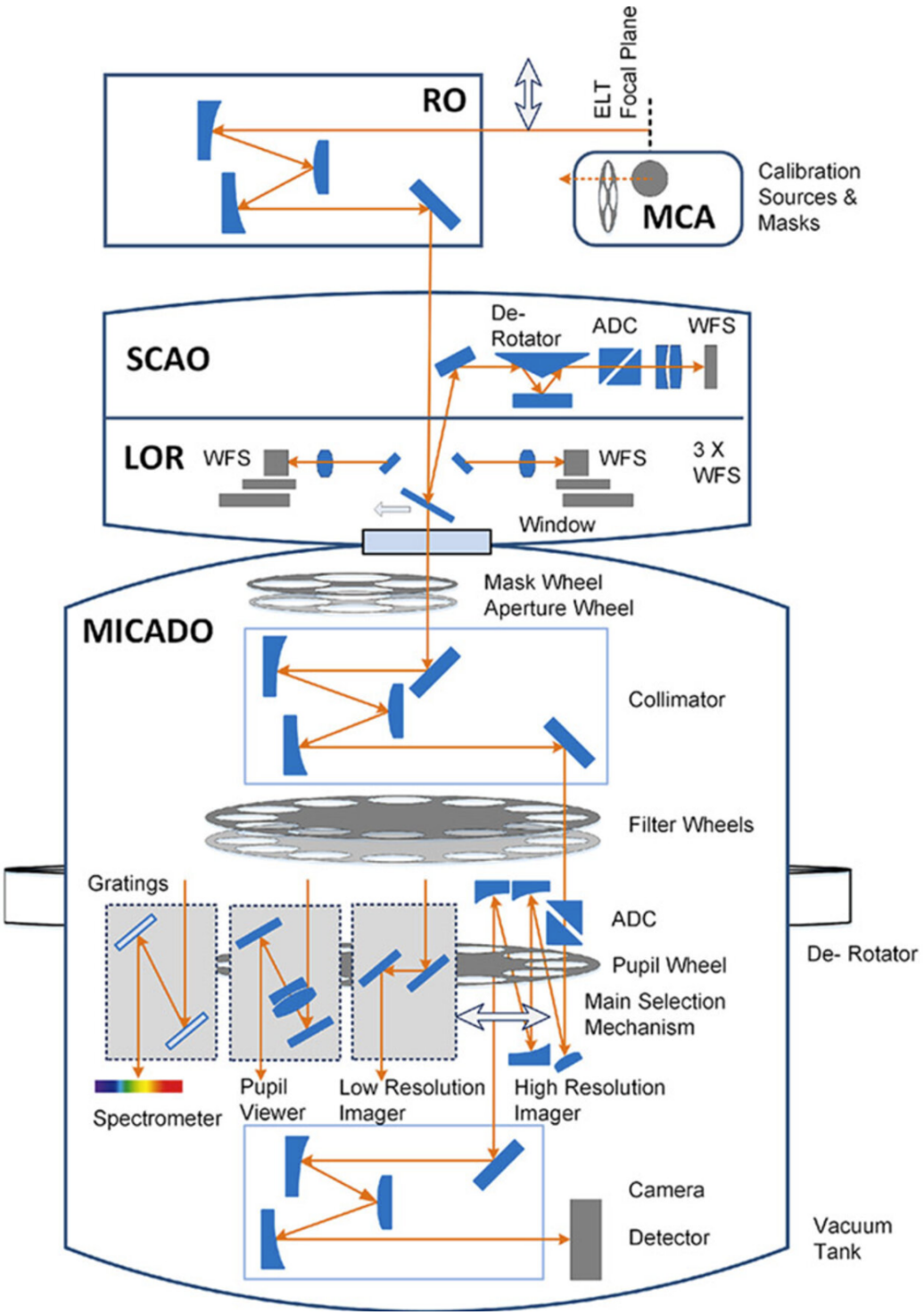

Figure III.5: Schematic of MICADO instrument layout with the MORFEO adaptive optics module and detector focal plane. Adapted from the ESO MICADO instrument page Figures 1 [32].

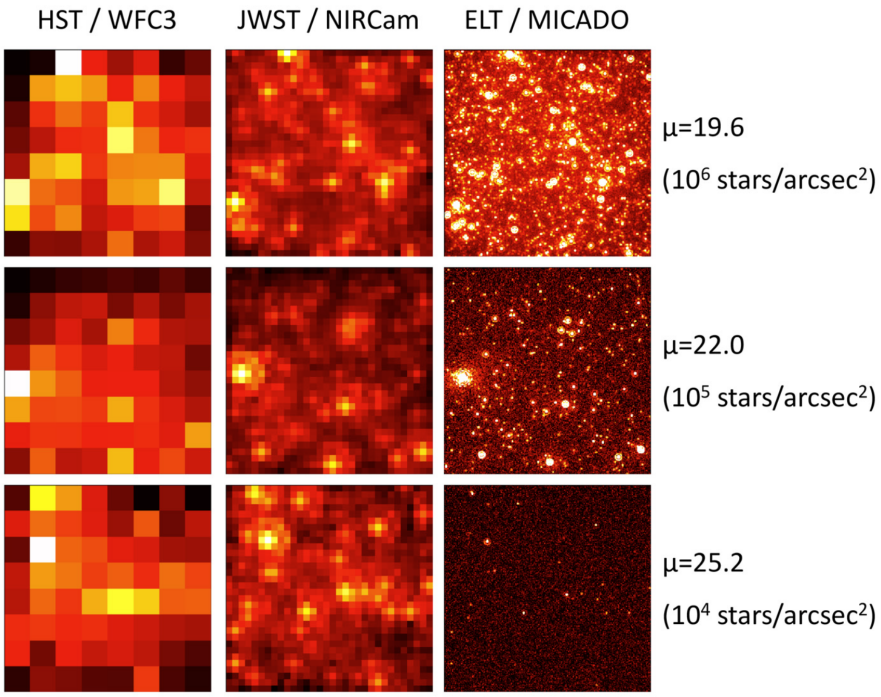

Figure III.6: MICADO pixel scale and field of view illustrations highlighting its high spatial resolution for Galactic Center astronomy. The simulated MICADO field of view is approximately 50.5"×50.5" in its wide-field imaging mode with 4 mas pixels. Adapted from ESO MICADO Figures 2 [32].

such as MORFEO, to deliver diffraction-limited images with exquisite spatial resolution. This capability is crucial for penetrating the dense dust clouds obscuring the Galactic Center and resolving individual stars in crowded fields.

Figure III.5 illustrates the instrument layout, including the MORFEO adaptive optics module and camera design, showing the focal plane array and detector arrangement. Figure III.6 compares MICADO's pixel scale and field of view, emphasizing its ability to resolve faint and crowded sources at the Galactic Center.

MICADO's design includes high-precision astrometry, allowing it to measure stellar motions near the supermassive black hole to unprecedented accuracy. Its spectral resolving power, ranging from about 10,000 to 20,000, permits detailed studies of stellar populations, chemical abundances, and gas kinematics in complex environments, with radial velocity measurements achievable at the 2–20 km/s level.

The instrument will significantly advance our understanding of the dynamics and evolution of the Galactic Center, the role of black holes in galaxy formation, and the physics of extreme gravitational environments. More information about MICADO's technical specifications, scientific goals, and developmental status are available from ESO [32], the Max Planck Institute for Extraterrestrial Physics [45], and partner collaborations [18].

Part 2

Presenting the framework and modeling the simulation tools

Chapter IV

Relativistic orbits

Contents

IV.1 Reference frames 72

IV.1.1 Observer frame 72

IV.1.2 Orbit frame 74

IV.1.3 Black hole frame 75

IV.1.4 Gaussian frame 77

IV.2 Orbit parametrization 79

IV.2.1 Newtonian orbits 79

IV.2.2 Relativistic orbits and osculating orbital parameters 80

IV.3 Differences between coordinate systems in orbit simulations 81

IV.3.1 Non-uniqueness of relativistic orbital parameterizations 82

IV.3.2 Estimating the coordinate system discrepancy 83

IV.1 Reference frames

Let us start this work by properly laying out the framework and present the four reference frames[1] that will be needed. We illustrate some them in Figure IV.1 before detailing them in the next subsections.

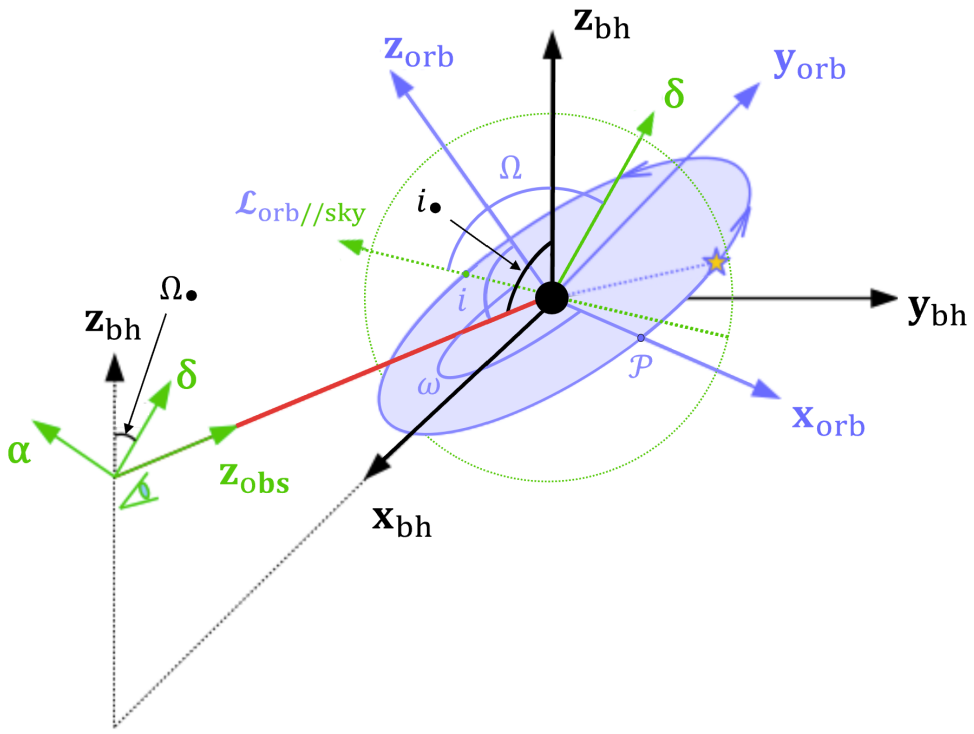

Figure IV.1: Illustration of all reference frames that will be detailed subsections IV.1.1 to IV.1.3.

IV.1.1 Observer frame

Following the convention of [112] and [97], we introduce a so-called fundamental frame $(\mathbf{X}, \mathbf{Y}, \mathbf{Z})$ that we use as a reference for describing the problem. The choice of this frame is arbitrary and will be made just below. The problem we want to study is about a star in a bound orbit around a rotating black hole, meaning that we need to describe two vectors in the fundamental frame; the angular momentum of the orbit and the angular momentum of the black hole, which will naturally define

[1] All reference frames in this work are right-handed and centered on Sgr A*.

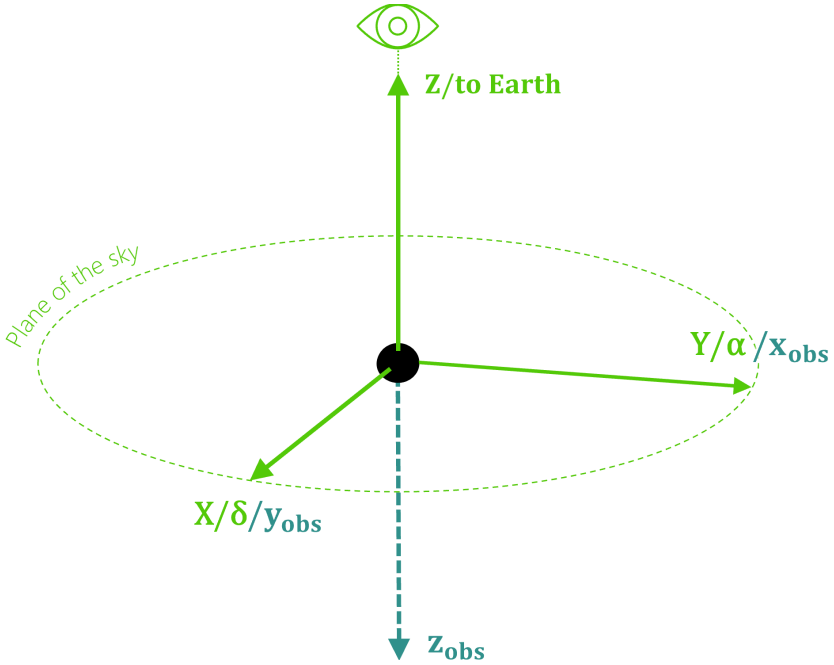

Figure IV.2: Different vectors describing the observer frame. Here we illustrate the fundamental frame when it matches that of a distant observer.

two other frames, that of the orbit and that of the black hole. Alternatively, to the fundamental frame $(\mathbf{X}, \mathbf{Y}, \mathbf{Z})$ it is common to define the observer frame $(\mathbf{x}_{\rm obs}, \mathbf{y}_{\rm obs}, \mathbf{z}_{\rm obs})$ as displayed in Figure IV.2, such that $\mathbf{z}_{\rm obs}$ represents the line of sight and thus points away from the observer. This frame is the one used in the ray-tracing code `GYOTO` mentioned in subsection V.1.1 and in the work of [104] and [73, 74].

Our choice of the fundamental frame: observer's frame

At this point, we need to make a choice of a fundamental frame. Considering that we eventually want to model the observable in the sky plane, it is natural to choose the observer's frame as the fundamental one. As illustrated in Figure IV.2, to do so, we take $\mathbf{Z}$ as pointing towards the observer and $(\mathbf{X}, \mathbf{Y}) = (\delta, \alpha) = (\mathbf{DEC}, \mathbf{RA})$ corresponding to the observer's screen with α or RA, and δ or DEC referring to the right ascension and declination, respectively. In other words, we define the fundamental plane as the sky plane and center it on the apparent position of Sgr A*. This choice has a crucial impact on the definition of orbital parameters considering that the angular parameters are defined with respect to the fundamental frame. In literature, we find different definitions of the observer's frame and fundamental frame. This leads to different results and thus cause apparent contradictions, as will be mentioned in the following sections.

IV.1.2 Orbit frame

The orbit frame $(\mathbf{x}_{\rm orb}, \mathbf{y}_{\rm orb}, \mathbf{z}_{\rm orb})$ is illustrated by Figure IV.3. We remind that the orbital plane of a relativistic orbit is not fixed (see the notion of osculating orbital parameters reminded in subsection IV.2). The axis $\mathbf{z}_{\rm orb}$ is defined along the angular momentum of the orbit, such that the plane $(\mathbf{x}_{\rm orb}, \mathbf{y}_{\rm orb})$ matches the instantaneous plane[2] of the orbit. Also, $\mathbf{x}_{\rm orb}$ always points to the instantaneous pericenter of the orbit. We define the line of nodes as the intersection between the orbit and sky planes, and its director vector $\mathcal{L}_{\mathbf{orb//sky}}$ goes from the black hole to $\mathcal{AN}_{\rm orb//sky}$, the ascending node of the orbit with respect to the observer. The latter is the intersection between the sky plane and the trajectory where the star passes from behind the sky plane ($Z < 0$) to the front ($Z > 0$). The orbital parameters that are included in Figure IV.3 will be discussed further in subsection IV.2.1. For the time being, it is useful to note that the orientation of an orbit is characterized by three angles: the two angles ι and Ω define the orientation of the orbital plane relative to the fundamental frame, and the third angle ω defines the position of the pericenter inside the orbital plane.

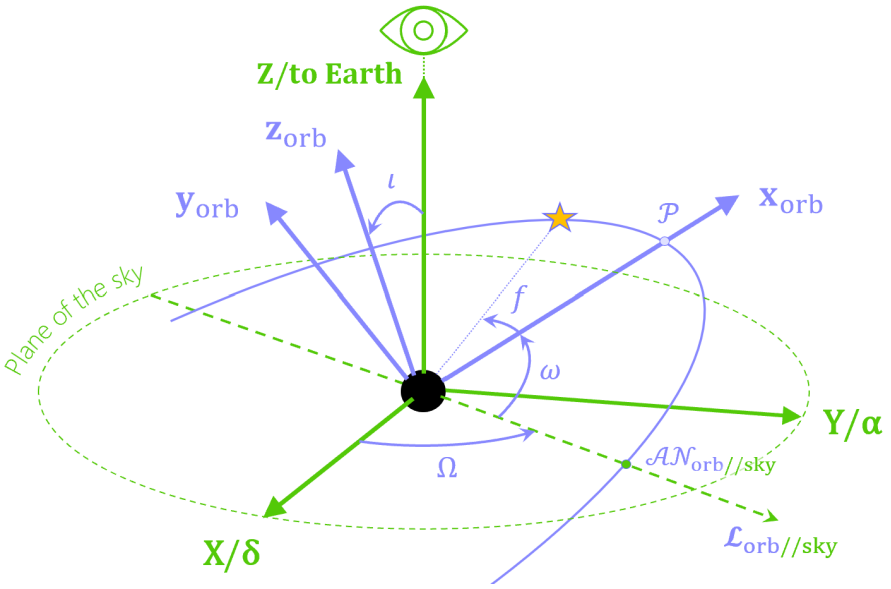

Figure IV.3: The orbit frame $(\mathbf{x}_{\rm orb}, \mathbf{y}_{\rm orb}, \mathbf{z}_{\rm orb})$ and orbital elements are represented in purple; and the observer frame $(\mathbf{X}, \mathbf{Y}, \mathbf{Z})$ in green. The pericenter, represented by the point $\mathcal{P}$, is also added. We display the inclination ι, the longitude of the ascending node Ω as well as the argument of periapsis ω, which will all be detailed in subsection IV.2.1. Finally, $\mathcal{L}_{\mathbf{orb//sky}}$ denotes the line of nodes of the orbit frame and sky plane.

[2]The plane containing the black hole, the star and the three-velocity.

Note also that to characterize the position of the star along the orbit, we use the true anomaly $f \in [0; 2\pi]$, defined as the rotation angle about $\mathbf{z}_{\rm orb}$, from $\mathbf{x}_{\rm orb}$ to the current position of the star (see subsection IV.1.4).

IV.1.3 Black hole frame

As opposed to studies assuming a Schwarzschild geometry [78], here we need to consider an additional frame describing the orientation of the angular momentum vector of the black hole, which will be referred to as "spin" vector. As introduced in section I.3, the dimensionless spin vector $\boldsymbol{\chi} = \chi \mathbf{z}_{\rm bh}$ is linked to the angular momentum $J = J\mathbf{z}_{\rm bh}$ of a black hole of mass $M_\bullet$ by:

$$\boldsymbol{\chi} = \mathbf{J}\frac{c}{GM_\bullet^2}. \tag{IV.1}$$

In Figure IV.4 we see the black hole frame $(\mathbf{x}_{\rm bh}, \mathbf{y}_{\rm bh}, \mathbf{z}_{\rm bh})$, labeled in Kerr-Schild coordinates, with the $\mathbf{z}_{\rm bh}$ axis being along the spin axis of the black hole. The choice of the orientation of $\mathbf{x}_{\rm bh}$ and $\mathbf{y}_{\rm bh}$ inside the black hole equatorial plane does not have any impact on the physics of the problem. Therefore, we arbitrarily choose $\mathbf{x}_{\rm bh}$ to be in the plane defined by $\mathbf{Z}$ and $\mathbf{z}_{\rm bh}$ and verifying $\mathbf{x}_{\rm bh} \cdot \mathbf{Z} > 0$. In other words, $\mathbf{x}_{\rm bh}$ is along $\mathbf{Z}_{//\rm bh}$, the projections of $\mathbf{Z}$ on the black hole equatorial plane, as illustrated in Figure IV.4.

As represented in Figures IV.4 and IV.5 it is natural to define the orientation of $\mathbf{z}_{\rm bh}$ by two sets of angles that are each convenient for different cases. On one hand, to characterize the orientation of the black hole with respect to the observer we use the angles $(i_\bullet, \Omega_\bullet)$[3]. This is particularly useful in the case of studying the spin of SgrA*; multiple stars would be used when constraining the spin and its orientation, meaning that defining the latter with respect to the orbit of one single star instead of the sky is unpractical, as will be seen in Chapter VIII. On the other hand, for the calculation of section IV.1.4 the use of (θ, β), which define the orientation of the spin vector relative to the star's orbit and $\mathcal{L}_{\mathbf{orb}//\mathbf{sky}}$, will be more practical. This allows us to define the black hole's angles[4] with respect to the sky plane as follows:

- $i_\bullet \in [0; \pi]$ is the rotation angle from $\mathbf{Z}$ to $\mathbf{z}_{\rm bh}$;
- $\Omega_\bullet \in [0; 2\pi]$ is the rotation angle about $\mathbf{Z}$, from $\mathbf{X}/\delta$ to $\mathbf{z}_{\rm bh//sky}$;

[3] In [37], they refer to the spin parameter as "a_*" and the black hole inclination with respect to the line of sight as "i". They use the following convention $a_* \in [-1; 1]$ and $i \in [0; \pi/2]$ instead of ours, which aligns with the work of [74].

[4] In this work, all angles are defined according to the right-hand rule. Namely, they have positive values when they represent a rotation that appears counterclockwise when looking in the negative direction of the axis, and negative values when the rotation appears clockwise.

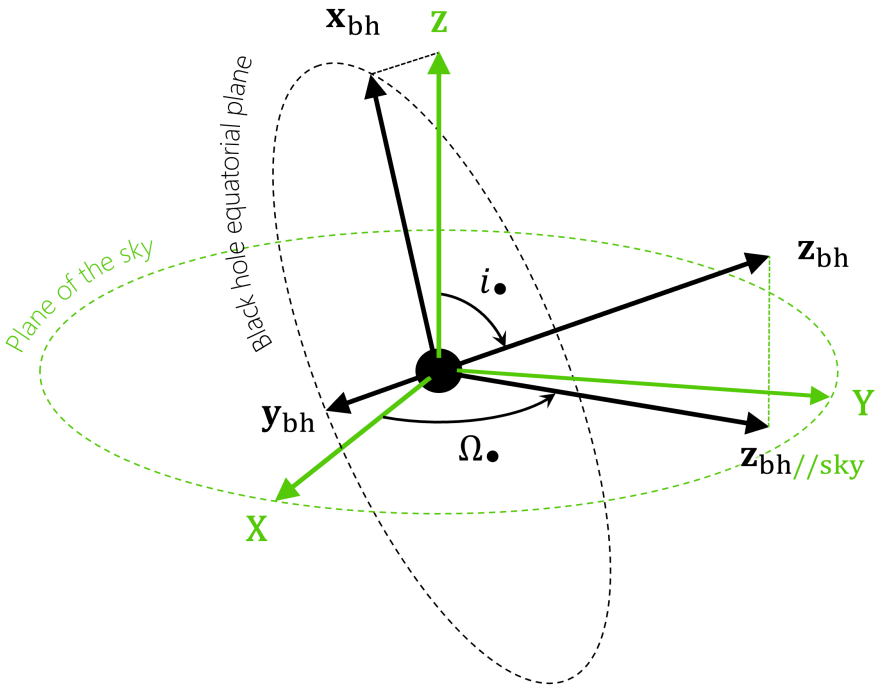

Figure IV.4: The angles $(i_\bullet, \Omega_\bullet)$ in black characterize the spin orientation of Sgr A* and give the position of the black-hole frame relative to the observer frame.

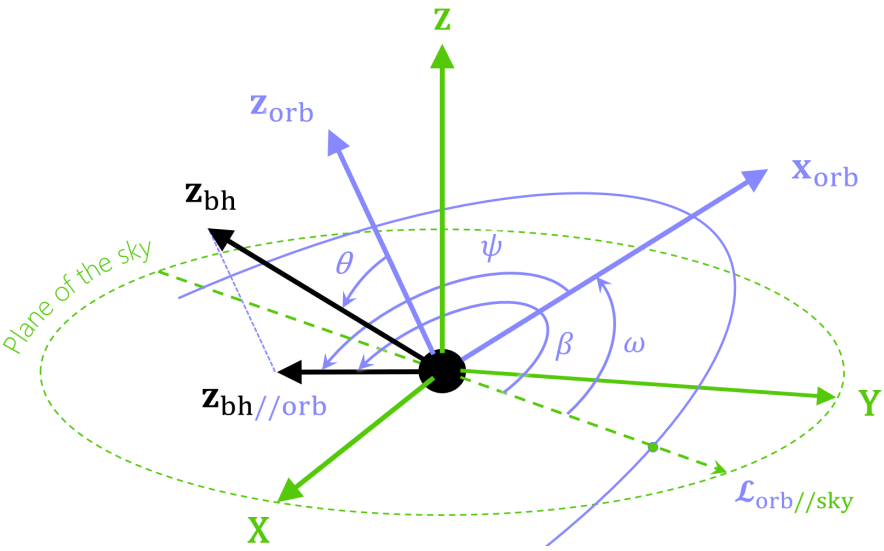

Figure IV.5: The angles (θ, β) in purple characterize the orientation of the spin vector $\mathbf{z}_{\rm bh}$ relative to the orbit frame. We also add the angle $\psi \equiv \beta - \omega$, so that (θ, ψ) are the spherical coordinates of the spin axis in the orbit frame. The projection of $\mathbf{z}_{\rm bh}$ on the orbit plane is denoted by $\mathbf{z}_{\rm bh//orb}$.

and with respect to the orbit plane as follows:

- $\theta \in [0;\pi]$ is the rotation angle from $\mathbf{z}_{\rm orb}$ to $\mathbf{z}_{\rm bh}$;
- $\beta \in [0;2\pi]$ is the rotation angle about $\mathbf{z}_{\rm orb}$, from $\boldsymbol{\mathcal{L}}_{\mathbf{orb//sky}}$ to $\mathbf{z}_{\rm bh//orb}$.

This allows us to have the following relations, which will become very handy in the calculations of section II.3.1:

$$\begin{aligned} \cos\theta &= \mathbf{z}_{\rm bh}\cdot\mathbf{z}_{\rm orb},\\ \sin\theta\cos(\beta) &= \mathbf{z}_{\rm bh}\cdot\boldsymbol{\mathcal{L}}_{\mathbf{orb//sky}},\\ \sin\theta\sin(\beta) &= \mathbf{z}_{\rm bh}\cdot\mathbf{Z}_{\rm //orb}. \end{aligned} \tag{IV.2}$$

Moreover, we assume the spin to be fixed in magnitude and direction.

IV.1.4 Gaussian frame

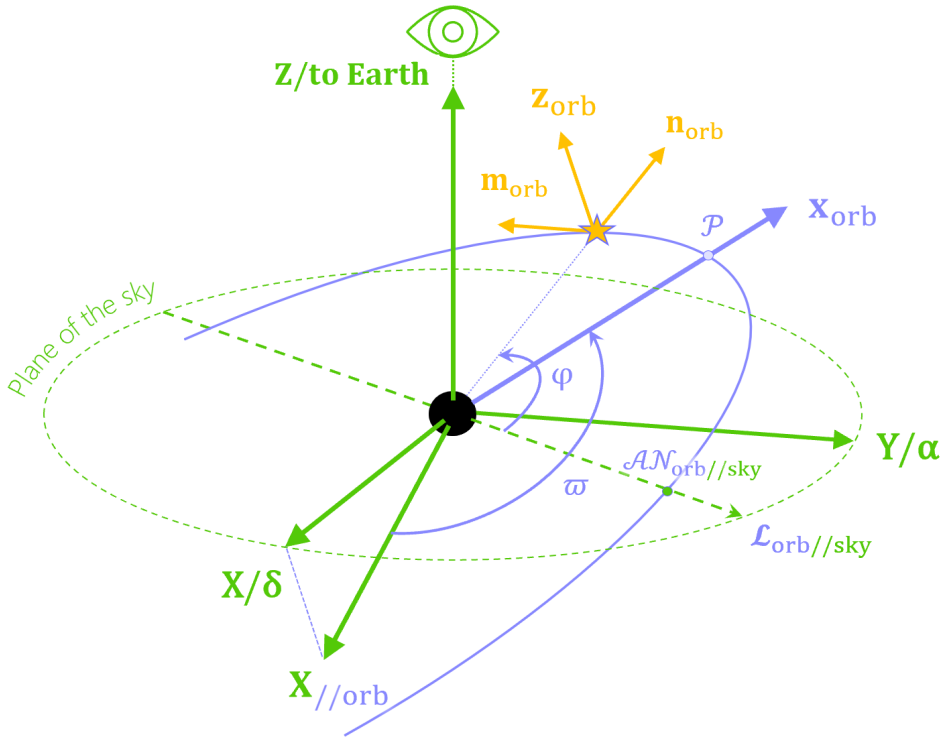

Figure IV.6: The Gaussian frame of the star is $(\mathbf{n}_{\rm orb},\mathbf{m}_{\rm orb},\mathbf{z}_{\rm orb})$ and the azimuthal angle $\varphi=\omega+f$. We also represent the projection of the $\mathbf{X}$ axis on the orbit plane denoted by $\mathbf{X}_{\rm //orb}$, and the angle ϖ which will be used in section VII.2.

In addition, it is useful to introduce the Gaussian frame[5] $(\mathbf{n}_{\rm orb}, \mathbf{m}_{\rm orb}, \mathbf{z}_{\rm orb})$, which follows the movement of the star as illustrated in Figure IV.6; $\mathbf{n}_{\rm orb}$ is the radial vector and $\mathbf{m}_{\rm orb}$ completes the orthonormal basis. This allows us to easily express the components of the various PN accelerations as was done in section II.2. We write the star's velocity vector $\mathbf{v}$ of norm v as:

$$\mathbf{v} = v_r \mathbf{n}_{\rm orb} + v_t \mathbf{m}_{\rm orb}, \tag{IV.3}$$

with:

$$v_r = \sqrt{\frac{Gm}{p}} e \sin f; \quad v_t = \sqrt{\frac{Gm}{p}} (1 + e \cos f). \tag{IV.4}$$

This holds true even in the presence of an "out-of-plane precession" (see Chapter VII) given that at any time we can consider the osculating Keplerian orbit (see subsection IV.2.2 below) which contains the velocity of the star at that time. In other words, the velocity is always within the momentarily orbital plane and thus never has a $\mathbf{z}_{\rm orb}$-component.

In addition to the true anomaly f, it is also useful to introduce the angle $\varphi \in [0; 2\pi]$, defined as the rotation angle about $\mathbf{z}_{\rm orb}$, from $\mathcal{L}_{\mathbf{orb}//\mathbf{sky}}$ to $\mathbf{n}_{\rm orb}$. This allows us to characterize the position of the star along the orbit relative to the ascending note and have $\varphi = \omega + f$ as illustrated in Figures IV.3 and IV.6. We know from Eq. (4.55) of [97] that by defining this quantity we can write:

$$\begin{aligned}
\mathbf{n}_{\rm orb} &= (\cos\varphi\cos\Omega - \cos\iota\sin\varphi\sin\Omega)\,\mathbf{X} \\
&\quad + (\cos\varphi\sin\Omega + \cos\iota\sin\varphi\cos\Omega)\mathbf{Y} \\
&\quad + \sin\iota\sin\varphi\,\mathbf{Z}; \\
\mathbf{m}_{\rm orb} &= (-\sin\varphi\cos\Omega - \cos\iota\cos\varphi\sin\Omega)\,\mathbf{X} \\
&\quad + (-\sin\varphi\sin\Omega + \cos\iota\cos\varphi\cos\Omega)\,\mathbf{Y} \\
&\quad + \sin\iota\cos\varphi\,\mathbf{Z}; \\
\mathbf{z}_{\rm orb} &= \sin\iota\sin\Omega\,\mathbf{X} \\
&\quad - \sin\iota\cos\Omega\,\mathbf{Y} \\
&\quad + \cos\iota\,\mathbf{Z}.
\end{aligned} \tag{IV.5}$$

Similarly to the expression of $\mathbf{z}_{\rm orb}$, we can write $\mathbf{z}_{\rm bh}$ in the fundamental frame of the observer as:

$$\begin{aligned}
\mathbf{z}_{\rm bh} &= \sin i_\bullet \cos\Omega_\bullet\,\mathbf{X} \\
&\quad + \sin i_\bullet \sin\Omega_\bullet\,\mathbf{Y} \\
&\quad + \cos i_\bullet\,\mathbf{Z}.
\end{aligned} \tag{IV.6}$$

[5] Also denoted as $(\mathbf{n}, \mathbf{m}, \mathbf{k})$ in Eq. (4.55) of [97].

Therefore, it is convenient to notice that, by using Eqs. (IV.2):

$$\begin{aligned}
\mathbf{z}_{\rm bh}\cdot\mathbf{n}_{\rm orb} &= \cos i_\bullet \sin\varphi \sin\iota \\
&\quad + \sin i_\bullet \left(\cos\varphi\cos(\Omega-\Omega_\bullet) - \sin\varphi\cos\iota\sin(\Omega-\Omega_\bullet)\right) \\
&= \sin\theta\cos(\beta-\varphi); \\
\mathbf{z}_{\rm bh}\cdot\mathbf{m}_{\rm orb} &= \cos i_\bullet \cos\varphi \sin\iota \\
&\quad - \sin i_\bullet \big(\sin\varphi\cos(\Omega-\Omega_\bullet) + \cos\varphi\cos\iota\sin(\Omega-\Omega_\bullet)\big) \\
&= \sin\theta\sin(\beta-\varphi); \\
\mathbf{z}_{\rm bh}\cdot\mathbf{z}_{\rm orb} &= \cos i_\bullet\cos\iota + \sin i_\bullet\sin\iota\sin(\Omega-\Omega_\bullet) \\
&= \cos\theta.
\end{aligned} \tag{IV.7}$$

This will become very handy for the derivation of the components of the various PN accelerations in Eqs. (V.40) to (V.48).

IV.2 Orbit parametrization

Let us present the different ways to parameterize our orbits.

IV.2.1 Newtonian orbits

A Newtonian orbit is defined by 6 Keplerian parameters that correspond to the 6 Newtonian degrees of freedom (3 positions + 3 velocities). The typical set of Keplerian parameters is the following:

- $a_{\rm sma}$ the semi-major axis;
- e the eccentricity of the orbit;
- $\iota \in [0;\pi]$ is the inclination[6] between the fundamental and orbital planes, and encodes the rotation about $\boldsymbol{\mathcal{L}}_{\mathbf{orb//sky}}$, from $\mathbf{Z}$ to $\mathbf{z}_{\rm orb}$;
- $\Omega \in [0;2\pi]$ is the position angle of the line of nodes $\boldsymbol{\mathcal{L}}_{\mathbf{orb//sky}}$, intersection between the orbital and fundamental planes; it encodes the rotation about $\mathbf{Z}$, from $\mathbf{X}$ to $\boldsymbol{\mathcal{L}}_{\mathbf{orb//sky}}$;
- $\omega \in [0;2\pi]$ is the angular position of the pericenter within the orbital plane, counted from the line of nodes; it encodes the rotation about $\mathbf{z}_{\rm orb}$, from $\boldsymbol{\mathcal{L}}_{\mathbf{orb//sky}}$ to $\mathbf{x}_{\rm orb}$;

[6] Note that the inclination ι we use here is different from the definition of the inclination "i" used in [60] which used the opposite convention for the sense of rotation of the inclination (see Appendix C of [78]).

- $t_{\rm peri}$ the time of pericenter passage.

The first two parameters are sufficient to define (i) geometrically the ellipse of the orbit (that is, the semi-major and semi-minor axes), and (ii) the energetics of the orbit, that is, the total energy E and angular momentum L of the two-body system. There is a one-to-one correspondence between $(a_{\rm sma}, e)$ and (E, L). Note that these parameters are independent of the choice of fundamental frame. In addition, we defined the three angles ι, Ω and ω (see Figure IV.3) that encode the orientation of the ellipse; they are the three Euler angles, allowing to rotate the orbit frame into the observer's frame. We highlight the dependency of the 3 angular orbital parameters on the choice of fundamental plane. For instance, [139] use the black hole equatorial plane as their fundamental plane, while we use the plane of the sky. As a consequence, the inclination angle of our work is not the same as in theirs, and we will see that this has obviously profound consequences on the evolution equations that we will obtain later on. Moreover, we need the initial condition along the orbit, so we introduce $t_{\rm peri}$ the time of pericenter passage. Finally, to characterize the position of the star along the orbit, we use the true anomaly f (see Figure IV.3) or the azimuthal angle $\varphi = \omega + f$ (see Figure IV.6), as mentioned in subsections IV.1.2 and IV.1.4.

IV.2.2 Relativistic orbits and osculating orbital parameters

In general relativity (GR) and post-Newtonian (PN) frameworks, orbits are no longer closed ellipses, and the classical Keplerian orbital elements become time-dependent. However, it is still useful to describe the relativistic trajectory in terms of a family of instantaneous Newtonian orbits that "kiss" the real orbit at each moment. This leads to the concept of *osculating orbital elements*: at any given time, the relativistic orbit can be approximated by a Keplerian ellipse whose parameters vary continuously over time.

This formalism is not specific to relativity: it is a general method for describing motion under perturbations to Newtonian gravity. In this sense, the PN equations of motion can be viewed as perturbed Newtonian dynamics (see subsectionII.3.1), where the time-evolving orbital elements naturally describe the effect of relativistic corrections. This is why the notion of osculating elements is well suited to the PN framework.

However, the analogy has its limits. While the PN equations resemble Newtonian perturbations, they arise in a curved spacetime: PN theory does not simply perturb Newtonian gravity—it perturbs flat spacetime geometry into a weakly curved one. As such, the geodesic structure and the geometry itself are fundamentally different from the Newtonian case. Nevertheless, for interpreting orbital evolution and data analysis, it is insightful to use this Newtonian-like language as a pedagogical and practical tool.

It is customary to represent a relativistic orbit by providing the set of orbital parameters at a particular time $t_{\rm osc}$, when it is osculated by the Newtonian orbit described by this same set of orbital parameters. A relativistic orbit is thus described by the 6 usual orbital parameters, plus the osculating time $t_{\rm osc}$. The time-varying orbital parameters of a relativistic orbit can therefore be seen as the orbital parameters of a family of osculating Newtonian elliptical orbits. From this point onward, we will consider ($a_{\rm sma}$, e, ι, Ω, ω) as functions of time such that ($a_{\rm sma}(t_{\rm osc})$, $e(t_{\rm osc})$, $\iota(t_{\rm osc})$, $\Omega(t_{\rm osc})$, $\omega(t_{\rm osc})$)=($a_{\rm sma,\,osc}$, $e_{\rm osc}$, $\iota_{\rm osc}$, $\Omega_{\rm osc}$, $\omega_{\rm osc}$).

As for the osculating $t_{\rm peri}$, we take the most recent time of pericenter passage before the first observation date of each star [see table D.1 of 58, for the first observation dates].

Moreover, it is worth mentioning that adding a certain time T to $t_{\rm osc}$ does not mean that the orbit will be temporally translated by T; taking $t_{\rm osc} = t_0 + T$ instead of $t_{\rm osc} = t_0$ does not mean that we will observe the same orbit if we wait for T. This would only be true if we also add T to $t_{\rm peri}$ as well. Since it is common not to find in literature[7] any mention of the osculating time when giving the numerical values of the orbital parameters of S stars, one can misinterpret these parameters.

IV.3 Differences between coordinate systems in orbit simulations

As discussed in subsection IV.2.2, a relativistic orbit is typically parametrized by six orbital elements defining the osculating Keplerian ellipse at a reference time $t_{\rm osc}$. While this approach is widely used due to its intuitive connection with Newtonian mechanics, it introduces a strong *coordinate dependence*: orbital elements are not covariant quantities. They implicitly assume a specific coordinate system in which the orbit is defined and integrated. Consequently, applying the same set of orbital parameters across different coordinate systems—such as Boyer–Lindquist (BL), Kerr–Schild (KS), or Schwarzschild Harmonic (SH)—can yield significantly different orbital trajectories.

This non-covariance is not a bug, but rather an inherent feature of our modeling framework. In practice, what we do is:

1. Fix a set of orbital elements (e.g., $a, e, \iota, \omega, \Omega, t_{\rm peri}$),
2. Convert these parameters into a 4-position and 4-velocity (x^μ, u^μ) assuming a specific coordinate system (e.g., BL),

[7] When not mentioned, the osculation times of S stars actually correspond to the time of the most recent apocenter before the first observation date of each star, as mentioned in [59, 60].

3. Evolve this initial condition using `GYOTO` (see subsection V.1.1) or `OOGRE` (see subsection V.1.2) within the chosen coordinate system.

If we then interpret this same set of orbital parameters in another coordinate system (say, KS), and repeat the same conversion and integration, we are no longer evolving the same physical orbit. The 4-position and 4-velocity computed from the same orbital elements differ because the mapping from orbital parameters to spacetime coordinates is coordinate-dependent.

This explains why significant discrepancies were observed in previous versions of the `GYOTO` code (see section V.1.1) when comparing relativistic orbits across coordinate systems, even when using the same orbital parameters. These differences are not due to physical effects, but purely due to coordinate ambiguities. The key message is that relativistic orbital elements must always be interpreted and used within a specified coordinate framework.

IV.3.1 Non-uniqueness of relativistic orbital parameterizations

Before examining the magnitude of the coordinate system discrepancy, let us dive deeper into their origin as explained in [79] (in preparation).

Starting from a chosen set of initial orbital elements, we apply an orthogonal projection followed by a local flat-space transformation from Cartesian to spherical coordinates to obtain the initial position and velocity. These coordinates are then interpreted in two different systems: once in Kerr coordinates $x^\mu = (t, r, \theta, \phi)$ (or Schwarzschild coordinates for $\chi = 0$), and once in Harmonic coordinates $\tilde{x}^\mu = (t, r_H, \theta, \phi)$, following the definitions in [112, Eqs. (5.163) and (5.169)]. The spatial coordinates are related via Eq. (II.3), while the angular and temporal components remain unchanged (see subsection II.1.1). However, in our setup, we deliberately set the initial radius and velocity components to be identical in both systems (i.e., $r_0 = r_{H0}$), without accounting for the coordinate mapping. This implies that the initial position and velocity refer to different physical points in spacetime in the two charts. As a result, the timelike geodesics integrated using `GYOTO` from these respective initial conditions evolve into different physical orbits. This procedure is illustrated in the right panel of Fig. IV.7 and elaborated in [79] (in preparation), where we showed that the same coordinate-space orbit in $\mathbb{E}$ yields different worldlines in the physical spacetime $\mathbb{M}$ when transformed through different coordinate charts.

In conclusion, the analysis of this section ensures that results are reproducible and that coordinate effects are not misinterpreted as physical phenomena. While fully covariant parametrizations or complete ray-tracing could eliminate this ambiguity, consensus on such methods has not yet been reached in the Galactic Center orbit–fitting community. Therefore, clear documentation of the modeling framework and coordinates remains the most effective mitigation strategy for the time

being.

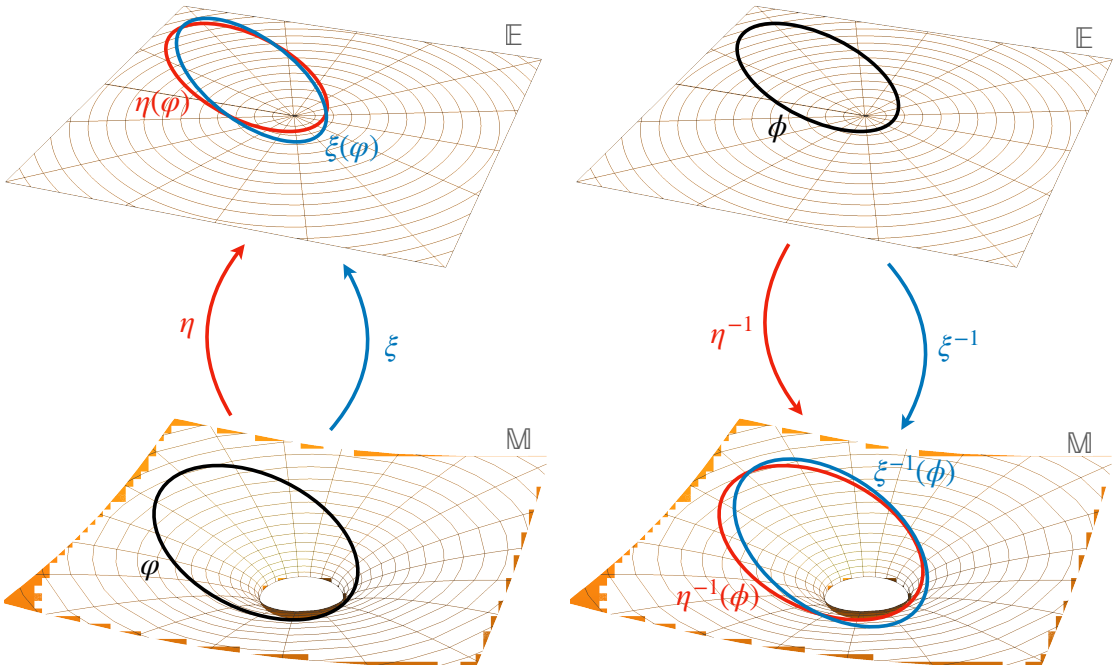

Figure IV.7: [Extracted from [79] in preparation] Left: A unique orbit φ in relativistic (curved) space $\mathbb{M}$ is represented by different expressions $\eta(\varphi), \xi(\varphi)$ in coordinate space $\mathbb{E}$, where η, ξ are the coordinate maps. If $\mathbb{E}$ is interpreted as Euclidean space, then $\eta(\varphi), \xi(\varphi)$ are distinct orbits in $\mathbb{E}$ and hence differ in their parametrisation by orbital elements. Right: Conversely, given a unique orbit ϕ in $\mathbb{E}$, parametrized by a set of orbital elements, then the two orbits $\eta^{-1}(\phi), \xi^{-1}(\phi)$ in $\mathbb{M}$, which share ϕ as their coordinate expression, and thus their parametrisation in terms of orbital elements, are distinct.

IV.3.2 Estimating the coordinate system discrepancy

The aim of this section is to quantify this coordinate dependence. We compute the observable differences in astrometry (RA and DEC) and spectroscopy (RV) when simulating the same set of osculating orbital elements in different coordinate systems. The shifts are defined as:

$$\begin{aligned} \Delta\mathrm{RA}_{\mathrm{BL-KS}} &= \mathrm{RA}_{\mathrm{BL}} - \mathrm{RA}_{\mathrm{KS}}; \\ \Delta\mathrm{DEC}_{\mathrm{BL-KS}} &= \mathrm{DEC}_{\mathrm{BL}} - \mathrm{DEC}_{\mathrm{KS}}; \\ \Delta\mathrm{RV}_{\mathrm{BL-KS}} &= \mathrm{RV}_{\mathrm{BL}} - \mathrm{RV}_{\mathrm{KS}}. \end{aligned} \tag{IV.8}$$

To compare SH and KS coordinates, we restrict to the Schwarzschild case with

$\chi = 0$, and define:

$$\begin{aligned}
\Delta\mathrm{RA}_{\mathrm{SH-KS}} &= \mathrm{RA}_{\mathrm{SH}} - \mathrm{RA}_{\mathrm{KS}}(\chi = 0);\\
\Delta\mathrm{DEC}_{\mathrm{SH-KS}} &= \mathrm{DEC}_{\mathrm{SH}} - \mathrm{DEC}_{\mathrm{KS}}(\chi = 0);\\
\Delta\mathrm{RV}_{\mathrm{SH-KS}} &= \mathrm{RV}_{\mathrm{SH}} - \mathrm{RV}_{\mathrm{KS}}(\chi = 0).
\end{aligned} \tag{IV.9}$$

These comparisons reveal coordinate-dependent effects that can reach the level of current instrumental precision—especially when analyzing relativistic spin signatures. This highlights the need for explicitly stating not only the orbital elements and osculation time but also the coordinate system in which they are defined. Only then can the orbit be uniquely and unambiguously specified [see also 16, 79].

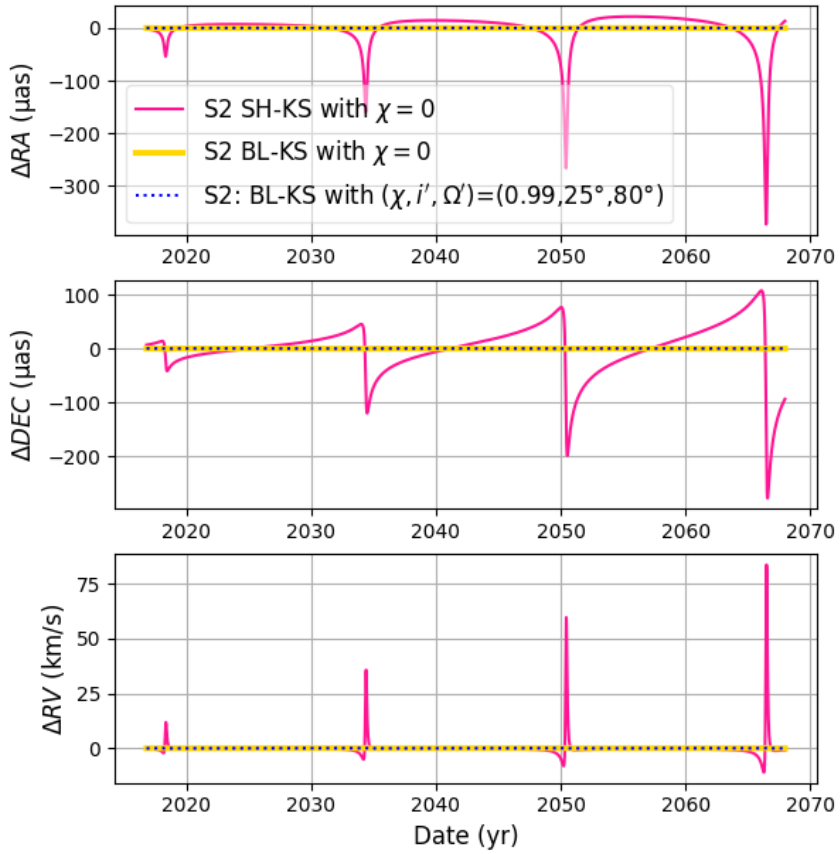

Figure IV.8: Right ascension (top), declination (middle), and radial velocity (bottom) BL-KS and SH-KS coordinate systems shifts, simulated over more than 4 orbits of the star S2. We use $(\chi, i_\bullet, \Omega_\bullet) = (0.99, 25°, 80°)$ as spin parameters for the dotted blue curve and $\chi = 0$ to be in the Schwarzschild configuration for the solid pink and gold curves.

In Figures IV.8 and IV.9 the BL-KS and SH-KS coordinate system discrepancies are compared for $\chi = 0$, using the stars S2 and the hypothetical star S2/10. For the BL-KS shift, we also show the residuals for $(\chi, i_\bullet, \Omega_\bullet) = (0.99, 25°, 80°)$[8], but we obtain comparable results for $\chi = 0.7$ and different values of $\Omega_\bullet$.

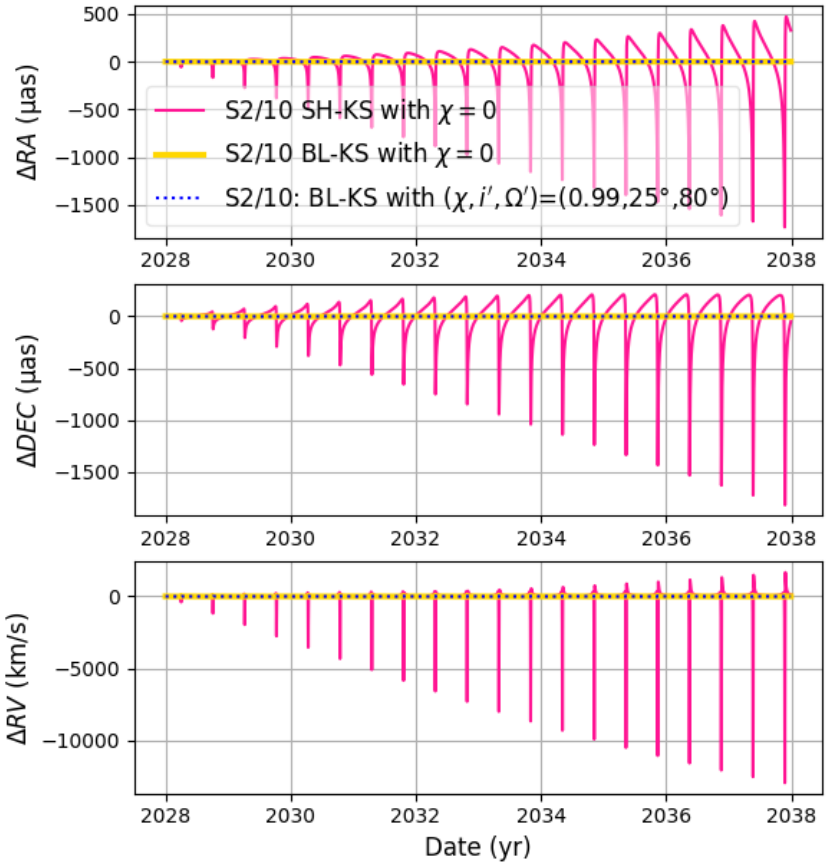

Figure IV.9: Same as Figure IV.8 but using the hypothetical star S2/10 and a 10-year observing period.

By zooming in on Figures IV.8 and IV.9, we see that the BL-KS shifts appear to be practically identical for a spinning and non-spinning black hole. The BL-KS astrometric and spectroscopic shifts remain under 1μas and 1km/s in Figure IV.8 and under 2μas and 15km/s in Figure IV.9. As for the SH-KS difference, it can go up to hundreds of μas and dozens of km/s in Figure IV.8 and more than 1700μas and 12900km/s in Figure IV.9, mainly due to the difference in the definition of the redial coordinate (see Eq. (II.3)). This proves the importance of specifying the coordinate system along with the orbital parameters and osculating time when working in general relativity.

[8]Since [37] suggests that $i_\bullet \lesssim 30°$ and higher values of χ are likely.

Nevertheless, if we want to estimate a higher order effect that can be simulated by evaluating the difference of two orbits (with and without the effect), the coordinate system choice would have considerably less to no impact. For example, if we want to measure the spin effect in a certain coordinate system as:

$$\begin{aligned}\Delta\mathrm{RA}_\chi &= \mathrm{RA}_{\chi=0.99} - \mathrm{RA}_{\chi=0};\\ \Delta\mathrm{DEC}_\chi &= \mathrm{DEC}_{\chi=0.99} - \mathrm{DEC}_{\chi=0};\\ \Delta\mathrm{RV}_\chi &= \mathrm{RV}_{\chi=0.99} - \mathrm{RV}_{\chi=0},\end{aligned} \tag{IV.10}$$

then, the disagreement between the KS and BL coordinates over these quantities would only amount to less than 5nas and 0.8m/s over four orbits of S2 or less than 0.15µas and 1.3km/s over twenty orbits of S2/10.

Finally, as summarized in Figure IV.10, the maximal spin effect (dark green) remains larger than the KS–BL discrepancy at $\chi = 0$ (purple) across the observation interval (2016.81–2060) and for a representative spin orientation $(i_\bullet, \Omega_\bullet) = (25°, 80°)$. However, the two quantities become comparable in magnitude for weak spins ($\chi \sim 0.1$), suggesting that further reduction of coordinate inconsistencies could still improve sensitivity to weak spin detection.

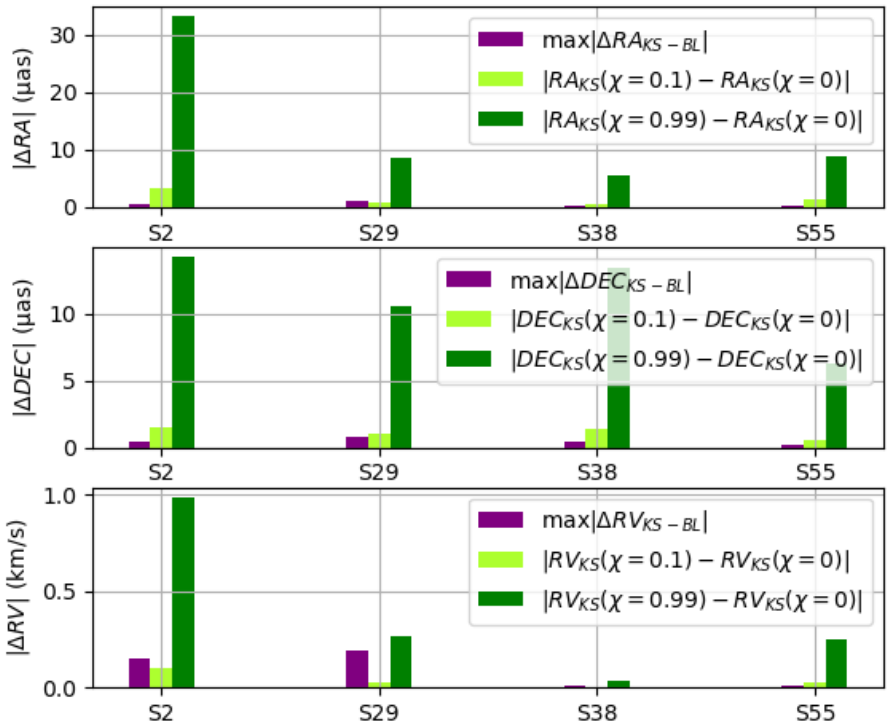

Figure IV.10: Comparison of the spin effect (dark green) and the maximal KS–BL difference using $(\chi, i_\bullet, \Omega_\bullet) = (0, 25°, 80°)$ (purple) over the interval 2016.81–2060, with weak spin differences shown in light green.

To summarize, while Keplerian elements provide a natural parameterization of Newtonian orbits, their relativistic counterparts must be understood as osculating orbital elements that evolve with time. These quantities are not invariant: their definition depends on the chosen coordinate system in which the orbit is expressed. As a result, the same numerical values of the orbital elements may correspond to different physical orbits when interpreted on different coordinate charts. This section showed that failing to specify this framework can lead to large discrepancies in simulated orbits, comparable to or exceeding instrumental precision. Therefore, a clear and explicit definition of the parameterization scheme—including the choice of fundamental plane, osculation time, and coordinate system—is indispensable for reproducibility and for disentangling genuine relativistic signatures from coordinate artifacts.

Chapter V

Extending our palette of relativistic models

Contents

V.1 Codes for relativistic simulations 88

V.1.1 GYOTO 89

V.1.2 OOGRE 89

V.1.3 Orbit models 90

V.2 Development of the spin aspects in the GR_proj model 92

V.2.1 Detailed derivation of the redshift formula in curved spacetime 92

V.2.2 Approximate expression without ray tracing 95

V.3 Extending OOGRE to higher order effects 98

V.1 Codes for relativistic simulations

V.1.1 GYOTO

The ray-tracing code GYOTO (General relativitY Orbit Tracer of the Observatory of Paris) was originally developed to model stellar orbits and flares in the vicinity of Sgr A*, in the context of the GRAVITY instrument's development. Initiated during the PhD thesis of Frédéric Vincent, the project was carried out in collaboration with Thibaut Paumard, Éric Gourgoulhon, and Guy Perrin [131].

GYOTO is an open-source, modular C++ code capable of computing null and timelike geodesics—i.e., the trajectories of photons and massive particles—in arbitrary spacetimes. The underlying spacetime metric can be specified either analytically or numerically, allowing the code to be used in both analytical and numerical relativity contexts. In addition to ray-tracing, GYOTO includes a solver for the radiative transfer equation along null geodesics, enabling the generation of realistic simulations of observations in the strong-field regime of general relativity.

Since its creation, the code has seen significant developments. Thibaut Paumard has led the architectural design of the code, including the definition of input/output formats, implementation of multithreading and MPI-based parallelization, development of a Python interface, and cross-platform compilation support for macOS and Linux.

While the focus of GYOTO's original development was on the modeling of phenomena near black holes, the code includes a wide library of astrophysical source models—such as stars, accretion disks, and jets—making it suitable for a variety of applications in relativistic astrophysics.

As mentioned previously, we consider two kinds of observables in our study: the astrometric positions and the radial velocities of a star. For orbit integration and observable simulations of S stars we sometimes consider a fully GR model (later referred to as GR_rt) by using the ray-tracing code GYOTO. At the time being, if we choose to work in Harmonic coordinates when using GYOTO, we will have to consider a null black hole spin (we refer to this coordinate system as Schwarzschild Harmonic or SH when using GYOTO). If we want to consider a rotating black hole, the Boyer-Lindquist (KerrBL or BL) and Kerr-Schild (KerrKS or KS) coordinates are also available. Coding a Kerr version of the Harmonic coordinate system in GYOTO in the future, would prove useful when properly[1] comparing GYOTO's general relativistic orbits with to OOGRE's post-Newtonian ones (see subsection V.1.2 below) which are only available in Harmonic coordinates.

V.1.2 OOGRE

OOGRE (Osculating Orbits in General Relativistic Environments) is a Python-based code designed to simulate stellar motion near compact objects, such as

[1] As explained in section IV.3 the osculating orbital elements are not covariant quantities and in order to simulate precisely the same orbits in GYOTO and OOGRE one needs to use the same coordinate system in both models.

the Galactic center black hole, by modeling relativistic perturbations to Keplerian orbits. Originally developed by Heißel et al. [78], it provides a framework for integrating osculating orbits in a variety of post-Newtonian settings using a perturbative approach.

The core methodology behind `OOGRE` is to treat relativistic effects—such as Schwarzschild precession or spin-induced frame dragging—as post-Newtonian corrections to Newtonian motion. This allows for efficient and physically interpretable simulations, particularly useful in the context of S-stars, where relativistic effects are small but measurable with high-precision astrometry and spectroscopy.

`OOGRE` is well-suited for sensitivity studies, orbit fitting, and the simulation of potential deviations from general relativity in the Galactic center. It has been used to investigate the detectability of extended mass distributions [78] as well as the imprint of dark-mass signatures on the orbit of S2 and other short-period stars. Its Python interface makes it easy to integrate into larger simulation pipelines, while its modular structure allows for flexible adaptation to various relativistic environments.

Compared to full geodesic integrators such as `GYOTO`, `OOGRE` offers significant advantages in terms of computational speed and interpretability of physical effects. In the present work, `OOGRE` is used for most of the orbital parameter fitting and for separately studying the Lense-Thirring and quadrupole moment effects on the orbit of S stars as will be seen in part 3.

V.1.3 Orbit models

In the study of the stars in the Sgr A* environment, our team uses different orbit models depending on the problem to consider. In order of increasing complexity and computing time, we list these models below and divide them into three groups, in order of increasing complexity, accuracy and computational time.

First:

- `"Kepler"` model: Keplerian model without any of the relativistic effects.

Second, we have the non-ray-traced relativistic orbit models:

- `"1PN"` model: Keplerian model with the relativistic correction to the Newtonian two-body equations of motion to first Post-Newtonian (1PN) order.
- `"1.5PN"` model: Same as the `1PN` model but with the relativistic correction of the dominant term of the Lense-Thirring effect on the orbit of the star.
- `"2PN"` model: Same as the `1.5PN` model but with the relativistic correction to the Newtonian two-body equations of motion to second Post-Newtonian (2PN) order.

- `"2PN_Q"` model: Same as the `2PN` model but with the relativistic correction of the dominant term of the mass quadrupole moment effect on the orbit of the star.
- `"2.5PN"` model: Same as the `2PN_Q` model but with the relativistic correction of the second dominant term of the Lense-Thirring effect on the orbit of the star.
- `"3PN"` model: Same as the `2.5PN` model but with the relativistic correction to the Newtonian two-body equations of motion to third Post-Newtonian (3PN) order.
- `"GR_proj"` model: GR model for the orbit of the star, without ray-tracing the photon path.

In this group of models, the photon is evolved in a flat spacetime to project[2] the orbit onto the observer's screen. The astrometric effect of gravitational lensing, transverse Doppler shift, and the gravitational redshift (see subsection I.2.3) can all be added as supplement effects to these models if desired.

Finally, the completely general relativistic and ray-traced model:

- `"GR_rt"` model: Full-GR model, with relativistic ray-tracing of the photon to the distant observer's screen. All previous effects are naturally taken into account in this model as well as their effect on the photon trajectory.

The Roemer effect (see subsection I.2.3) and proper motion of the observer can be added as supplement effects to all of the models above if desired.

When I arrived in the team, the `Kepler`, `1PN`, Schwarzschild version of `2PN`, `GR_proj` excluding the effect of the spin in the redshift factor, and `GR_rt` models where already coded. One of my first tasks was to extend these models to the case of a rotating black hole, by implementing, the `1.5PN`, the Kerr version of `2PN`, `GR_proj` including the effect of the spin in the redshift factor, on the basis of the existing models. Later on, I also needed to add the `2PN_Q`, `2.5PN`, and `3PN` models to the palette for analyzing the effect of the quadrupole moment and evaluating the level of subleading orders of the Schwarzschild precession and Lense-Thirring effect. The implementation details of these models will be the subject of subsections V.2 and V.3.

V.2 Development of the spin aspects in the `GR_proj` model

[2]Hence the `"proj"` subscript in `GR_proj`, which should be added onto the PN models as well for homogeneous notation but are dropped to lighten the notation.

As discussed in the previous subsection, I developed a new general relativistic (GR) model based on earlier work conducted within the team, and in collaboration with my supervisors. A pre-existing model had already been implemented, in which the exact GR trajectory of the star is computed while the photon propagation is approximated via a flat-space orthogonal projection, thereby avoiding full ray-tracing. This approach significantly reduces computational time while preserving key relativistic effects on the stellar orbit.

Building upon this framework, the goal was to introduce an analytical correction to the radial velocity, $V_{\rm rad}$, to approximate the influence of black hole spin on stellar motion. Such a correction is particularly relevant for stars on tight orbits—like the proposed source S2/10—where spin-induced effects are expected to be more pronounced. In the remainder of this section, we present the analytical approximation used to compute $V_{\rm rad}$, and discuss its range of applicability.

V.2.1 Detailed derivation of the redshift formula in curved spacetime

In this subsection, we will focus on the `GR_proj` model, which does not involve ray tracing of light geodesics. While this significantly reduces the computational cost, it presents a major challenge when it comes to computing the radial velocity observable (or redshift), since this quantity depends on the photon's energy at both emission and reception. These energies are not directly accessible without integrating the full null geodesic.

To address this, our goal in this section is to derive an approximate but general analytical expression for the redshift in curved spacetime, expressed in terms of locally measurable quantities. This derivation will allow us to estimate the spectroscopic signal within the `GR_proj` model without resorting to full ray tracing, while still retaining essential relativistic corrections.

In General Relativity, the observed redshift of light emitted from a star orbiting a massive object (such as a black hole) is a key observable. We aim to derive a general expression for the redshift (or equivalently, the observed radial velocity) that is valid in any spacetime and can be expressed in terms of locally measurable quantities. This derivation is written in a way that requires only basic familiarity with four-vectors and their scalar products in curved spacetime.

We start by considering $G = M = c = 1$, and we write the KerrBL metric as in Eqs. (II.5) and (II.6) (see subsection II.1.2).

Photon energy as measured by an observer

In General Relativity, the energy of a photon as measured by an observer with four-velocity $\mathbf{u}$ is given by the scalar product:

$$E = -\mathbf{u} \cdot \mathbf{p}, \tag{V.1}$$

where $\mathbf{p}$ is the photon's four-momentum (a null vector). The minus sign arises because we are using the $(-,+,+,+)$ metric signature. While this quantity can, in principle, be negative for particular configurations, the minus sign is essential to ensure consistency with the standard non-relativistic Doppler formula.

This definition follows from the fact that the energy is the time component of the photon's momentum as seen in the observer's rest frame.

Redshift definition

Let $\mathbf{p}_{\text{em}}$ be the four-momentum of a photon at the moment of emission, and $\mathbf{p}_{\text{obs}}$ be the four-momentum of the same photon when it reaches the observer. Let $\mathbf{u}_{\text{em}}$ and $\mathbf{u}_{\text{obs}}$ be the four-velocities of the emitter and observer respectively. The redshift factor g is then defined as the ratio of the observed photon energy to the emitted one:

$$g \equiv \frac{E_{\text{obs}}}{E_{\text{em}}} = \frac{-\mathbf{u}_{\text{obs}} \cdot \mathbf{p}_{\text{obs}}}{-\mathbf{u}_{\text{em}} \cdot \mathbf{p}_{\text{em}}} = \frac{\mathbf{u}_{\text{obs}} \cdot \mathbf{p}_{\text{obs}}}{\mathbf{u}_{\text{em}} \cdot \mathbf{p}_{\text{em}}}. \tag{V.2}$$

Both numerator and denominator are negative (since the scalar product of a future-pointing timelike and null vector is always negative), so the ratio is positive.

Use of an intermediate "coincident" observer

To understand the denominator $\mathbf{u}_{\text{em}} \cdot \mathbf{p}_{\text{em}}$ in a more intuitive way, we introduce an auxiliary observer $\mathcal{O}_{cd}$ (for "coincident"), who is located at the same spacetime point as the star at the time of emission, but may have a different four-velocity. This is a standard technique in relativity that allows us to decompose four-vectors in the locally flat frame of the observer.

Let the four-velocity of this observer be $\mathbf{u}_{cd}$. The four-velocity of the star (emitter) and the four-momentum of the photon at emission can be decomposed in the local frame of $\mathcal{O}_{cd}$ as:

$$\mathbf{u}_{\text{em}} = \Gamma_{cd} \left(\mathbf{u}_{cd} + \mathbf{V}_{cd} \right), \tag{V.3}$$

$$\mathbf{p}_{\text{em}} = E_{cd} \left(\mathbf{u}_{cd} + \mathbf{n}_{cd} \right). \tag{V.4}$$

Here:

- $\mathbf{V}_{cd}$ is the 3-velocity of the emitter (the star) in the frame of $\mathcal{O}_{cd}$,
- $\Gamma_{cd} = (1 - \mathbf{V}_{cd} \cdot \mathbf{V}_{cd})^{-1/2}$ is the Lorentz factor,
- E_{cd} is the energy of the photon as measured by $\mathcal{O}_{cd}$,
- $\mathbf{n}_{cd}$ is the spatial direction of photon emission as measured by $\mathcal{O}_{cd}$ (a unit spatial vector orthogonal to $\mathbf{u}_{cd}$),

- All dot products are taken with the spacetime metric (e.g., Kerr or Schwarzschild).

Note that $\mathbf{u}_{cd} \cdot \mathbf{u}_{cd} = -1$, $\mathbf{n}_{cd} \cdot \mathbf{u}_{cd} = 0$, and $\mathbf{n}_{cd} \cdot \mathbf{n}_{cd} = 1$.

Computing the denominator

We now compute the scalar product of the emitter 4-velocity and photon momentum at emission:

$$\begin{aligned} \mathbf{u}_{\rm em} \cdot \mathbf{p}_{\rm em} &= \Gamma_{cd} E_{cd} \left(\mathbf{u}_{cd} + \mathbf{V}_{cd}\right) \cdot \left(\mathbf{u}_{cd} + \mathbf{n}_{cd}\right) && \text{(V.5)} \\ &= \Gamma_{cd} E_{cd} \left[\mathbf{u}_{cd} \cdot \mathbf{u}_{cd} + \mathbf{u}_{cd} \cdot \mathbf{n}_{cd} + \mathbf{V}_{cd} \cdot \mathbf{u}_{cd} + \mathbf{V}_{cd} \cdot \mathbf{n}_{cd}\right] && \text{(V.6)} \\ &= \Gamma_{cd} E_{cd} \left[-1 + \mathbf{V}_{cd} \cdot \mathbf{n}_{cd}\right], && \text{(V.7)} \end{aligned}$$

since the cross-terms $\mathbf{u}_{cd} \cdot \mathbf{n}_{cd} = \mathbf{V}_{cd} \cdot \mathbf{u}_{cd} = 0$ by construction.

Finally:

$$\boxed{\mathbf{u}_{\rm em} \cdot \mathbf{p}_{\rm em} = -\Gamma_{cd} E_{cd} (1 - \mathbf{n}_{cd} \cdot \mathbf{V}_{cd})} \qquad \text{(V.8)}$$

Energy measured at infinity

If the observer is located far from the black hole (e.g., in asymptotically flat spacetime), and is stationary with respect to the coordinates, then their four-velocity is simply $\mathbf{u}_{\rm obs} = \boldsymbol{\partial_t}$ (the coordinate time vector). Since $\boldsymbol{\partial_t}$ is a Killing vector in Kerr spacetime, the energy measured at infinity is conserved and given by:

$$\boxed{E_{\rm geod} = -\mathbf{u}_{\rm obs} \cdot \mathbf{p}_{\rm obs} = -p_t}, \qquad \text{(V.9)}$$

which is a constant of motion along the photon's geodesic.

General redshift expression

Combining the results above, the redshift factor becomes:

$$g = \frac{\mathbf{u}_{\rm obs} \cdot \mathbf{p}_{\rm obs}}{\mathbf{u}_{\rm em} \cdot \mathbf{p}_{\rm em}} = \frac{E_{\rm geod}}{\Gamma_{cd} E_{cd} (1 - \mathbf{n}_{cd} \cdot \mathbf{V}_{cd})}. \qquad \text{(V.10)}$$

and the redshift $\mathcal{Z}$ writes:

$$\mathcal{Z} = \frac{1}{g} - 1 = \frac{\Gamma_{cd} E_{cd} (1 - \mathbf{n}_{cd} \cdot \mathbf{V}_{cd})}{E_{\rm geod}} - 1. \qquad \text{(V.11)}$$

Finally, the redshift observable used in GRAVITY is the apparent radial velocity, defined as:

$$\boxed{V_{\rm rad} = c\mathcal{Z} = c \left(\frac{\Gamma_{cd} E_{cd} (1 - \mathbf{n}_{cd} \cdot \mathbf{V}_{cd})}{E_{\rm geod}} - 1 \right)}, \qquad \text{(V.12)}$$

where we reintroduce the c factor to make units explicit. This is the quantity that can be directly compared to spectroscopic data. The advantage of this decomposition is that it separates the purely kinematical and local terms (which can sometimes be approximated analytically) from the ray-traced quantities like $\mathbf{n}_{cd}$, which generally require numerical integration of the photon geodesic.

The next section is trying to define a framework where it is possible to compute an approximate form of Eq. (V.12) without ray tracing.

V.2.2 Approximate expression without ray tracing

We aim to derive an approximate expression for the redshift $\mathcal{Z}$ experienced by a photon emitted by a source moving near a black hole, without relying on full ray tracing. Instead, we will make a number of simplifying assumptions that still capture the key physical effects: gravitational redshift, transverse Doppler effect, and line-of-sight Doppler shift.

Choice of reference frame. To proceed analytically without ray tracing, we introduce a local observer $\mathcal{O}_{cd}$ at the emission point, whose four-velocity is aligned with the coordinate time direction: $\boldsymbol{\partial}_t$. This choice corresponds to a *static observer*—one who remains at fixed spatial coordinates in the spacetime.

This specific choice is not arbitrary. It is motivated by the fact that $\boldsymbol{\partial}_t$ is a Killing vector in any stationary spacetime (such as Schwarzschild or Kerr), which implies the existence of a conserved energy along a photon's geodesic:

$$E_{\text{geod}} \equiv -p_t = \text{constant}.$$

By aligning the local observer's four-velocity with $\boldsymbol{\partial}_t$, we ensure a direct relation between this conserved energy and the energy measured locally by $\mathcal{O}_{cd}$. This simplifies the redshift computation in the absence of ray tracing, and will later allow us to extract an approximate analytic expression for the redshift in terms of orbit quantities.

Imposing the normalization condition $\mathbf{u}_{cd} \cdot \mathbf{u}_{cd} = -1$ (using the mostly-plus signature), we obtain:

$$\mathbf{u}_{cd} = (-g_{tt})^{-1/2}\, \boldsymbol{\partial}_t, \tag{V.13}$$

where the metric component g_{tt} is evaluated at the emission point. In Schwarzschild spacetime, this is exactly the Zero Angular Momentum Observer (ZAMO), but since we allow for non-zero spin (e.g., in Kerr), we avoid calling it that.

Photon energy measured by this observer. Let $\mathbf{p}_{\text{em}}$ be the four-momentum of the emitted photon. The energy E_{cd} measured by $\mathcal{O}_{cd}$ is:

$$E_{cd} = -\mathbf{u}_{cd} \cdot \mathbf{p}_{\rm em} \tag{V.14}$$
$$= -(-g_{tt})^{-1/2}\, \boldsymbol{\partial}_t \cdot \mathbf{p}_{\rm em} \tag{V.15}$$
$$= (-g_{tt})^{-1/2}\, E_{\rm geod}, \tag{V.16}$$

where $E_{\rm geod} \equiv -p_t^{\rm em}$ is the conserved energy of the photon along its geodesic, which is what a distant observer would measure in flat spacetime.

Lorentz factor between emitter and static observer. We define the Lorentz factor between the emitter and the static observer $\mathcal{O}_{cd}$ as:

$$\Gamma_{cd} = -\mathbf{u}_{\rm em} \cdot \mathbf{u}_{cd} \tag{V.17}$$
$$= -\left(g_{tt} u^t_{\rm em} + g_{t\varphi} u^\varphi_{\rm em}\right) \cdot (-g_{tt})^{-1/2}. \tag{V.18}$$

We now assume that $g_{tt} u^t_{\rm em} \gg g_{t\varphi} u^\varphi_{\rm em}$, i.e., that the φ-component of the emitter's motion (related to black hole spin) is negligible[3]. Then:

$$\Gamma_{cd} \approx (-g_{tt})^{1/2}\, u^t_{\rm em}. \tag{V.19}$$

Velocity of the emitter as measured by $\mathcal{O}_{cd}$. From the decomposition of the emitter's four-velocity in terms of the static observer's frame:

$$\mathbf{u}_{\rm em} = \Gamma_{cd}\left(\mathbf{u}_{cd} + \mathbf{V}_{cd}\right), \tag{V.20}$$

we can solve for the spatial velocity $\mathbf{V}_{cd}$. In components:

$$\mathbf{V}_{cd} = \left(\frac{u^t_{\rm em}}{(-g_{tt})^{1/2} u^t_{\rm em}} - (-g_{tt})^{-1/2},\ \frac{u^i_{\rm em}}{(-g_{tt})^{1/2} u^t_{\rm em}}\right) \tag{V.21}$$
$$= (-g_{tt})^{-1/2} \left(0, \frac{u^i_{\rm em}}{u^t_{\rm em}}\right) \tag{V.22}$$
$$\equiv (-g_{tt})^{-1/2}\, \boldsymbol{\mathcal{V}}_\infty, \tag{V.23}$$

where we introduced:

$$\boldsymbol{\mathcal{V}}_\infty \equiv \left(0, \frac{dx^i}{dt}\right), \tag{V.24}$$

which corresponds to the 3D coordinate velocity of the emitter as seen by a static observer at infinity.

[3]The ratio $g_{t\varphi} u^\varphi_{\rm em} / (g_{tt} u^t_{\rm em}) < 10^{-9}$ for S2 and $< 10^{-6}$ for S2/10.

Projection along the line of sight. Without ray tracing, we cannot compute the actual photon geodesic. We therefore make a strong but practical approximation: we assume the photon propagates along a straight line in flat spacetime. In other words, the photon's direction $\mathbf{n}_{cd}$ is taken to be a unit vector pointing from the emitter to the observer in Euclidean 3D space.

This simplifies the redshift expression but introduces an uncontrolled approximation—unlike typical PN expansions, we do not neglect a small parameter like ϵ whose size we can easily track. The validity of this approach must therefore be assessed *a posteriori* by comparing its predictions with full ray-tracing simulations (`GR_rt`), which serve as the ultimate reference.

One might ask whether intermediate approaches, such as post-Newtonian ray tracing, could offer improved accuracy with modest computational cost. While such alternatives merit exploration, they fall outside the scope of the present work.

We adopt this approximation primarily because `GR_rt` simulations are computationally expensive, making them unsuitable for large-scale orbit fitting. In contrast, our method—based on `GR_proj`—offers orders-of-magnitude faster evaluation while still capturing the leading relativistic effects relevant for current observations.

Under this flat-spacetime assumption, the projection of the star's velocity onto the photon's direction becomes:

$$\mathbf{n}_{cd} \cdot \mathbf{V}_{cd} = (-g_{tt})^{-1/2}\, \mathbf{n}_{cd} \cdot \boldsymbol{\mathcal{V}}_\infty \tag{V.25}$$

$$\equiv (-g_{tt})^{-1/2}\, \mathcal{V}_{\mathrm{rad,flat}}, \tag{V.26}$$

where $\mathcal{V}_{\mathrm{rad,flat}}$ is the flat-space radial velocity, projected along the Euclidean line of sight from the emitter to the observer.

Expanding in small quantities. Assuming the emitter is far from the black hole, we write:

$$-\, g_{tt} = 1 - \epsilon_\chi, \tag{V.27}$$

where $\epsilon_\chi = 2r/(r^2 + a^2\cos^2\theta) \ll 1$ for emission far from the black hole[4]. Then:

$$\frac{E_{cd}}{E_{\mathrm{geod}}} = (1-\epsilon_\chi)^{-1/2}, \tag{V.28}$$

$$\mathbf{n}_{cd} \cdot \mathbf{V}_{cd} = (1-\epsilon_\chi)^{-1/2}\, \mathcal{V}_{\mathrm{rad,flat}}, \tag{V.29}$$

$$\Gamma_{cd} = \left(1 - (1-\epsilon_\chi)^{-1}\, \mathcal{V}_\infty^2\right)^{-1/2}. \tag{V.30}$$

[4]We have $\epsilon_\chi < 10^{-3}$ for S2 and $< 10^{-2}$ for S2/10. This quantity is not be confused with ϵ of the PN expansion which is similar to $\epsilon_c hi(\chi = 0)$.

Total redshift. Combining all terms, the redshift becomes:

$$\mathcal{Z} = \frac{1}{g} - 1 = \frac{\Gamma_{cd} E_{cd}(1 - \mathbf{n}_{cd} \cdot \mathbf{V}_{cd})}{E_{\text{geod}}} - 1. \tag{V.31}$$

$$= (1 - \epsilon_\chi)^{-1/2} \cdot \left(1 - \frac{\mathcal{V}_\infty^2}{1 - \epsilon_\chi}\right)^{-1/2} \cdot \left(1 - (1 - \epsilon_\chi)^{-1/2}\, \mathcal{V}_{\text{rad,flat}}\right) - 1. \tag{V.32}$$

Expanding this in small parameters (ϵ_χ, $\mathcal{V}_\infty/c$, and $\mathcal{V}_{\text{rad,flat}}/c$), and keeping terms to second order:

$$\mathcal{Z} \approx \left(1 + \frac{1}{2}\epsilon_\chi\right)\left(1 + \frac{1}{2}\mathcal{V}_\infty^2\right)(1 - \mathcal{V}_{\text{rad,flat}}) - 1 \tag{V.33}$$

$$\approx 1 + \frac{1}{2}\epsilon_\chi + \frac{1}{2}\mathcal{V}_\infty^2 - \mathcal{V}_{\text{rad,flat}} - 1 \tag{V.34}$$

$$\approx \frac{1}{2}\epsilon_\chi + \frac{1}{2}\mathcal{V}_\infty^2 - \mathcal{V}_{\text{rad,flat}}. \tag{V.35}$$

Thus, the total redshift splits into:

- Gravitational redshift: $\frac{1}{2}\epsilon_\chi$
- Transverse Doppler effect: $\frac{1}{2}\mathcal{V}_\infty^2$
- Line-of-sight Doppler shift: $-\mathcal{V}_{\text{rad,flat}}$

The minus sign in the last term arises because $\mathbf{n}_{cd}$ points *from the source to the observer*, while the conventional definition of radial velocity assumes the opposite.

Final result.

$$\boxed{\mathcal{Z} \approx \frac{1}{2}\epsilon_\chi + \frac{1}{2}\mathcal{V}_\infty^2 - \mathcal{V}_{\text{rad,flat}}} \tag{V.36}$$

This formula uses quantities that are directly accessible in the orbit-fitting pipeline: $\mathcal{V}_\infty$ is the magnitude of the coordinate velocity, and $\mathcal{V}_{\text{rad,flat}}$ is its projection onto the flat-space line of sight, computed via a rotation matrix (e.g., in `BH2sky`).

V.3 Extending `OOGRE` to higher order effects

The purpose of this section is to explain how I extended the existing relativistic models to the case of a rotating black hole, by implementing, the `1.5PN`, `2PN` with

the spin contribution, `2PN_Q`, `2.5PN`, and `3PN` models. We have seen in subsection V.1.2 that `OOGRE` is a perturbed Kepler-orbit model code and that we can use the orbital perturbation theory (see section II.2) to write the Lagrange planetary equations: the derivative of each orbital parameter with respect to time, as a function of the various perturbative accelerations expressed in the Gaussian frame (see Eqs. (II.12) to (II.16)). These equations were already part of the perturbed Kepler model of `OOGRE` and my contribution was to derive the expression of the perturbative acceleration due to the Lense-Thirring effect (at 1.5PN and 2.5PN), quadrupole moment effect (2PN), and third order Schwarzschild precession (3PN).

We start by extracting the expressions of $a_{1.5\mathrm{PN}}$, $a_{2.5\mathrm{PN}}$, $a_{3\mathrm{PN}}$ from [139] before expressing them in the Gaussian frame $(\mathbf{n}_{\mathrm{orb}}, \mathbf{m}_{\mathrm{orb}}, \mathbf{z}_{\mathrm{orb}})$ as:

1PN (Schwarzschild)

$$\mathcal{R}_{\mathrm{Sch}}^{1\mathrm{PN}} = \mathbf{a}_{\mathrm{Sch}}^{1\mathrm{PN}} \cdot \mathbf{n}_{\mathrm{orb}} = \epsilon \frac{Gm}{p^2}(1+e\cos f)^2 \left(3(e^2+1) + 2e\cos f - 4e^2\cos^2 f\right) \tag{V.37}$$

$$\mathcal{S}_{\mathrm{Sch}}^{1\mathrm{PN}} = \mathbf{a}_{\mathrm{Sch}}^{1\mathrm{PN}} \cdot \mathbf{m}_{\mathrm{orb}} = 4\epsilon \frac{Gm}{p^2}(1+e\cos f)^3 e\sin f \tag{V.38}$$

$$\mathcal{W}_{\mathrm{Sch}}^{1\mathrm{PN}} = \mathbf{a}_{\mathrm{Sch}}^{1\mathrm{PN}} \cdot \mathbf{z}_{\mathrm{orb}} = 0; \tag{V.39}$$

1.5PN (Lense–Thirring)

$$\mathcal{R}_{\mathrm{LT}}^{1.5\mathrm{PN}} = \mathbf{a}_{\mathrm{LT}}^{1.5\mathrm{PN}} \cdot \mathbf{n}_{\mathrm{orb}} = 2\epsilon^{3/2} \frac{Gm}{p^2}\chi(1+e\cos f)^4 \cos\theta; \tag{V.40}$$

$$\mathcal{S}_{\mathrm{LT}}^{1.5\mathrm{PN}} = \mathbf{a}_{\mathrm{LT}}^{1.5\mathrm{PN}} \cdot \mathbf{m}_{\mathrm{orb}} = -2\epsilon^{3/2} \frac{Gm}{p^2}\chi e\sin f(1+e\cos f)^3 \cos\theta; \tag{V.41}$$

$$\begin{aligned}\mathcal{W}_{\mathrm{LT}}^{1.5\mathrm{PN}} = \mathbf{a}_{\mathrm{LT}}^{1.5\mathrm{PN}} \cdot \mathbf{z}_{\mathrm{orb}} &= 2\epsilon^{3/2} \frac{Gm}{p^2}\chi(1+e\cos f)^3 \sin\theta \\ &\times \left[2(1+e\cos f)\cos(\beta-\varphi) + e\sin f \sin(\beta-\varphi)\right];\end{aligned} \tag{V.42}$$

2PN (Schwarzschild)

$$\mathcal{R}_{\mathrm{Sch}}^{2\mathrm{PN}} = \mathbf{a}_{\mathrm{Sch}}^{2\mathrm{PN}} \cdot \mathbf{n}_{\mathrm{orb}} - 9\epsilon^2 \frac{Gm}{p^2}(1+e\cos f)^4; \tag{V.43}$$

$$\mathcal{S}_{\mathrm{Sch}}^{2\mathrm{PN}} = \mathbf{a}_{\mathrm{Sch}}^{2\mathrm{PN}} \cdot \mathbf{m}_{\mathrm{orb}} = -2\epsilon^2 \frac{Gm}{p^2} e(1+e\cos f)^4 \sin f; \tag{V.44}$$

$$\mathcal{W}_{\mathrm{Sch}}^{2\mathrm{PN}} = \mathbf{a}_{\mathrm{Sch}}^{2\mathrm{PN}} \cdot \mathbf{z}_{\mathrm{orb}} = 0; \tag{V.45}$$

2PN (Quadrupole moment)

$$\mathcal{R}_Q^{\rm 2PN} = \mathbf{a}_Q^{\rm 2PN}\cdot\mathbf{n}_{\rm orb} = -\frac{3}{2}\epsilon^2\frac{Gm}{p^2}\chi^2(1+e\cos f)^4(1-3\sin^2\theta\cos^2(\beta-\varphi)); \quad \text{(V.46)}$$

$$\mathcal{S}_Q^{\rm 2PN} = \mathbf{a}_Q^{\rm 2PN}\cdot\mathbf{m}_{\rm orb} = -3\epsilon^2\frac{Gm}{p^2}\chi^2(1+e\cos f)^4\sin^2\theta\cos(\beta-\varphi)\sin(\beta-\varphi); \quad \text{(V.47)}$$

$$\mathcal{W}_Q^{\rm 2PN} = \mathbf{a}_Q^{\rm 2PN}\cdot\mathbf{z}_{\rm orb} = -3\epsilon^2\frac{Gm}{p^2}\chi^2(1+e\cos f)^4\cos\theta\sin\theta\cos(\beta-\varphi). \quad \text{(V.48)}$$

2.5PN (Lense–Thirring)

$$\mathcal{R}_{\rm LT}^{\rm 2.5PN} = \mathbf{a}_{\rm LT}^{\rm 2.5PN}\cdot\mathbf{n}_{\rm orb} = -2\,\epsilon^{5/2}\,\frac{Gm}{p}\,\chi\,(1+e\cos f)^4\cos\theta\left[10(1+e\cos f)+3e^2\sin^2 f\right], \quad \text{(V.49)}$$

$$\mathcal{S}_{\rm LT}^{\rm 2.5PN} = \mathbf{a}_{\rm LT}^{\rm 2.5PN}\cdot\mathbf{m}_{\rm orb} = -6\,\epsilon^{5/2}\,\frac{Gm}{p}\,\chi\,e\sin f\,(1+e\cos f)^5\cos\theta, \quad \text{(V.50)}$$

$$\mathcal{W}_{\rm LT}^{\rm 2.5PN} = \mathbf{a}_{\rm LT}^{\rm 2.5PN}\cdot\mathbf{z}_{\rm orb} = -4\,\epsilon^{5/2}\,\frac{Gm}{p}\,\chi\,(1+e\cos f)^4\sin\theta \quad \text{(V.51)}$$

$$\times\left[3(1+e\cos f)\cos(\beta-u)+e\sin f\sin(\beta-u)\right], \quad \text{(V.52)}$$

3PN (Schwarzschild)

$$\mathcal{R}^{\rm 3PN} = \mathbf{a}^{\rm 3PN}\cdot\mathbf{n}_{\rm orb} = \epsilon^3\,\frac{Gm}{p^2}\,(1+e\cos f)^4\left[16(1+e\cos f)+e^2\sin^2 f\right], \quad \text{(V.53)}$$

$$\mathcal{S}^{\rm 3PN} = \mathbf{a}^{\rm 3PN}\cdot\mathbf{m}_{\rm orb} = 4\,\epsilon^3\,\frac{Gm}{p^2}\,e\sin f\,(1+e\cos f)^5, \quad \text{(V.54)}$$

$$\mathcal{W}_{\rm Sch}^{\rm 3PN} = \mathbf{a}_{\rm Sch}^{\rm 3PN}\cdot\mathbf{z}_{\rm orb} = 0; \quad \text{(V.55)}$$

with $\epsilon = GM/(c^2p)$. Then we plug each perturbation $\mathcal{P}$ (representing $\mathcal{R}$, $\mathcal{S}$, or $\mathcal{W}$) in `OOGRE` such that:

- 1.5PN model gets: $\mathcal{P} = \mathcal{P}^{\rm 1PN} + \mathcal{P}^{\rm 1.5PN}$
- 2.5PN model gets: $\mathcal{P} = \mathcal{P}^{\rm 1PN} + \mathcal{P}^{\rm 1.5PN} + \mathcal{P}^{\rm 2PN} + \mathcal{P}^{\rm 2.5PN}$
- 3PN model gets: $\mathcal{P} = \mathcal{P}^{\rm 1PN} + \mathcal{P}^{\rm 1.5PN} + \mathcal{P}^{\rm 2PN} + \mathcal{P}^{\rm 2.5PN} + \mathcal{P}^{\rm 3PN}$

Chapter VI

Evaluating the detectability of various effects

Contents

VI.1 Which model for which orbit? 101

VI.1.1 Code Verification with S2 102

VI.1.2 Comparing the Various Relativistic Effects 104

VI.1.3 Assessing the required model for accuracy and efficiency . . . 108

VI.2 Evaluating the detectability of the spin using orbit fitting . 111

VI.2.1 Methodology 112

VI.2.2 Fitting Kerr Data with a Zero-Spin Model 114

VI.1 Which model for which orbit?

In this section, we will first compare the results of our machinery to the state of the art. Second, we will evaluate most of the effects mentioned in subsection I.2.3 in order understand which will be necessary to include in this work. Third, we will do the same but for the PN order to use depending on the star we want

to consider. In addition to the star S2, we also simulate orbits of the hypothetical star that we call S2/10, (a star sharing the exact same osculating orbital elements as S2, with the exception of having a semi-major axis 10 times smaller: $a_{sma}|_{S2} = 10a_{sma}|_{S2/10}$). Therefore, using Kepler's third law which states that $4\pi^2 a_{sma}^3/P^2 = GM_\bullet = \text{cte}$, we obtain the following relation for the period of S2/10: $P_{\text{S2/10}} = 10^{-3/2} P_{\text{S2}} = 0.5074\text{yrs}$. Also, we arbitrarily take the osculating time as ($t_{\text{osc}} = t_p - P_{\text{S2/10}} = 2018,1253\text{yrs}$) considering that the code tends to be more stable near the apocenters.

VI.1.1 Code Verification with S2

In Section I.3, we reviewed prior work on the influence of the spin of Sgr A* on its surroundings and the prospects for detecting such effects. Before progressing further, we first validate our computational framework by comparing it to results from the literature.

The study by Grould et al. [74] served as a benchmark for this verification. Their results were obtained using a `YORICK`-based interface. Since then, Thibaut Paumard and Frédéric Vincent have reimplemented and significantly improved this interface in `Python`, completely overhauling the computational backend. Consequently, reproducing the published results for the star S2 was not a straightforward task and represents the first substantial outcome of my work.

Figure VI.1 presents a comparison between the new implementation (bottom panels) and the original results from [74] for spin-induced effects on both astrometry (right panels) and radial velocity (left panels). Unlike Eq. (I.6), here the *spin effect* is defined as:

$$\begin{aligned} \Delta\text{RA}_\chi &= \text{RA}_{\chi=0} - \text{RA}_{\chi=0.99}; \\ \Delta\text{DEC}_\chi &= \text{DEC}_{\chi=0} - \text{DEC}_{\chi=0.99}; \\ \Delta\text{RV}_\chi &= \text{RV}_{\chi=0.99} - \text{RV}_{\chi=0}, \end{aligned} \tag{VI.1}$$

for the right ascension, the declination, and radial velocity, respectively. The orbital parameters used by the authors are the best-fit values evaluated by [53]: $T = 15.8\text{yrs}, a_{\text{sma}} = 0.12300, e = 0.88, t_{\text{peri}} = 2002.32\text{yrs}, \Omega = 225.39°, \omega = 63.56°, \iota = 135.25°$. However, no mention of the osculating time was given in [74] nor [52]. After trying to reproduce the simulation with various characteristic values of the osculating time (time of initial observation date, times of pericenters, times of apocenters) and identified the osculating time to be near the apocenter after t_{peri} ($t_{\text{osc}} = t_{\text{peri}} + P/2$). They also considered the distance between the observer and the center of our galaxy and the black hole's mass equal to the best-fit found by the same authors: $R_0 = 8.33\text{kpc}$ and $M_0 = 4.31 \cdot 10^6 M_\odot$. For the spin parameters of the black hole, they choose $\chi = 0.99, i_\bullet = 45°$ and $\Omega_\bullet = 160°$. As shown, the results exhibit excellent agreement across both observables, confirming the consistency and reliability of the new code.

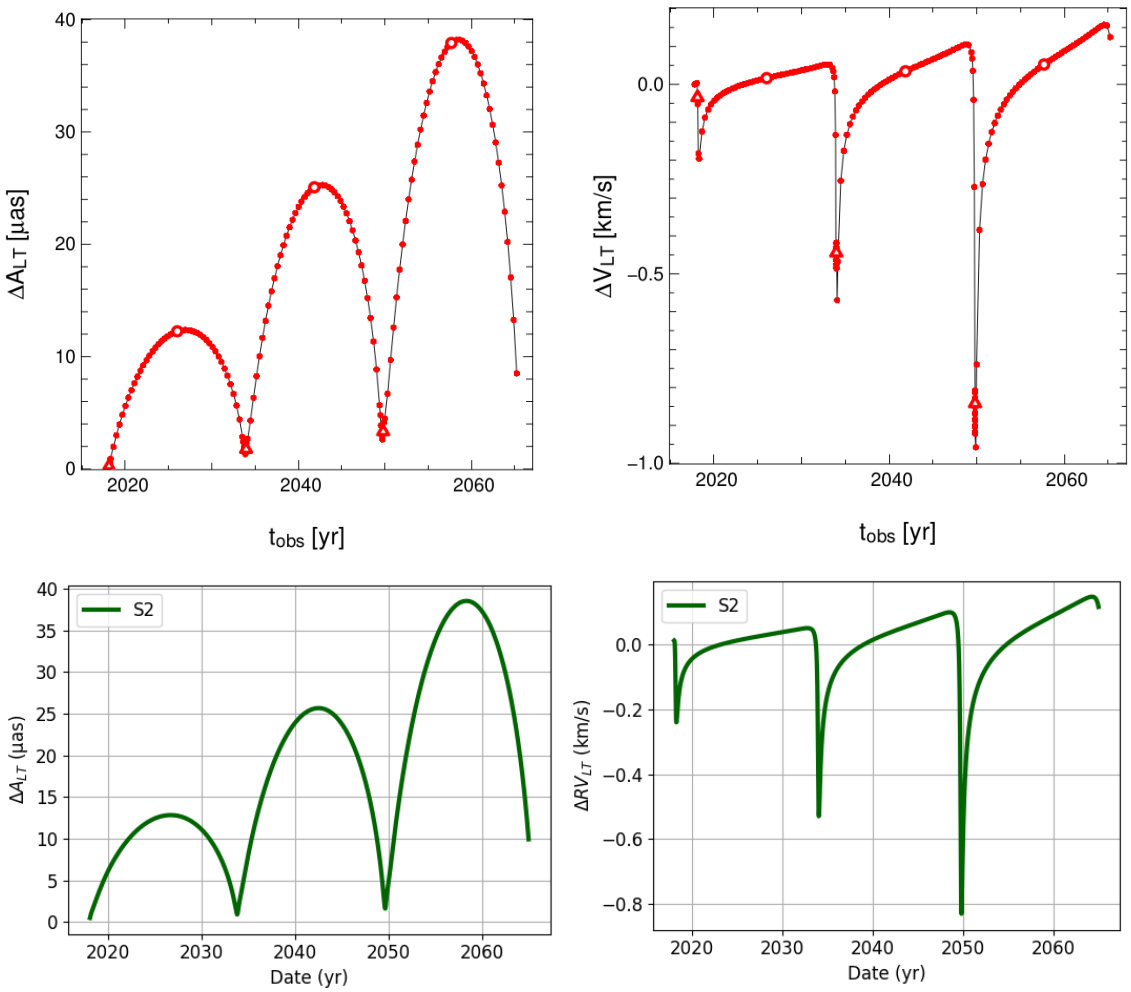

Figure VI.1: Comparison of our results (bottom) with those from [74] for spin-induced astrometric (right) and spectroscopic (left) effects.

It is important to note a caveat in the method used to compute spin-induced effects: its validity can break down for stars in closer-in orbits, or when the initial integration date is significantly displaced from the osculating time. Ideally, both the astrometric and spectroscopic spin-induced deviations—denoted ΔA_{LT} and ΔRV_{LT}, respectively—should be zero at the initial integration time. This condition holds only when the integration starts exactly at the osculating time.

A more robust approach involves first integrating the orbit under the Schwarzschild metric from the original osculating time (as defined by the orbital elements of [52]) up to the desired integration start date. One can then extract the updated orbital parameters at this point and adopt them as a new set of osculating elements, using the new integration date as the corresponding osculation time. This procedure

still neglects the spin's dynamical influence during the interval between the original and updated osculating times, but it offers improved accuracy over the method proposed by [74], especially when the time gap is moderate.

Having successfully validated our code against the reference results from [74], we are now in a position to confidently apply our framework to explore new configurations and predictions. This initial comparison demonstrates the robustness of our implementation, confirming that it captures the relativistic spin effects with the required accuracy.

In the following sections, we will present the results obtained using this upgraded machinery for a broader set of orbits and spin configurations, providing insights into the detectability of relativistic effects in future observations.

VI.1.2 Comparing the Various Relativistic Effects

In this section, we aim to assess which physical effects must be included in modeling stellar orbits for high-precision instruments such as GRAVITY+ or ERIS. To do this, we systematically compare a suite of relativistic models incorporating different combinations of effects—ranging from Schwarzschild precession to gravitational lensing and black hole spin—using mock orbits of the well-known star S2 and the hypothetical closer-in analog, S2/10. This comparison allows us to determine the observability of subtle relativistic features and the necessity of including each effect based on its magnitude relative to instrumental uncertainties. As mentioned in subsection IV.3.2, if we want to estimate a higher order effect that can be simulated by evaluating the difference of two orbits (with and without the effect), the coordinate system choice would have considerably little to no impact (e.g. the disagreement between the KS and BL coordinates over the spin effect amounts to less than 5nas and 0.8m/s over four orbits of S2 or less than 0.15µas and 1.3km/s over twenty orbits of S2/10).

We introduce the following model hierarchy:

- $\mathcal{M}_A$: Schwarzschild precession only; Euclidean projection;
- $\mathcal{M}_B$: $\mathcal{M}_A$ + Lense–Thirring effect on the orbit;
- $\mathcal{M}_C$: $\mathcal{M}_B$ + quadrupole moment;
- $\mathcal{M}_D$: $\mathcal{M}_C$ + Rømer delay;
- $\mathcal{M}_E$: $\mathcal{M}_D$ + transverse Doppler + gravitational redshift;
- $\mathcal{M}_F$: $\mathcal{M}_E$ + gravitational lensing (GL), either approximated or ray-traced;
- $\mathcal{M}_G$: $\mathcal{M}_F$ + spin-induced lensing + Shapiro delay.

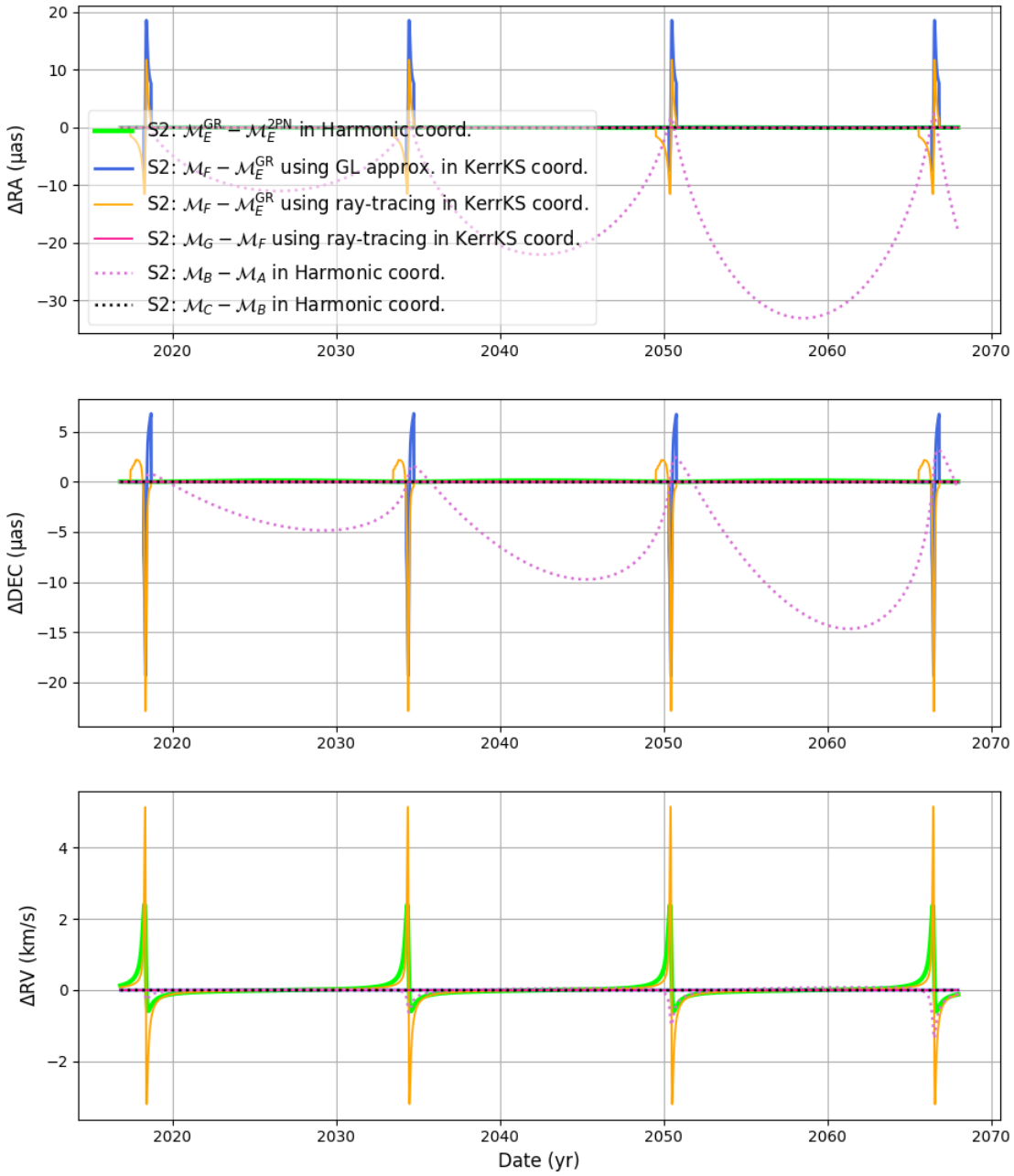

Figure VI.2: Right ascension (top), declination (middle), and radial velocity (bottom) residuals between models $\mathcal{M}_A$–$\mathcal{M}_G$ simulated over more than 4 orbits of the star S2. We use $(\chi, i_\bullet, \Omega_\bullet) = (0.99, 25°, 80°)$ for rotating BH models (dotted purple, black, and solid pink). Schwarzschild-only comparisons use $\chi = 0$ (green, blue, and orange-yellow). The yellow-orange curves refer to the use of the Gravitational Lensing approximation in model $\mathcal{M}_F$, whereas the blue ones refer to the use of ray tracing instead. We use harmonic coordinates for the dotted purple, dotted black, and solid green comparisons, and the KS coordinates for the last blue, orange-yellow and pink ones.

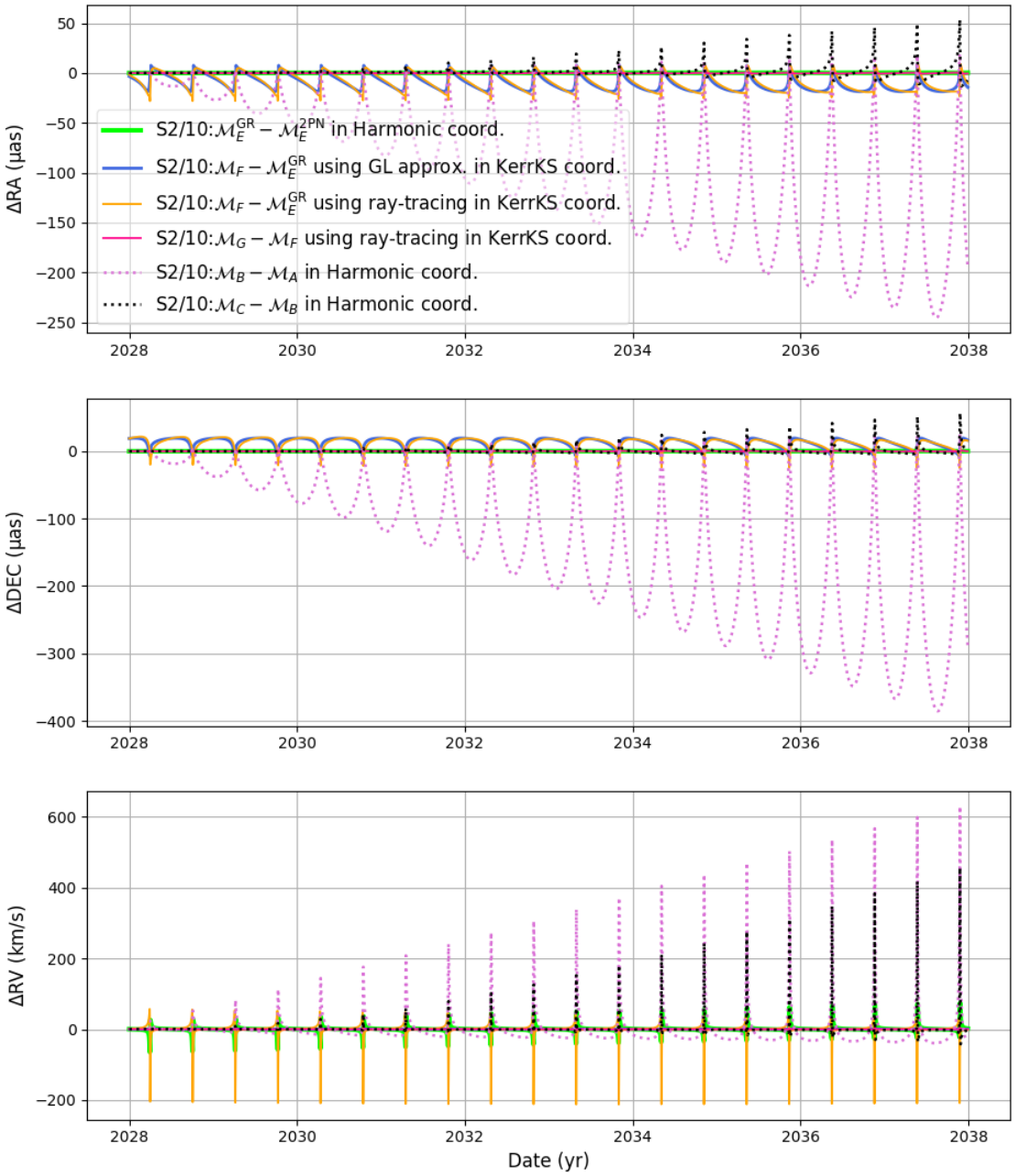

Figure VI.3: Same as Figure VI.2 but for the hypothetical star S2/10, over a 10-year observing period.

PN vs. GR Comparison ($\mathcal{M}_E^{\rm PN}$ vs. $\mathcal{M}_E^{\rm GR}$): Using harmonic coordinates (green curves in Figures VI.2 and VI.3), the astrometric differences between PN and full GR are below 0.5 μas for both S2 and S2/10—well below GRAVITY+'s sensitivity. However, the radial velocity differences reach 2.4 km/s for S2 and up to 75 km/s for S2/10 (beyond ERIS's 10 km/s canonical precision). Therefore, for spectroscopic modeling of closer-in stars like S2/10, the full GR model is necessary.

Gravitational Lensing ($\mathcal{M}_F$ vs. $\mathcal{M}_E^{\rm GR}$): We compare GL effects in KS coordinates using both an analytical approximation [121] (blue curves in Figures VI.2 and VI.3) and ray tracing (orange-yellow), both with $\chi = 0$. The astrometric differences remain marginal, hovering around 10 μas, even after 20 orbits of S2/10. Since the GL effect is not cumulative, model $\mathcal{M}_E$ remains acceptable for astrometry in most cases. If one adds the gravitational lensing analytical approximation to the PN model, then a PN version of model $\mathcal{M}_F$ becomes very sufficient for studying such astrometric data. Note that this assumes that the residuals when using the harmonic coordinates are nearly identical to those estimated here with the KS coordinates, which was demonstrated in subsection IV.3. However, RV differences reach 200 km/s for S2/10, making GL negligible in astrometry but not in spectroscopy.

Spin-Related Photon Effects ($\mathcal{M}_G$ vs. $\mathcal{M}_F$): Spin-induced light bending and the Shapiro delay (pink curves in Figures VI.2 and VI.3) are essentially undetectable for both astrometry and spectroscopy in our simulations.

Lense–Thirring and Quadrupole Moment Effects: Dotted orchid (LT) and black (Q) curves in Figures VI.2 and VI.3 represent spin-induced precessions. These effects are cumulative, growing over time. With S2/10, they reach detectable amplitudes within a decade, making tests of the no-hair theorem feasible on human timescales—unlike with S2, where decades to a century would be required.

Inclination and Weak-Field Regime: As shown in [135], the weak-field approximation remains valid for orbits with $a_{\rm sma} > 100\ R_S$, except when the orbital inclination is extreme. For example, with $r_{\rm peri} = 100\ R_S$, photons approach within 20 R_S if $\iota \gtrsim 78°$. The probability of such inclinations is $\sim 2\%$ for random orbits. In such rare cases, lensing and redshift signatures during conjunction may enhance spin constraints.

Conclusion: Our results show that while many relativistic effects are negligible (e.g., spin-induced lensing), others—especially GR corrections to RVs and spin precession—are critical for interpreting observations of stars like S2/10. Accurate modeling requires careful inclusion of these effects depending on the stellar orbit and instrument sensitivity.

VI.1.3 Assessing the required model for accuracy and efficiency

A central objective of this study is to model relativistic stellar orbits near Sgr A* with high accuracy while minimizing computational overhead. To this end, we first identify the optimal post-Newtonian (PN) order necessary to capture the relevant physical effects for closer-in stars. This choice must ensure that all detectable relativistic contributions—both in astrometry and spectroscopy—are accurately modeled, without introducing unnecessary complexity. We begin by comparing the 1PN, 2PN, and 3PN orders in the Schwarzschild metric and then extend the analysis to the Kerr case by including spin-related terms at the 2.5PN level. Once the 2PN order is confirmed as both necessary and sufficient for our target parameter space, we assess its performance relative to two general relativistic models: the computationally intensive ray-traced model (GRrt) and the more efficient projected approximation (GRproj). This final comparison provides practical guidance on the trade-offs between accuracy and simulation speed in different modeling frameworks.

PN Order Requirements. We begin by comparing the 1PN and 2PN orders for Schwarzschild dynamics. Figure VI.4a shows the maximal astrometric and spectroscopic differences between 1PN and 2PN simulations for the star S2 and a sample of hypothetical closer-in stars, assuming a 10-year observing campaign starting in $t_0 = 2028$.

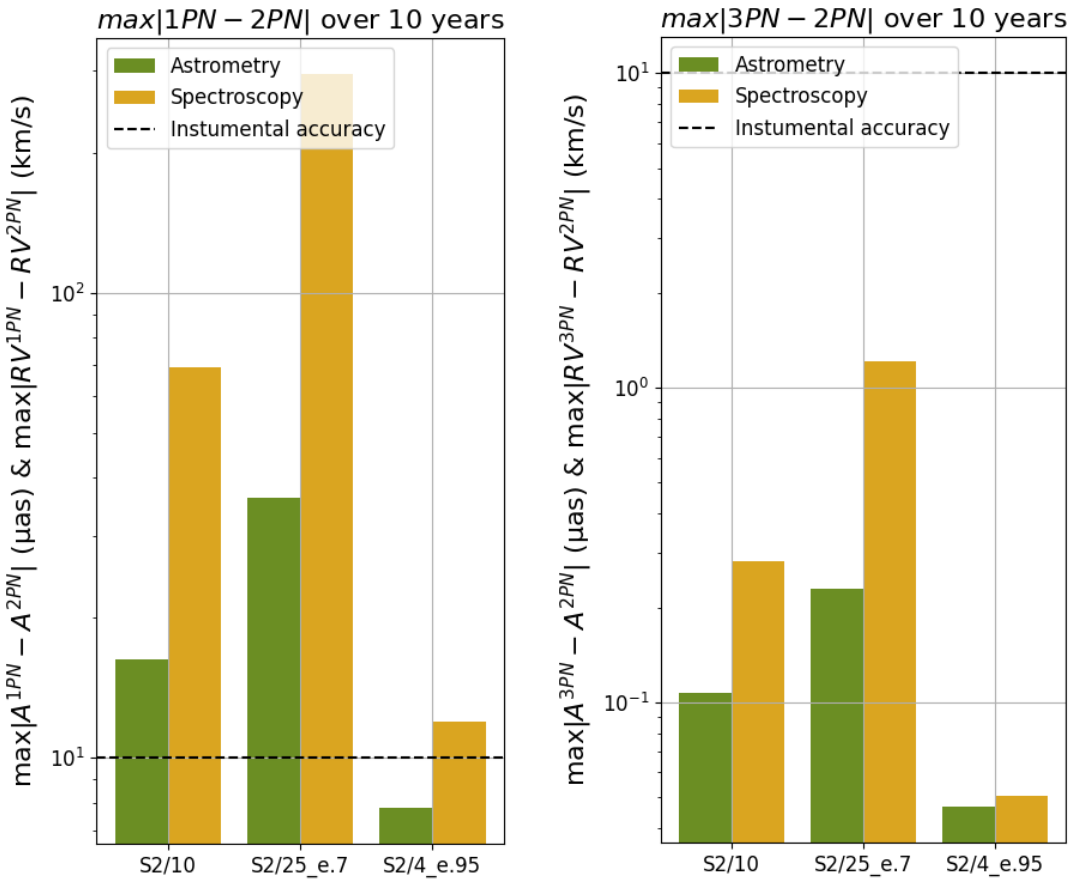

(a) 1PN vs 2PN **(b)** 3PN vs 2PN

Figure VI.4: Maximal astrometric (green) and spectroscopic (yellow) differences between PN orders using the Schwarzschild metric, over a 10-year simulation ($t_0 = 2028$ to $t_{\text{end}} = 2038$). (a) Differences between 1PN and 2PN can exceed instrumental thresholds of $(\sigma_A, \sigma_{RV}) = (10\,\mu\text{as}, 10\,\text{km/s})$ for some stars. (b) Differences between 3PN and 2PN remain well below detection limits, confirming the sufficiency of the 2PN order.

These results demonstrate that while 1PN accuracy may suffice for S2, higher-order terms become necessary for closer-in stars. Differences between 1PN and 2PN simulations occasionally surpass instrumental thresholds, making 2PN the minimal required order in such cases.

Next, we examine whether extending beyond 2PN adds significant improvement. Figure VI.4b shows the 3PN–2PN difference, which remains consistently below observational thresholds. This confirms that 2PN is sufficient for modeling Schwarzschild orbits of the stars under consideration.

We now move to Kerr orbits and test whether 2PN remains sufficient when spin

is included. Specifically, we compare simulations at 2PN (including the leading 1.5PN Lense–Thirring term) and 2.5PN (including next-order spin contributions), for spin magnitudes $\chi = 0.5$ and $\chi = 0.99$ and orientation $(i_\bullet, \Omega_\bullet) = (95°, 0°)$.

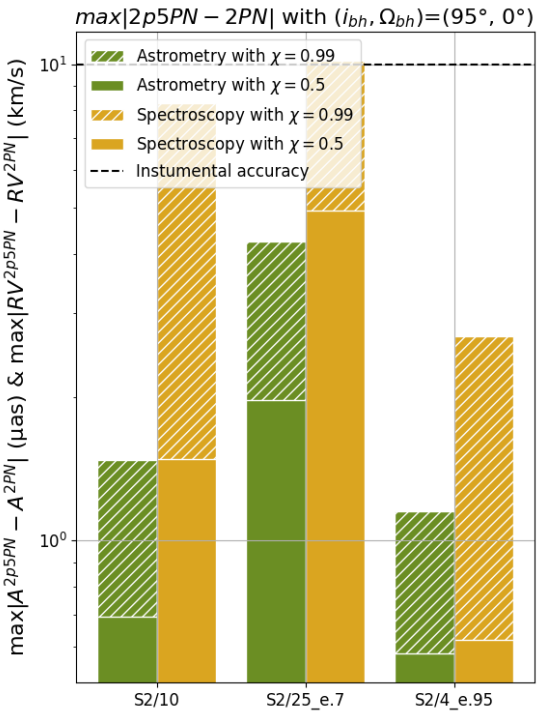

Figure VI.5: Maximal difference between 2.5PN and 2PN Kerr simulations for $\chi = 0.5$ (solid) and $\chi = 0.99$ (striped), using a fixed spin orientation. The second-order LT term remains below detection thresholds in both astrometry and spectroscopy.

Figure VI.5 confirms that second-order LT contributions are largely undetectable given current astrometric precisions ($\sigma_A = 10\,\mu$as). While small spectroscopic differences may arise, they are localized near pericenters and unlikely to be captured in practice due to sparse sampling. Thus, the 2PN order remains the optimal choice, balancing completeness and parsimony.

Model Accuracy vs. Computational Cost. Having established that 2PN accuracy is sufficient, we compare it to two implementations of relativistic modeling: the ray-traced `GR_rt` and the projected approximation `GR_proj`. The former is more accurate but computationally intensive; the latter offers significant speed gains.

Table VI.1 summarizes the peak differences across three channels, confirming that `GR_proj` and `2PN` are reliable tools for astrometry, but can become questionable for RV when using closer-in stars.

Table VI.1: Maximum residuals in astrometry (ΔA, in μas) and radial velocity (ΔRV, in km/s) for S2 and S2/10. The residuals in SH coordinates are computed using $\chi = 0$ and the ones in KerrKS coordinates using $(\chi, i_\bullet, \Omega_\bullet) = (0.99, 25°, 80°)$.

	S2		S2/10	
Residual type	$\lvert\Delta A\rvert$ (μas)	$\lvert\Delta$RV$\rvert$ (km/s)	$\lvert\Delta A\rvert$ (μas)	$\lvert\Delta$RV$\rvert$ (km/s)
`2PN` – `GR_rt` (SH)	43.546	8.173	19.847	327.112
`GR_proj` – `GR_rt` (SH)	21.259	5.157	28.156	288.766
`GR_proj` – `GR_rt` (KerrKS)	21.255	5.158	28.127	289.380

Table VI.2: Computation times (in seconds) for the different methods applied to S2 and S2/10. The coordinate system or spin parameters do not significantly change the computing time.

Star	`2PN`	`GR_proj`	`GR_rt`
S2	0.10	3.77	12.97
S2/10	0.11	2.24	8.63

As shown in Table VI.2, the computational advantage of `GR_proj` or especially `2PN` is substantial—more than an order of magnitude in speed—making it especially suitable for orbit-fitting applications requiring thousands of model evaluations.

Conclusion. The 2PN approximation offers the necessary and sufficient accuracy to model relativistic effects for stars within $\sim 100\, R_S$ of Sgr A*. For computational efficiency, it is highly suitable, particularly for astrometric analyses and orbit fitting, while `GR_rt` may still be required for precise spectroscopic modeling near pericenter.

VI.2 Evaluating the detectability of the spin using orbit fitting

Having the effect exceed the error bar does not necessarily translate to the detectability of the effect, but only rejects the impossibility of detecting the spin. In order to affirm the detectability of the latter we need to check that no model with zero spin, even after changing all the possible parameters, can fit a mock data set generated with the Kerr model. This will be the object of this section in which we use a mock data script adapted from [78]. For this we will consider two possible observation campaigns, and use a curve-fit method of python to determine when will the Schwarzschild model fail to fit the Kerr mock observation data.

VI.2.1 Methodology

To generate the mock data for S2/10, we use a given model with a fixed set of orbital parameters. This model includes eight fit parameters: the seven standard osculating orbital elements plus the distance R_0 to the black hole. The semi-major axis $a_{\rm sma}$ is not directly fitted, but derived via Kepler's third law. In addition to these parameters, we also have the norm and the two angles giving the direction of the spin of the black hole: χ, $i_\bullet$ and $\Omega_\bullet$. As mentioned in section III, the best astrometric and spectroscopic precisions of GRAVITY/GRAVITY+ and ERIS are given by (σ_A,σ_{RV})=(10µas,10km/s). By adding random noise (with a standard deviation corresponding to more realistic values such as (σ_A,σ_{RV})=(30µas,20km/s)) on the data generated by a given model, we generate mock observation data.

Throughout this section, we adopt `GR_proj` for both data generation and fitting, and comparable results are obtained with `GR_rt` or `2PN`. We take the initial guesses of the parameters that are given by $\boldsymbol{P}_{init} = \boldsymbol{P}_{GC} + \mathbf{1}\boldsymbol{\sigma}_{GC}$ where $\boldsymbol{P}_{GC}$ is the vector containing the best-fit parameters of [60] with the exception of the period P which is multiplied by $10^{-3/2}$ since we are considering S2/10. Moreover, $\mathbf{1}\boldsymbol{\sigma}_{GC}$ is the vector containing the error of each parameter of [60], again with the exception of the error period dP which is multiplied by $10^{-3/2}$. The values of all these parameters are listed in Table VI.3.

Table VI.3: Initial conditions based on the best-fit orbital parameters from [57]. The values apply to S2 and are adapted for S2/10 as described in the text.

Parameter	Value	1σ Error	Unit
$M_\bullet$	4.2996	0.0118	$10^6\,M_\odot$
R_0	8275.9	8.6	pc
e	0.88444	6×10^{-5}	–
ι	134.67	0.02	°
ω	66.279	0.029	°
Ω	228.21	0.03	°
P	0.50698	0.00066	yr
t_p	2018.3789	0.0001	yr
χ	0.000	0.000	–

As for the observation dates, we consider two realistic campaigns of lasting 8 and 20 complete orbits of S2/10, corresponding to almost 4 and 10 years respectively. The starting date was arbitrarily taken as 2018.13, matching the date of apocenter passage right before t_p. The temporal sampling is constructed to reflect realistic observing cadences. Around each pericenter passage, I assume two observations per night within a one-week window, followed by monthly observations over the next six months, and then one measurement every four months for the

rest of the orbit.

To evaluate the fit quality, we analyze the residuals normalized by measurement uncertainties:

$$\frac{X_{\text{model}} - X_{\text{data}}}{\sigma_X}, \quad \text{with } X = \text{RA}, \text{DEC}, \text{RV}$$

A statistically valid fit satisfies:

- Centered residuals around zero;
- $\sim$68% of points within $\pm 1\sigma_X$;
- $\sim$95% of points within $\pm 2\sigma_X$;
- $\sim$99.7% of points within $\pm 3\sigma_X$.

Since, we are not trying to constrain the spin itself but only an estimation of its detectability, it is very sufficient for this purpose to check the validity of a fit by looking at the reduced χ^2 defined by:

$$\chi^2_r = \frac{\chi^2}{k} = \frac{1}{k}\sum_{i=1}^{N}\left[\frac{(RA_{\text{obs},i} - RA_{\text{m},i})^2 + (DEC_{\text{obs},i} - DEC_{\text{m},i})^2}{\sigma_A^2} + \frac{(RV_{\text{obs},i} - RV_{\text{m},i})^2}{\sigma_{RV}^2}\right] \tag{VI.2}$$

where N is the number of observation dates. The quantities labeled "obs" correspond to the mock observations generated with the `GR_rt` model. Those labeled "m" are obtained with the `GR_proj` model. Also, k represents the degrees of freedom and verifies the relation $k = 3N - n$, with n being the number of fitted parameters and where the factor three corresponds to the fact that we consider both astrometry (RA, DEC) and RV. If a fit generates a χ^2_r close to 1, this can translate to a good quality of a fit. In addition, we can also check with the naked eye if the 3 points above do not seem to be incorrect.

According to [15], besides the reduced χ^2, model comparison can also be performed using information criteria such as the Bayesian Information Criterion (BIC) and Akaike Information Criterion (AIC). If IC denotes BIC or AIC, the difference ΔIC between the values of these criteria for two competing models is used to assess their relative support by the data. Using Jeffreys' scale for interpretation,

$$\Delta\text{IC} > 5$$

is considered strong evidence, and

$$\Delta\text{IC} > 10$$

is considered decisive evidence against the model with the higher information criterion value.

VI.2.2 Fitting Kerr Data with a Zero-Spin Model

We now test the ability of a Schwarzschild model to reproduce mock data generated with and without spin. Specifically, we compare two datasets:

- Dataset 1: $\chi = 0$ (non-spinning),
- Dataset 2: $\chi = 0.99$, $i_\bullet = 25°$, $\Omega_\bullet = 80°$.

Both datasets are fitted with the spin being fixed to zero.

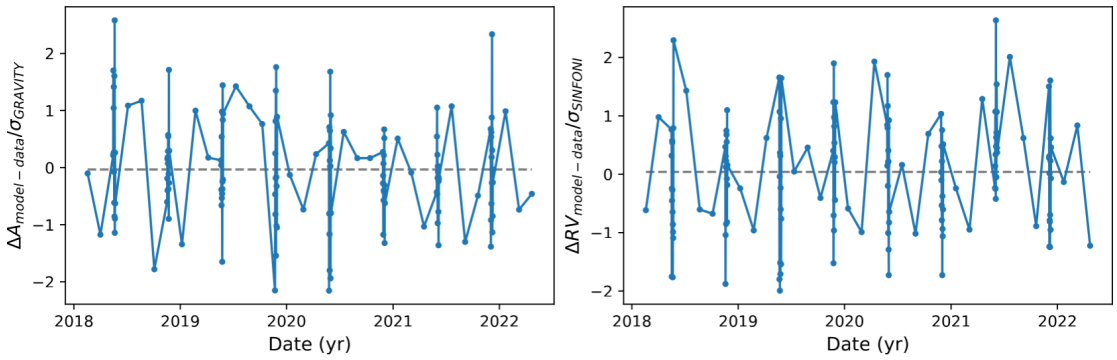

Figure VI.6: Model–data residuals for the 8-orbit dataset with $\chi = 0$ fitted using a Schwarzschild model. The fit yields $\chi^2_r = 0.9 \pm 0.07$. The mock data is generated with random noise of (σ_A,σ_{RV})=(30µas,20km/s).

Figure VI.6 confirms that the non-spinning dataset is well described by the Schwarzschild model, with all residuals within $3\sigma_X$ and a reduced χ^2 close to unity.

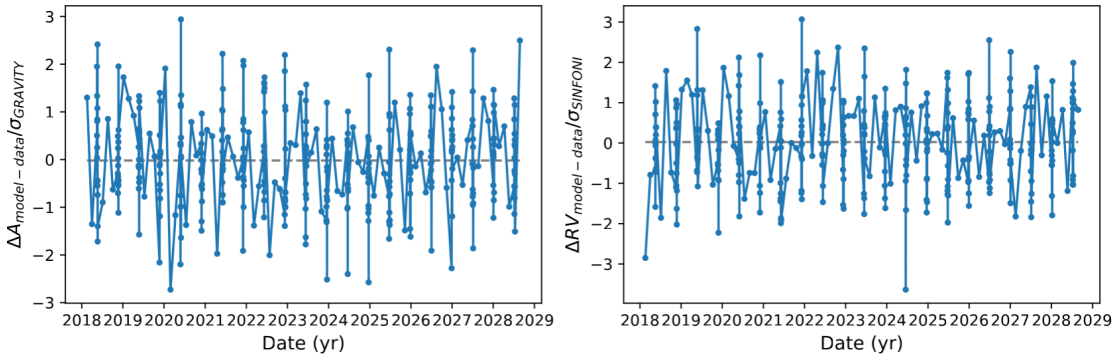

Figure VI.7: Same as Fig. VI.6, but for a 20-orbit campaign. The fit yields $\chi^2_r = 0.96 \pm 0.04$. The mock data is generated with random noise of (σ_A,σ_{RV})=(30µas,20km/s).

As expected, extending the campaign to 20 orbits improves the statistical precision without altering the conclusion: the Schwarzschild model remains valid for a zero-spin system.

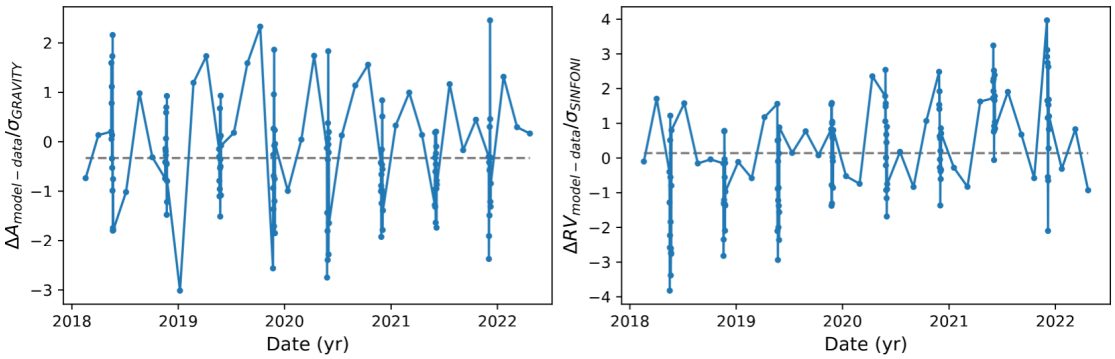

Figure VI.8: Fit of the $\chi = 0.99$ dataset of S2/10 using a Schwarzschild model. The fit yields a poor result with $\chi^2_r = 1.85 \pm 0.07$. The mock data is generated with random noise of (σ_A,σ_{RV})=(30µas,20km/s)

In contrast, Fig. VI.8 shows a more significant mismatch when fitting the spinning dataset with a zero-spin model. The χ^2_r, although more elevated, does not by itself rule out the Schwarzschild case. However, when comparing the ΔIC to a fitting of the data using a fixed spin magnitude of $\chi = 0.1$ and $\chi = 0.99$ we find $\Delta\text{IC} \simeq 80$ and $\Delta\text{IC} \simeq 400$, respectively. This large difference of IC indicates a very clear preference for the Kerr model compared to the Schwarzschild one.

The residuals exhibit systematic patterns: astrometric deviations peak near apocenter, while spectroscopic deviations peak near pericenter. This is consistent with theoretical expectations:

- At apocenter, spin-induced astrometric effects are amplified due to lever-arm geometry.
- At pericenter, the enhanced gravitational field magnifies relativistic corrections in RV.

These results confirm that the spin of Sgr A* can, in principle, be detected through orbit fitting, provided sufficient temporal coverage and instrumental precision.

Part 3

Spin-induced dynamics and observational prospects

Chapter VII

The effects of the spin and quadrupole moment on the star orbits

Contents

VII.1 Post-Newtonian expressions of the secular shifts 118

VII.1.1 Analytical integration at the dominant order 119

VII.1.2 Secular evolution in the PN formalism and two-timescale analysis 122

VII.2 Spin impact on the orientation of the orbit 133

VII.2.1 Instantaneous orientation change 133

VII.2.2 Secular shifts for S2 and S2/10 137

VII.2.3 Time-averaged orientation change 140

VII.2.4 Numerical illustration 141

This chapter investigates the relativistic effects of a rotating (Kerr) black hole's spin on the orbital dynamics of a hypothetical star, S2/10, with a semi-major axis ten times smaller than that of the S star S2, orbiting the Galactic Center's supermassive black hole, Sgr A*. Using numerical simulations with the 2PN `OOGRE` code and analytical post-Newtonian (PN) expressions, we explore instantaneous

and secular precession effects, including Schwarzschild (1PN and 2PN), Lense-Thirring (1.5PN), and quadrupole moment (2PN) contributions. By analyzing equatorial, polar, and mid-inclined orbital configurations, the study isolates the distinct impacts of these effects on the orbital frame orientation, providing insights into how spin-induced precessions manifest and their dependence on orbital geometry, crucial for interpreting observations in the goal of testing the no-hair theorem.

VII.1 Post-Newtonian expressions of the secular shifts

The large-scale motion of stars in the gravitational field of a massive black hole is often described by Newtonian dynamics. However, in the vicinity of a supermassive black hole, such as Sagittarius A*, relativistic effects become significant and lead to observable deviations from purely Keplerian orbits, described by constant orbital elements (see their definition in section IV.2.1). These deviations manifest as *secular shifts* in the orbital elements — cumulative changes that grow with time and do not average out over an orbit.

To accurately model and predict these effects, it is essential to account for *post-Newtonian* (PN) corrections to the equations of motion. These corrections arise from expanding general relativity in powers of small parameters like the orbital velocity v over the speed of light c, and $GM/(pc^2)$, where $p = a_{\rm sma}(1-e^2)$ is the semi-latus rectum and M is the black hole mass. For a Keplerian orbit, we can show that these two quantities are of the same order:

$$\frac{GM}{r} = v^2 \quad \Rightarrow \quad \frac{GM}{pc^2} \sim \left(\frac{v}{c}\right)^2,$$

where r is the orbital radius. We therefore define a single small dimensionless parameter,

$$\epsilon \equiv \frac{GM}{pc^2},$$

and organize the PN expansion as a series in powers of ϵ. This parameter varies with time as p is not a constant. In subsection we defined an alternative constant small parameter $\tilde{\epsilon}$ as:

$$\tilde{\epsilon} \equiv \frac{GM}{\tilde{p}c^2}, \tag{VII.1}$$

where $\tilde{p}$ is the orbit averaged value of p. In what follows, the "PN order" refers to the order in this small parameter ϵ, with Newtonian dynamics corresponding to ϵ^0, 1PN terms to ϵ^1, and so on.

In this section, we present the explicit post-Newtonian expressions for the secular shifts in the key orbital elements of a test particle orbiting a non-spinning or

spinning black hole. These include the advance of the pericenter (Schwarzschild precession), the precession of the orbital plane due to frame-dragging (Lense-Thirring effect), and the leading-order contribution from the black hole's mass quadrupole moment, which captures deviations from spherical symmetry induced by its spin (quadrupole moment effect).

These expressions form the theoretical foundation for interpreting stellar orbits around the Galactic Center and are essential for testing general relativity in the strong-field regime. Since astrometry is the primary observable of the GRAVITY instrument, we will focus especially on how these relativistic effects manifest in the astrometric signal, where secular shifts accumulate measurably over multiple orbits.

VII.1.1 Analytical integration at the dominant order

In section II.2 we gave the expression of the Lagrange planetary equations. We saw that in the context of a small perturbing force, it is possible to get a good estimation of the orbital dynamics by only looking at the dominant contribution of each effect. To do so, we solve the equations within the framework of perturbation theory and find that, to express the leading order of such an effect, it is appropriate to take the 0PN terms in the right-hand side of Eqs. (II.12) to (II.17), before integrating these equations over t. Even more convenient would be to use f as an independent variable instead of t, considering it has the same fixed integration interval over one period for any star. We make use of the fact that the term

$$\left(\frac{\mathrm{d}f}{\mathrm{d}t}\right)_{\text{Kepler}} = \sqrt{\frac{Gm}{p^3}}(1+e\cos f)^2 = \left(\frac{\mathrm{d}\varphi}{\mathrm{d}t}\right)_{\text{Kepler}}$$

is Keplerian (0PN) and that the non-Keplerian terms on the right-hand side of Eq. (II.17) start at 1PN, 1.5PN and 2PN orders for the Schwarzschild, Lense-Thirring and quadrupole moment effects respectively. This means that we are allowed to express the temporal variation as:

$$\frac{\mathrm{d}t}{\mathrm{d}f} = \sqrt{\frac{p^3}{Gm}}\frac{1}{(1+e\cos f)^2}\left[1+\mathcal{O}\left(\epsilon\right)\right], \tag{VII.2}$$

before multiplying Eqs. (II.12) to (II.16) by the zeroth-order term of Eq. (VII.2) to get the dominant order derivative of each orbital parameter with respect to the true anomaly f:

$$\frac{\mathrm{d}p}{\mathrm{d}f} = 2\frac{p^3}{Gm}\frac{1}{(1+e\cos f)^3}\mathcal{S}; \tag{VII.3}$$

$$\frac{\mathrm{d}e}{\mathrm{d}f} = \frac{p^2}{Gm}\left[\frac{\sin f}{(1+e\cos f)^2}\mathcal{R} + \frac{2\cos f + e(1+\cos^2 f)}{(1+e\cos f)^3}\mathcal{S}\right]; \tag{VII.4}$$

$$\frac{\mathrm{d}\iota}{\mathrm{d}f} = \frac{p^2}{Gm}\frac{\cos(\omega+f)}{(1+e\cos f)^3}\mathcal{W}; \tag{VII.5}$$

$$\sin\iota\frac{\mathrm{d}\Omega}{\mathrm{d}f} = \frac{p^2}{Gm}\frac{\sin(\omega+f)}{(1+e\cos f)^3}\mathcal{W}; \tag{VII.6}$$

$$\begin{aligned}\frac{\mathrm{d}\omega}{\mathrm{d}f} = \frac{1}{e}\frac{p^2}{Gm}\Bigg[&-\frac{\cos f}{(1+e\cos f)^2}\mathcal{R} + \frac{2+e\cos f}{(1+e\cos f)^3}\sin f\mathcal{S} \\ &- e\cot\iota\frac{\sin(\omega+f)}{(1+e\cos f)^3}\mathcal{W}\Bigg].\end{aligned} \tag{VII.7}$$

Then, we integrate them between $f = f_0$ and $f = f_0 + 2\pi$[1] to find the dominant terms of the secular evolution of the orbital parameters. By considering the keplerian dominant constant term of p, e, ω and β in the right hand side of Langrange planetary equations, we find that p and e (and consequently a_{sma} and P) do not show any secular variations after one orbit at the dominant orders. As for the other parameters, we find that the precessions per orbit of a star's argument of periapsis $\Delta\omega$, longitude of the ascending node $\Delta\Omega$, and inclination $\Delta\iota$ (illustrated Figure IV.3) write[2] as a function of θ and β (illustrated in Figure IV.5):

$$\Delta\omega_{\mathrm{Sch}}\big|^{\mathrm{1PN}} = 6\pi\epsilon, \tag{VII.8}$$

$$\Delta\omega_{\mathrm{LT}}\big|^{\mathrm{1.5PN}} = -4\pi\epsilon^{3/2}(2\cos\theta + \cot\iota\sin\theta\sin\beta)\,\chi, \tag{VII.9}$$

$$\Delta\omega_{Q}\big|^{\mathrm{2PN}} = -\frac{3\pi}{2}\epsilon^2\left(1-3\cos^2\theta - 2\cot\iota\cos\theta\sin\theta\sin\beta\right)\chi^2, \tag{VII.10}$$

[1] This is one way of defining the pericenter advance. Another way to derive the pericenter advance is by directly integrating the timelike geodesic equation which, by means of the conservation of energy and angular momentum, leads to an ordinary differential equation for the radius r in terms of the angle ϕ of the Boyer-Lindquist coordinates [56, 128]. The angle between successive turning points, or extrema of r, can be obtained exactly from a radial integral. The expansion of that result in a post-Newtonian sequence agrees with the osculating element method at lowest order and the differences at higher orders are illusory, because the semilatus rectum and eccentricity have different meanings in the two approaches [128]. However, note that the quasi-Keplerian notion of pericenter advance breaks down in the case of a "zoom-whirl" behavior [56]. In other words, the very concept of a "pericenter shift per orbit" loses its meaning when the orbit does not resemble a closed ellipse anymore.

[2] With the different contribution of the Schwarzschild, Lense-Thirring and quadrupole moment effects denoted with the "Sch", "LT" and "Q" subscripts.

$$\Delta\iota_{\rm Sch}|^{\rm 1PN} = 0, \tag{VII.11}$$
$$\Delta\iota_{\rm LT}|^{\rm 1.5PN} = 4\pi\epsilon^{3/2}\sin\theta\cos\beta\ \ \chi, \tag{VII.12}$$
$$\Delta\iota_{Q}|^{\rm 2PN} = -3\pi\epsilon^{2}\cos\theta\sin\theta\cos\beta\ \ \chi^2, \tag{VII.13}$$

$$\sin\iota\Delta\Omega_{\rm Sch}|^{\rm 1PN} = 0, \tag{VII.14}$$
$$\sin\iota\Delta\Omega_{\rm LT}|^{\rm 1.5PN} = 4\pi\epsilon^{3/2}\sin\theta\sin\beta\ \ \chi, \tag{VII.15}$$
$$\sin\iota\Delta\Omega_{Q}|^{\rm 2PN} = -3\pi\epsilon^{2}\cos\theta\sin\theta\sin\beta\ \ \chi^2, \tag{VII.16}$$

We stress that the choice of fundamental frame is crucial, as it determines the very definition of the angular orbital parameters. Two works may use the same symbols (ι, Ω, etc.) but refer to different quantities if their fundamental planes differ. In our case, the fundamental frame is the plane of the sky (see subsection IV.1.1), as in [142], which is why our variations of the angular parameters agree with theirs. By contrast, [139] and [128] adopt the black hole equatorial plane as the fundamental frame[3]. As a result, their definitions of ι and Ω (and consequently the corresponding evolution equations) are not directly comparable to our results.

We saw in subsection VI.1.3 that the most suitable PN order to use for our study is the 2PN model. These secular trends are valid at this PN order for the Lense-Thirring and quadrupole moment shifts, for which subleading contributions appear at orders higher than 2PN. However, for the Schwarzschild terms, we need to compute the subleading 2PN contribution in addition to the leading 1PN contribution provided above. To do so, the two-timescale method detailed in subsection VII.1.2 and [128, 139] is necessary to include the contribution of the periodic evolution of the orbital parameters. This allows us to obtain the following:

$$\Delta\omega_{\rm Sch}|^{\rm 2PN} = 6\pi\tilde{\epsilon} + \frac{3\pi}{2}\tilde{\epsilon}^2\left(2+\tilde{e}^2\right) \tag{VII.17}$$
$$\Delta\iota_{\rm Sch}|^{\rm 2PN} = 0, \tag{VII.18}$$
$$\Delta\Omega_{\rm Sch}|^{\rm 2PN} = 0, \tag{VII.19}$$

where the tilde in $\tilde{e}$ and $\tilde{\epsilon}$ represent the orbit-averaged values of e and ϵ defined by Eq. (VII.27), as will be detailed in subsection VII.1.2. These expressions differ from the analytical expressions given in [1], where the authors do not account for the periodic variations of other orbital parameters when deriving the secular shift of a certain parameter.

Notice that if $\iota = 0$, $\mathcal{L}_{\mathbf{orb//sky}}$ cannot be defined as it is degenerate, then ω and Ω, and thus Eqs. (VII.9), (VII.10), (VII.15) and (VII.16) will not be defined either. This issue will be addressed by the introduction of new variables in subsection VII.2.

[3]So our Eqs. (VII.12) and (VII.13) should not be compared with Eqs. (3.23a) of [139] and (5) of [128]

Finally, it is interesting to note that even though we do not share the same definition of the parameter ω as in [139] and [128], our Eq. VII.17 is in agreement with their Eqs. (3.23a) and (5), respectively. This is because both versions of ω are measured in the orbital plane, making the different $\Delta\omega$ boil down to the same expression. However, this does not apply for $\Delta\iota$ nor $\Delta\Omega$ which are measured in different planes. For instance, if one ignores that the orbital elements mentioned in [139] do not correspond to the observer-related orbital elements as in this work or that of [142], one would assume that the inclination of the orbit relative to the sky plane (ι) is not affected by the Lense-Thirring or quadrupole moment effects at the 2PN order (see Eq. "(3.22d)") which is wrong as Eqs. (VII.12) and (VII.13) show.

VII.1.2 Secular evolution in the PN formalism and two-timescale analysis

It is possible to derive the secular evolution of orbital parameters at an arbitrary post-Newtonian order using a perturbative method known as *two-timescale analysis*. This technique has been widely applied in the literature to study relativistic orbits, particularly by Clifford M. Will and collaborators, who have used it in several works over the years (e.g., [128, 139, 142, 143]). While the method is well known in this context, those references typically only sketch the core ideas without presenting the full, step-by-step derivation, which is in fact quite complex.

The purpose of this section is therefore to pedagogically expose the method, including all intermediate steps in a self-contained way. In doing so, we aim to clarify the practical implementation of the two-timescale analysis and demonstrate how it leads to explicit expressions for the secular shifts in observable quantities such as the inclination, argument of pericenter, and longitude of ascending node.

Importantly, our formulation uses orbital elements defined relative to the observer's frame, rather than the black hole's equatorial frame[4]. This choice ensures that the secular shifts we derive apply directly to quantities that are observable by instruments like GRAVITY+.

Two-timescale method

Let us label generically all orbital elements by X_α, where α is an index, running typically from 1 to 5 to label the 5 standard orbital elements $(p, e, \iota, \Omega, \omega)$. We will use here the orbital plane azimuthal angle $\varphi = \omega + f$ as the parameter, rather than time. So we consider functions $X_\alpha(\varphi)$. Equations (II.12) to (II.16) give the

[4]Note that in [128, 139], the angular parameters "ι", "ω", and "Ω" follow a different convention than the one adopted here, or than in [1, 142, 143]. For instance, their inclination "ι" corresponds to θ in our convention, not to our ι.

time evolution $\mathrm{d}X_\alpha/\mathrm{d}t$. By using Eq. (II.17) we can easily get:

$$\begin{aligned}\frac{\mathrm{d}\varphi}{\mathrm{d}t} &= \frac{\mathrm{d}\omega}{\mathrm{d}t} + \frac{\mathrm{d}f}{\mathrm{d}t} \\ &= \left(\frac{\mathrm{d}f}{\mathrm{d}t}\right)_{\text{Kepler}} - \cos\iota\frac{\mathrm{d}\Omega}{\mathrm{d}t} \\ &= \sqrt{\frac{Gm}{p^3}}(1+e\cos f)^2 - \sqrt{\frac{p}{Gm}}\cot\iota\frac{\sin\varphi}{1+e\cos f}\mathcal{W},\end{aligned} \tag{VII.20}$$

and convert $\mathrm{d}X_\alpha/\mathrm{d}t$ to $\mathrm{d}X_\alpha/\mathrm{d}\varphi$. The expressions of the various perturbing accelerations up to 2PN order are given by Eqs. (V.37) to (V.48). Using all this material, the evolution of the orbital elements will finally read

$$\frac{\mathrm{d}X_\alpha}{\mathrm{d}\varphi} = \tilde{\epsilon}\,Q_\alpha^{(1)} + \tilde{\epsilon}^{3/2}\,Q_\alpha^{(3/2)} + \tilde{\epsilon}^2\,Q_\alpha^{(2)}, \tag{VII.21}$$

where we express the PN small parameter[5] $\tilde{\epsilon}$ as:

$$\tilde{\epsilon} = \frac{GM}{\tilde{p}c^2}. \tag{VII.22}$$

Here, we use an orbit-averaged value of the semilatus rectum, $\tilde{p}$, which is *constant* in the evolution. The functions $\tilde{\epsilon}Q_\alpha^{(1)}$, $\tilde{\epsilon}^{3/2}\,Q_\alpha^{(3/2)}$, and $\tilde{\epsilon}^2 Q_\alpha^{(2)}$, denote the 1PN, 1.5PN, and 2PN components of the evolution equation, respectively, and the $Q_\alpha^{(i)}$ are by definition 0PN quantities.

The evolution of the orbital parameters under these PN components will take the form of a long-term (compared to the orbital period) secular evolution, on top of which there are quickly-varying (at the orbital timescale) oscillations. Such a behavior can be well captured in the framework of a two-timescale analysis. Based on this understanding of what the solution should look like, we will consider that X_α is no longer a function $X_\alpha(\varphi)$ of the orbital plane azimuthal angle, but rather a function of two variables, $X_\alpha(\Phi,\varphi)$, where:

$$\Phi = \tilde{\epsilon}\varphi \tag{VII.23}$$

captures the long-term behavior of the element, while φ captures the quickly-varying oscillations. We will use the trick of considering that φ and Φ are independent variables (which is only a trick, they are actually directly related by $\Phi = \tilde{\epsilon}\varphi$), and derive evolution equations for X_α, now considered as a function of two independent variables Φ and φ.

[5] Not to be confused with the varying ϵ defined in Eq. (VII.1).

Let us rewrite with more details the evolution of X_α, which now reads:

$$\frac{\mathrm{d}X_\alpha(\Phi,\varphi)}{\mathrm{d}\varphi} = \tilde{\epsilon}\, Q_\alpha^{(1)}\left(X_\beta(\Phi,\varphi);\varphi\right) + \tilde{\epsilon}^{3/2}\, Q_\alpha^{(3/2)}\left(X_\beta(\Phi,\varphi);\varphi\right) + \tilde{\epsilon}^2\, Q_\alpha^{(2)}(X_\beta(\Phi,\varphi);\varphi), \tag{VII.24}$$

where we remind that $\tilde{\epsilon}$ does not depend on any variable quantity, and $Q_\alpha^{(1)}$, $Q_\alpha^{(3/2)}$ and $Q_\alpha^{(2)}$ now depend on the various orbital parameters considered as functions of two variables, $X_\beta(\Phi,\varphi)$, and explicitly also on φ. We will now look for a solution that reads:

$$X_\alpha(\Phi,\varphi) = \tilde{X}_\alpha(\Phi) + \tilde{\epsilon}\, Y_\alpha^{(1)}(\tilde{X}_\beta(\Phi);\varphi) + \tilde{\epsilon}^{3/2}\, Y_\alpha^{(3/2)}(\tilde{X}_\beta(\Phi);\varphi) + \tilde{\epsilon}^2\, Y_\alpha^{(2)}(\tilde{X}_\beta(\Phi);\varphi), \tag{VII.25}$$

where $\tilde{X}_\alpha(\Phi)$ captures the long-term, secular evolution of the orbital element, while $Y_\alpha^{(i)}$ capture the quickly-varying evolution due to the different perturbing accelerations, the upper index i reminding the PN order of the small oscillating correction to the secular evolution. We will assume that these $Y_\alpha^{(i)}$ are 2π-periodic in φ.

There is not unicity of this ansatz of solution but it is natural to consider:

$$\tilde{X}_\alpha(\Phi) = \langle X_\alpha(\Phi,\varphi)\rangle\,, \qquad \left\langle Y_\alpha^{(i)}(\tilde{X}_\beta(\Phi),\varphi)\right\rangle = 0, \tag{VII.26}$$

where

$$\langle F(\Phi,\varphi)\rangle = \frac{1}{2\pi}\int_0^{2\pi} F(\Phi,\varphi)d\varphi, \tag{VII.27}$$

is the orbit average of some function $F(\Phi,\varphi)$, where we consider that Φ remains constant in the average, and that the result does not depend on the value of Φ. So we consider that $\tilde{X}_\alpha$ is simply the orbit average of X_α, and that the oscillating term $Y_\alpha^{(i)}$ averages to zero over one orbit. Note that this means that $\tilde{X}_\alpha$ depends only on Φ, and thus effectively on φ given the link of Eq. (VII.23). So it is important to keep in mind that the definition of Eq. (VII.26) *does not mean that* $\tilde{X}_\alpha$ *is independent of* φ, it simply means that $\tilde{X}_\alpha$ is an orbit-averaged quantity. Now that we have this ansatz of solution, let us reexpress the evolution of the orbital parameter X_α. We write the derivative with respect to Φ as:

$$\frac{\mathrm{d}}{\mathrm{d}\varphi} = \tilde{\epsilon}\frac{\partial}{\partial\Phi} + \frac{\partial}{\partial\varphi}, \tag{VII.28}$$

and Eq. (VII.24) becomes:

$$\begin{aligned}\frac{\mathrm{d}X_\alpha}{\mathrm{d}\varphi} &= \frac{\mathrm{d}\tilde{X}_\alpha}{\mathrm{d}\Phi}\frac{\mathrm{d}\Phi}{\mathrm{d}\varphi} \\ &+ \tilde{\epsilon}\sum_\beta\left(\frac{\partial Y_\alpha^{(1)}}{\partial\tilde{X}_\beta}\frac{\mathrm{d}\tilde{X}_\beta}{\mathrm{d}\Phi}\frac{\mathrm{d}\Phi}{\mathrm{d}\varphi}\right) + \tilde{\epsilon}\frac{\partial Y_\alpha^{(1)}}{\partial\varphi} \\ &+ \tilde{\epsilon}^{3/2}\sum_\beta\left(\frac{\partial Y_\alpha^{(3/2)}}{\partial\tilde{X}_\beta}\frac{\mathrm{d}\tilde{X}_\beta}{\mathrm{d}\Phi}\frac{\mathrm{d}\Phi}{\mathrm{d}\varphi}\right) + \tilde{\epsilon}^{3/2}\frac{\partial Y_\alpha^{(3/2)}}{\partial\varphi} \\ &+ \tilde{\epsilon}^{2}\sum_\beta\left(\frac{\partial Y_\alpha^{(2)}}{\partial\tilde{X}_\beta}\frac{\mathrm{d}\tilde{X}_\beta}{\mathrm{d}\Phi}\frac{\mathrm{d}\Phi}{\mathrm{d}\varphi}\right) + \tilde{\epsilon}^{2}\frac{\partial Y_\alpha^{(2)}}{\partial\varphi} \\ &= \tilde{\epsilon}\,Q_\alpha^{(1)} + \tilde{\epsilon}^{3/2}\,Q_\alpha^{(3/2)} + \tilde{\epsilon}^{2}\,Q_\alpha^{(2)}.\end{aligned} \tag{VII.29}$$

Using $\mathrm{d}\Phi/\mathrm{d}\varphi = \tilde{\epsilon}$ and dividing by $\tilde{\epsilon}$, we get:

$$\begin{aligned}\frac{\mathrm{d}\tilde{X}_\alpha}{\mathrm{d}\Phi} &= Q_\alpha^{(1)} + \tilde{\epsilon}^{1/2}\,Q_\alpha^{(3/2)} + \tilde{\epsilon}\,Q_\alpha^{(2)} \\ &- \tilde{\epsilon}\sum_\beta\left(\frac{\partial Y_\alpha^{(1)}}{\partial\tilde{X}_\beta}\frac{\mathrm{d}\tilde{X}_\beta}{\mathrm{d}\Phi}\right) - \tilde{\epsilon}^{3/2}\sum_\beta\left(\frac{\partial Y_\alpha^{(3/2)}}{\partial\tilde{X}_\beta}\frac{\mathrm{d}\tilde{X}_\beta}{\mathrm{d}\Phi}\right) \\ &- \tilde{\epsilon}^{2}\sum_\beta\left(\frac{\partial Y_\alpha^{(2)}}{\partial\tilde{X}_\beta}\frac{\mathrm{d}\tilde{X}_\beta}{\mathrm{d}\Phi}\right) - \frac{\partial Y_\alpha^{(1)}}{\partial\varphi} - \tilde{\epsilon}^{1/2}\frac{\partial Y_\alpha^{(3/2)}}{\partial\varphi} - \tilde{\epsilon}\frac{\partial Y_\alpha^{(2)}}{\partial\varphi}.\end{aligned} \tag{VII.30}$$

Keep in mind that we have divided by $\tilde{\epsilon}$, so a term of order kPN in $\mathrm{d}X_\alpha/\mathrm{d}\varphi$ will become of order $(k-1)$PN in $\mathrm{d}\tilde{X}_\alpha/\mathrm{d}\Phi$.

We know that:

$$\left\langle\frac{\partial Y_\alpha^{(i)}}{\partial\varphi}\right\rangle = \frac{1}{2\pi}\int_0^{2\pi}\frac{\partial Y_\alpha^{(i)}}{\partial\varphi}d\varphi = \frac{1}{2\pi}\left[Y_\alpha^{(i)}\right]_0^{2\pi} = 0, \tag{VII.31}$$

considering that $Y_\alpha^{(i)}$ is 2π-periodic. Also, if we assume that Φ and φ are independent, we can write:

$$\left\langle\frac{\partial Y_\alpha^{(i)}}{\partial\tilde{X}_\beta}\right\rangle \equiv \left\langle Y_{\alpha,\beta}^{(i)}\right\rangle = 0, \tag{VII.32}$$

where we use the standard coma notation for partial derivatives. Then:

$$\left\langle\frac{\partial Y_\alpha^{(i)}}{\partial\tilde{X}_\beta}\frac{\mathrm{d}\tilde{X}_\beta}{\mathrm{d}\Phi}\right\rangle = \left\langle\frac{\partial Y_\alpha^{(i)}}{\partial\tilde{X}_\beta}\right\rangle\frac{\mathrm{d}\tilde{X}_\beta}{\mathrm{d}\Phi} = 0. \tag{VII.33}$$

and by taking the orbit average, we get:

$$\begin{aligned}\frac{\mathrm{d}\tilde{X}_\alpha}{\mathrm{d}\Phi} &= \left\langle Q_\alpha^{(1)}(X_\beta(\Phi,\varphi),\varphi)\right\rangle + \tilde{\epsilon}^{1/2}\left\langle Q_\alpha^{(3/2)}\left(X_\beta(\Phi,\varphi);\varphi\right)\right\rangle \\ &\quad + \tilde{\epsilon}\left\langle Q_\alpha^{(2)}(X_\beta(\Phi,\varphi),\varphi)\right\rangle .\end{aligned} \tag{VII.34}$$

Let us now consider the Taylor expansions:

$$\begin{aligned}Q_\alpha^{(i)}(X_\beta;\varphi) &= Q_\alpha^{(i)}(\tilde{X}_\beta + \tilde{\epsilon}\,Y_\beta^{(1)} + \tilde{\epsilon}^{3/2}\,Y_\beta^{(3/2)} + \tilde{\epsilon}^2\,Y_\beta^{(2)};\varphi) \\ &= Q_\alpha^{(i)}(\tilde{X}_\beta;\varphi) \\ &\quad + \sum_\gamma \left(\tilde{\epsilon}\,Y_\gamma^{(1)} + \tilde{\epsilon}^{3/2}\,Y_\gamma^{(3/2)} + \tilde{\epsilon}^2\,Y_\gamma^{(2)}\right) Q_{\alpha,\gamma}^{(i)} + ... \\ &= Q_\alpha^{(i)}(\tilde{X}_\beta;\varphi) + \tilde{\epsilon}\sum_\gamma \left(Y_\gamma^{(1)}\,Q_{\alpha,\gamma}^{(i)}(\tilde{X}_\beta;\varphi)\right) \\ &\quad + \tilde{\epsilon}^{3/2}\sum_\gamma \left(Y_\gamma^{(3/2)}\,Q_{\alpha,\gamma}^{(i)}(\tilde{X}_\beta;\varphi)\right) + O(\tilde{\epsilon}^2),\end{aligned} \tag{VII.35}$$

where the same coma notation for partial derivative is used. The summation is done on all parameters $\tilde{X}_\gamma$ that appear in $Q_\alpha^{(i)}$. Note that $Q_\alpha^{(i)}(\tilde{X}_\beta,\varphi)$ in this expression means that we consider the orbital parameters to be only secularly varying, and constant at the orbital timescale considered in the average process. So considering all terms up to 1PN order, Eq. (VII.34) becomes:

$$\begin{aligned}\frac{\mathrm{d}\tilde{X}_\alpha(\Phi)}{\mathrm{d}\Phi} &= \langle Q_\alpha^{(1)}(\tilde{X}_\beta;\varphi)\rangle \\ &\quad + \tilde{\epsilon}^{1/2}\langle Q_\alpha^{(3/2)}(\tilde{X}_\beta;\varphi)\rangle \\ &\quad + \tilde{\epsilon}\left[\sum_\gamma \left(\langle Y_\gamma^{(1)}\,Q_{\alpha,\gamma}^{(1)}(\tilde{X}_\beta;\varphi)\rangle\right) + \langle Q_\alpha^{(2)}(\tilde{X}_\beta;\varphi)\rangle\right].\end{aligned} \tag{VII.36}$$

This is the final expression of the secular evolution of the orbital parameters. This expression is in agreement with the formulas of [128, 139] provided that only $Q_\alpha^{(1)}$ is considered[6]. Reference [128, 139] derive the following expression for $Y_\alpha^{(1)}$:

$$Y_\alpha^{(1)} = \int_0^\varphi Q_\alpha^{(1)}\,d\varphi' - (\varphi+\pi)\left\langle Q_\alpha^{(1)}\right\rangle + \left\langle \varphi Q_\alpha^{(1)}\right\rangle . \tag{VII.37}$$

The first term in the square brackets of Eq. (VII.36) then becomes:

$$\begin{aligned}\left\langle Y_\gamma^{(1)}\,Q_{\alpha,\gamma}^{(1)}(\tilde{X}_\beta,\varphi)\right\rangle &= \left\langle Q_{\alpha,\gamma}^{(1)}\int_0^\varphi Q_\gamma^{(1)}\right\rangle + \left\langle \varphi Q_\gamma^{(1)}\right\rangle\left\langle Q_{\alpha,\gamma}^{(1)}\right\rangle \\ &\quad - \pi\left\langle Q_\gamma^{(1)}\right\rangle\left\langle Q_{\alpha,\gamma}^{(1)}\right\rangle - \left\langle Q_\gamma^{(1)}\right\rangle\left\langle \varphi Q_{\alpha,\gamma}^{(1)}\right\rangle ,\end{aligned} \tag{VII.38}$$

[6]Note that [128, 139] call $Q_\alpha^{(0)}$ the quantity labeled $Q_\alpha^{(1)}$ in these notes. This is because they consider it as a 0PN quantity in $d\tilde{X}/d\Phi$, while we consider it as a 1PN quantity in $dX/d\varphi$. The two points of view are exactly equivalent.

so that provided that the $Q_\alpha^{(i)}$ are known for all elements, the secular evolution can be derived. Finally we can come back to the evolution equation as a function of φ by remembering that Φ and φ are actually the same quantity up to a factor $\tilde{\epsilon}$. So we get:

$$\begin{aligned}\frac{\mathrm{d}\tilde{X}_\alpha(\varphi)}{\mathrm{d}\varphi} &= \tilde{\epsilon}\,\langle Q_\alpha^{(1)}(\tilde{X}_\beta;\varphi)\rangle \\ &\quad + \tilde{\epsilon}^{3/2}\,\langle Q_\alpha^{(3/2)}(\tilde{X}_\beta;\varphi)\rangle \\ &\quad + \tilde{\epsilon}^2\left[\sum_\gamma\left(\langle Y_\gamma^{(1)}\,Q_{\alpha,\gamma}^{(1)}(\tilde{X}_\beta;\varphi)\rangle\right) + \langle Q_\alpha^{(2)}(\tilde{X}_\beta;\varphi)\rangle\right],\end{aligned} \tag{VII.39}$$

which is the second order secular evolution of the orbital element, here considered as a function of φ only (the variable Φ was just a mathematical trick to derive the equation).

Application to the 2PN Schwarzschild shift

In this section we neglect the spin effects and consider a 2PN Schwarzschild spacetime. So in particular the $Q_\alpha^{(3/2)}$ is zero.

Let us start from the expression of $d\omega/dt$ given in Eq. (II.16). Eq. (VII.20) leads to:

$$\frac{\mathrm{d}\varphi}{\mathrm{d}t} = \sqrt{\frac{GM}{p^3}}\,(1+e\cos f)^2\,, \tag{VII.40}$$

as Ω is constant in Schwarzschild (the evolution of Ω depends on $\mathcal{W}$, which is linked to the spin). The evolution of ω as a function of φ then reads:

$$\begin{aligned}\frac{\mathrm{d}\omega}{\mathrm{d}\varphi} &= \frac{1}{e}\sqrt{\frac{p}{GM}}\left[-\cos f\mathcal{R} + \frac{2+e\cos f}{1+e\cos f}\sin f\mathcal{S}\right] \\ &\quad \times \sqrt{\frac{p^3}{GM}}\,(1+e\cos f)^{-2}\,,\end{aligned} \tag{VII.41}$$

by combining Eqs. (II.12) to (II.16) and (VII.40). Using the 2PN expressions of $\mathcal{R}$ and $\mathcal{S}$ given in Eqs. (V.37), (V.43), (V.38) and (V.44), we get:

$$\begin{aligned}\frac{\mathrm{d}\omega}{\mathrm{d}\varphi} &= \epsilon\,\frac{1}{e}\Big[-\cos f\left(3+2e\cos f+e^2\left(4\sin^2 f-1\right)\right) \\ &\qquad +4\,\frac{2+e\cos f}{1+e\cos f}\sin f\,(1+e\cos f)\,e\sin f\Big] \\ &\quad + \epsilon^2\,\frac{1}{e}\Big[-\cos f\left(-9\,(1+e\cos f)^2\right) \\ &\qquad -2\,\frac{2+e\cos f}{1+e\cos f}\sin f\,(1+e\cos f)^2\;e\sin f\Big]\,.\end{aligned} \tag{VII.42}$$

We want to replace ϵ by $\tilde{\epsilon} = GM/\tilde{p}c^2$, for a constant value of the semilatus rectum $\tilde{p}$ to obtain:

$$\begin{aligned}\frac{\mathrm{d}\omega}{\mathrm{d}\varphi} = \tilde{\epsilon}\,\frac{1}{e}\,\frac{\tilde{p}}{p}\,\Big[&-\cos f\left(3+2e\cos f+e^2\left(4\sin^2 f-1\right)\right)\\ &+4\,\frac{2+e\cos f}{1+e\cos f}\sin f\,(1+e\cos f)\,e\sin f\Big]\\ +\tilde{\epsilon}^2\,\frac{1}{e}\left(\frac{\tilde{p}}{p}\right)^2\Big[&-\cos f\left(-9\,(1+e\cos f)^2\right)\\ &-2\,\frac{2+e\cos f}{1+e\cos f}\sin f\,(1+e\cos f)^2\;e\sin f\Big]\,,\end{aligned} \tag{VII.43}$$

which takes the exact same form as the general expression of Eq. (VII.24). The quantity in factor of $\tilde{\epsilon}$ in the first line corresponds to $Q^{(1)}_\omega$, while that in factor of $\tilde{\epsilon}^2$ in the second line corresponds to $Q^{(2)}_\omega$. They both depend on three orbital parameters, ω itself (through $f = \varphi - \omega$), p and e, as well as explicitly on φ (again through f). They are 2π-periodic in φ. Let us simplify a bit to get:

$$\begin{aligned}Q^{(1)}_\omega &= \frac{\tilde{p}}{p}\left(8+\left(e-\frac{3}{e}\right)\cos f-10\cos^2 f\right);\\ Q^{(2)}_\omega &= \left(\frac{\tilde{p}}{p}\right)^2\left(-4+3\left(\frac{3}{e}-2e\right)\cos f+2\left(11-e^2\right)\cos^2 f\right.\\ &\qquad\left.+15e\cos^3 f+2e^2\cos^4 f\right).\end{aligned} \tag{VII.44}$$

We now want to compute Eq. (VII.39) for ω. Remember that this implies taking the orbit average of the previous equation, see Eq. VII.34. Because of the special form of our ansatz of solution, this averaging leads to:

$$\begin{aligned}\frac{\mathrm{d}\tilde{\omega}}{\mathrm{d}\varphi} &= \tilde{\epsilon}\,\left\langle Q^{(1)}_\omega(\tilde{p},\tilde{e},\tilde{\omega},\varphi)\right\rangle\\ &+\tilde{\epsilon}^2\left[\left\langle Y^{(1)}_p\,Q^{(1)}_{\omega,p}(\tilde{p},\tilde{e},\tilde{\omega},\varphi)\right\rangle+\left\langle Y^{(1)}_e\,Q^{(1)}_{\omega,e}(\tilde{p},\tilde{e},\tilde{\omega},\varphi)\right\rangle\right.\\ &\qquad\left.+\left\langle Y^{(1)}_\omega\,Q^{(1)}_{\omega,\omega}(\tilde{p},\tilde{e},\tilde{\omega},\varphi)\right\rangle+\left\langle Q^{(2)}_\omega(\tilde{p},\tilde{e},\tilde{\omega},\varphi)\right\rangle\right],\end{aligned} \tag{VII.45}$$

where we remind that the orbital elements appearing in the various functions Q and Y are considered to vary only secularly (see the comment following Eq. (VII.35)). That's why they are tilded, and as such are not affected by the orbit averaging. For instance, we have $\langle\tilde{e}\cos f\rangle = \tilde{e}\,\langle\cos f\rangle$, which would not be true if the full dependence of e on φ was considered, and not only its secular dependence. Also note that the ω on the LHS is considered just as well to vary only secularly, and is also tilded. This might seem surprising as $\tilde{\omega}$ depends on Φ and not on φ, but see again the discussion below Eq. (VII.27).

The first and last terms of Eq. (VII.45) are trivial to compute:

$$\begin{aligned} \left\langle Q_\omega^{(1)} \right\rangle &= 3, \\ \left\langle Q_\omega^{(2)} \right\rangle &= 7 - \frac{\tilde{e}^2}{4}, \end{aligned} \tag{VII.46}$$

where $\tilde{e}$ is used because the $\langle Q_\alpha \rangle$ functions are evaluated at the tilded values of the orbital parameters. We have used the following relations:

$$\langle \cos f \rangle = 0, \langle \cos^2 f \rangle = \frac{1}{2}, \langle \cos^3 f \rangle = 0, \langle \cos^4 f \rangle = \frac{3}{8}. \tag{VII.47}$$

An important remark must be made here. The averages above are computed as follows:

$$\langle \cos f \rangle = \frac{1}{2\pi} \int_{\varphi=0}^{\varphi=2\pi} \cos(\varphi - \tilde{\omega})\, d\varphi = 0, \tag{VII.48}$$

and the key point is that, because the Q_ω depend on the secularly varying parameters $\tilde{X}_\alpha$, we can replace f by $\varphi - \tilde{\omega}$ rather than $\varphi - \omega(\varphi)$, and this $\tilde{\omega}$ is constant in the integration. But it is indeed an average on φ that we perform, as prescribed by the formalism, and not an average on f.

The value of $\langle Q_\omega^{(1)} \rangle$ leads to the well-known textbook result:

$$\frac{d\tilde{\omega}_{\rm 1PN}}{d\varphi} = 3\tilde{\epsilon}, \tag{VII.49}$$

at 1PN order. However here, we need to go to 2PN, so a we also need to consider the three $\langle YQ \rangle$ terms in the bracket of Eq. (VII.45). They read:

$$\begin{aligned} &\left\langle Y_p^{(1)}\, Q_{\omega,p}^{(1)} \right\rangle + \left\langle Y_e^{(1)}\, Q_{\omega,e}^{(1)} \right\rangle + \left\langle Y_\omega^{(1)}\, Q_{\omega,\omega}^{(1)} \right\rangle = \\ &\qquad \left\langle Q_{\omega,p}^{(1)} \int_0^\varphi Q_p^{(1)} \right\rangle + \left\langle Q_{\omega,e}^{(1)} \int_0^\varphi Q_e^{(1)} \right\rangle + \left\langle Q_{\omega,\omega}^{(1)} \int_0^\varphi Q_\omega^{(1)} \right\rangle \\ &\qquad + \left\langle \varphi Q_p^{(1)} \right\rangle \left\langle Q_{\omega,p}^{(1)} \right\rangle + \left\langle \varphi Q_e^{(1)} \right\rangle \left\langle Q_{\omega,e}^{(1)} \right\rangle + \left\langle \varphi Q_\omega^{(1)} \right\rangle \left\langle Q_{\omega,\omega}^{(1)} \right\rangle \\ &\qquad - \pi \left\langle Q_p^{(1)} \right\rangle \left\langle Q_{\omega,p}^{(1)} \right\rangle - \pi \left\langle Q_e^{(1)} \right\rangle \left\langle Q_{\omega,e}^{(1)} \right\rangle - \pi \left\langle Q_\omega^{(1)} \right\rangle \left\langle Q_{\omega,\omega}^{(1)} \right\rangle \\ &\qquad - \left\langle Q_p^{(1)} \right\rangle \left\langle \varphi Q_{\omega,p}^{(1)} \right\rangle - \left\langle Q_e^{(1)} \right\rangle \left\langle \varphi Q_{\omega,e}^{(1)} \right\rangle - \left\langle Q_\omega^{(1)} \right\rangle \left\langle \varphi Q_{\omega,\omega}^{(1)} \right\rangle, \end{aligned} \tag{VII.50}$$

where we use Eq. (VII.38) to express the $Y_\alpha^{(1)}$. We thus need to compute quite a few more terms. Let us start by:

$$\begin{aligned} Q_{\omega,p}^{(1)} &= -\frac{1}{\tilde{p}} Q_\omega^{(1)}, \\ Q_{\omega,e}^{(1)} &= \cos f \left(1 + \frac{3}{\tilde{e}^2} \right), \\ Q_{\omega,\omega}^{(1)} &= \sin f \left(\tilde{e} - \frac{3}{\tilde{e}} - 20 \cos f \right). \end{aligned} \tag{VII.51}$$

The last two have zero average, because $\langle \cos f \rangle = \langle \sin f \rangle = \langle \cos f \sin f \rangle = 0$. So, this cancels a few terms in the second and third lines of the RHS of Eq. (VII.50). Following the exact same procedure as for ω, we can write $\mathrm{d}p/\mathrm{d}\varphi$ and $\mathrm{d}e/\mathrm{d}\varphi$, and extract their 1PN component to get:

$$\begin{aligned} Q_p^{(1)} &= 8\,\tilde{p}\,\tilde{e}\,\sin f, \\ Q_e^{(1)} &= \left(3 + 7\tilde{e}^2\right)\sin f + 10\tilde{e}\cos f \sin f, \end{aligned} \tag{VII.52}$$

both of which have zero average (no secular evolution of p and e at 1PN order). This cancels the first two terms of the last two lines in Eq. (VII.50). So we are left with:

$$\begin{aligned} &\left\langle Y_p^{(1)}\, Q_{\omega,p}^{(1)} \right\rangle + \left\langle Y_e^{(1)}\, Q_{\omega,e}^{(1)} \right\rangle + \left\langle Y_\omega^{(1)}\, Q_{\omega,\omega}^{(1)} \right\rangle = \\ &\qquad \left\langle Q_{\omega,p}^{(1)} \int_0^\varphi Q_p^{(1)} \right\rangle + \left\langle Q_{\omega,e}^{(1)} \int_0^\varphi Q_e^{(1)} \right\rangle + \left\langle Q_{\omega,\omega}^{(1)} \int_0^\varphi Q_\omega^{(1)} \right\rangle \\ &\qquad + \left\langle \varphi Q_p^{(1)} \right\rangle \left\langle Q_{\omega,p}^{(1)} \right\rangle - 3 \left\langle \varphi Q_{\omega,\omega}^{(1)} \right\rangle . \end{aligned} \tag{VII.53}$$

It is easy to get:

$$\begin{aligned} \left\langle \varphi Q_p^{(1)} \right\rangle &= -8\,\tilde{p}\,\tilde{e}\,\cos\tilde{\omega}, \\ \left\langle \varphi Q_{\omega,\omega}^{(1)} \right\rangle &= -\cos\tilde{\omega}\left(\tilde{e} - \frac{3}{\tilde{e}}\right) + 5\,\cos 2\tilde{\omega}, \end{aligned} \tag{VII.54}$$

using:

$$\langle \varphi \sin f \rangle = -\cos\tilde{\omega}, \quad \langle \varphi \cos f \sin f \rangle = -\frac{1}{4}\cos 2\tilde{\omega}. \tag{VII.55}$$

The terms with integrals of $Q_\beta^{(1)}$ are a bit more cumbersome, but it is still straightforward to obtain:

$$\begin{aligned} \left\langle Q_{\omega,p}^{(1)} \int_0^\varphi Q_p^{(1)} \right\rangle &= -24\tilde{e}\cos\tilde{\omega} + 4\tilde{e}\left(\tilde{e} - \frac{3}{\tilde{e}}\right), \\ \left\langle Q_{\omega,\tilde{e}}^{(1)} \int_0^\varphi Q_e^{(1)} \right\rangle &= -12 - \frac{7}{2}\tilde{e}^2 - \frac{9}{2\tilde{e}^2}, \\ \left\langle Q_{\omega,\omega}^{(1)} \int_0^\varphi Q_\omega^{(1)} \right\rangle &= \frac{25}{2} + \left(\tilde{e} - \frac{3}{\tilde{e}}\right)\left(-3\cos\tilde{\omega} + \frac{1}{2}\left(\tilde{e} - \frac{3}{\tilde{e}}\right)\right) \\ &\quad + 15\cos 2\tilde{\omega}. \end{aligned} \tag{VII.56}$$

Putting everything together, we finally arrive at:

$$\frac{\mathrm{d}\tilde{\omega}}{\mathrm{d}\varphi} = 3\,\tilde{\epsilon} - \frac{3}{4}\tilde{\epsilon}^2\,\left(10 - \tilde{e}^2\right). \tag{VII.57}$$

Eq. (VII.57) agrees with the 2PN result of [139], see their Eq. (3.23a). The 2PN secular shift is now at hand, but one should certainly not simply multiply by 2π the quantity above to get it. Indeed, it is clear from Fig. IV.3, when f goes from 0 to 2π, the star by definition of the origin of f goes from pericenter to pericenter, that is, draws a full radial cycle. This is our definition of an orbit: a full radial cycle from pericenter back to pericenter. On the contrary, when φ goes from 0 to 2π (that is, when the star goes from the line of nodes, to back to the same line of nodes, which is fixed in Schwarzschild), there is no reason that the star draws a full radial cycle, because the pericenter constantly moves with the star. In Newtonian gravity of course the two notions of 2π cycles for f and φ coincide, but not so in PN. Therefore, the secular shift of a parameter is the integral of its variation over a 2π cycle of f, not φ. In order to derive the secular shift from $d\tilde{\omega}/d\varphi$, we should find by what quantity $\Delta\varphi$ the angle φ varies, when f varies by $\Delta f = 2\pi$. Using perturbation method we will expand ω in powers of the PN small parameter

$$\omega(f) = \omega_0(f) + \epsilon_0\omega_1(f) + \epsilon_0^2\omega_2(f) + o(\epsilon_0^2),$$

where

$$\epsilon_0 = \frac{GM}{p_0c^2}$$

is yet another flavor of the PN small parameter, this time expressed in terms of a constant value of the semilatus rectum, p_0.

To get the relation we are looking for, let us start from the 1PN expansion of Eq. (VII.1.2) and write

$$\varphi(f) = f + \omega(f) = f + \omega_0 + \epsilon_0\omega_1(f), \tag{VII.58}$$

where

$$\omega_1(f) = 3(f - f_0) + \left(e_0 - \frac{3}{e_0}\right)(\sin f - \sin f_0) - 5(\sin f \cos f - \sin f_0 \cos f_0). \tag{VII.59}$$

Plugging the expression of ω_1, we get

$$\varphi(f) = f + \omega_0 + \epsilon\left[3(f - f_0) + \left(e_0 - \frac{3}{e_0}\right)(\sin f - \sin f_0) - 5(\sin f \cos f - \sin f_0 \cos f_0)\right]. \tag{VII.60}$$

From this relation, we can easily deduce that

$$f = f_0 \quad \Leftrightarrow \quad \varphi = \varphi_0 = f_0 + \omega_0, \tag{VII.61}$$

$$f = f_0 + 2\pi \quad \Leftrightarrow \quad \varphi = \varphi_0 + 2\pi + 6\pi\epsilon + o(\epsilon), \tag{VII.62}$$

so we obtain that at 1PN order (and we do not need to go to higher PN order)

$$\Delta f = 2\pi \quad \Leftrightarrow \quad \Delta\varphi = 2\pi + 6\pi\epsilon. \tag{VII.63}$$

We can now express the 2PN secular shift of the argument of pericenter as

$$\Delta\tilde{\omega}_{\rm Sch} = \frac{d\tilde{\omega}}{d\varphi} \times \Delta\varphi = 6\pi\tilde{\epsilon} + \tilde{\epsilon}^2\left(3\pi + \frac{3}{2}\pi\tilde{e}^2\right), \tag{VII.64}$$

where the quantities $d\tilde{\omega}/d\varphi$ and $\Delta\varphi$ in the equation above are as defined by Eqs. (VII.57) and (VII.63), respectively. Also note that a term $\epsilon\tilde{\epsilon}$ has been replaced by a term $\tilde{\epsilon}^2$, which is justified by the fact that:

$$\epsilon = \tilde{\epsilon} + 2\text{PN term}. \tag{VII.65}$$

Finally, we get the 2PN expression of the secular shift of the pericenter/apocenter in Schwarzschild:

$$\boxed{\Delta\omega_{\rm Sch} = \Delta\tilde{\omega}_{\rm Sch} = 6\pi\tilde{\epsilon} + \frac{3\pi}{2}\tilde{\epsilon}^2\left(2 + \tilde{e}^2\right)} \tag{VII.66}$$

Here, the quantities $\tilde{\epsilon}$ and $\tilde{e}$ refer to orbit-averaged parameters. If, in the 2PN term of Eq. (VII.66), we replace $\tilde{\epsilon}$ and $\tilde{e}$ with their osculating counterparts ϵ and e, this substitution would only modify the result at 3PN order—meaning the 2PN expression remains unchanged. However, replacing $\tilde{\epsilon}$ with ϵ in the 1PN term would already introduce a discrepancy at 2PN order.

This is why, when expressing the pericenter advance to 2PN accuracy, it is essential to keep the orbit-averaged quantity $\tilde{\epsilon}$ in the 1PN term ($6\pi\tilde{\epsilon}$ and not $6\pi\epsilon$). Alternatively, if one prefers to work with osculating elements throughout, the entire perturbative approach—including the ansatz for the solution (e.g., Eq. (VII.26))—must be adjusted accordingly. In that case, the expression for the 2PN pericenter advance would take a different form, reflecting the difference in parameterization.

In contrast, for the 2PN-order secular shifts due to the Lense–Thirring effect and the black hole's quadrupole moment, the expressions involve only leading-order contributions. Therefore, one may safely use either averaged or osculating values of p, θ, and ψ without affecting the accuracy at the given order.

Finally, by using Eq. (VII.37) we easily obtain:

$$\begin{aligned} Y_p^{(1)} &= -8\tilde{p}\, e\, \cos f, \\ Y_\omega^{(1)} &= \sin f\left(e - \frac{3}{e} - 5\cos f\right), \\ Y_e^{(1)} &= -\frac{5}{2}e\cos 2\omega - \cos f\left(3 + 7e^2\right) + 5e\sin\varphi\,\sin\left(\varphi - 2\omega\right). \end{aligned} \tag{VII.67}$$

such that Eq. (VII.32) is indeed valid for this special case.

VII.2 Spin impact on the orientation of the orbit

First, we want to understand analytically the effect of spin on the evolution of the orientation of the orbit. This will lead us to introduce several precession movements, either instantaneous or secular. The secular evolution is well known [see e.g 87], it consists of a precession movement of $\mathbf{z}_{\rm orb}$ about $\mathbf{z}_{\rm bh}$. Instantaneous evolution is both less known and more useful in the perspective of orbital fits. We will therefore focus on the latter. Second, we will illustrate this analytical understanding by performing simulations for the hypothetical S2/10.

VII.2.1 Instantaneous orientation change

Orbital frame orientation change

Let us characterize the evolution of the orientation of the orbit by expressing the temporal evolution of the orbit frame. Using the Lagrange planetary equations, it is possible to reexpress the temporal variations of the orbit frame vectors as functions of the temporal variations of the orbital elements. We get [see 140]:

$$\begin{aligned}\frac{\mathrm{d}\mathbf{x}_{\rm orb}}{\mathrm{d}t} &= \frac{\mathrm{d}\varpi}{\mathrm{d}t}\mathbf{y}_{\rm orb} + \frac{\mathrm{d}\Theta}{\mathrm{d}t}\,\mathbf{z}_{\rm orb} \\ &= \frac{\mathrm{d}\varpi}{\mathrm{d}t}\mathbf{z}_{\rm orb}\times\mathbf{x}_{\rm orb} - \frac{\mathrm{d}\Theta}{\mathrm{d}t}\mathbf{y}_{\rm orb}\times\mathbf{x}_{\rm orb},\end{aligned} \tag{VII.68}$$

$$\begin{aligned}\frac{\mathrm{d}\mathbf{y}_{\rm orb}}{\mathrm{d}t} &= -\frac{\mathrm{d}\varpi}{\mathrm{d}t}\mathbf{x}_{\rm orb} + \frac{\mathrm{d}\Xi}{\mathrm{d}t}\mathbf{z}_{\rm orb} \\ &= -\frac{\mathrm{d}\varpi}{\mathrm{d}t}\mathbf{y}_{\rm orb}\times\mathbf{z}_{\rm orb} + \frac{\mathrm{d}\Xi}{\mathrm{d}t}\mathbf{x}_{\rm orb}\times\mathbf{y}_{\rm orb},\end{aligned} \tag{VII.69}$$

$$\begin{aligned}\frac{\mathrm{d}\mathbf{z}_{\rm orb}}{\mathrm{d}t} &= -s_{\mathcal{W}}\sqrt{\left(\frac{\mathrm{d}\iota}{\mathrm{d}t}\right)^2 + \sin^2\iota\left(\frac{\mathrm{d}\Omega}{\mathrm{d}t}\right)^2}\,\mathbf{m}_{\rm orb} \\ &= -\frac{\mathrm{d}\Theta}{\mathrm{d}t}\mathbf{x}_{\rm orb} + \frac{\mathrm{d}\Xi}{\mathrm{d}t}\mathbf{y}_{\rm orb} \\ &= -\frac{\mathrm{d}\Theta}{\mathrm{d}t}\mathbf{y}_{\rm orb}\times\mathbf{z}_{\rm orb} - \frac{\mathrm{d}\Xi}{\mathrm{d}t}\mathbf{x}_{\rm orb}\times\mathbf{z}_{\rm orb},\end{aligned} \tag{VII.70}$$

where $s_{\mathcal{W}}$ is the sign of $\mathcal{W}$ and:

$$\frac{\mathrm{d}\varpi}{\mathrm{d}t} \equiv \frac{\mathrm{d}\omega}{\mathrm{d}t} + \cos\iota\,\frac{\mathrm{d}\Omega}{\mathrm{d}t}; \tag{VII.71}$$

$$\frac{\mathrm{d}\Theta}{\mathrm{d}t} \equiv \sin\omega\frac{\mathrm{d}\iota}{\mathrm{d}t} - \sin\iota\cos\omega\frac{\mathrm{d}\Omega}{\mathrm{d}t}; \tag{VII.72}$$

$$\frac{\mathrm{d}\Xi}{\mathrm{d}t} \equiv -\cos\omega\frac{\mathrm{d}\iota}{\mathrm{d}t} - \sin\iota\sin\omega\frac{\mathrm{d}\Omega}{\mathrm{d}t}. \tag{VII.73}$$

We add the last lines of Eqs. (VII.68) to (VII.70) to reveal the precession aspect of the equations and their different components.

We obtain:

$$\frac{\mathrm{d}\mathbf{x}_{\rm orb}}{\mathrm{d}t}\cdot\mathbf{y}_{\rm orb} = -\frac{\mathrm{d}\mathbf{y}_{\rm orb}}{\mathrm{d}t}\cdot\mathbf{x}_{\rm orb} = \frac{\mathrm{d}\varpi}{\mathrm{d}t}, \tag{VII.74}$$

encoding the change of direction of the major and minor axes in the orbit plane;

$$\frac{\mathrm{d}\mathbf{x}_{\rm orb}}{\mathrm{d}t}\cdot\mathbf{z}_{\rm orb} = -\frac{\mathrm{d}\mathbf{z}_{\rm orb}}{\mathrm{d}t}\cdot\mathbf{x}_{\rm orb} = \frac{\mathrm{d}\Theta}{\mathrm{d}t}, \tag{VII.75}$$

encoding the change of the major axis orthogonal to the orbit plane, or equivalently the change of the orbital angular momentum direction along the major axis;

$$\frac{\mathrm{d}\mathbf{z}_{\rm orb}}{\mathrm{d}t}\cdot\mathbf{y}_{\rm orb} = -\frac{\mathrm{d}\mathbf{y}_{\rm orb}}{\mathrm{d}t}\cdot\mathbf{z}_{\rm orb} = \frac{\mathrm{d}\Xi}{\mathrm{d}t}, \tag{VII.76}$$

encoding the change of the minor-axis direction orthogonal to the orbit plane, or equivalently the change of the orbital angular momentum along the minor axis. We note that $\mathbf{x}_{\rm orb}\cdot\frac{\mathrm{d}\mathbf{x}_{\rm orb}}{\mathrm{d}t} = \mathbf{y}_{\rm orb}\cdot\frac{\mathrm{d}\mathbf{y}_{\rm orb}}{\mathrm{d}t} = \mathbf{z}_{\rm orb}\cdot\frac{\mathrm{d}\mathbf{z}_{\rm orb}}{\mathrm{d}t} = 0$, as it should for unit vectors. Therefore, we can decompose the overall precession into two components: the precession of the argument of periapsis within the changing orbital plane, with associated characteristic frequency $\frac{\mathrm{d}\varpi}{\mathrm{d}t}$, hereafter referred to as "in-plane[7] precession"; and the precessions of the orbit plane, with characteristic associated frequencies $\frac{\mathrm{d}\Theta}{\mathrm{d}t}$ and $\frac{\mathrm{d}\Xi}{\mathrm{d}t}$, hereafter referred to as "out-of-plane precession".

These scalar quantities are also presented[8] in [140], and are independent from the observer's location, which is obvious from their definition: they depend only on $(\mathbf{x}_{\rm orb}, \mathbf{y}_{\rm orb}, \mathbf{z}_{\rm orb})$ which depends only on the orbit. As such, ϖ, Θ and Ξ appear to be very useful for expressing observer-independent statements on the variation of the pericenter and angular momentum directions.

Secular orientation change

Let us introduce the secular shifts $\Delta\varpi$, $\Delta\Theta$ and $\Delta\Xi$, as the integration over an orbit of the temporal variations of ϖ, Θ and Ξ. Following the same methodology as in section VII.1, the secular in-plane shift of the pericenter can be expressed at 2PN order as:

$$\Delta\varpi_{\rm Sch}\big|^{\rm 2PN} = \Delta\omega_{\rm Sch}\big|^{\rm 2PN} = 6\pi\tilde{\epsilon} + \frac{3\pi}{2}\tilde{\epsilon}^2\left(2+\tilde{e}^2\right); \tag{VII.77}$$

$$\Delta\varpi_{\rm LT}\big|^{\rm 2PN} = -8\pi\epsilon^{3/2}\cos\theta\ \chi; \tag{VII.78}$$

$$\Delta\varpi_{Q}\big|^{\rm 2PN} = -\frac{3\pi}{2}\epsilon^2\left(1-3\cos^2\theta\right)\ \chi^2. \tag{VII.79}$$

[7] In the case where we have out-of-plane precession, the notion of in-plane becomes more delicate considering that the orbital plane changes all the time. In the following, we use this formulation to refer to instantaneous in-plane precession.

[8] In the second line of equation "(3)" of [140] the unit vector "$\mathbf{e}_X$" should read "$\mathbf{e}_Y$".

Notice that Eqs. (VII.78) and (VII.79) will still be valid if $\iota = 0$, as opposed to Eqs. (VII.9), (VII.10), (VII.15) and (VII.16). Using ϖ allows us to quantify the precession inside the orbital plane without using the notion of $\mathcal{L}_{\mathbf{orb//sky}}$ which is degenerate in the case of a face-on[9] orbit. From Eqs. (VII.78) and (VII.79) we see that the Lense-Thirring and quadrupole moment in-plane precession depend on the polar angle θ but not on the azimuthal angle ψ of the spin vector spherical coordinates defined in Figure IV.5. We see that the in-plane precession of the Lense-Thirring effect is maximal for orbits in the equatorial plane of the black hole, i.e for $\theta = 0 \pmod{\pi}$, and vanishes for polar[10] orbits, i.e for $\theta = \pi/2 \pmod{\pi}$. The quadrupole moment in-plane precession, however, is maximized for both equatorial and polar orbits, and vanishes for $\theta = \arccos\left(\pm 1/\sqrt{3}\right)$.

The secular out-of-plane shift of the major axis can be expressed at 2PN order from Eq. (VII.72) as:

$$\Delta\Theta = \sin\omega\Delta\iota - \sin\iota\cos\omega\Delta\Omega \tag{VII.80}$$

to characterize the out-of-plane component of the pericenter precession. When using the secular shifts of the orbital parameters derived in subsection VII.1.1 in Eq. (VII.80), we obtain the following expressions as function of θ and $\psi = \beta - \omega$ (illustrated in Figure IV.5):

$$\Delta\Theta_{\rm LT}|^{\rm 2PN} = -4\pi\epsilon^{3/2}\sin\theta\sin\psi \;\; \chi; \tag{VII.81}$$
$$\Delta\Theta_{Q}|^{\rm 2PN} = 3\pi\epsilon^{2}\cos\theta\sin\theta\sin\psi \;\; \chi^2, \tag{VII.82}$$

corresponding to the out-of-plane movement of the major axis precession (also referred to as out-of-plane apocenter shift) due to the Lense-Thirring and quadrupole moment effects, as illustrated in Figure VII.1. The Schwarzschild precession does not contribute to the out-of-plane shifts at any PN order.

Finally, the secular out-of-plane shift of the minor axis can be expressed at 2PN order from Eq. (VII.73) as:

$$\Delta\Xi = -\cos\omega\Delta\iota - \sin\omega\sin\iota\Delta\Omega. \tag{VII.83}$$

We obtain the following expressions:

$$\Delta\Xi_{\rm LT}|^{\rm 2PN} = -4\pi\epsilon^{3/2}\sin\theta\cos\psi \;\; \chi; \tag{VII.84}$$
$$\Delta\Xi_{Q}|^{\rm 2PN} = 3\pi\epsilon^{2}\cos\theta\sin\theta\cos\psi \;\; \chi^2. \tag{VII.85}$$

[9]The evolution of the orbital angular momentum direction makes the notion of face-on or edge-on view of the orbit tricky when $\theta \neq 0$, therefore, when talking about a face-on or edge-on view of the orbit in this article, we will be referring to the initial view of the orbit.

[10]Meaning that the orbit plane contains the spin axis of the black hole or equivalently that $\mathbf{z}_{\rm orb}$ is perpendicular to $\mathbf{z}_{\rm bh}$. Considering that θ has a periodic variation due to the Lense-Thirring effect in this case, but not a secular one (see subsection VII.2.3), a polar orbit will only remain polar on a secular scale.

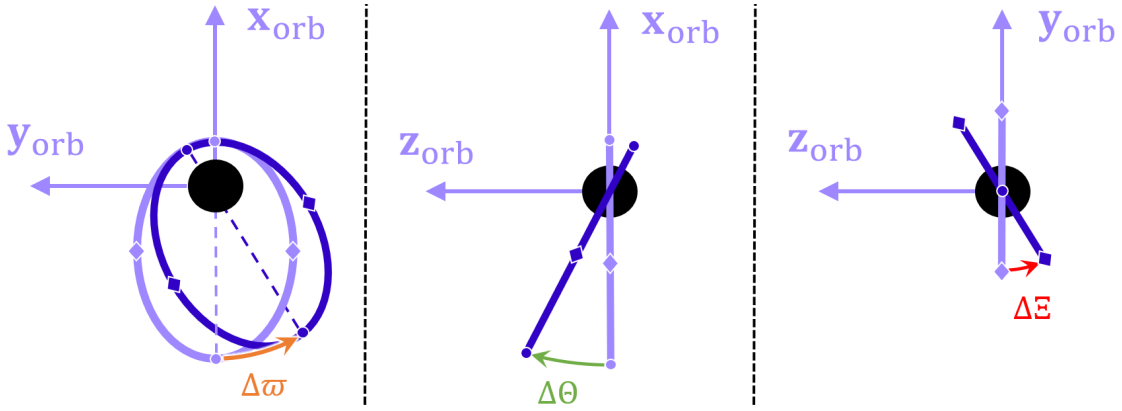

(a) Orbital timescale orientation change

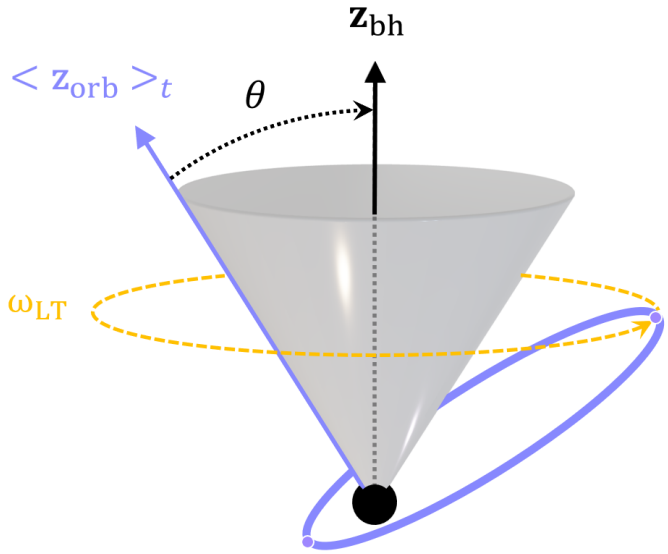

(b) Secular timescale orientation change

Figure VII.1: Figure VII.1a shows the evolution of the orbit orientation on an orbital period P timescale. Three precessions are experienced: an in-plane precession (left panel) with contributions at 1PN, 1.5PN and 2PN; two out-of-plane precessions, one around the minor axis (middle panel) and another around the major axis (right panel) with contributions at 1.5PN and 2PN. Figure VII.1b shows the evolution of the orbit orientation on a secular timescale $P^{\rm cone} \gg P$ (see Eq. (9)). The orbital angular momentum experiences a precession around the black hole spin axis.

The expressions of $\Delta\Theta$ and $\Delta\Xi$ above show that these quantities depend on both θ and ψ. If we take $\psi = \pi/2 \pmod{\pi}$, i.e when the projection of the spin axis of the black hole on the orbit is along the minor axis, then $\Delta\Theta$ would be maximized, while $\Delta\Xi$ would be null, i.e the major axis precesses in a plane orthogonal to the minor axis. Conversely, with $\psi = 0 \pmod{\pi}$, i.e when the projection of the spin axis on the orbit is along the major axis, $\Delta\Theta$ would be null, while $\Delta\Xi$ would be maximized, i.e the minor axis precesses in a plane orthogonal to the major axis. Note that due to the in-plane precession, this can be true only instantaneously.

The Lense-Thirring effect generates a maximal out-of-plane precession for polar orbits and a vanishing one for equatorial orbits. We also see that the configuration that allows for the most apocenter displacement due to the Lense-Thirring effect (the maximum of $\Delta\Lambda_{\rm LT} \equiv \sqrt{\Delta\varpi_{\rm LT}^2 + \Delta\Theta_{\rm LT}^2}$), would be an equatorial orbit.

As for the quadrupole moment effect, it does not induce any out-of-plane precessions for polar orbits. In addition, we observe that the out-of-plane precession is maximized for $\theta = \pi/4 \pmod{\pi}$. This behavior is similar to the Newtonian case of a particle orbiting an oblate mass ; if the particle is mid-inclined with respect to the equatorial plane of the central mass[11], the particle would experience the highest level of asymmetries along the orbit leading to the highest out-of-plane shifts among all possible relative orientations [13]. In terms of overall apocenter angular shift, we also see that the configuration that maximizes $\Delta\Lambda_Q \equiv \sqrt{\Delta\varpi_Q^2 + \Delta\Theta_Q^2}$ would be an equatorial orbit.

Even though ω and β are observer dependent, $\psi = \beta - \omega$, the angle between $\mathbf{z}_{\rm bh//orb}$ and $\mathbf{x}_{\rm orb}$, rotating around $\mathbf{z}_{\rm orb}$ in Figure VII.1, is observer independent. Therefore, $\Delta\Theta$ and $\Delta\Xi$ are as well.

In subsection VII.2.4, we will focus primarily on three representative orbital configurations: equatorial, polar, and mid-inclined orbits. This choice is motivated by the fact that the various relativistic precessions—both in-plane and out-of-plane—reach their maximum amplitudes in these configurations. Equatorial orbits maximize the in-plane precession due to both the Lense–Thirring and quadrupole moment effects, polar orbits maximize the Lense–Thirring–induced out-of-plane motion, and mid-inclined orbits (e.g., $\theta = \pi/4$) produce the strongest out-of-plane contribution from the quadrupole moment. These three cases thus offer the best prospects for detecting and distinguishing the different relativistic effects.

VII.2.2 Secular shifts for S2 and S2/10

Let us consider the star S2, as well as a hypothetical star S2/10. In Figure VII.2, we summarize the dependence on θ of the Lense-Thirring and quadrupole moment precessions that was detailed in subsection VII.2.1 using S2 and S2/10 at

[11] which is flattened around the poles.

fixed $\psi = 3\pi/2$ for the in-plane and out-of-plane precession of the major axis, and $\psi = 0$ for the out-of-plane precession of the minor axis.

In table VII.1 we evaluate the angular shifts $\Delta\varpi$, $\Delta\Theta$, $\Delta\Xi$ of the star S2, for the values of the black hole spin orientation angles (θ, ψ) that maximize these shifts.

Table VII.1: Comparing the various secular shifts of the star S2, when using values of θ and ψ that maximize the LT and Q angular shifts given in Eqs. (VII.77) to (VII.85). We use a single set of orbital parameters for all shifts, the osculating one at apocenter, in order to compare them.

$\Delta X^{\rm 2PN}_{\rm S2}$	$\lvert\max(\Delta X)\rvert$	$\frac{\lvert\max(\Delta X)\rvert}{\Delta\varpi_{\rm Sch}}$	θ	ψ
$\Delta\varpi_{\rm Sch}$	732 "/rev	100%	-	-
$\Delta\varpi_{\rm LT}$	13.3 "/rev	1.81%	0 (mod π)	-
$\Delta\Theta_{\rm LT}$	6.63 "/rev	0.91%	$\pi/2$ (mod π)	$\pi/2$ (mod π)
$\Delta\Xi_{\rm LT}$	6.63 "/rev	0.91%	$\pi/2$ (mod π)	0 (mod π)
$\Delta\varpi_Q$	0.0675 "/rev	0.01%	0 (mod π)	-
$\Delta\Theta_Q$	0.0338 "/rev	0.005%	$\pi/4$ (mod π)	$\pi/2$ (mod π)
$\Delta\Xi_Q$	0.0338 "/rev	0.005%	$\pi/4$ (mod π)	0 (mod π)

When computing the secular shifts for S2/10, we see that

$$\begin{aligned}
\Delta\varpi^{\rm S2/10}_{\rm Sch} &= 10\Delta\varpi_{\rm Sch}|^{\rm S2}_{\rm 1PN} + 10^2\Delta\varpi_{\rm Sch}|^{\rm S2}_{\rm 2PN} \approx 10\,\Delta\varpi^{\rm S2}_{\rm Sch},\\
\Delta X^{\rm S2/10}_{\rm LT} &= 10^{3/2}\,\Delta X^{\rm S2}_{\rm LT},\\
\Delta X^{\rm S2/10}_{Q} &= 10^{2}\,\Delta X^{\rm S2}_{Q},
\end{aligned}$$

with X denoting either in-plane (ϖ) or out-of-plane (Θ, Ξ) precession components. This scaling between the Schwarzschild precession, the Lense-Thirring and the quadrupole moment effects stem from the dependencies in ϵ (i.e the PN order).

Not only do all relativistic effects become significantly larger, but having smaller periods allows us to observe more pericenter/apocenter passages, thus accumulating more secular shifts in given amount of time. For instance, the period of the star S2 ($\approx$ 16yr) corresponds to $10^{3/2} \approx 30$ orbits of the star S2/10. Therefore, when working with S2/10 instead of S2 over one period of S2, the angular shift due to the Schwarzschild precession is increased by a factor $\approx 10^{3/2} \times 10 \approx 300$, the Lense-Thiring precessions by a factor $10^{3/2} \times 10^{3/2} = 10^3$, and the quadrupole moment shifts by a factor $10^{3/2} \times 10^2 = 10^{5/2} \approx 3000$. These scaling behaviors emphasize the scientific value of observing closer-in stars, providing a powerful means to probe both the spin and higher-order mass moments of Sgr A*.

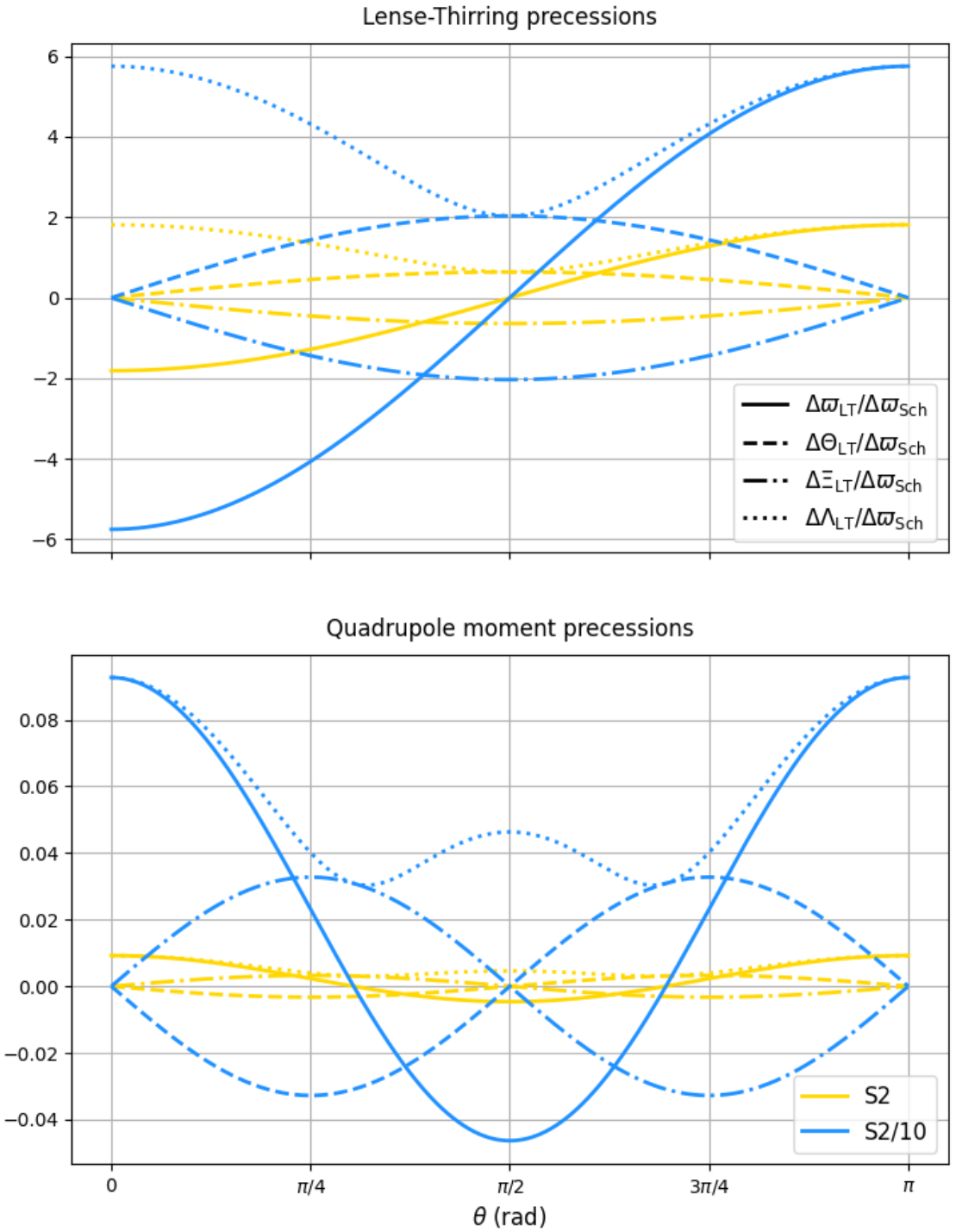

Figure VII.2: Analytical secular in-plane and out-of-plane precession of the major axis generated by the Lense-Thirring (up) and quadrupole moment (down) effects, relative to the Schwarzschild precession of each star (units of %), as a function of the angle θ, using $\omega - \beta = \pi/2 \pmod{\pi}$. The out-of-plane precession of the minor axis, $\Delta\Xi$, has the same behavior as that of the major axis, $\Delta\Theta$, for $\omega - \beta = 0 \pmod{\pi}$

VII.2.3 Time-averaged orientation change

After having described the instantaneous orientation change of the orbital frame, we will here discuss its secular evolution over timescales long compared to the orbital period. We know from Eqs. (VII.70), (II.14), (II.15), and the corresponding expression of the perturbative acceleration given in (V.42) that the Lense-Thirring effect acts on the orbital angular momentum such that:

$$\left.\frac{\mathrm{d}\mathbf{z}_{\rm orb}}{\mathrm{d}t}\right|_{\rm LT} = -2\frac{G^2m^2}{c^3r^3}\chi\left[\frac{e\sin f}{1+e\cos f}(\mathbf{z}_{\rm bh}\cdot\mathbf{m}_{\rm orb})+2(\mathbf{z}_{\rm bh}\cdot\mathbf{n}_{\rm orb})\right]\mathbf{m}_{\rm orb}. \tag{VII.86}$$

From this we obtain[12]:

$$\left\langle\left.\frac{\mathrm{d}\mathbf{z}_{\rm orb}}{\mathrm{d}t}\right|_{\rm LT}\right\rangle_t = \boldsymbol{\omega}_{\rm LT}(\mathbf{z}_{\rm bh}\times\mathbf{z}_{\rm orb}), \tag{VII.87}$$

where[13]:

$$\boldsymbol{\omega}_{\rm LT} = 2n\epsilon^{3/2}\chi, \tag{VII.88}$$

and $n = \sqrt{Gm/a_{\rm sma}^3}$ is the Newtonian mean motion. Moreover, we have the expression (see Figure IV.5):

$$\mathbf{z}_{\rm bh} = \sin\theta\cos\psi\mathbf{x}_{\rm orb}+\sin\theta\sin\psi\mathbf{y}_{\rm orb}+\cos\theta\mathbf{z}_{\rm orb}, \tag{VII.89}$$

that we insert into Eq. (VII.87). Then, by identifying to the time average of Eq. (VII.70), we choose to define:

$$\left.\frac{\mathrm{d}\tilde{\Theta}}{\mathrm{d}t}\right|_{\rm LT} \equiv -\boldsymbol{\omega}_{\rm LT}\sin\theta\sin\psi; \tag{VII.90}$$

$$\left.\frac{\mathrm{d}\tilde{\Xi}}{\mathrm{d}t}\right|_{\rm LT} \equiv -\boldsymbol{\omega}_{\rm LT}\sin\theta\cos\psi, \tag{VII.91}$$

and thus get:

$$\Delta\tilde{\Theta}_{\rm LT} = P\left.\frac{\mathrm{d}\tilde{\Theta}}{\mathrm{d}t}\right|_{\rm LT} = \frac{2\pi}{n}\left.\frac{\mathrm{d}\tilde{\Theta}}{\mathrm{d}t}\right|_{\rm LT} = -4\pi\epsilon^{3/2}\chi\sin\theta\sin\psi; \tag{VII.92}$$

$$\Delta\tilde{\Xi}_{\rm LT} = P\left.\frac{\mathrm{d}\tilde{\Xi}}{\mathrm{d}t}\right|_{\rm LT} = \frac{2\pi}{n}\left.\frac{\mathrm{d}\tilde{\Xi}}{\mathrm{d}t}\right|_{\rm LT} = -4\pi\epsilon^{3/2}\chi\sin\theta\cos\psi. \tag{VII.93}$$

[12] by using the following definition for the time-average of a quantity F, $\langle F\rangle_t = \frac{1}{P}\int_0^P F(t)dt = \frac{1}{2\pi a_{\rm sma}^2\sqrt{1-e^2}}\int_0^{2\pi} r^2F(\varphi)d\varphi$, which is different from the azimuthally-averaged definition of Eq. (VII.27) used in the two-timescale analysis.

[13] not to be confused with the longitude of the ascending node.

This shows that $\frac{\mathrm{d}\tilde{\Theta}}{\mathrm{d}t}$ and $\frac{\mathrm{d}\tilde{\Xi}}{\mathrm{d}t}$ are the time-average of $\frac{\mathrm{d}\Theta}{\mathrm{d}t}$ and $\frac{\mathrm{d}\Xi}{\mathrm{d}t}$ and that $\Delta\tilde{\Theta}_{\mathrm{LT}} = \Delta\Theta_{\mathrm{LT}}$ and $\Delta\tilde{\Xi}_{\mathrm{LT}} = \Delta\Xi_{\mathrm{LT}}$. In other words, we end up with the same results given by the instantaneous formalism used in subsection VII.2.1, which links the two aspects of instantaneous and averaged precession shifts.

If we do the same exercise for the quadrupole moment using Eq. (VII.70) and (V.48) we get:

$$\left\langle \left.\frac{\mathrm{d}\mathbf{z}_{\mathrm{orb}}}{\mathrm{d}t}\right|_Q \right\rangle_t = -\omega_Q(\mathbf{z}_{\mathrm{bh}}\cdot\mathbf{z}_{\mathrm{orb}})(\mathbf{z}_{\mathrm{bh}}\times\mathbf{z}_{\mathrm{orb}}), \tag{VII.94}$$

where:

$$\omega_Q = \frac{3n}{2}\epsilon^2\chi^2, \tag{VII.95}$$

Once again, we see that $\Delta\tilde{\Theta}_Q = \Delta\Theta_Q$ and $\Delta\tilde{\Xi}_Q = \Delta\Xi_Q$ as with the the Lense-Thirring effect above.

We see from Eqs. (VII.87) and (VII.94) that $\mathbf{z}_{\mathrm{orb}}$ has an average precession around $\mathbf{z}_{\mathrm{bh}}$, meaning that the angle θ between $\mathbf{z}_{\mathrm{orb}}$ and $\mathbf{z}_{\mathrm{bh}}$ has no secular evolution. In other words, the secular out-of-plane precession is done at fixed[14] θ, of $\mathbf{z}_{\mathrm{orb}}$ about $\mathbf{z}_{\mathrm{bh}}$ (as illustrated in Figure VII.1), and Eqs. (VII.88) and (VII.95) are the frequencies at which the out-of-plane precession spans the cone of angle θ represented in Figure VII.1, due to the Lense-Thirring (at the 1.5PN order) and quadrupole moment (at the 2PN order) effects, respectively. We also see that the direction of secular rotation of $\mathbf{z}_{\mathrm{orb}}$ due to the Lense-Thirring effect is the same as that of the spin. The direction of secular rotation of $\mathbf{z}_{\mathrm{orb}}$ due to the quadrupole moment effect depends on the sign of $-\mathbf{z}_{\mathrm{bh}}\cdot\mathbf{z}_{\mathrm{orb}} = -\cos\theta$ (see Eq. (VII.94)): in the case of $\theta > \pi/2$ (a retrograde orbit relative to the black hole), the direction of rotation is the same as that of the spin for example, but opposite in the case of prograde orbits relative to the black hole.

In conclusion, we stress that both the in-plane and out-of-plane precessions can be considered differently on two timescales: time-averaged (on the cone defined by Eqs. (VII.87) and (VII.94) for the out-of-plane precession), and instantaneously, which corresponds to a rotation of the axes around each other, given by Eqs. (VII.68) and (VII.70) (and which can deviate from the cone defined by Eqs. (VII.87) and (VII.94) for the out-of-plane precession).

VII.2.4 Numerical illustration

We illustrate the instantaneous variations in the orientation of the orbital frame using numerical integrations of the post-Newtonian Lagrange planetary equations (see section II.2). These simulations are tailored to maximize the impact of each relativistic effect (see the analysis of subsection VII.2.1). To do so, we will align

[14] θ can have periodic variations but no secular ones at the 2PN level.

$\mathbf{z}_{\rm bh}$ on each axis of the orbit frame $\mathbf{z}_{\rm bh}//\mathbf{z}_{\rm orb}$ (maximizing the in-plane precession of all effects), $\mathbf{z}_{\rm bh}//\mathbf{x}_{\rm orb}$ and $\mathbf{z}_{\rm bh}//\mathbf{y}_{\rm orb}$ (maximizing the out-of-plane precession of the Lense-Thirring effect); these three configurations will be referred to as "equatorial orbit", "polar orbit with polar major axis" and "polar orbit with equatorial major axis", respectively. Finally, we refer to appendix A the study of "mid-inclined orbits", that maximize the out-of-plane precession of the quadrupole moment, and are such that $\mathbf{z}_{\rm bh} = -\mathbf{y}^{\rm pro}_{\rm orb} + \mathbf{z}^{\rm pro}_{\rm orb} = \mathbf{y}^{\rm ret}_{\rm orb} - \mathbf{z}^{\rm ret}_{\rm orb}$. This will provide intuition on the way the spin of the black hole can impact the orbit, independently from the observer.

The simulated star is taken to have orbital parameters identical to S2/10 in terms of semi-major axis and eccentricity. We perform a Euclidean projection of the orbit onto a plane—this is for illustrative purposes only and does not aim at reproducing observables. Effects such as the Rømer delay, gravitational redshift or lensing are deliberately omitted, as they fall outside the scope of this analysis.

In the following subsections, we will see that the simulated variations in these configurations reproduce the expected post-Newtonian trends, both in direction and in structure.

We define a prograde and retrograde orbit relative to the black hole, with angular momentum along $\mathbf{z}^{\rm pro}_{\rm orb}$ and $\mathbf{z}^{\rm ret}_{\rm orb}$, as orbits that verify $\mathbf{z}^{\rm pro}_{\rm orb} \cdot \mathbf{z}_{\rm bh} > 0$ and $\mathbf{z}^{\rm ret}_{\rm orb} \cdot \mathbf{z}_{\rm bh} < 0$, respectively.

In-plane precession: focusing on equatorial orbits

In this subsection, we will examine the impact of the in-plane precession due to Kerr effects, independently from the projection on the screen of a distant observer. For this purpose, we simulate orbits that are in the equatorial plane of the black hole, thus maximizing the in-plane precession, and eliminating the out-of-plane ones[15].

Let us consider 2 orbits in the equatorial plane of the black hole, one is prograde ($\theta = 0$) with $\Delta\varpi^{\rm pro}_{\rm Kerr} = \Delta\varpi^{\rm pro}_{\rm LT} + \Delta\varpi^{\rm pro}_{Q}$, and the other is retrograde ($\theta = \pi$) with $\Delta\varpi^{\rm ret}_{\rm Kerr} = \Delta\varpi^{\rm ret}_{\rm LT} + \Delta\varpi^{\rm ret}_{Q}$, making ψ degenerate. For understanding the in-plane precession, we perform in Figures VII.3 and VII.4 a Euclidean projection of these orbits onto a face-on plane.

Let us start with the well-known Schwarzschild precession. We know that ω is measured in the same direction as the movement of the star in its orbit. When looking at the analytical expressions, we see that Eq. (VII.77) is independent from θ, it leads to the same positive $\Delta\varpi_{\rm sch}$ for prograde and retrograde orbits, regardless of the orientation of the black hole with respect to the orbit. This means that the prograde and retrograde apocenter displacements will go in opposite ways. We

[15] We know that the quantities $\mathcal{W}^{\rm 1.5PN}_{\rm LT}$ and $\mathcal{W}^{\rm 2PN}_{Q}$, the expressions of which are given in Eqs. (V.42) and (V.48) yield zero for equatorial orbits, i.e for $\theta = 0 \pmod{\pi}$. This leads to Eqs. (II.14) and (II.15) also yielding zero, meaning that no out-of-plane movement is induced by the BH's spin. So an initially equatorial orbit will remain so, even in the presence of a spin.

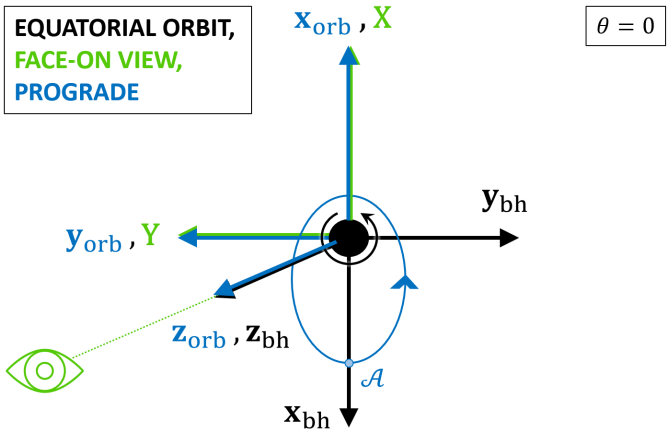

(a) Schematic illustration of the osculating Keplerian orbit (see subsection VII.2.4)

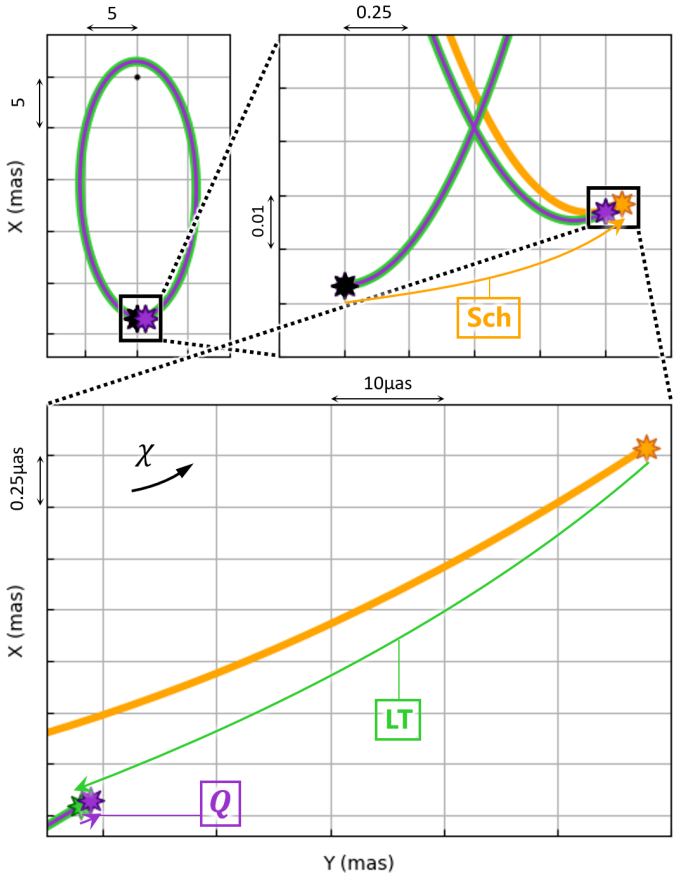

(b) Simulation using the 2PN code

Figure VII.3: Prograde orbits in the equatorial plane of the black hole with a face-on view. In Figure VII.3a the apocenter is represented by the letter $\mathcal{A}$. In Figure VII.3b we show an orbit of the hypothetical star S2/10 simulated in 2PN using OOGRE: the "✷" denotes the apocenters (the first apocenter in black corresponds to the osculating time, which is also the initial date, and is in common for the three orbits). We simulate one orbit for the Schwarzschild precession ("Sch" in orange), one orbit for both the Schwarzschild and Lense-Thirring precessions ("LT" in green), and one orbit for the Schwarzschild, spin and quadrupole moment precessions ("Q" in thin purple). We see that the Lense-Thirring and quadrupole moment effects shift the apocenter clockwise and counterclockwise, respectively, as seen by this face-on observer. All numbers are expressed in mas except otherwise noted.

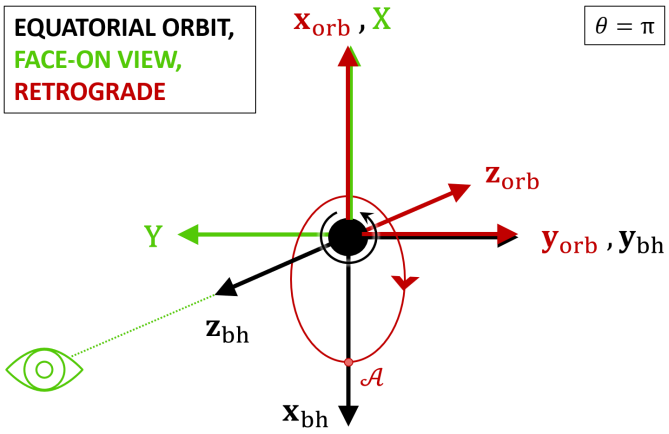

(a) Schematic illustration of the osculating Keplerian orbit (see subsection VII.2.4)

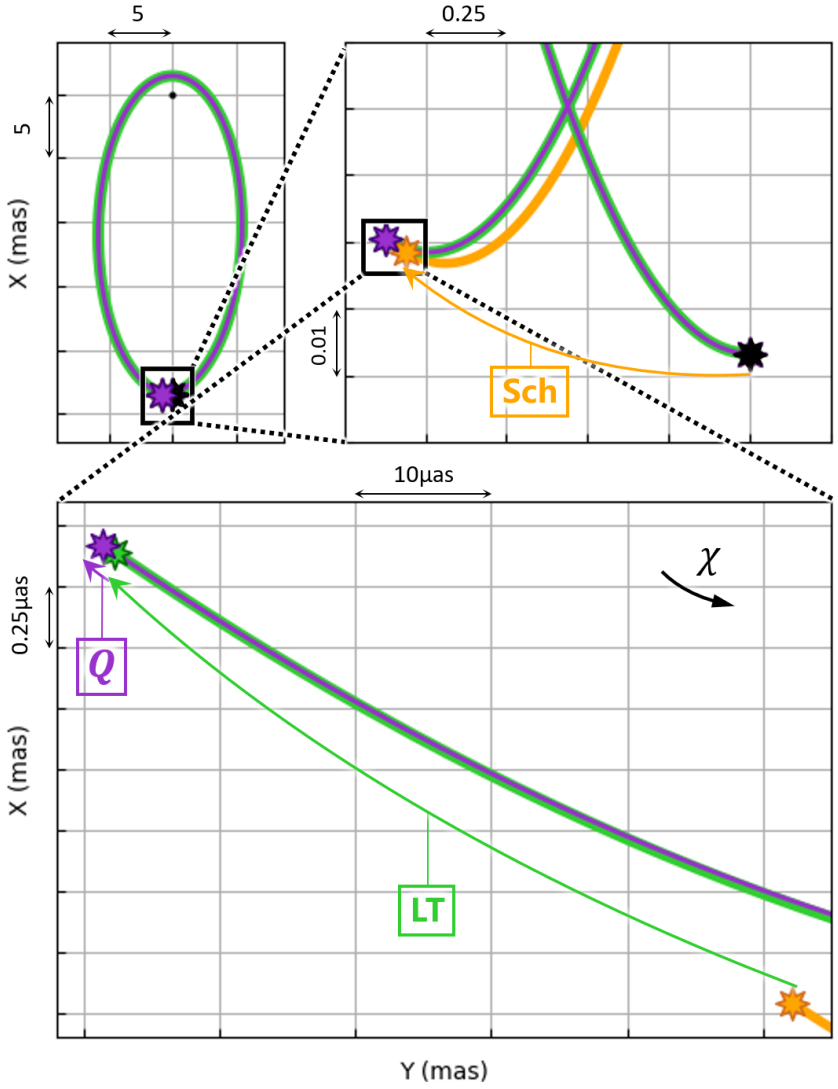

(b) Simulation using the 2PN code

Figure VII.4: Same as Figure VII.3 but for retrograde orbits. We see that both the Lense-Thirring and quadrupole moment effects shift the apocenter clockwise as seen by this face-on observer.

see on Figures VII.3b and VII.4b that the Schwarzschild precession shifts the apocenters of the prograde and retrograde orbits counterclockwise and clockwise, respectively. In simpler words, the simulations agree with Eq. (VII.77) in terms of orientation on the projection plane.

Now, let us examine the Lense-Thirring effect. Figure VII.3b indicates an apocenter shift opposite to the direction of the spin, and the same is observed in Figure VII.4b. Indeed, when looking at Eqs. (VII.78), we see that for the prograde orbit, $\Delta\varpi_{\rm LT}^{\rm pro} < 0$ and $\Delta\varpi_{\rm LT}^{\rm ret} > 0$, meaning that both the prograde and retrograde apocenters will be shifted clockwise, i.e. opposite to the direction of the spin.

Finally, we see in Figures VII.3b and VII.4b that, similarly to the Schwarzschild precession, the quadrupole moment shifts the apocenters in the same direction as the movement of the star in its orbit. Indeed, when looking at Eq. (VII.79), we see that the sign of $\Delta\varpi_Q$ depends only on the value of $\cos^2\theta$ meaning that $\Delta\varpi_Q^{\rm pro} = \Delta\varpi_Q^{\rm ret} > 0$.

Finally, it is important to remember that all these effects do not share the same dominant PN order, and therefore do not act on the same scale. This is very visible in Figures VII.3b and VII.4b where the Schwarzschild precession dominates the Lense-Thirring effect, which in turn dominates the quadrupole moment effect. Also, it is interesting to notice that the total secular shift of orbits in the equatorial plane of a rotating black hole will differ in absolute value in the prograde and retrograde configurations; in the first case the Lense-Thirring and quadrupole moment effects counter each other, whereas in the second case they push the apocenter in the same direction.

If we summarize all the above, we get the following statements illustrated in Figure VII.5:

1. The Schwarzschild precession pushes the apocenter in the same direction as the movement of the star in its orbit.

2. The secular shift due to the Lense-Thirring effect pushes the apocenter of an equatorial orbit in the direction opposite to the black hole's rotation.

3. The secular shift due to the quadrupole moment pushes the apocenter of an equatorial orbit in the same direction as the movement of the star in its orbit.

4. The analytical total Kerr secular shift of equatorial orbits verifies $|\Delta\varpi_{\rm Kerr}^{\rm pro}| < |\Delta\varpi_{\rm Kerr}^{\rm ret}|$.

Lense-Thirring out-of-plane precession

In this section, we choose to illustrate configurations that maximize the dominant spin-induced effect: the Lense–Thirring precession. As suggested in section VII.2.1, to better understand the out-of-plane precession of the Lense-Thirring and quadrupole moment effects, it is useful to split it into two subtypes, precession

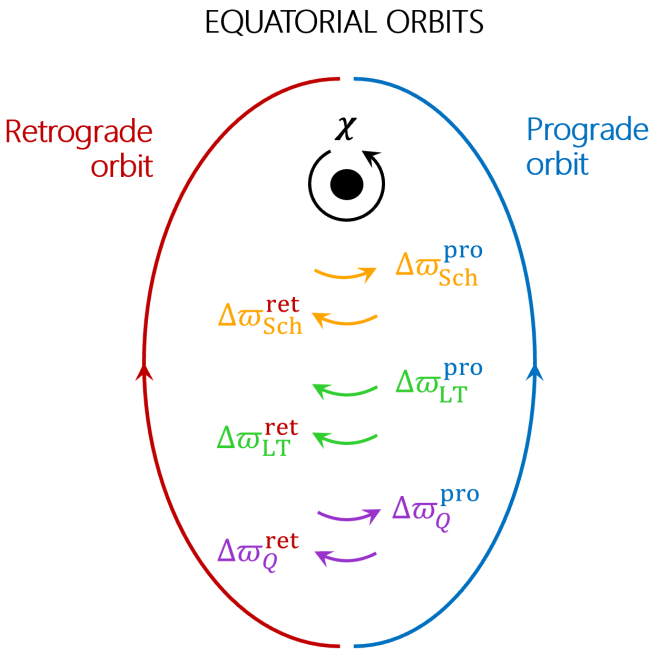

Figure VII.5: Schematic illustration of the secular precessions for a prograde and a retrograde equatorial orbit. We note that Schwarzschild precession and quadrupole moment effect push the apocenter in the direction of stellar motion, and the Lense-Thirring precession pushes against the spin.

around the major axis of the orbit and precession around the minor axis, encoded by Eqs. (VII.73) and (VII.72), respectively. Therefore, we focus on two types of polar orbits, for which the out-of-plane component of this effect is strongest (see subsection VII.2.1):

1. Polar orbit with polar major axis[16]: $\mathbf{z}_{\rm bh}//\mathbf{x}_{\rm orb}$ i.e $(\theta,\psi)=(\pi/2,0)$;
2. Polar orbit with equatorial major axis: $\mathbf{z}_{\rm bh}//\mathbf{y}_{\rm orb}$ i.e $(\theta,\psi)=(\pi/2,\pi/2)$.

In order to visualize the out-of-plane components independently from the projection effects, we perform an edge-on Euclidean projection, and consider that the osculating orbit is a vertical line with the apocenter at the bottom of the projection plane (see Figures VII.6a and VII.7a).

Let us start with the first subtype, illustrated by Figure VII.6, where the orbit lies in the polar plane of the BH and verifies $\mathbf{z}_{\rm bh}//\mathbf{x}_{\rm orb}$. As opposed to the equatorial orbits of subsection VII.2.4, here the notion of prograde and retrograde orbits is more delicate. Polar orbits cannot be categorized as prograde or retrograde relative to the black hole, and an orbit with an edge-on view cannot be categorized as prograde or retrograde relative to the observer. Therefore, we will instead consider an orbit such that the star is moving towards the observer at apocenter (as illustrated in VII.6a).

We saw in subsection VII.2.1, that by having $(\theta,\psi)=(\pi/2,0)$ the Lense-Thirring effect maximally contributes to the out-of-plane precession while not contributing to the in-plane one, and that, interestingly enough, the quadrupole moment has the opposite tendency. We remind that having here $\Delta\varpi_{\rm LT}=0$, $\Delta\Theta_{\rm LT}=0$ and $\Delta\Xi_{\rm LT}\neq 0$ means that, instantaneously, the apocenter will not experience any secular precession due to the Lense-Thirring effect. However, as soon as the apocenter is shifted out of the spin axis due to other effects, the Lense-Thirring effect will start contributing as well to the apocenter displacement. Indeed, in Figure VII.6b, we see that the Lense-Thirring effect consists of an out-of-plane precession that shifts the minor axis in the same direction as the spin of the black hole, gradually turning the orbit plane from being edge-on to face-on, having a counterclockwise rotation in the projection plane. Conversely, the quadrupole moment effect is in-plane and shifts the apocenters in the direction opposite to the movement of the star in its orbit. All this is in agreement with Eqs. (VII.81) to (VII.85).

Now, let us consider the second subtype of out-of-plane precession: the one around the minor axis of the orbit. To study this type of precession we take a polar orbit but this time with its minor axis being along the spin axis of the black hole ($\mathbf{z}_{\rm bh}//\mathbf{y}_{\rm orb}$), as illustrated in Figure VII.7. Since we still have $\theta=\pi/2$ in this configuration, we observe the same tendencies for the evolution of $\Delta\varpi$.

[16]Due to the ever present in-plane precession, the major axis can only instantaneously be polar or equatorial. Here we refer to the osculating state.

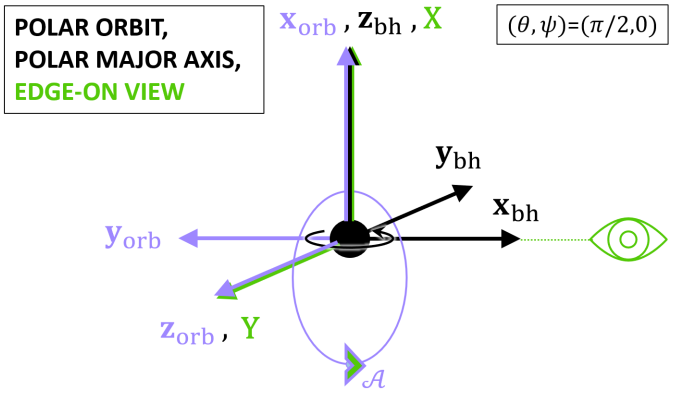

(a) Schematic illustration of the osculating Keplerian orbit (see subsection VII.2.4)

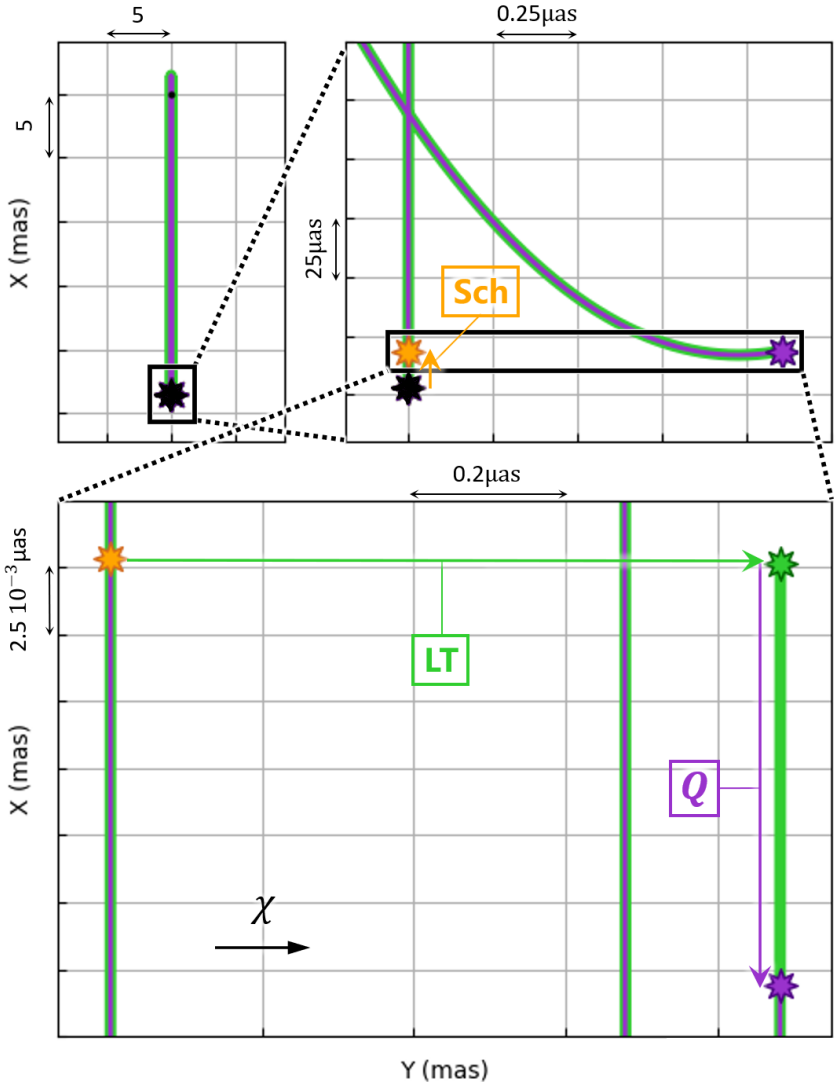

(b) Simulation using the 2PN code

Figure VII.6: Same as Figure VII.3 but with orbits in a polar plane and having a major axis on the spin axis of the black hole. We see that the Lense-Thirring effect shifts the minor axis in the same direction as the the spin of the black hole, gradually shifting the orbit plane from edge-on towards face-on. The quadrupole moment effect shifts the apocenter clockwise as seen on face-on projection of Figure VII.3a.

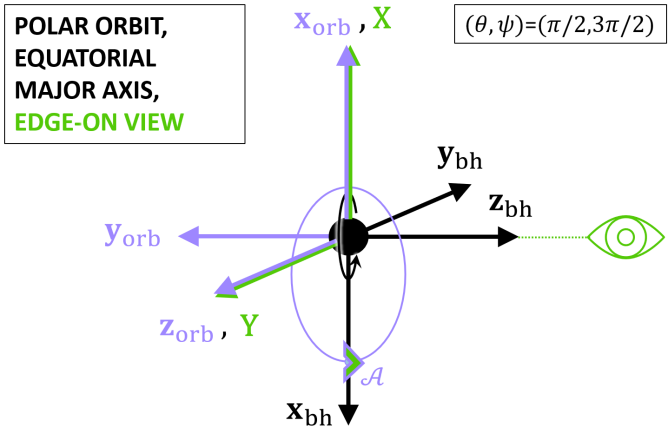

(a) Schematic illustration of the osculating Keplerian orbit (see subsection VII.2.4)

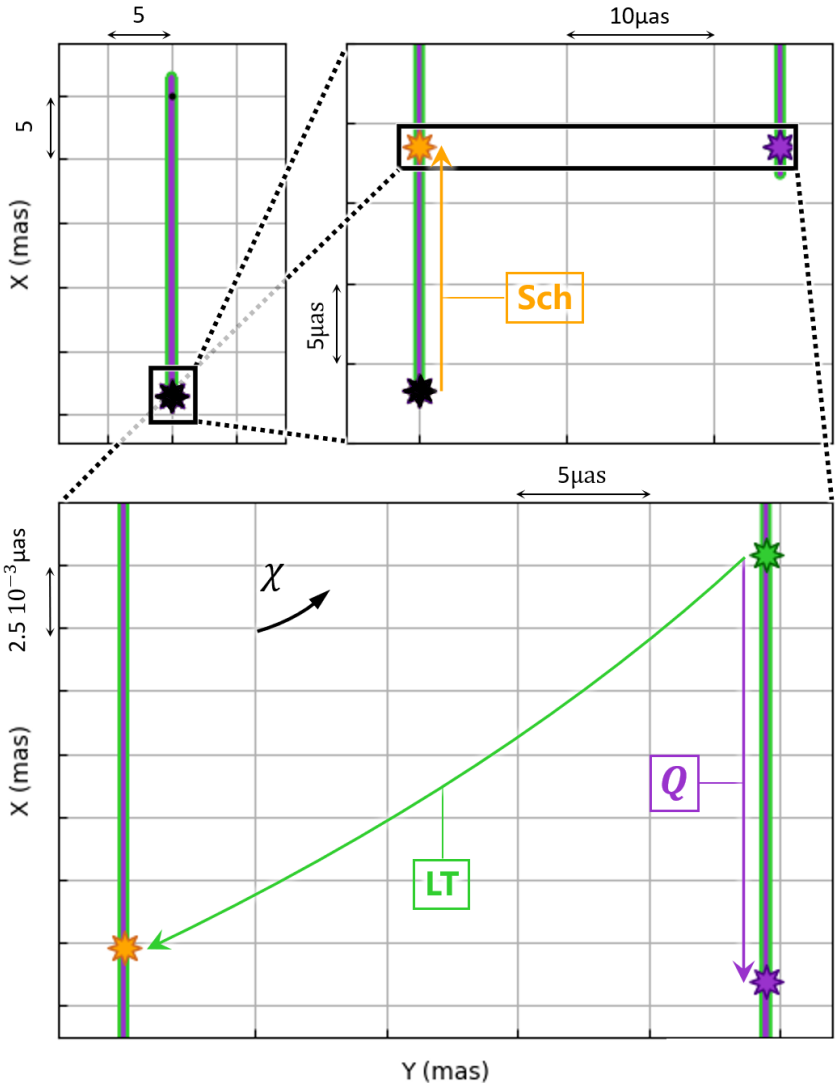

(b) Simulation using the 2PN code

Figure VII.7: Same as Figure VII.3 but with orbits in the polar plane and having a major axis on the equatorial plane of the black hole. We see that the Lense-Thirring effect shifts the apocenter in the counterclockwise direction as seen on this projection. The quadrupole moment effect shifts the apocenter clockwise as seen on the face-on projection of Figure VII.3a.

However, now we have $\psi = \pi/2$, Eqs. (VII.81) and (VII.82) yield $\Delta\Theta \neq 0$ meaning that, as opposed to the previous case, we observe a direct out-of-plane apocenter displacement. Conversely, Eqs. (VII.84) and (VII.85) yield $\Delta\Xi = 0$, which means that there is no precession about the major axis, naturally because the spin is along the minor axis. Indeed, in Figure VII.7b, we see that the Lense-Thirring effect shifts the major axis in the same direction as the spin of the black hole, while keeping the orbit plane edge-on this time. Similarly to the polar orbit with a polar major axis configuration above, the quadrupole moment effect is in-plane and shifts the apocenters in the direction opposite to the movement of the star in its orbit. Once more, all this is in agreement with Eqs. (VII.81) to (VII.85).

Finally, we present in Appendix A the study of "mid-inclined orbits", that maximize the out-of-plane precession of the quadrupole moment. We now have insight into the different types of precession that can manifest around a rotating black hole and comprehend how a random relative orientation between the orbit and black hole can be decomposed into these precession categories. With this new understanding, one can have a better intuition over the possible black hole orientations that can generate the secular precessions that we observe on the orbits of currently, and potential closer-in stars.

All this shows that, while in principle a single randomly oriented orbit contains signatures of all relativistic effects, the relative contributions are often entangled. Observing orbits with diverse orientations provides complementary information and helps to disentangle the in-plane and out-of-plane precession components.

Chapter VIII

Detecting the spin parameters using multiple S stars

Contents

VIII.1 Fitting the spin orientation 152

VIII.1.1 Special orientations for sky-projected apocenter shifts 154

VIII.1.2 Curve-fitting the spin angles using a single star at a time . . 157

VIII.1.3 Multi-star fitting of the spin angles 159

VIII.1.4 Exploring three-dimensional spin parameter space 160

VIII.2 Detectability of the spin parameters using multi-star fitting 163

VIII.2.1 Only fitting the spin magnitude 163

VIII.2.2 Fitting all spin parameters 170

In this chapter, I investigate how combining the astrometric and spectroscopic data of multiple S stars can improve the constraints on the spin magnitude and orientation of the supermassive black hole Sgr A*. We will see that the star S301, recently discovered by the GRAVITY consortium (paper to be published), has a potential to constrain the spin related effects comparable to S2/10. While such a star will certainly lead the detectability of the spin parameters, it is still interesting to explore whether jointly fitting the orbits of the currently known S

stars, which have diverse orbital orientations, with S301 can mitigate the strong parameter degeneracies and reduce the observational time required to constrain the spin parameters.

In this chapter, we adopt the 2PN framework for orbit generation and fitting. While full GR ray tracing (`GR_rt`) is required to model effects such as gravitational lensing with the accuracy needed for real observational data VI.1.3, the 2PN approximation is fully sufficient for the present purpose. The reason is twofold: first, the goal here is not to reproduce every subtle effect in detail, but rather to validate and showcase the methodology of multi-star combined fitting; second, 2PN offers a much lighter computational cost, allowing us to explore a wide parameter space and test the robustness of our approach. The methodology itself is general, and when applied to real data it will be straightforward to replace the 2PN code with the full GR ray-traced one.

VIII.1 Fitting the spin orientation

The spin direction may help to reveal the assembly history of SgrA*, which can be understood as follows. If the supermassive black hole spun up by continuous disk accretion with the same orientation as that of the young stellar disk at the galactic center, the spin direction should align with the normal of the disk; and if the supermassive black hole grew up via many episodes of disk accretion with random orientations, then the spin value may be small and the spin direction may be significantly different from that of the normal of the young stellar disk (as inferred from [86]).

Although monitoring stars closer-in stars such as S301, which are much more sensitive to spin-induced relativistic effects, would immensely improve the constraints on the spin parameters, a complementary approach could be useful for reducing the degeneracies between parameters. By fitting the orbits of several currently known S stars simultaneously, one can exploit the diversity of their orbital inclinations and orientations to constrain both the spin magnitude and its direction. Figure VIII.1 illustrates the orbits of some of the closest-in known S-stars. Since each star experiences distinct secular precessions depending on its geometry relative to the spin axis, their combined data can significantly improve the precision and robustness of spin measurements.

This multi-star fitting strategy thus has the potential to complement the use of a future detected closer-in star, enhancing the detectability of spin- and quadrupole-induced effects. In the following sections, I present the mock data construction, fitting procedure, and results for both single-star and multi-star analyses.

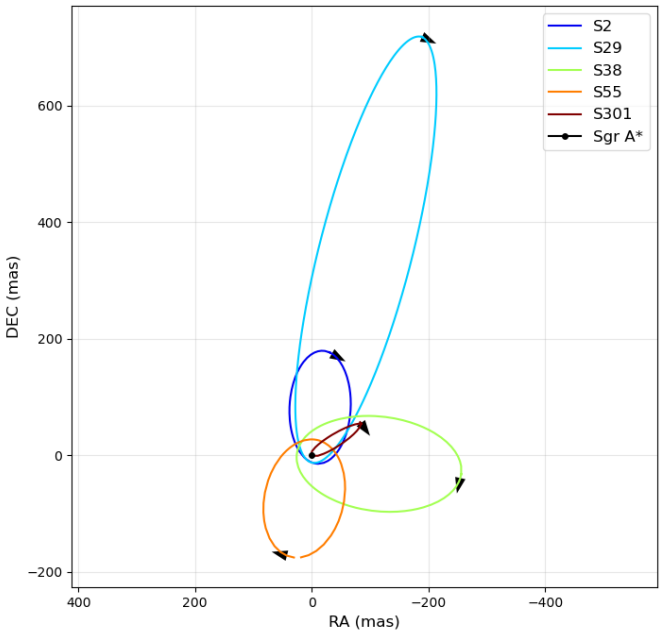

Figure VIII.1: Orbits of some of the closest S stars.

Table VIII.1: Best-fit orbital parameters for stars S2, S29, S38, and S55 from [57]. I also add the best estimates of the orbital parameters of the very promising recently discovered star S301, recently discovered by the GRAVITY consortium (paper to be published). Note, however, that these estimates are a work in progress and would likely change in the course of the following years. Semi-latus rectum values are added using $p = a_{\rm sma}(1 - e^2)$.

Parameter	**S2**	**S29**	**S38**	**S55**	**S301**
e	0.88444	0.96880	0.81807	0.72980	0.98418
1σ error	6×10^{-5}	9×10^{-5}	0.00022	0.00018	0.00184
ι [°]	134.67	144.24	168.69	159.59	127.79
1σ error	0.02	0.09	0.19	0.17	1.17
ω [°]	66.279	203.68	40.065	327.77	289.47
1σ error	0.029	0.17	1.118	0.930	3.57
Ω [°]	228.21	4.9259	122.43	319.43	64.538
1σ error	0.03	0.159	1.12	0.97	5.621
P [yr]	16.032	88.47	19.804	12.374	7.6774
1σ error	0.021	0.32	0.0007	0.006	0.3979
t_p [yr]	2018.3789	2021.4102	2022.6843	2009.4738	2023.1531
1σ error	0.0001	10^{-4}	8×10^{-4}	0.0076	0.0123
p [mas]	27.225	23.972	47.130	48.721	2.3994
1σ error	0.030	0.094	0.040	0.03	0.289

Among all the published S stars, four of them have small enough semi latus rectum to become useful to some extent in the study of the Lense-Thirring effect: S2, S29, S38, and S55. I take the orbital parameters of [57] and present them in table VIII.1. In addition to these four stars, I also want to consider the very promising recently discovered star S301, even though its parameters are still a work in progress and would likely change in the course of the following years. These parameters should be interpreted as orbital osculating parameters[1] with an osculating time close to the apocenter time $t_{\rm osc} = t_{\rm peri} - P/2$. For $t_{\rm peri}$, we take the most recent time of pericenter passage before the first observation date of each star [see table D.1 of 58, for the first observation dates].

In the following analysis, I use $M_\bullet = (4.2996 \pm 0.0118) \times 10^6\ M_\odot$ and $R_0 = 8275.9 \pm 8.6$ pc from [57]. For simplicity, I assume the position and velocity of Sgr A* in the AO imaging/spectroscopic reference frame to be zero. All subsequent calculations are performed using the 2PN model implemented in `OOGRE` in harmonic coordinates.

VIII.1.1 Special orientations for sky-projected apocenter shifts

I have defined in Figure IV.5 the orientation of $\mathbf{z}_{\rm bh}$ in the orbit frame by introducing the angles (θ, β), which are thus specific to a single star that we use as reference. These angles are very useful for simplifying the computations of the quantities appearing in Lagrange planetary equations. Alternatively, $(i_\bullet, \Omega_\bullet)$ defined in Figure IV.4 allow us to characterize the orientation of the black hole with respect to the observer. This is particularly useful in the case of using multiple stars to constrain the spin and its orientation, whereas defining the latter with respect to the orbit of one single star instead of the sky is unpractical. In this section the goal is to use the results of section VII.2 to estimate the orientations of the black hole that maximizes and minimizes the flat spacetime sky projection of the total secular shifts due to the spin-related effects. I will then use these three sets of $(i_\bullet, \Omega_\bullet)$ to study the configurations that yield a maximal, intermediate and minimal astrometric spin effect in section VIII.2. Considering that the precession of the major axis is what will drive the detectability of the spin parameters (and not that of the minor axis), I will focus on the projected total apocenter secular shifts (flat[2] projections of the vector going from one apocenter to the next). Therefore, in this subsection I first present the impact of the observer's position when using flat spacetime projections. Second, I estimate the values of (θ, β) (and their $(i_\bullet, \Omega_\bullet)$ counterparts) that produce a maximal, intermediate, and minimal projected total

[1] For result reproducibility, we take Harmonic and KerrKS coordinates when using the PN and GR models, respectively.

[2] At apocenter the effect of ray-tracing is around or below the detectability limit as displayed in Figure VI.3 for S2/10 which allows us make flat projections in this region of the orbit.

secular apocenter shift. I do not consider ray-tracing in the estimation of these characteristic spin orientations considering that the objective is only to get close to these special configurations when generating the results of section VIII.2.

Impact of the observer's position when using flat spacetime projections

Previously, when considering face-on and edge-on flat-space-time projections in subsection VII.2.4, I was trying to ignore the contribution of the projection effects by making the inclination take specific values[3] that practically cancel the impact of the sky projection.

When considering a nonspecific observer, however, the observed precessions will be reduced compared to the raw shifts, because the orbit must be projected onto the plane of a non specific sky.

I know that any vector $\mathbf{V}$ can be projected onto the sky plane $(\mathbf{X}, \mathbf{Y})$ as:

$$\mathbf{V}^{\perp} = (\mathbf{V}.\mathbf{X})\mathbf{X} + (\mathbf{V}.\mathbf{Y})\mathbf{Y} \tag{VIII.1}$$
$$= \mathbf{V} - (\mathbf{V}.\mathbf{Z})\mathbf{Z} \tag{VIII.2}$$
$$= \mathbf{Z} \times \mathbf{V} \times \mathbf{Z}. \tag{VIII.3}$$

Considering Eqs. (VII.68), (VII.74) and (VII.75), I can write any in-plane apocenter displacement vector as $\mathbf{V}_{\rm in} = V_{\rm in}\ \mathbf{y}_{\rm orb}$, and any out-of-plane apocenter displacement vector as $\mathbf{V}_{\rm out} = -V_{\rm out}\ \mathbf{z}_{\rm orb}$, with $V_{\rm in} = 2r_{\rm apo}\sin(\Delta\varpi/2)$, $V_{\rm out} = 2r_{\rm apo}\sin(\Delta\Theta/2)$ and $r_{\rm apo} = p/(1-e)$. Then I project these vectors onto the sky plane as:

$$\mathbf{V}_{\rm in//sky} = \mathbf{Z} \times \mathbf{V}_{\rm in} \times \mathbf{Z} = V_{\rm in}(\mathbf{y}_{\rm orb} - (\mathbf{y}_{\rm orb} \cdot \mathbf{Z})\mathbf{Z}) = V_{\rm in}(\mathbf{y}_{\rm orb} - \cos\omega \sin\iota \mathbf{Z}), \tag{VIII.4}$$

$$\mathbf{V}_{\rm out//sky} = \mathbf{Z} \times \mathbf{V}_{\rm out} \times \mathbf{Z} = -V_{\rm out}(\mathbf{z}_{\rm orb} - (\mathbf{z}_{\rm orb} \cdot \mathbf{Z})\mathbf{Z}) = -V_{\rm out}(\mathbf{z}_{\rm orb} - \cos\iota \mathbf{Z}). \tag{VIII.5}$$

This leads to a rescaling of in-plane shifts by a factor:

$$\frac{||\mathbf{V}_{\rm in//sky}||}{V_{\rm in}} = \sqrt{1 - (\cos\omega \sin\iota)^2}, \tag{VIII.6}$$

and out-of-plane shifts by a factor:

$$\frac{||\mathbf{V}_{\rm out//sky}||}{V_{\rm out}} = \sin\iota. \tag{VIII.7}$$

This means that, if the observer has a face-on and edge-on views of the osculating orbit, we will have no projection factor for the in-plane ($||\mathbf{V}_{\rm in//sky}|| = V_{\rm in}$) and out-of plane ($||\mathbf{V}_{\rm out//sky}|| = V_{\rm out}$) apocenter displacement vectors, respectively. This is why I was allowed to ignore the projection effects when studying the out-of-plane precession in subsection VII.2.4.

[3] Namely $\iota = 0 \pmod{\pi}$ for the face-on projection and $\iota = \pi/2 \pmod{\pi}$ for the edge-on ones.

Estimation of the characteristic spin orientation

To guide the selection of black hole spin orientations that lead to a maximal, minimal, or intermediate[4] projected total apocenter shift on the sky, I summarize in Table VIII.2 the results of a detailed analytical study presented in Appendix B. This analysis is based on the explicit expressions above for the sky-projected Lense-Thirring and quadrupole-induced shifts, derived as functions of the spin orientation angles. For each effect, I identify the orientations $(i_\bullet, \Omega_\bullet)$ that yield extremal or intermediate values of the projected total apocenter shift

$$V_{\mathrm{LT}//\mathrm{sky}} = \sqrt{\left(V_{\mathrm{in}//\mathrm{sky}}|_{\mathrm{LT}}\right)^2 + \left(V_{\mathrm{out}//\mathrm{sky}}|_{\mathrm{LT}}\right)^2}. \tag{VIII.8}$$

The tables display the most generic and commonly occurring cases, which depend on the relative magnitudes of two dimensionless coefficients, $C_1 = 1 - (\cos\omega \sin\iota)^2$ and $C_2 = \sin^2\iota$, that encode the geometry of the observer's position. These configurations are representative of the typical parameter regimes relevant to currently known S stars. However, for completeness, the appendix includes a thorough derivation and discussion of rarer configurations. In subsection VIII.2.1 we illustrate the $V_{\mathrm{LT}//\mathrm{sky}}$ profile of S301 and display an example of these characteristic orientations (see Figure VIII.6).

Table VIII.2: Examples of spin orientations $(i_\bullet, \Omega_\bullet)$ that extremize or yield an intermediate projected apocenter shift $\Delta\Lambda_{\mathrm{LT}//\mathrm{sky}}$. Here, $C_1 = 1 - (\cos\omega \sin\iota)^2$ and $C_2 = \sin^2\iota$.

Shift Type	**Orientation** $(i_\bullet, \Omega_\bullet)$	**Description**
Maximal	$\left(\iota,\ \Omega - \frac{\pi}{2}\right)$	Equatorial orbit. Dominated by in-plane precession. Occurs when $4C_1 > C_2$.
Minimal	$(\arccos(\sin\iota \sin\omega),$ $\Omega + \mathrm{atan2}(\cos\iota \sin\omega,\ \cos\omega))$	Polar orbit with a polar major axis. Always corresponds to minimum LT shift.
Intermediate	$\left(\arccos\left(\frac{\cos\iota + \sin\iota \sin\omega}{\sqrt{2}}\right),\right.$ $\left.\Omega + \mathrm{atan2}(\sin\omega\cos\iota - \sin\iota,\ \cos\omega)\right)$	Intermediate spin inclination with projection of the spin axis on the orbit parallel to the major axis. Occurs when $2C_1 > C_2$.

[4]The intermediate configuration is defined as the one producing average of the minimal and maximal total apocenter shift projected on the sky

VIII.1.2 Curve-fitting the spin angles using a single star at a time

I first perform an analysis using each star individually, following a procedure similar to that described in Section VI.2.1. Mock data sets for the stars S2, S29, S38, and S55 are generated between 2016.81 (the first light of the GRAVITY instrument) and 2060. I also generate an extra mock dataset for S301, this time from 2023.5 to 2033.5. The temporal sampling strategy is designed to emulate realistic observational cadences: during each pericenter passage, I simulate two observations per night over a one-week window, then one observation per month over six months, and finally one observation every four months for the remainder of the orbit. Also, to take into account the fact that the galactic center is only observable from early March to late September from Paranal (location of the VLTI in Chile), I remove all dates outside this period.

In this section, I assume the spin parameters of Sgr A* to be $(\chi, i_\bullet, \Omega_\bullet) = (0.9, 25°, 80°)$, motivated by the upper limit on the inclination $i_\bullet \lesssim 30°$ suggested by [37] and by the expectation that the black hole spin is high. The choice of $\Omega_\bullet$, however, is arbitrary and does not impact the conclusions of this subsection. Gaussian noise with standard deviations of $\sigma_A = 30$ μas in astrometry and $\sigma_{RV} = 20$ km/s in radial velocity is added to simulate measurement errors by GRAVITY+ and ERIS.

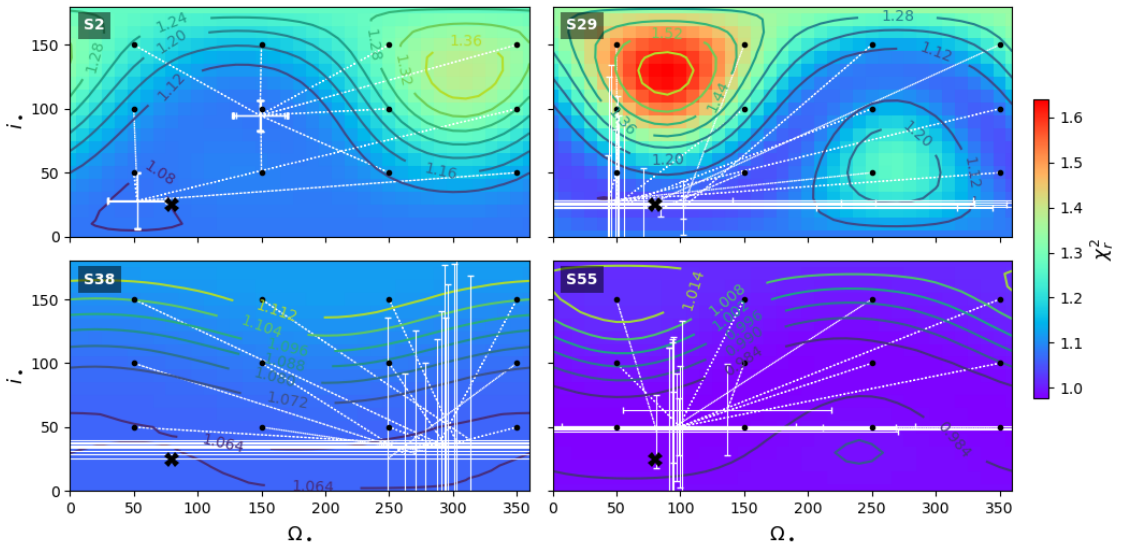

Figure VIII.2: Map of $\chi^2_{\rm r}$ in 2PN with $(\sigma_A, \sigma_{RV}) = (30\,\mu{\rm as}, 20\,{\rm km/s})$ from 2016.81 to 2060 and $(\chi, i_\bullet, \Omega_\bullet) = (0.9, 25°, 80°)$ using exact first guesses for all parameters except $i_\bullet$ and $\Omega_\bullet$. The orientation used in the mock data is represented by the symbol "✖". I also add curve-fits represented by white dotted lines starting from twelve spin orientations (black dots) and ending with error bars around the best-fit values.

For each star, I split the parameter space of $i_\bullet$ and $\Omega_\bullet$ into 10° wide cells (19 values for $i_\bullet$ and 37 values for $\Omega_\bullet$) to fit the mock data by scanning this grid of $19 \times 37 = 703$ combinations of $(i_\bullet, \Omega_\bullet)$ while keeping all other parameters fixed to their exact values given in Table VIII.1. This produces a map of the reduced χ^2, denoted $\chi^2_{\rm r}$, across the $(i_\bullet, \Omega_\bullet)$ plane. Figure VIII.2 displays these maps, revealing characteristic degeneracy patterns between $i_\bullet$ and $\Omega_\bullet$. As expected, the rows corresponding to $i_\bullet = 0°$ and $i_\bullet = 180°$, which correspond to face-on spins, exhibit no dependence on $\Omega_\bullet$, since the projection of the spin vector onto the sky is zero in these configurations, making $\Omega_\bullet$ degenerate and physically meaningless. Conversely, the row at $i_\bullet = 90°$ (edge-on spins) shows maximum variability in χ^2 with $\Omega_\bullet$, indicating that in this configuration the effect of $\Omega_\bullet$ is most pronounced.

To further explore how the fitting converges starting from different initial guesses, I select twelve starting points on the $(i_\bullet, \Omega_\bullet)$ grid, chosen to span $i_\bullet \in \{50°, 100°, 150°\}$ and $\Omega_\bullet \in \{50°, 150°, 250°, 350°\}$. Each of these is used as an initial guess for a full fit, allowing the optimizer to adjust $i_\bullet$ and $\Omega_\bullet$ while keeping all other parameters fixed. The arrows in Figure VIII.2 indicate the evolution from each initial guess to the corresponding best-fit solution. The size of the error bars around the final points provides a measure of the uncertainty at the best-fit. In the case of S2 (Top left of Figure VIII.2), the final uncertainties on $i_\bullet$ and $\Omega_\bullet$ are on the order of $\sim 10°$ each. For S29 and S55, the uncertainties are much larger, and the degeneracy between $i_\bullet$ and $\Omega_\bullet$ becomes more pronounced, and the error bars grow significantly for S38. This is due to the fact that it has one of the highest semi-latus rectum and periods among the selected stars (see Table VIII.1 and discussion of subsection VII.2.2). Moreover, the contrast in $\chi^2_{\rm r}$ becomes too low to reliably distinguish the global minimum from local minima, rendering S38 and S55 unsuitable for constraining the spin orientation when used individually on human timescales. This illustrates how the detectability of spin parameters depends strongly on the individual star's orbital geometry relative to the spin axis of the black hole. Nevertheless, we see that $\chi^2_{\rm r}$ distribution varies a lot depending on the star, especially when comparing the patterns of S2 and S29, considering their different orientations. This indicates that by combining the data of these different stars together, we can potentially lower the level of degeneracy between $i_\bullet$ and $\Omega_\bullet$. However, it is important to stress that at this level of contrast ($\chi^2_{\rm r}$ between 1 and 1.7) it will be extremely difficult to constrain the spin parameters.

Interestingly, the recently discovered star S301 (Figure VIII.3) shows a much sharper contrast in $\chi^2_{\rm r}$, with a difference of over one order of magnitude between the maximal and minimum $\chi^2_{\rm r}$ values. Indeed, when we look at the $\chi^2_{\rm r}$ values of the minima where the twelve first guesses converge, we notice that, the values are less comparable, as opposed to earlier when the values were nearly identical. Here with S301 we identify four local minima at various values of $(\Omega_\bullet, i_\bullet)$: on the middle left at $(36°, 83°)$ with $\chi^2_{\rm r} = 5.04$, on the lower right at $(274°, 59°)$ with $\chi^2_{\rm r} = 3.17$, and on the middle right at $(308°, 108°)$ with $\chi^2_{\rm r} = 1.68$. The global minimum on

the lower left at $(\Omega_\bullet, i_\bullet) = (81.08 \pm 2.03°, 25.56 \pm 0.70°)$ with $\chi^2_r = 0.92 \pm 0.12$, is in agreement with the true value. This dramatically improves the ability to detect the global minimum with tighter error bars (units to fractions of degrees as illustrated in Figure VIII.3). I caution, however, that these results should be regarded as indicative, since the orbital elements of S301 remain under refinement as more data become available.

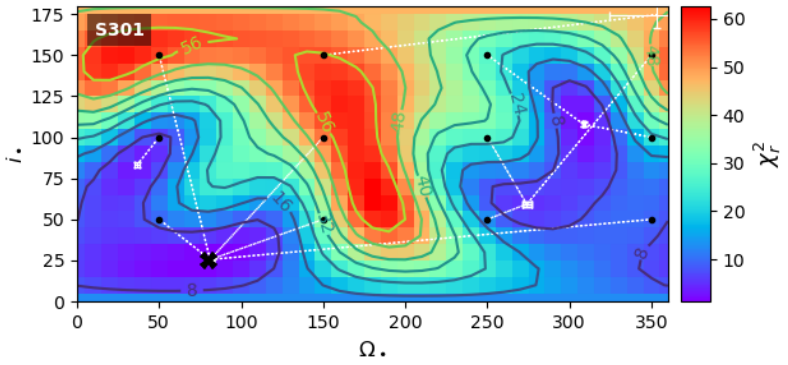

Figure VIII.3: Same as Figure VIII.2, but using the recently discovered star S301, with dates from 2023.5 to 2033.5.

VIII.1.3 Multi-star fitting of the spin angles

Having assessed the potential of each star individually, I now combine the data from multiple stars to fit the spin orientation parameters jointly. This approach takes advantage of the complementary orbital geometries of the stars, as each experiences different secular precessions depending on its inclination and node relative to the spin axis. By combining their data, one can partially break degeneracies and achieve tighter constraints.

Figure VIII.4 shows the results of multi-star fits. On the left, fitting S2, S29, S38 and S55 together shows that, when comparing to Figure VIII.2, the χ^2_r pattern is dominated by the contribution of S2 and S29 as expected. The error bars of $\Omega_\bullet$ and $i_\bullet$ shrink by 21% and 50% on average, respectively, compared to the single-star fits of S2 in Figure VIII.2. This suggests that the complementary orientations of S2 and S29 enhance the robustness of the solution. Finally, I include S301 along with S2, S29, S38, and S55 in the fit (right of Figure VIII.4), and see that the contrast distribution of the χ^2 map is completely dominated by the contribution of S301 considering the similarities with Figure VIII.3, confirming its primary role in constraining the spin parameters. The inclusion of S301 significantly improves the convergence to the true orientation as well as the error bars, despite the reduced

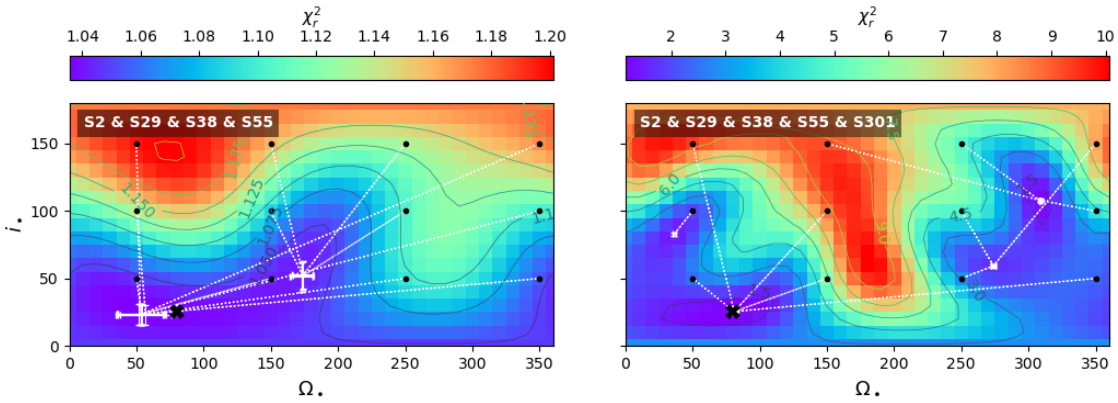

Figure VIII.4: Same as Figure VIII.2 but fitting the data of multiple stars at once. Left: We fit the data of S2, S29, S38 and S55 from 2016.81 to 2060. Right: the integration time is done from 2016.81 to 2033.5 for S2, S29, S38 and S55, and from 2023.5 to 2033.5 for S301. The color map is different for each subfigure.

integration time that I imposed (integration until 2033.2 for all stars instead of 2060). As for the comparaison to Figure VIII.3, we see that here the error bars of $\Omega_\bullet$ and $i_\bullet$ shrink by 11% and 24% on average, respectively, compared to the single-star fits of S301, a more modest improvement.

VIII.1.4 Exploring three-dimensional spin parameter space

I also explore the full three-dimensional spin parameter space $(\chi, i_\bullet, \Omega_\bullet)$ by constructing χ^2_r cubes, sampled at three different spin magnitude values ($\chi \in \{0.1, 0.5, 0.9\}$). Figure VIII.5 displays 2D slices of these cubes. As expected, at low spin magnitudes, the χ^2_r surface is relatively homogeneous. This reflects the fact that the spin orientation has little physical impact when the spin magnitude is small: in the limit $\chi \to 0$, the notion of spin orientation loses any physical meaning, and it is therefore natural that its influence gradually increases with the spin magnitude. At higher spin magnitude values, the χ^2_r surface develops pronounced minima that are sensitive to the orientation parameters.

I again test the convergence of twelve initial guesses per slice, allowing the optimizer to adjust all three parameters simultaneously. As shown in Figure VIII.5a, introducing the spin magnitude as a free parameter increases the degeneracy between the free parameters, and only one of the initial guesses converges to the correct solution within 1σ when using the data of S2, S29, S38 and S55 from 2016.81 to 2060. The results also depend more strongly on the random seeds used for the mock noise, highlighting the challenges of measuring all three spin parameters jointly with this set of data.

However, when S301 is included (Figures VIII.5b and VIII.5c), the χ^2_r contrast improves dramatically even over a shorter integration period (2023.5–2033.5 for S301 and 2016.81-2033.5 for other stars), allowing more than one initial guess to converge and the error bars to tighten further, especially when the data of S2, S29, S38 and S55 are added onto those of S301 in Figure VIII.5c. This emphasizes the unique importance of S301 in breaking the degeneracy between spin magnitude and orientation, and suggests that future observational campaigns focused on S301 could significantly enhance our ability to constrain the spin parameters.

In summary, I have examined the ability of currently known and the recently discovered S-star called S301 to constrain the spin parameters of Sgr A*. Individually, S2 and S29 provide the most robust constraints among the well established S-stars, though still subject to significant degeneracies. S38 and S55 are less effective due to their wider orbits. The inclusion of S301 remarkably improves the sensitivity and helps break the degeneracies between spin magnitude and orientation. Combining S301 with S2, S29, S38 and S55 in a multi-star fit provides the best performance, demonstrating the power of multi-star strategies in probing the strong-field relativistic regime.

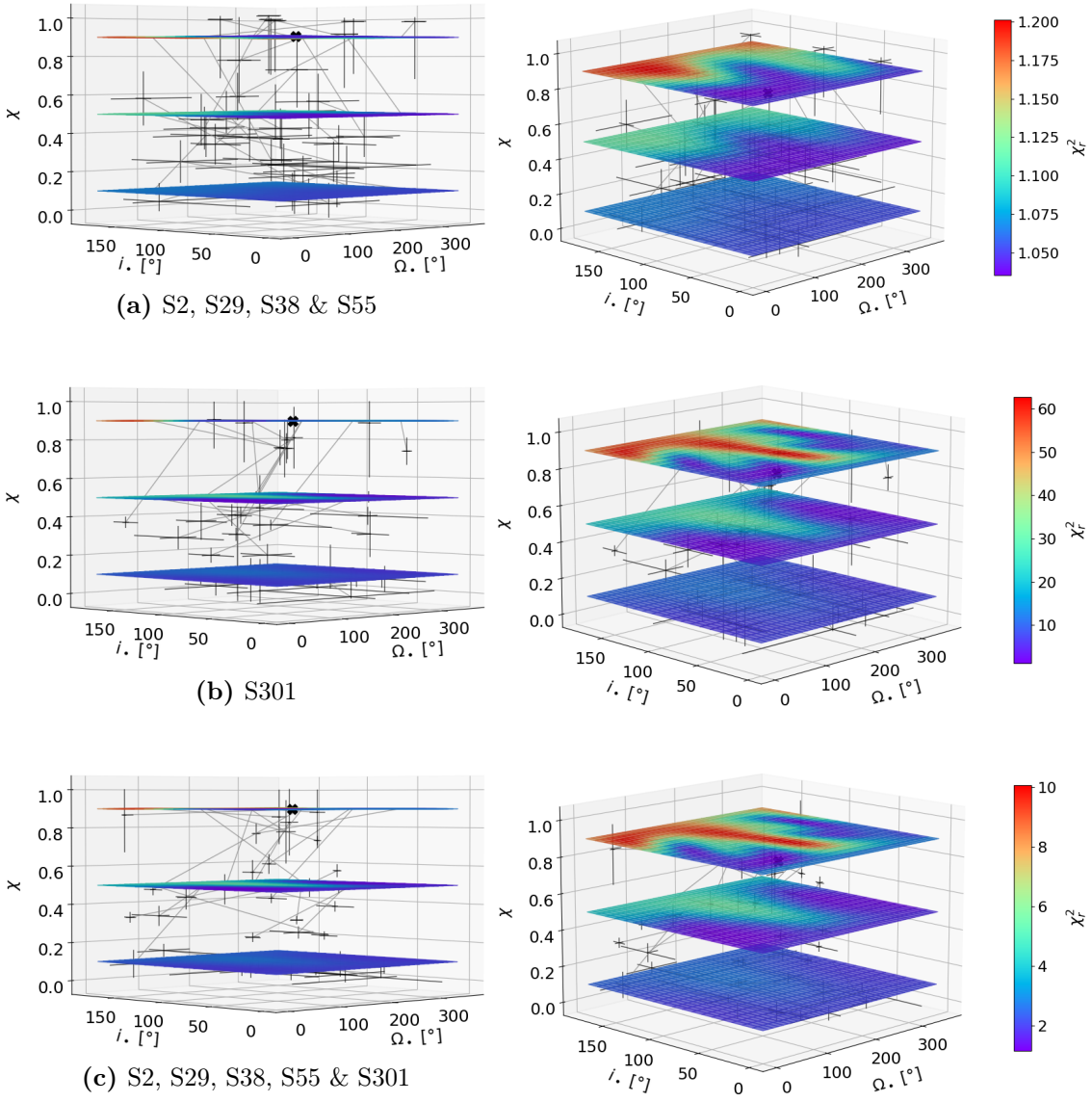

(a) S2, S29, S38 & S55

(b) S301

(c) S2, S29, S38, S55 & S301

Figure VIII.5: Same as Figure VIII.4 but with an added dimension corresponding to the spin magnitude. We display three slices corresponding to χ^2_r map with 0.1, 0.5 and 0.9 as first guesses for the spin. We take $(\chi, i_\bullet, \Omega_\bullet) = (0.9, 25°, 80°)$ for the mock data, and use exact first guesses for all parameters except χ, $i_\bullet$ and $\Omega_\bullet$ for the twelve curvefits per slice.

VIII.2 Detectability of the spin parameters using multi-star fitting

Let us use the multi-fit code and its cube method presented in subsection VIII.1.4 using the stars S2, S29, S38, S55 and S301 to assess the detectability of the spin parameters of Sgr A*.

VIII.2.1 Only fitting the spin magnitude

I want to determine the observing time windows needed to detect the spin magnitude depending on the true spin parameters used in the mock data and the different parameters that I free during the fitting. When simulating the mock data, I arbitrarily take three spin orientations from Table VIII.2, one producing a maximal, one producing an intermediate, and one producing a minimal total Lense-Thirring secular apocenter shift of S301, and three spin magnitudes for each orientation. I can use S301 alone for the determination of these characteristic orientations considering that it leads the detection of the spin magnitude as demonstrated in Figure VIII.4. These characteristic orientations are displayed along with the total projected apocenter displacement vector profile in Figure VIII.6.

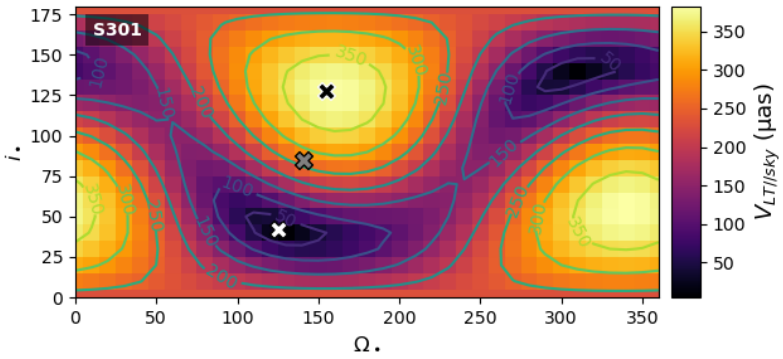

Figure VIII.6: Total projected apocenter displacement vector profile after one orbit of S301. The characteristic configurations used in this section are also displayed using black, gray, and white crosses for the ideal, intermediate, and least ideal black hole orientations, respectively.

According to it and to subsection VIII.1.1, the orientation of the black hole that maximizes the total secular apocenter shift on sky is such that the S301 is in the equatorial plane of the black hole. In terms of $i_\bullet$ and $\Omega_\bullet$, I arbitrarily choose the prograde configuration with respect to the black hole as the true values used

in the mock data:

$$(i_\bullet, \Omega_\bullet) = (\iota_{\mathrm{S301}}, \Omega_{\mathrm{S301}} + \pi/2) \approx (128^\circ, 155^\circ)$$

In Figure VIII.7 I illustrate the evolution of the best-fit value of the spin magnitude as a function of the end year of the observation campaign. The data start at 2023.5 for S301 and at 2016.81 for S2, S29, S38, and S55. I fit three sets of mock data, all using $(i_\bullet, \Omega_\bullet) = (128^\circ, 155^\circ)$, the ideal spin orientation, maximizing the astrometric Lense-Thirring apocenter shift. One set uses $\chi = 0.99$ (bottom row of VIII.7), one set uses $\chi = 0.5$ (middle row of VIII.7), and the last one uses $\chi = 0.1$ (top row of VIII.7) as a spin magnitude value. All parameters are fixed at their exact values except the spin magnitude which is fitted starting with three initial guesses $\chi \in \{0.1, 0.5, 0.9\}$.

To represent an intermediate LT apocenter shift, I take a mid-inclined orbit, such that the projection of the spin axis of Sgr A* on the orbit is parallel to the major axis of S301, as explained in subsection VIII.1.1. This corresponds to many orientations, I arbitrarily choose the configuration where the spin axis is halfway between $\mathbf{x}_{\mathrm{orb}}$ and $\mathbf{z}_{\mathrm{orb}}$:

$$\begin{aligned}(i_\bullet, \Omega_\bullet) = \Bigg(&\arccos\left(\frac{\cos\iota_{\mathrm{S301}} + \sin\iota_{\mathrm{S301}}\,\sin\omega_{\mathrm{S301}}}{\sqrt{2}}\right), \\ &\Omega_{\mathrm{S301}} + \mathrm{atan2}\left(\sin\omega_{\mathrm{S301}}\cos\iota_{\mathrm{S301}} - \sin\iota_{\mathrm{S301}},\ \cos\omega_{\mathrm{S301}}\right)\Bigg) \\ \approx\ &(85^\circ, 141^\circ)\end{aligned}$$

Figure VIII.8 also illustrates the evolution of the best-fit value of the spin magnitude as a function of the end year of the observation campaign, but this time when fitting three sets of mock data, all using $(i_\bullet, \Omega_\bullet) = (85^\circ, 141^\circ)$, the spin orientation that produces an intermediate astrometric Lense-Thirring apocenter shift. One set uses $\chi = 0.99$ (bottom row of VIII.8), one set uses $\chi = 0.5$ (middle row of VIII.8), and the last one uses $\chi = 0.1$ (top row of VIII.8) as a spin magnitude value.

To represent a minimal LT apocenter shift, I take a polar orbit, such that the major axis of S301 is along the spin axis of Sgr A*, as detailed in subsection VIII.1.1. I arbitrarily choose:

$$\begin{aligned}(i_\bullet, \Omega_\bullet) &= \left(\arccos\left(\sin\iota_{\mathrm{S301}}\,\sin\omega_{\mathrm{S301}}\right),\ \Omega_{\mathrm{S301}} + \mathrm{atan2}\left(\cos\iota_{\mathrm{S301}}\,\sin\omega_{\mathrm{S301}},\ \cos\omega_{\mathrm{S301}}\right)\right) \\ &\approx (42^\circ, 125^\circ)\end{aligned}$$

Once more, Figure VIII.9 illustrates the evolution of the best-fit value of the spin magnitude as a function of the end year of the observation campaign, but using $(i_\bullet, \Omega_\bullet) = (42^\circ, 125^\circ)$, the least ideal spin orientation, minimizing the astrometric Lense-Thirring apocenter shift for all mock datasets. One set uses $\chi = 0.99$ (bottom row of VIII.9), one set uses $\chi = 0.5$ (middle row of VIII.9), and the last one uses $\chi = 0.1$ (top row of VIII.9) as a spin magnitude value.

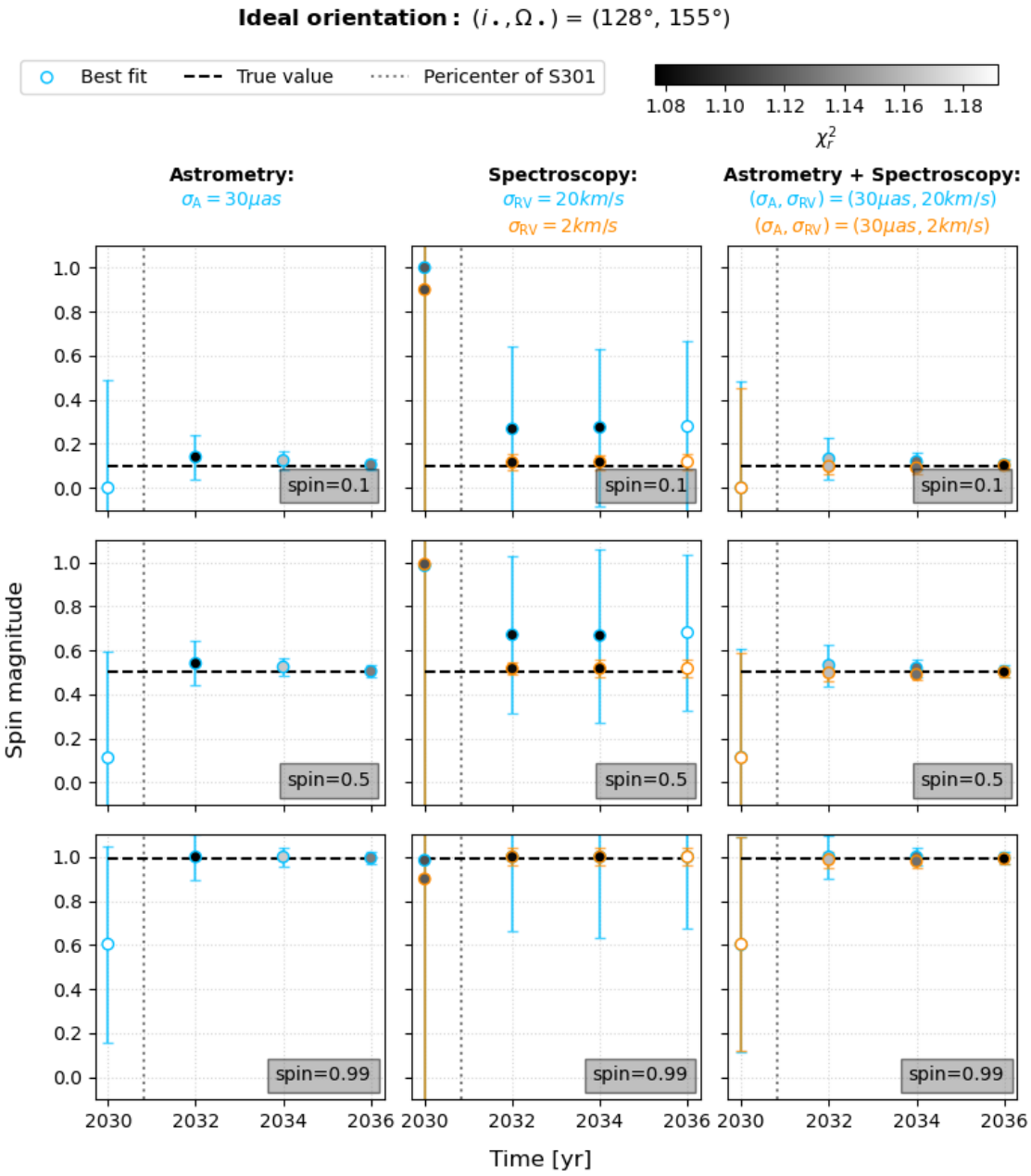

Figure VIII.7: Spin orientation yielding a maximal projected astrometric apocenter shift: evolution of the best-fit value of the spin magnitude as a function of time, using $(\chi, i_\bullet, \Omega_\bullet) = (0.99, 128°, 155°)$ (bottom row), $(\chi, i_\bullet, \Omega_\bullet) = (0.5, 128°, 155°)$ (middle row), and $(\chi, i_\bullet, \Omega_\bullet) = (0.1, 128°, 155°)$ (top row). We use only the astrometric data (left column), only the spectroscopic data (middle column) or both astrometric and spectroscopic data (right column). We use two spectroscopic sets of random noise, one of 20km/s (in blue) representing what can be achieved with ERIS, and one of 2km/s (in orange) representing what is expected to be achieved with MICADO. The data start at 2023.5 for S301 and at 2016.81 for S2, S29, S38, and S55. I also display the χ^2_r value corresponding to each best-fit of the spin magnitude, using the color bar.

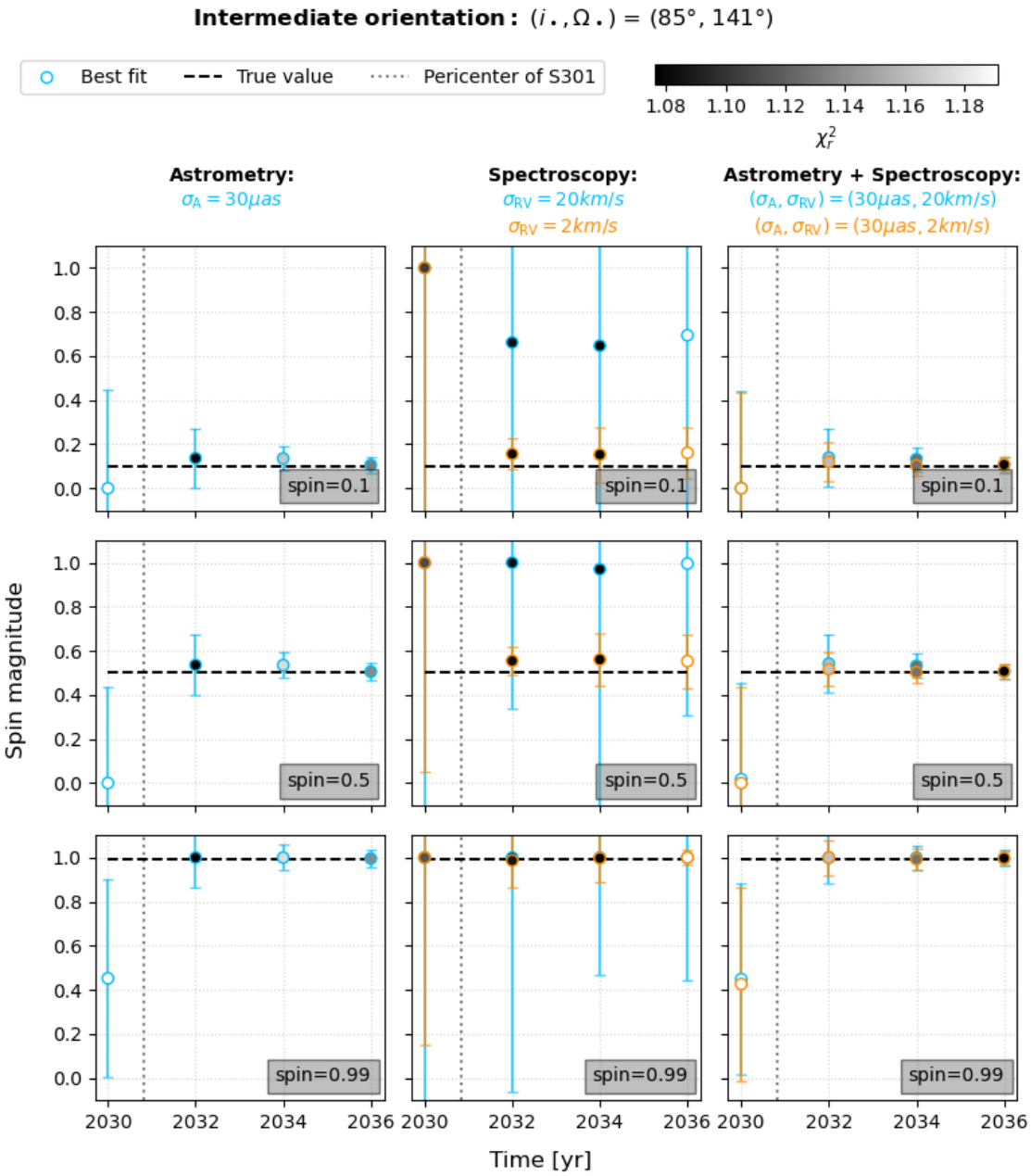

Figure VIII.8: Spin orientation yielding an intermediate projected astrometric apocenter shift: Same as Figure VIII.7 but using $(\chi, i_\bullet, \Omega_\bullet) = (0.99, 85°, 141°)$ (bottom row), $(\chi, i_\bullet, \Omega_\bullet) = (0.5, 85°, 141°)$ (middle row), and $(\chi, i_\bullet, \Omega_\bullet) = (0.1, 85°, 141°)$ (top row).

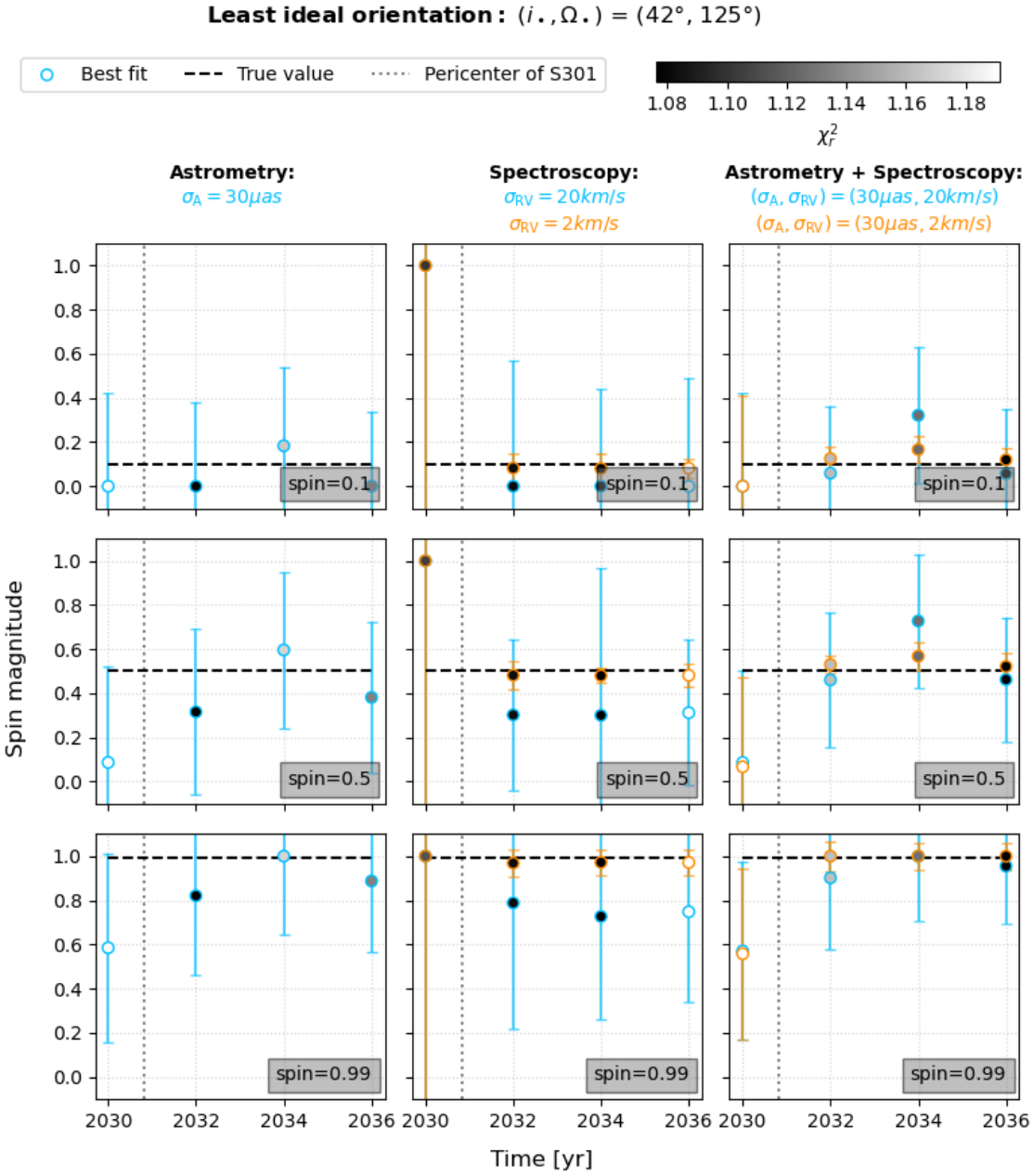

Figure VIII.9: Spin orientation yielding a minimal projected astrometric apocenter shift: Same as Figure VIII.7 but using $(\chi, i_\bullet, \Omega_\bullet) = (0.99, 42°, 125°)$ (bottom row), $(\chi, i_\bullet, \Omega_\bullet) = (0.5, 42°, 125°)$ (middle row), and $(\chi, i_\bullet, \Omega_\bullet) = (0.1, 42°, 125°)$ (top row).

In Figures VIII.7 to VIII.9, we see that when fitting only the spin magnitude and fixing all other parameters to their exact values:

- Unless we are close to least ideal configuration of the black hole orientation,

whether we use only the astrometric data (left columns) or both astrometric and spectroscopic data (right columns), we can easily recover the true value of the spin magnitude with a 1-σ error of $\sigma_\chi \approx 0.1$, $\sigma_\chi \approx 0.05$ and $\sigma_\chi \approx 0.03$ by observing the S2, 29, S38, S55, and most importantly S301 until 2032, 2034, and 2036, respectively.

- The true spin magnitude has much less impact on the detectability as opposed to the true spin orientation, suggesting that with sufficient data quality, the spin can be measured very precisely, regardless of its values[5].

- The χ^2_r values do not decrease monotonically. For instance, the best-fit of the data ending in 2030 can have a better χ^2_r value than the of the data ending in 2036. This is due to the fact that the contrast in χ^2_r increases with the observation end year, i.e., the best-fit values of 2030 when evaluated in 2036 will generate a higher χ^2_r than those of 2036.

- When using astrometric data, the improvement of the detectability of the spin magnitude with time is more pronounced between the pericenter and the apocenter than between the apocenter and the pericenter (due to the lever arm effect), but remains nonetheless present throughout the orbit.

- When using spectroscopic data, the improvement of the detectability of the spin magnitude with time is done by stair steps, improving after each pericenter and remaining relatively constant until the next one (due to the fact that the effect of the spin on radial velocity is very localized around the pericenter). However, this improvement assumes that the sampling of the observation dates has data close enough to the pericenter. If, for example, the pericenter is outside the observability window of the galactic center (early March to late September), spectroscopic monitoring will be rendered useless for direct spin detection[6].

- Using a mock dataset with random noise of 20km/s, corresponding to the current precision of ERIS, the spectroscopic data has little to no impact on the detectability of the spin magnitude, as opposed to astrometry which leads the detection in that case.

- Using a mock dataset with random noise of 2km/s, corresponding to the expected precision of MICADO, the spectroscopic data becomes much more useful, and leads the detectability right after each pericenter. Astrometry is

[5] Except if the spin orientation is close to the least ideal configuration and if the mock dataset has random noise of 20km/s on radial velocity instead of 2km/s.

[6] In practice, however, spectroscopic data will still be useful for constraining the other parameters of the problem, such as the orbital parameters of the stars, and thus still indirectly help with the spin detection.

nevertheless still important to include, especially from apocenter to pericenter.

- Astrometry becomes less useful when the orientation of the black hole is close the least ideal configuration (when the leading star is polar with a polar major axis), and the inclusion of S2, S29, S38 and S55 to the data of S301 become crucial[7] if spectroscopic data is not considered.

To illustrate the last point, we show in Figure VIII.10 how the use of S2, S29, S38, and S55 helps reduce the error bar on the spin magnitude when their data are added onto those of S301, when the black hole orientation is close to the least ideal configuration and when we only use astrometric data. For this, we consider mock data with $\chi = 0.1$ and $\chi = 0.99$, between 2016.81 (the first light of GRAVITY) and 2036 for S2, S29, S38 and S55, and between 2023.5 and 2036 for S301. We see that the use of other stars in addition to S301 reduces the uncertainty on the spin measurement by up to an order of magnitude in the 10° by 10° area surrounding the least favorable configuration.

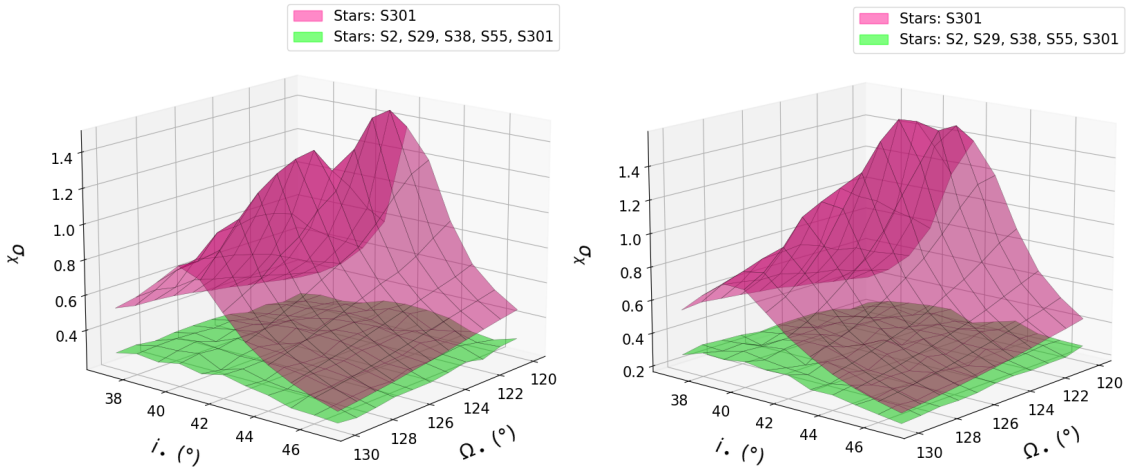

(a) $\chi = 0.1$ **(b)** $\chi = 0.99$

Figure VIII.10: Error bar on the best-fit of the black hole spin magnitude in the surrounding of the least favorable spin orientation configuration when fitting the astrometric data of S2, S29, S38, S55, and S301 (green), or only S301 (pink). Mock datasets are generated for two spin magnitudes, $\chi = 0.1$ (left) and $\chi = 0.99$ (right). The observing window is 2016.81–2036 for S2, S29, S38, and S55, and 2023.5–2036 for S301.

[7] Simulations show that the error bars of the left panels of Figure VIII.9 become larger than the range of the spin magnitude when only using the data of S301 in the least ideal configuration, meaning that no constraints are acquired in that case.

VIII.2.2 Fitting all spin parameters

Now, let us increase the difficulty by freeing all three spin parameters instead of only the magnitude. The same process of simulating the mock data with three spin orientations and three spin magnitudes is repeated for each orientation.

In Figure VIII.11 I illustrate once again the evolution of the best-fit value of the spin magnitude as a function of the end year of the observation campaign. Similarly to the 3D χ^2_r cube method of subsection VIII.1.4, all parameters are fixed at their exact values except the spin magnitude and its orientation. I use three different configurations: $(\chi, i_\bullet, \Omega_\bullet) = (0.1, 42°, 125°)$ (left column), $(0.5, 85°, 141°)$ (middle column), and $(0.99, 128°, 155°)$ (right column). The analysis includes both astrometric and spectroscopic data, with two levels of spectroscopic noise: 20 km/s (blue) and 2 km/s (orange), matching the settings used in the right panels of Figures VIII.7–VIII.9.

We see that when fitting all spin parameters instead of only the magnitude, most of the conclusions of subsection VIII.2.1 still hold true and also apply to the detectability of the spin orientation. We note few key differences:

- As expected, we can a little less easily recover the true value of the spin magnitude, on average the error bars on the spin magnitude increase by a factor $\lesssim 2$, but are still of exquisite quality. For reference, the BHEX instrument, designed with spin fitting as its top priority, is expected to deliver typical uncertainties of order $\sigma_\chi \sim 0.1$ on the spin magnitude of Sgr A* [84].
- When multiple parameters are fitted simultaneously, the detectability of a given parameter does not necessarily improve monotonically with longer observation times. For example, in the less ideal configuration (left panel of Figure VIII.11), the error bars on the spin orientation are actually larger when monitoring continues until 2036 rather than 2034. This does not imply that detectability generally worsens; rather, it reflects a trade-off between parameters. In this case, extending the monitoring improves the constraints on the spin magnitude, but at the expense of larger uncertainties on the spin orientation.

Overall, these simulations demonstrate that the spin parameters of Sgr A* can be robustly constrained with multi-star monitoring, provided that the other parameters of the problem are well known. The detectability of the spin magnitude is generally strong, largely independent of its true value, and primarily limited by the orientation of the spin axis relative to the leading stars. When freeing all spin parameters simultaneously, degeneracies naturally appear, leading to trade-offs between the constraints on the spin magnitude and orientation. Nonetheless, with observational campaigns extending into the mid-2030s and improved spectroscopic precision (e.g. MICADO-level), both the spin magnitude and orientation of Sgr A*

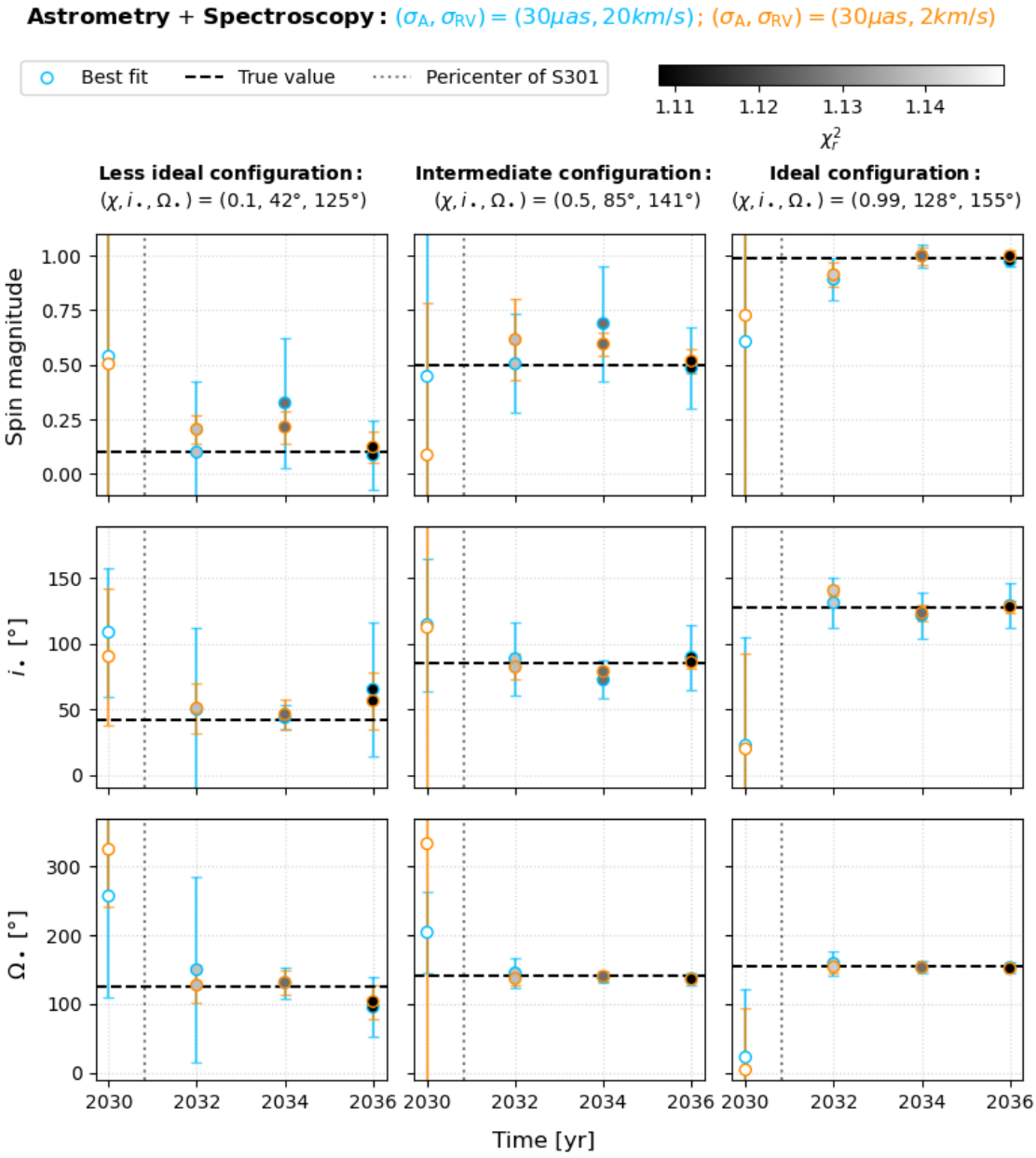

Figure VIII.11: Evolution of the best-fit value of all spin parameters as a function of time, using $(\chi, i_\bullet, \Omega_\bullet) = (0.1, 42°, 125°)$ (left column), $(\chi, i_\bullet, \Omega_\bullet) = (0.5, 85°, 141°)$ (middle column), and $(\chi, i_\bullet, \Omega_\bullet) = (0.99, 128°, 155°)$ (right column). We use only both astrometric and spectroscopic data with two spectroscopic sets of random noise, one of 20km/s (in blue), and one of 2km/s (in orange) as in the right columns of Figures VIII.7-VIII.9.

should become measurable with high significance, even in the least favorable geometric configurations. This highlights the importance of combining multi-star astrometry and spectroscopy in order to break parameter degeneracies and secure a reliable measurement of the black hole spin.

Conclusion

In this thesis I have investigated the relativistic dynamics of stellar orbits around the Galactic Center black hole, with a particular focus on the impact of spin–related effects at post–Newtonian orders beyond the first order Schwarzschild precession.

I start by stressing the importance of careful modeling choices. The use of osculating orbital elements in a PN framework provides an intuitive Newtonian–like interpretation of relativistic orbits, but it also introduces a dependence on the chosen coordinate system. We demonstrated how discrepancies at the μas and km/s levels can arise when using different coordinate charts (Schwarzschild–Harmonic, Boyer–Lindquist, Kerr–Schild), and why documenting the coordinate conventions is essential for reproducibility.

I presented the different types of orbital precession arising at 1.5PN and 2PN orders due to the black hole spin and quadrupole moment. On an orbital timescale, the orbital plane undergoes both in–plane precession (parametrized by the rate $\dot{\varpi}$ defined in Eq. (VII.71)) and out–of–plane precessions (parametrized by $\dot{\Xi}$ and $\dot{\Theta}$ defined in Eqs. (VII.72) and (VII.73), respectively). Integrating over one period, we derived analytical 2PN expressions for the shifts $\Delta\varpi$, $\Delta\Xi$, and $\Delta\Theta$ (Eqs. (VII.77)–(VII.85)), which correspond to the tilt angle between two successive pericenters, and to the out-of-plane tilt of the minor and major axes, respectively (see Figure VII.1). Moreover, we show how these orbital timescale precessions are linked to the well-known secular timescale precession of the orbital angular momentum around the black hole spin axis.

Numerical orbit integrations with the PN code `OOGRE` showed consistency with the analytical predictions and illustrated which orbital orientations maximize the various precession components. A key result is that no single orbit optimally probes all relativistic effects: equatorial orbits enhance both Lense–Thirring and quadrupole in-plane precessions, while polar or mid–inclined orbits isolate specific out-of-plane contributions. This emphasizes the need for a diversity of orbital orientations for disentangling the different types of precessions.

We also quantified the astrometric signatures of these precessions for the well–known S2 star and for a hypothetical star on an orbit ten times tighter, S2/10. Scaling with the PN parameter $\epsilon = GM/(c^2 p)$ shows that relativistic effects grow rapidly for smaller orbits: compared to S2, S2/10 would exhibit Schwarzschild precessions ~ 300 times larger, Lense–Thirring precessions $\sim 10^3$ times larger, and quadrupole shifts ~ 3000 times larger, accumulated over the same observational time span. Such stars would therefore provide an extraordinarily powerful probe of the spin and multipolar structure of Sgr A*, compared to further-out stars.

From an observational perspective, I highlighted two complementary pathways for constraining the spin parameters of the Galactic Center black hole. The first is the monitoring of the star S301, newly discovered by the GRAVITY consortium, whose orbit is much more sensitive to spin-induced relativistic effects and whose constraining power is already found to be comparable to that of the hypothetical

S2/10. Although uncertainties in S301's orbital parameters remain relatively large given its recent discovery, it is clear that such a star will play a leading role in future spin measurements. The second pathway is to exploit the complementary information provided by the currently known S-stars (S2, S29, S38, S55, etc.): by jointly fitting their orbits together with S301, one can take advantage of their diverse orbital orientations to mitigate parameter degeneracies and reduce the observation time needed for meaningful constraints.

A detailed quantitative assessment leads to the following conclusions arising from mock data fitting of the known S-stars:

- **Fitting only the spin magnitude, all other parameters being fixed to their true values.** Except near the least favorable black hole orientations, the true spin magnitude can be recovered with 1-σ uncertainties of order
  - $\sigma_\chi \approx 0.1$ (monitoring until 2032),
  - $\sigma_\chi \approx 0.05$ (until 2034),
  - $\sigma_\chi \approx 0.03$ (until 2036).

  Detectability depends far more on the orientation of the spin than on its magnitude. Astrometry plays the dominant role, as its precision continuously improves constraints throughout the orbit, with the strongest gains occurring between pericenter and apocenter. Spectroscopy, by contrast, contributes more intermittently: its impact comes in discrete steps following pericenter passages, and only if the sampling near pericenter is sufficiently dense. The level of radial-velocity precision also matters. With an accuracy of about 20 km/s, as expected from ERIS, spectroscopy adds little to the spin constraints. At the higher precision of around 2 km/s, attainable with MICADO, spectroscopy becomes much more powerful, especially immediately after pericenter. In all cases, astrometry remains indispensable, and when the black hole orientation is particularly unfavorable, adding multiple stars such as S2, S29, S38, and S55 alongside S301 is essential to recover meaningful constraints if spectroscopy is not available.

- **Fitting all spin parameters (magnitude + orientation), all other parameters being fixed to their true values.** As expected, freeing more parameters reduces accuracy: the error bars on the spin magnitude increase by at most a factor of $\lesssim 2$. Detectability does not always improve monotonically with observing time, since trade–offs between parameters can occur. Nevertheless, the main conclusions remain: spin detectability is very robust with sufficient monitoring when the other parameters of the problem are well known, the spin orientation is the critical factor, and combining astrometry with high–precision spectroscopy is important for optimal constraints.

In summary, the work of this thesis establishes a detailed mapping between orbital geometries, relativistic precessions, and their observable signatures, and provides a consistent PN framework for confronting future high–precision data with theory. Looking ahead, a natural extension of this work will be to perform orbit fitting with all spin and orbital parameters released simultaneously, thereby assessing more realistically the achievable constraints and possible parameter correlations. In addition, applying the methodology of the last chapter to the quadrupole moment will make it possible to estimate the observational timescales required to test the no-hair theorem directly. With the advent of next–generation instruments, the improvement of the constraints of the orbital parameters of S301, and even the possible discovery of additional closer–in stars, the prospects of detecting the spin and quadrupole moment of Sgr A* are promising, bringing us closer to a definitive test of the no–hair theorem at the Galactic Center.

Bibliography

[1] Yael Alush and Nicholas C. Stone. Revisiting stellar orbits and the sgr a* quadrupole moment. *Phys. Rev. D*, 106:123023, Dec 2022.

[2] P. et al. Amaro-Seoane. Laser interferometer space antenna. *arXiv:1702.00786*, 2017.

[3] R. Angélil and P. Saha. Toward relativistic orbit fitting of galactic center stars and pulsars. *Monthly Notices of the Royal Astronomical Society*, 444(4):3780–3791, 2014.

[4] S. et al. Babak. Science with the space-based interferometer lisa. v. extreme mass-ratio inspirals. *Physical Review D*, 2020.

[5] F. K. Baganoff, Y. Maeda, M. Morris, et al. Chandra x-ray spectroscopic imaging of sagittarius a* and the central parsec of the galaxy. *The Astrophysical Journal*, 591:891–915, 2003.

[6] F. K. Baganoff, Y. Maeda, M. Morris, et al. Chandra x-ray spectroscopic imaging of sagittarius a* and the central parsec of the galaxy. *Astrophysical Journal*, 591:891, 2003.

[7] B. Balick and R. L. Brown. Intense sub-arcsecond structure in the galactic center. *Astrophysical Journal*, 194:265, 1974.

[8] J. M. Beckers. Adaptive optics for astronomy: Principles, performance and applications. *Annual Review of Astronomy and Astrophysics*, 31:13–62, 1993.

[9] T. Belloni. X-ray variability in black hole systems. *Astronomy & Astrophysics Review*, 2012.

[10] L. Blanchet and B. Iyer. Third post-newtonian dynamics of compact binaries: Equations of motion in the center-of-mass frame. 2003.

[11] Luc Blanchet. Gravitational radiation from post-newtonian sources and inspiralling compact binaries. *Living Reviews in Relativity*, 17(2), 2014.

[12] R. D. Blandford and R. L. Znajek. Electromagnetic extraction of energy from kerr black holes. *Monthly Notices of the Royal Astronomical Society*, 179:433, 1977.

[13] J. Ronald Boain. A-b-cs of sun-synchronous orbit mission design. 2004.

[14] Encyclopedia Britannica. Spectroscopy | definition, types, & facts, 2025.

[15] Avery E. Broderick, Vincent L. Fish, Sheperd S. Doeleman, and Abraham Loeb. Evidence for low black hole spin and physically motivated accretion models from millimeter-vlbi observations of sagittarius a*. 2011.

[16] V A Brumberg. *Essential relativistic celestial mechanics*. CRC Press, 2017.

[17] V. Coudé du Foresto, G. Perrin, and J.-M. Mariotti. The fluor/iota fiber stellar interferometer. *IAU Symposium Proceedings*, 158:115–118, 1997.

[18] Observatoire de Paris. The elt's micado instrument enters the construction phase. https://observatoiredeparis.psl.eu/the-elt-s-micado-instrument.html, 2024.

[19] J. Dexter and P. C. Fragile. Jets and winds from black hole accretion disks. *Monthly Notices of the Royal Astronomical Society*, 462, 2016.

[20] J. et al. Dexter. Grmhd simulations of accretion and jets from sagittarius a*. *Monthly Notices of the Royal Astronomical Society*, 524, 2023.

[21] T. Do, A. M. Ghez, M. R. Morris, et al. Flicker noises in astronomy and elsewhere. *Astrophysical Journal*, 691:1021, 2009.

[22] R. P. et al. Eatough. Observations of pulsars near the galactic center: Status and prospects. *Monthly Notices of the Royal Astronomical Society*, 2017.

[23] A. Eckart and R. Genzel. Stellar proper motions in the central 0.1 pc of the galaxy. *Monthly Notices of the Royal Astronomical Society*, 284:576, 1997.

[24] A. S. Eddington. *The Internal Constitution of the Stars*. Cambridge University Press, Cambridge, 1926.

[25] A. Einstein. Zur elektrodynamik bewegter körper. *Annalen der Physik*, 17:891–921, 1905.

[26] A. Einstein. On the influence of gravitation on the propagation of light. *Annalen der Physik*, 35:898–908, 1911.

[27] A. Einstein. Die feldgleichungen der gravitation. *Sitzungsberichte der Preussischen Akademie der Wissenschaften zu Berlin*, pages 844–847, 1915.

[28] A. Einstein. Lens-like action of a star by the deviation of light in the gravitational field. *Science*, 84:506–507, 1936.

[29] F. Eisenhauer, P. Garcia, R. Genzel, S. Hönig, L. Kreidberg, J.-B. Le Bouquin, P. Léna, T. Paumard, C. Straubmeier, et al. Gravity+: Towards faint science, all sky, high contrast, milli-arcsecond optical interferometric imaging – white paper and proposal, 2020. White Paper provided as source material for this query.

[30] ESO. Eris - eso. https://www.eso.org/sci/facilities/paranal/instruments/eris.html. accessed August 2025.

[31] ESO. Eris - eso public information. https://www.eso.org/public/teles-instr/paranal-observatory/vlt/vlt-instr/eris/. accessed August 2025.

[32] ESO. Micado - elt instrument. https://elt.eso.org/instrument/MICADO/, 2025. accessed August 2025.

[33] Event Horizon Telescope Collaboration et al. Magnetic field morphology near the event horizon of sagittarius a*. *Astronomy & Astrophysics*, 670:A25, 2024.

[34] Event Horizon Telescope Collaboration et al. Polarimetric imaging of sagittarius a* with the eht: Spin and magnetic field structure. *Astrophysical Journal Letters*, 935:L14, 2024.

[35] F. Eisenhauer et al. The enhanced resolution imager and spectrograph for the vlt. *Astronomy & Astrophysics*, 665:A123, 2023.

[36] Abuter et al. (GRAVITY Collaboration). Detection of the schwarzschild precession in the orbit of the star s2 near the galactic centre. *Astronomy & Astrophysics*, 636:L5, 2020.

[37] K. Event Horizon Telescope Collaboration, Akiyama, A. Alberdi, W. Alef, J. C. Algaba, R. Anantua, K. Asada, R. Azulay, U. Bach, A.-K. Baczko, et al. First sagittarius a* event horizon telescope results. i. the shadow of the supermassive black hole in the center of the milky way. *Astrophysical Journal Letters*, 930(2):L12, 2022.

[38] A. C. Fabian. Observational evidence of active galactic nuclei feedback. *Annual Review of Astronomy and Astrophysics*, 50:455–489, September 2012.

[39] H. Falcke and S. Markoff. The jet model for sgr a* : Radio and x-ray spectrum. *Astronomy & Astrophysics*, 362:113, 2000.

[40] H. Falcke and S. Markoff. Toward the event horizon - the galactic center black hole. *Classical and Quantum Gravity*, 2019.

[41] L. Ferrarese and D. Merritt. A fundamental relation between supermassive black holes and their host galaxies. *The Astrophysical Journal Letters*, 539:L9–L12, 2000.

[42] G. Finger, I. Baker, D. Alvarez, et al. Sub-electron read noise and millisecond full-frame readout with the near infrared eapd array saphira. In *Adaptive Optics Systems V, Proc. SPIE*, volume 9909, page 990912, 2016.

[43] H. Fizeau. Sur les franges d'interférence produites par la lumière blanche traversant un système de fentes parallèles, et sur la mesure des diamètres angulaires des étoiles. *Comptes Rendus de l'Académie des Sciences*, 66:932, 1868.

[44] Max Planck Institute for Extraterrestrial Physics. Eris instrument. https://www.mpe.mpg.de/ir/ERIS. accessed August 2025.

[45] Max Planck Institute for Extraterrestrial Physics. Micado instrument. https://www.mpe.mpg.de/ir/micado. accessed August 2025.

[46] K. Gebhardt, R. Bender, G. Bower, et al. A relationship between nuclear black hole mass and galaxy velocity dispersion. *The Astrophysical Journal Letters*, 539:L13–L16, 2000.

[47] R. Genzel, R. Schödel, T. Ott, et al. Near-infrared flares from accreting gas around the supermassive black hole at the galactic centre. *Nature*, 425:934, 2003.

[48] Reinhard Genzel, Frank Eisenhauer, and Stefan Gillessen. The galactic center massive black hole and nuclear star cluster. *Rev. Mod. Phys.*, 82:3121–3195, Dec 2010.

[49] O. Gerhard. The galactic center he i stars : Remains of a dissolved young cluster ? *Astrophysical Journal*, 546.

[50] A. M. Ghez, B. L. Klein, M. Morris, and E. E. Becklin. High proper-motion stars in the vicinity of sagittarius a*: Evidence for a supermassive black hole at the center of our galaxy. *Astrophysical Journal*, 509(2):678–686, 1998.

[51] A. M. Ghez, S. Salim, N. N. Weinberg, J. R. Lu, T. Do, J. K. Dunn, K. Matthews, M. R. Morris, S. Yelda, E. E. Becklin, T. Kremenek, M. Milosavljevic, and J. Naiman. Measuring distance and properties of the milky way's central supermassive black hole with stellar orbits. *The Astrophysical Journal*, 689(2):1044–1062, dec 2008.

[52] S. Gillessen, F. Eisenhauer, S. Trippe, T. Alexander, R. Genzel, F. Martins, and T. Ott. MONITORING STELLAR ORBITS AROUND THE MASSIVE BLACK HOLE IN THE GALACTIC CENTER. *The Astrophysical Journal*, 692(2):1075–1109, feb 2009.

[53] S. Gillessen, P. M. Plewa, F. Eisenhauer, R. Sari, I. Waisberg, M. Habibi, O. Pfuhl, E. George, J. Dexter, S. von Fellenberg, T. Ott, and R. Genzel. An update on monitoring stellar orbits in the galactic center. *The Astrophysical Journal*, 837(1):30, feb 2017.

[54] K. Glampedakis and D. Kennefick. Zoom-whirl orbits in black hole spacetimes and their gravitational waveforms. *Physical Review D*, 2006.

[55] E. Gourgoulhon. *Relativité générale*. Observatoire de Paris, 2013.

[56] Eric Gourgoulhon. *Geometry and physics of black holes*. Lecture notes.

[57] GRAVITY Collaboration, Abd El Dayem, K., Abuter, R., Aimar, N., Amorim, A., Ball, J., Bauböck, M., Berger, J. P., Bonnet, H., Bourdarot, G., Brandner, W., Cardoso, V., Clénet, Y., Dallilar, Y., Davies, R., de Zeeuw, P. T., Dexter, J., Drescher, A., Eisenhauer, F., Förster Schreiber, N. M., Foschi, A., Garcia, P., Gao, F., Gendron, E., Genzel, R., Gillessen, S., Habibi, M., Haubois, X., Heißel, G., Henning, T., Hippler, S., Horrobin, M., Jochum, L., Jocou, L., Kaufer, A., Kervella, P., Lacour, S., Lapeyrère, V., Le Bouquin, J.-B., Léna, P., Lutz, D., Ott, T., Paumard, T., Perraut, K., Perrin, G., Pfuhl, O., Rabien, S., Shangguan, J., Shimizu, T., Scheithauer, S., Stadler, J., Stephens, A.W., Straub, O., Straubmeier, C., Sturm, E., Tacconi, L. J., Tristram, K. R. W., Vincent, F., von Fellenberg, S., Widmann, F., Wieprecht, E., Wiezorrek, E., Woillez, J., Yazici, S., and Young, A. Improving constraints on the extended mass distribution in the galactic center with stellar orbits. *A&A*, 692, 2024.

[58] GRAVITY Collaboration, Abuter, R., Aimar, N., Amorim, A., Ball, J., Bauböck, M., Berger, J. P., Bonnet, H., Bourdarot, G., Brandner, W., Cardoso, V., Clénet, Y., Dallilar, Y., Davies, R., de Zeeuw, P. T., Dexter, J., Drescher, A., Eisenhauer, F., Förster Schreiber, N. M., Foschi, A., Garcia, P., Gao, F., Gendron, E., Genzel, R., Gillessen, S., Habibi, M., Haubois, X., Heißel, G., Henning, T., Hippler, S., Horrobin, M., Jochum, L., Jocou, L., Kaufer, A., Kervella, P., Lacour, S., Lapeyrère, V., Le Bouquin, J.-B., Léna, P., Lutz, D., Ott, T., Paumard, T., Perraut, K., Perrin, G., Pfuhl, O., Rabien, S., Shangguan, J., Shimizu, T., Scheithauer, S., Stadler, J., Stephens, A.W., Straub, O., Straubmeier, C., Sturm, E., Tacconi, L. J., Tristram, K. R. W., Vincent, F., von Fellenberg, S., Widmann, F., Wieprecht, E., Wiezorrek, E., Woillez, J., Yazici, S., and Young, A. Mass distribution in the galactic

center based on interferometric astrometry of multiple stellar orbits. *A&A*, 657:L12, 2022.

[59] GRAVITY Collaboration, Abuter, R., Amorim, A., Anugu, N., Bauböck, M., Benisty, M., Berger, J. P., Blind, N., Bonnet, H., Brandner, W., Buron, A., Collin, C., Chapron, F., Clénet, Y., dCoudé u Foresto, V., de Zeeuw, P. T., Deen, C., Delplancke-Ströbele, F., Dembet, R., Dexter, J., Duvert, G., Eckart, A., Eisenhauer, F., Finger, G., Förster Schreiber, N. M., Fédou, P., Garcia, P., Garcia Lopez, R., Gao, F., Gendron, E., Genzel, R., Gillessen, S., Gordo, P., Habibi, M., Haubois, X., Haug, M., Haußmann, F., Henning, Th., Hippler, S., Horrobin, M., Hubert, Z., Hubin, N., Jimenez Rosales, A., Jochum, L., Jocou, L., Kaufer, A., Kellner, S., Kendrew, S., Kervella, P., Kok, Y., Kulas, M., Lacour, S., Lapeyrère, V., Lazareff, B., Le Bouquin, J.-B., Léna, P., Lippa, M., Lenzen, R., Mérand, A., Müler, E., Neumann, U., Ott, T., Palanca, L., Paumard, T., Pasquini, L., Perraut, K., Perrin, G., Pfuhl, O., Plewa, P. M., Rabien, S., Ramírez, A., Ramos, J., Rau, C., Rodríguez-Coira, G., Rohloff, R.-R., Rousset, G., Sanchez-Bermudez, J., Scheithauer, S., Schöller, M., Schuler, N., Spyromilio, J., Straub, O., Straubmeier, C., Sturm, E., Tacconi, L. J., Tristram, K. R. W., Vincent, F., von Fellenberg, S., Wank, I., Waisberg, I., Widmann, F., Wieprecht, E., Wiest, M., Wiezorrek, E., Woillez, J., Yazici, S., Ziegler, D., and Zins, G. Detection of the gravitational redshift in the orbit of the star s2 near the galactic centre massive black hole. *A&A*, 615:L15, 2018.

[60] GRAVITY Collaboration, Abuter, R., Amorim, A., Bauböck, M., Berger, J. P., Bonnet, H., Brandner, W., Cardoso, V., Clénet, Y., de Zeeuw, P. T., Dexter, J., Eckart, A., Eisenhauer, F., Förster Schreiber, N. M., Garcia, P., Gao, F., Gendron, E., Genzel, R., Gillessen, S., Habibi, M., Haubois, X., Henning, T., Hippler, S., Horrobin, M., Jiménez-Rosales, A., Jochum, L., Jocou, L., Kaufer, A., Kervella, P., Lacour, S., Lapeyrère, V., Le Bouquin, J.-B., Léna, P., Nowak, M., Ott, T., Paumard, T., Perraut, K., Perrin, G., Pfuhl, O., Rodríguez-Coira, G., Shangguan, J., Scheithauer, S., Stadler, J., Straub, O., Straubmeier, C., Sturm, E., Tacconi, L. J., Vincent, F., von Fellenberg, S., Waisberg, I., Widmann, F., Wieprecht, E., Wiezorrek, E., Woillez, J., Yazici, S., and Zins, G. Detection of the Schwarzschild precession in the orbit of the star S2 near the Galactic centre massive black hole. *A&A*, 636:L5, 2020.

[61] R. GRAVITY Collaboration, Abuter, M. Accardo, A. Amorim, N. Anugu, G. Ávila, N. Azouaoui, M. Benisty, J.-P. Berger, N. Blind, et al. First light for gravity: Phase referencing optical interferometry for the very large telescope interferometer. *Astronomy & Astrophysics*, 602:A94, 2017.

[62] R. GRAVITY+ Collaboration, Abuter, P. Alarcon, F. Allouche, A. Amorim,

C. Bailet, H. Bedigan, A. Berdeu, J.-P. Berger, P. Berio, et al. The gravity+ project: Towards all-sky, faint-science, high-contrast near-infrared interferometry at the vlti. *The Messenger*, 189:17–22, 2022.

[63] R. GRAVITY Collaboration, Abuter, A. Amorim, et al. The wind and the magnetospheric accretion onto the t tauri star s coronae australis at sub-au resolution. *Astronomy & Astrophysics*, 608:A78, 2017.

[64] R. GRAVITY Collaboration, Abuter, A. Amorim, et al. Detection of orbital motions near the last stable circular orbit of the massive black hole sgra*. *Astronomy & Astrophysics*, 618:L10, 2018.

[65] R. GRAVITY Collaboration, Abuter, A. Amorim, et al. Multiple star systems in the orion nebula. *Astronomy & Astrophysics*, 620:A116, 2018.

[66] R. GRAVITY Collaboration, Abuter, A. Amorim, et al. Spatially resolved rotation of the broad-line region of a quasar at sub-parsec scale. *Nature*, 563:657–660, 2018.

[67] R. GRAVITY Collaboration, Abuter, A. Amorim, et al. First direct detection of an exoplanet by optical interferometry: Astrometry and k band spectroscopy of hr8799e. *Astronomy & Astrophysics*, 623:L11, 2019.

[68] R. GRAVITY Collaboration, Abuter, A. Amorim, et al. A geometric distance measurement to the galactic center black hole with 0.33% accuracy. *Astronomy & Astrophysics*, 625:L10, 2019.

[69] R. GRAVITY Collaboration, Abuter, A. Amorim, et al. Test of einstein equivalence principle near the galactic center supermassive black hole. *Physical Review Letters*, 122:101102, 2019.

[70] R. GRAVITY Collaboration, Abuter, A. Amorim, et al. Detection of the schwarzschild precession in the orbit of the star s2 near the galactic centre massive black hole, 2020. in preparation.

[71] R. GRAVITY Collaboration, Abuter, A. Amorim, et al. Peering into the formation history of β pictoris b with vlti/gravity long-baseline interferometry. *Astronomy & Astrophysics*, 633:A110, 2020.

[72] M. Grould. *Études d'effets relativistes au Centre Galactique à l'aide de simulations d'observations d'orbites d'étoiles par l'instrument GRAVITY*. Phd thesis, LESIA, 2017.

[73] M. Grould, T. Paumard, and G. Perrin. Testing the validity of the ray-tracing code gyoto. *A&A*, 591:A116, 2016.

[74] M. Grould, F. H. Vincent, T. Paumard, and G. Perrin. General relativistic effects on the orbit of the s2 star with gravity. *A&A*, 608:A60, 2017.

[75] R. O. Hansen. Multipole moments of stationary space-times. *Journal of Mathematical Physics*, 15:46–52, 1974.

[76] P. J. Hargrave and M. Ryle. Observations of cygnus a at 5 ghz with the 5-km radio telescope. *Monthly Notices of the Royal Astronomical Society*, 166:305–316, 1974.

[77] A. Hees and F. H. Vincent. *Introduction to Special Relativity, General Relativity and Cosmology*. Observatoire de Paris, 2022.

[78] G. Heißel, T. Paumard, G. Perrin, and F. Vincent. The dark mass signature in the orbit of s2. *A&A*, 660:A13, 2022.

[79] G. Heißel, F. Vincent, K. Abd El Dayem, T Paumard, and G. Perrin. Non-uniqueness of relativistic orbital parametrisations. 2026.

[80] J. G. Hills. Hyper-velocity and tidal stars from binaries disrupted by a massive galactic black hole. *Nature*, 331:687, 1988.

[81] H. Hu and L. Shao. Measuring the spin of the galactic center supermassive black hole with multiple pulsars. *Physical Review Letters*, 133:231402, 2024.

[82] R. A. Hulse and J. H. Taylor. Discovery of a pulsar in a binary system. *The Astrophysical Journal Letters*, 195:L51–L53, 1975.

[83] W. Israel. Event horizons in static vacuum space-times. *Physical Review*, 164:1776–1779, 1967.

[84] Michael D. Johnson, Kazunori Akiyama, Rebecca Baturin, Bryan Bilyeu, Lindy Blackburn, Don Boroson, Alejandro Cárdenas-Avenda no, Andrew Chael, Chi kwan Chan, Dominic Chang, Peter Cheimets, Cathy Chou, Sheperd S. Doeleman, Joseph Farah, Peter Galison, Ronald Gamble, Charles F. Gammie, Zachary Gelles, José L. Gómez, Samuel E. Gralla, Paul Grimes, Leonid I. Gurvits, Shahar Hadar, Kari Haworth, Kazuhiro Hada, Michael H. Hecht, Mareki Honma, Janice Houston, Ben Hudson, Sara Issaoun, He Jia, Svetlana Jorstad, Jens Kauffmann, Yuri Y. Kovalev, Peter Kurczynski, Robert Lafon, Alexandru Lupsasca, Robert Lehmensiek, Chung-Pei Ma, Daniel P. Marrone, Alan P. Marscher, Gary J. Melnick, Ramesh Narayan, Kotaro Niinuma, Scott C. Noble, Eric J. Palmer, Daniel C. M. Palumbo, Lenny Paritsky, Eliad Peretz, Dominic Pesce, Alexander Plavin, Eliot Quataert, Hannah Rana, Angelo Ricarte, Freek Roelofs, Katia Shtyrkova, Laura C. Sinclair, Jeffrey Small, Sridharan Tirupati Kumara, Ranjani Srinivasan, Andrew Strominger, Paul Tiede, Edward Tong, Jade Wang, Jonathan

Weintroub, Maciek Wielgus, George Wong, and Xinyue Alice Zhang. The black hole explorer: Motivation and vision. *arXiv preprint arXiv:2406.12917*, 2024.

[85] R. P. Kerr. Gravitational field of a spinning mass as an example of algebraically special metrics. *Physical Review Letters*, 11:237–238, 1963.

[86] A. R. King and J. E. Pringle. Growing supermassive black holes by chaotic accretion. *MNRAS*, 2006. in press.

[87] B. Kocsis and S. Tremaine. Resonant relaxation and the warp of the stellar disc in the galactic centre. 2011.

[88] M. et al. Kramer. Strong-field tests of gravity with pulsars and black holes. *Progress of Theoretical and Experimental Physics*, 2016.

[89] Krishnendu, Saleem, Samajdar, Arun, Del Pozzo, and Chandra Kant Mishra. Constraints on the binary black hole nature of gw151226 and gw170608 from the measurement of spin-induced quadrupole moments. 2019.

[90] A. Labeyrie. Stellar interferometry methods. *The Astrophysical Journal*, 196:L71, 1975.

[91] J. Lense and H. Thirring. Über den einfluss der eigenrotation der zentralkörper auf die bewegung der planeten und monde nach der einsteinschen gravitationstheorie. *Physikalische Zeitschrift*, 19:156–163, 1918.

[92] Y. Levin. Starbursts near supermassive black holes : young stars in the galactic centre, and gravitational waves in lisa band. *Monthly Notices of the Royal Astronomical Society*, 374:515, 2007.

[93] LibreTexts. 4.1: Spectroscopy - basic elements and principles. https://chem.libretexts.org/Courses/Western_Washington_University/Biophysical_Chemistry_(Smirnov_and_McCarty)/04:_Spectroscopy_-_Types_Key_Features_Examples/4.01:_Spectroscopy-_Basic_Elements_and_Principles. accessed August 2025.

[94] K. et al. Liu. Probing the spacetime of sgr a* with pulsars. *Astrophysical Journal*, 747(1), 2012.

[95] D. Lynden-Bell and M. J. Rees. On quasars, dust and the galactic centre. *Monthly Notices of the Royal Astronomical Society*, 152:461, 1971.

[96] S. et al. Markoff. Jets or accretion flows? multiple wavelength observations of black hole candidates. *Astrophysical Journal*, 2007.

[97] David Merritt. *Dynamics and evolution of galactic nuclei*. Princeton series in astrophysics. Princeton University Press, 2013.

[98] A. A. Michelson and F. G. Pease. Measurement of the diameter of α orionis with the interferometer. *The Astrophysical Journal*, 53:249, 1921.

[99] M. et al. Mościbrodzka. Jet and outflow models from the galactic center black hole. *Monthly Notices of the Royal Astronomical Society*, 467, 2017.

[100] R. Narayan and I. Yi. Advection-dominated accretion: A self-similar solution. *The Astrophysical Journal*, 444:231–243, 1995.

[101] J. Nocedal and S. J. Wright. *Numerical Optimization*. Springer, 2 edition, 1999.

[102] B. Paczynski. A model of selfgravitating accretion disk with a hot corona. *Acta Astronomica*, 28:241, 1978.

[103] R. L. Particle Data Group, Workman et al. Review of particle physics. *Progress of Theoretical and Experimental Physics*, 2022:083C01, 2022.

[104] Paumard, T., Genzel, R., Martins, F., Nayakshin, S., Beloborodov, A. M., Levin, Y., Trippe, S., Eisenhauer, F., Ott, T., Gillessen, S., Abuter, R., Cuadra, J., Alexander, T., and Sternberg, A. The two young star disks in the central parsec of the galaxy: Properties, dynamics, and formation. *The Astrophysical Journal*, 643:1011–1035, 2006.

[105] T. J. Pearson, S. C. Unwin, M. H. Cohen, et al. Superluminal expansion in 3c 273. *Nature*, 290:365–367, 1981.

[106] R. Penrose. Gravitational collapse and space-time singularities. *Physical Review Letters*, 14:57–59, 1965.

[107] K. Perraut, L. Jocou, J. P. Berger, A. Chabliz, V. Cardin, G. Chamiot-Maitral, A. Delboulbé, F. Eisenhauer, Y. Gambérin, S. Gillessen, S. Giuuel, J. Guerrero, M. Haug, F. Hausmann, F. Joulain, P. Kervella, P. Labeye, S. Lacour, C. Lanthermann, V. Lapras, J. B. Le Bouquin, M. Lippa, Y. Magnard, T. Moulin, P. Noël, A. Nottel, F. Patru, G. Perrin, O. Pfuhl, S. Pocas, S. Poulain, C. Scibetta, E. Stadler, R. Templier, N. Ventura, C. Vizioz, A. Amorim, W. Brandner, and C. Straubmeier. Single-mode waveguides for gravity. i. the cryogenic 4-telescope integrated optics beam combiner. *Astronomy & Astrophysics*, 614:A70, 2018.

[108] G. Perrin. Spatial filtering in astronomical interferometry. *Astronomy & Astrophysics*, 331:619–626, 1998.

[109] G. Perrin, T. Paumard, F. Vincent, and G. Heißel. Single-mode waveguides and differential optical path delay control for interferometry. 2024.

[110] Guy Perrin. Principes de l'interférométrie astronomique, 2024. Lecture notes: Master Astronomie, Astrophysique et Ingénierie Spatiale, 2nde année, Parcours Recherche Astrophysique, Méthodologie 01 : interférométrie (2).

[111] E. Poisson. Gravitational waves from inspiraling compact binaries: The quadrupole-moment term. 1998.

[112] Eric Poisson and Clifford M. Will. *Gravity: Newtonian, Post-Newtonian, Relativistic*. Cambridge University Press, 2014.

[113] D. Psaltis. Probes and tests of strong-field gravity with pulsars and black holes. *Living Reviews in Relativity*, 2016.

[114] D. Psaltis. Testing general relativity with the event horizon telescope. *Living Reviews in Relativity*, 19:1, 2018.

[115] D. et al. Psaltis. Imaging and timing research for sagittarius a* and testing general relativity. *Astrophysical Journal*, 2016.

[116] M. et al. Punturo. The einstein telescope: A third-generation gravitational wave observatory. *Classical and Quantum Gravity*, 2020.

[117] C. S. et al. Reynolds. Accretion disk physics and spin constraints from x-ray variability. *Astrophysical Journal*, 2020.

[118] O. Rømer. Démonstration touchant le mouvement de la lumière. *Journal des Sçavans*, pages 233–236, 1676.

[119] S. Scheithauer, W. Brandner, C. Deen, et al. Ciao: wavefront sensors for gravity. In *Adaptive Optics Systems V, Proc. SPIE*, volume 9909, page 99092L, 2016.

[120] K. Schwarzschild. Über das gravitationsfeld eines massenpunktes nach der einsteinschen theorie. *Sitzungsberichte der Preussischen Akademie der Wissenschaften zu Berlin*, pages 189–196, 1916.

[121] Sereno, M. and de Luca, F. . Analytical kerr black hole lensing in the weak deflection limit. *Phys. Rev. D*, 2006.

[122] N. I. Shakura and R. A. Sunyaev. Black holes in binary systems. observational appearance. *Astronomy & Astrophysics*, 24:337–355, January 1973.

[123] M. Shao and D. H. Staelin. First fringe measurements with a phase-tracking stellar interferometer. *Applied Optics*, 19(9):1519–1522, 1980.

[124] I. I. Shapiro. Fourth test of general relativity. *Physical Review Letters*, 13:789–791, 1964.

[125] E. Stephan. Mesure des diamètres apparents des étoiles par l'interféromètre. *Comptes Rendus de l'Académie des Sciences (Paris)*, 78:1008, 1874.

[126] A. Tchekhovskoy, R. Narayan, and J. C. McKinney. Efficient generation of jets from magnetically arrested accretion on a rapidly spinning black hole. *Monthly Notices of the Royal Astronomical Society*, 418:L79, 2011.

[127] S. Trippe, T. Paumard, T. Ott, et al. A polarized infrared flare from sagittarius a* and the signatures of orbiting plasma hotspots. *Monthly Notices of the Royal Astronomical Society*, 375:764, 2007.

[128] A. Tucker and C. Will. Pericenter advance in general relativity: comparison of approaches at high post-newtonian orders. 2019.

[129] F. Vincent. *Études d'effets relativistes en champs gravitationnel fort*. Phd thesis, Observatoire de Meudon, 2011.

[130] F. H. Vincent. Probing strong-field gravity with electromagnetic radiation. Mémoire d'Habilitation à diriger des recherches, 2022.

[131] F H Vincent, T Paumard, E Gourgoulhon, and G Perrin. GYOTO: a new general relativistic ray-tracing code. *Classical and Quantum Gravity*, 28(22):225011, oct 2011.

[132] F. H. et al. Vincent. Modeling accretion and variability in black holes. *Monthly Notices of the Royal Astronomical Society*, 2014.

[133] M. Volonteri. Formation of supermassive black holes. *Astronomy and Astrophysics Review*, 18:279–315, 2010.

[134] Marta Volonteri, Mélanie Habouzit, and Monica Colpi. The origins of massive black holes. *Nature Reviews Physics*, 3(11):732–743, September 2021.

[135] Idel Waisberg, Jason Dexter, Stefan Gillessen, Oliver Pfuhl, Frank Eisenhauer, Phillip M Plewa, Michi Bauböck, Alejandra Jimenez-Rosales, Maryam Habibi, Thomas Ott, Sebastiano von Fellenberg, Feng Gao, Felix Widmann, and Reinhard Genzel. What stellar orbit is needed to measure the spin of the Galactic centre black hole from astrometric data? *Monthly Notices of the Royal Astronomical Society*, 476(3):3600–3610, 02 2018.

[136] N. N. Weinberg, M. Milosavljević, and A. M. Ghez. Stellar dynamics at the galactic center with an extremely large telescope. *The Astrophysical Journal*, 622:878–891, 2005.

[137] Steven Weinberg. *Gravitation and Cosmology: Principles and Applications of the General Theory of Relativity*. Wiley, 1972.

[138] N. Wex and S. Kopeikin. Frame dragging and other precessional effects in black hole-pulsar binaries. *The Astrophysical Journal*, 514:388–401, 1999.

[139] C. Will and M. Maitra. Relativistic orbits around spinning supermassive black holes. secular evolution to 4.5 post-newtonian order. 2016.

[140] C. Will, Naoz, S., Hees, A., Tucker, A., Zhang, E., Do, T., and Andrea, G. Constraining a companion of the galactic center black hole, sgr a*. 2023.

[141] C. M. Will. The confrontation between general relativity and experiment. *Living Reviews in Relativity*, 17:4, 2014.

[142] Clifford M. Will. Testing the general relativistic "no-hair" theorems using the galactic center black hole sagittarius a*. *The Astrophysical Journal*, 674(1):L25, jan 2008.

[143] Clifford M. Will. *Theory and experiment in Gravitational physics, second edition*. Cambridge University Press, 2018.

[144] E. R. Wollman, T. R. Geballe, J. H. Lacy, C. H. Townes, and D. M. Rank. Ne ii 12.8 micron emission from the galactic center. ii. *Astrophysical Journal*, 218:L103, 1977.

[145] Qingjuan Yu, Fupeng Zhang, and Youjun Lu. PROSPECTS FOR CONSTRAINING THE SPIN OF THE MASSIVE BLACK HOLE AT THE GALACTIC CENTER VIA THE RELATIVISTIC MOTION OF a SURROUNDING STAR. *The Astrophysical Journal*, 827(2):114, aug 2016.

[146] Feng Yuan and Ramesh Narayan. Hot accretion flows around black holes. *Annual Review of Astronomy and Astrophysics*, 52:529–588, August 2014.

[147] F. Zhang, Y. Lu, and Q. Yu. Relativistic effects in the orbits of stars around the galactic center black hole. *The Astrophysical Journal*, 843:96, 2017.

[148] F. et al. Zhang. Relativistic effects in the orbit of the s2 star around the galactic center black hole. *The Astrophysical Journal*, 844(2):99, 2017.

Appendix

A Numerical illustration: mid-inclined orbits

Let us investigate the case of a mid-inclined orbit, for example, the case where $\mathbf{z}_{\rm bh} = -\mathbf{y}^{\rm pro}_{\rm orb} + \mathbf{z}^{\rm pro}_{\rm orb} = \mathbf{y}^{\rm ret}_{\rm orb} - \mathbf{z}^{\rm ret}_{\rm orb}$, i.e $(\theta, \psi) = (\pi/4, 3\pi/2)$ or $(\theta, \psi) = (3\pi/4, \pi/2)$. we see from Eqs. (VII.78), (VII.81), and (VII.84), that with these values of θ and ψ we will observe both in-plane and out-of-plane precessions due to the Lense-Thirring effect, at moderate values. However, when looking at Eqs. (VII.82) and (VII.85) we see that the orbits will experience the most out-of-plane shift due to the quadrupole moment in this configuration. Indeed, when simulating a prograde and retrograde orbit relative to the black hole, we see in Figures 12 and 13 that the Lense-Thirring and quadrupole moment effects each make the apocenters experience both an in-plane and out-of-plane precession. The in-plane precessions are similar the the equatorial orbit case. As for the out-of-plane precessions, they mainly act on the major axis but also on the minor axis on much longer timescales (see Eq. (9) below). We also see that the quadrupole moment appears to oppose the Lense-Thirring effect for the out-of-plane shift when the orbit is prograde, but not for the retrograde orbit.

In practice, unless we have an equatorial (no out-of-plane precession) or polar (surface of the out-of-plane precession cone represented in Figure VII.1 being a plane for $\theta = \pi/2 \pmod{\pi}$) orbit with the major axis being equatorial or polar, both the major and minor axis will precess. However, the out-of-plane shift remains mainly along the tangent to the surface of the out-of-plane precession cone as long as the period of the orbit is much less than the precession period $P^{\rm cone}$ of the angular momentum of the orbit around the out-of-plane precession cone. To check that, we derive $P^{\rm cone}/P$ using Eqs. (VII.88) and (VII.95) at the 2PN order:

$$\frac{P^{\rm cone}_{\rm LT}}{P} = \frac{2\pi}{\omega_{\rm LT} P} \quad ; \quad \frac{P^{\rm cone}_{Q}}{P} = \frac{2\pi}{\omega_{Q} P} \tag{9}$$

If we apply this estimation for S2/10 for example, we get $\frac{P^{\rm cone}_{\rm LT}}{P}(\chi = 0.99) \sim 10^3$, $\frac{P^{\rm cone}_{\rm LT}}{P}(\chi = 0.1) \sim 10^4$, $\frac{P^{\rm cone}_{Q}}{P}(\chi = 0.99) \sim 10^5$ and $\frac{P^{\rm cone}_{Q}}{P}(\chi = 0.1) \sim 10^7$.

We summarize in a schematic way the results of Figures 12 and 13 in Figure 14, and how the quadrupole moment out-of-plane precession of the major axis, is studied through a mid-inclined orbits with $\mathbf{z}_{\rm bh//orb} // \mathbf{y}_{\rm orb}$. Alternatively, in order to maximize the quadrupole moment out-of-plane precession of the minor axis instead of the major axis, one would need to study a mid-inclined orbits with $\mathbf{z}_{\rm bh//orb} // \mathbf{x}_{\rm orb}$.

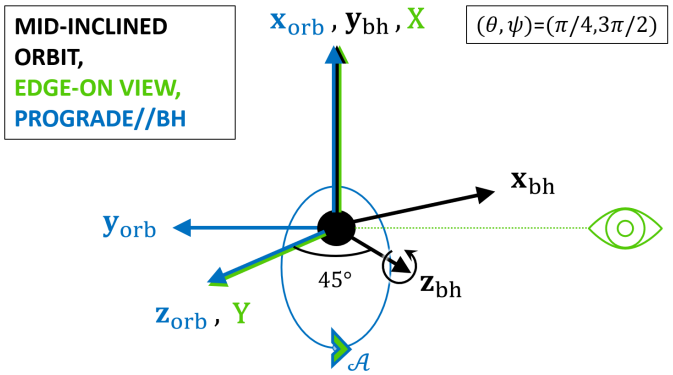

(a) Schematic illustration of the osculating Keplerian orbit (see subsection A)

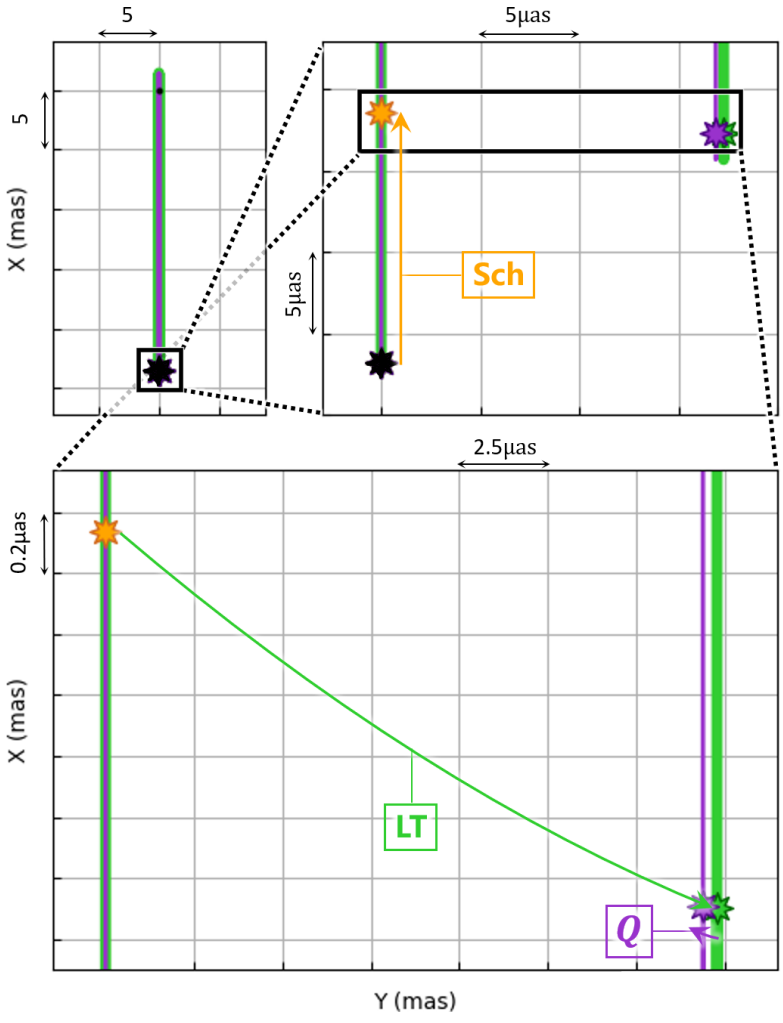

(b) Simulation using the 2PN code

Figure 12: Same as Figure VII.3 but with mid-inclined orbits relative to the equatorial plane of the black hole. We see that that the apocenter experiences both an in-plane and out-of-plane precession due to the Lense-Thirring effect. The in-plane precession is clockwise as seen on the face-on projection of Figure VII.3a, and the out-of-plane precession is mainly for the major axis but also acts on the minor axis. We also see that the quadrupole moment appears to have the opposite behavior to the Lense-Thirring effect for both the in-plane and out-of-plane shifts.

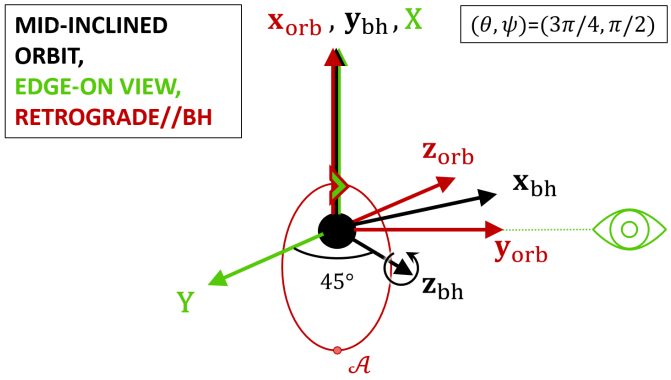

(a) Schematic illustration of the osculating Keplerian orbit (see subsection A)

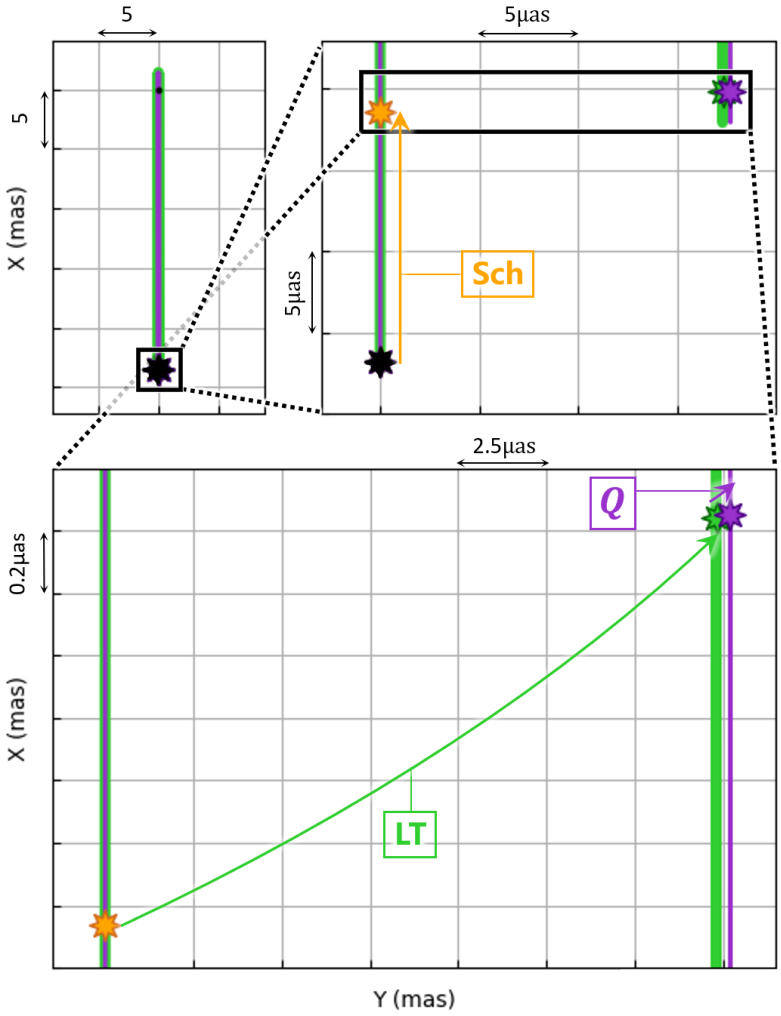

(b) Simulation using the 2PN code

Figure 13: Same as Figure 12 but for retrograde orbits, relative to the black hole. We see that the apocenter experiences both an in-plane and out-of-plane precession due to the Lense-Thirring effect. The in-plane precession is clockwise as seen on the face-on projection of Figure VII.4a, and the out-of-plane precession is mainly for the major axis but also acts on the minor axis. We also see that the quadrupole moment appears to have the same behavior as the Lense-Thirring effect for the both types of precession.

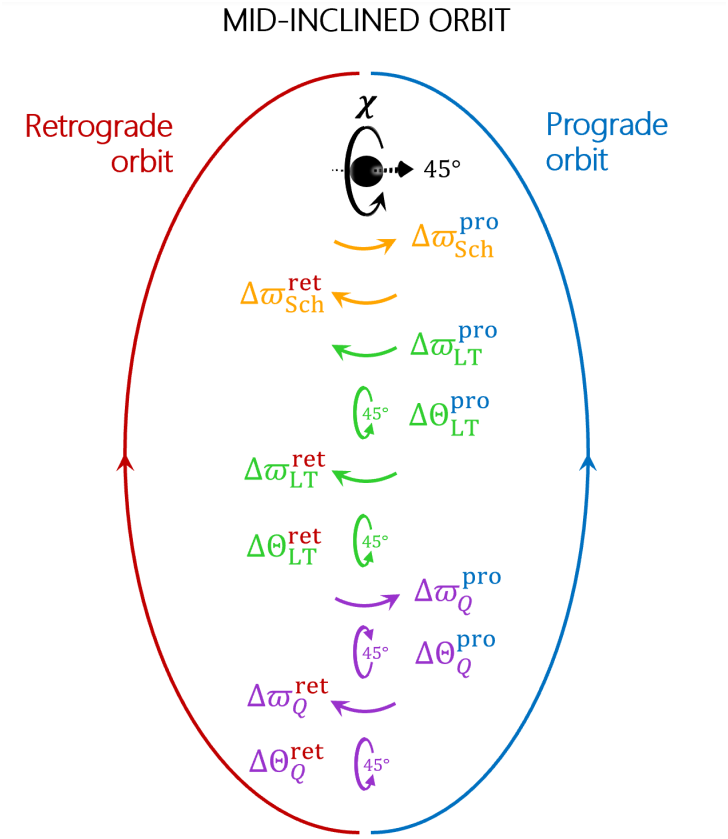

Figure 14: Schematic illustration of the secular precessions for a mid inclined orbit relative to the equatorial plane of the black hole. When we have $\mathbf{z}_{\rm bh} = -\mathbf{y}^{\rm pro}_{\rm orb} + \mathbf{z}^{\rm pro}_{\rm orb} = \mathbf{y}^{\rm ret}_{\rm orb} - \mathbf{z}^{\rm ret}_{\rm orb}$ for example, the in-plane precessions act in the same way as for equatorial orbits (see VII.5). As for the out-of-plane precessions, the Lense-Thirring precession pushes the apocenter in the same direction as the spin, and the quadrupole moment effect as well for the retrograde orbit but in the direction opposite to the the spin for the prograde orbit.

B Estimating characteristic spin orientations in the observer's frame

In this appendix, we will project the total apocenter displacement vector due to the Lense-Thirring effect onto the sky and explore the values of θ and ψ that maximize, minimize, and produce an intermediate norm of this projected vector. After that we will want to translate these characteristic values of θ and ψ into their $i_\bullet$ and $\Omega_\bullet$ counterparts. The details behind these translations will be presented in subsection B.1.

B.1 Relation between (θ, ψ) and $(i_\bullet, \Omega_\bullet)$

As first introduced in Chapter IV, we denote by (i, Ω, ω) the orbital elements defining the orientation of the orbit with respect to the observer as illustrated in Figure IV.3, and by (θ, ψ) the angles defining the orientation of the black hole's frame with respect to the orbital plane (see Figure IV.5).

Basis vectors

In the observer's frame (X, Y, Z), the orbital angular momentum vector is

$$\mathbf{z}_{\rm orb} = \begin{pmatrix} \sin\iota \, \sin\Omega \\ -\sin\iota \, \cos\Omega \\ \cos\iota \end{pmatrix}. \tag{10}$$

The line of nodes projected onto the sky is

$$\boldsymbol{\mathcal{L}}_{\rm orb//sky} = \begin{pmatrix} \cos\Omega \\ \sin\Omega \\ 0 \end{pmatrix}. \tag{11}$$

Finally, we define a third orthonormal vector

$$\boldsymbol{\mathcal{T}}_{\rm orb} = \frac{\mathbf{z}_{\rm orb} \times \boldsymbol{\mathcal{L}}_{\rm orb//sky}}{|\mathbf{z}_{\rm orb} \times \boldsymbol{\mathcal{L}}_{\rm orb//sky}|}. \tag{12}$$

Black hole axis

By definition, the spin axis of the black hole (unit vector $\mathbf{z}_{\rm bh}$) is expressed in the basis $(\boldsymbol{\mathcal{L}}_{\rm orb//sky}, \boldsymbol{\mathcal{T}}_{\rm orb}, \mathbf{z}_{\rm orb})$ as

$$\mathbf{z}_{\rm bh} = \cos\theta \, \mathbf{z}_{\rm orb} + \sin\theta \cos(\psi + \omega) \, \boldsymbol{\mathcal{L}}_{\rm orb//sky} + \sin\theta \sin(\psi + \omega) \, \boldsymbol{\mathcal{T}}_{\rm orb}. \tag{13}$$

This vector is then expressed in the observer's basis (X, Y, Z) using the above definitions.

Reading off the angles $(i_\bullet, \Omega_\bullet)$

By definition (cf. IV.4), the black hole axis in the observer's frame is also written as

$$\mathbf{z}_{\rm bh} = \begin{pmatrix} \sin i_\bullet \cos \Omega_\bullet \\ \sin i_\bullet \sin \Omega_\bullet \\ \cos i_\bullet \end{pmatrix}. \tag{14}$$

Thus we can directly identify:

$$i_\bullet = \arccos(z_{\rm bh}^{(Z)}), \tag{15}$$

$$\Omega_\bullet = \text{atan2}\left(z_{\rm bh}^{(Y)}, z_{\rm bh}^{(X)}\right), \tag{16}$$

where $z_{\rm bh}^{(X)}, z_{\rm bh}^{(Y)}, z_{\rm bh}^{(Z)}$ are the components of $\mathbf{z}_{\rm bh}$ in the basis (X, Y, Z).

Given a set of orbital angles (i, Ω, ω) and black hole orientation angles (θ, ψ), one obtains

$$(i_\bullet, \Omega_\bullet)$$

characterizing the orientation of the black hole in the observer's frame by constructing the vector $\mathbf{z}_{\rm bh}$ via Eq.(13), and then reading its inclination and longitude from Eqs. (15) and (16).

B.2 Projected apocenter displacement vector as a function of (θ, ψ)

Orienting the black hole to maximize the projected total Lense-Thirring apocenter shift

According to chapter VII, the orientation of the black hole that maximizes the total secular apocenter shift is such that $\theta = 0 \pmod{\pi}$, i.e., such that the considered star is in the equatorial plane of the black hole. Let us verify if this still holds when we project the total apocenter displacement vector due to the Lense-Thirring effect onto the sky by explicitly finding the values of θ and ψ that maximize:

$$V_{\rm LT//sky} = \sqrt{\left(V_{\rm in//sky}|_{\rm LT}\right)^2 + \left(V_{\rm out//sky}|_{\rm LT}\right)^2} \tag{17}$$

where:

$$\begin{aligned} V_{\rm in//sky}|_{\rm LT} &= 2r_{\rm apo}\sqrt{1-(\cos\omega\sin\iota)^2}\sin(\Delta\varpi_{\rm LT}/2) \\ &= -2r_{\rm apo}\sqrt{1-(\cos\omega\sin\iota)^2}\sin(4\pi\epsilon^{3/2}\cos\theta\,\chi), \end{aligned} \tag{18}$$

$$V_{\mathrm{out}//\mathrm{sky}}|_{\mathrm{LT}} = 2r_{\mathrm{apo}} \sin\iota \sin(\Delta\Theta_{\mathrm{LT}}/2) = -2r_{\mathrm{apo}} \sin\iota \sin(2\pi\epsilon^{3/2} \sin\theta \sin\psi\ \chi) \quad (19)$$

Squaring and collecting terms, we obtain:

$$V^2_{\mathrm{LT}//\mathrm{sky}} = 4r^2_{\mathrm{apo}} \left[C_1\ \sin^2\!\big(4\pi\epsilon^{3/2} \cos\theta\, \chi\big) + C_2\ \sin^2\!\big(2\pi\epsilon^{3/2} \sin\theta \sin\psi\, \chi\big)\right], \quad (20)$$

with

$$C_1 = 1 - (\cos\omega \sin\iota)^2, \qquad C_2 = \sin^2\iota,$$

both positive constants.

Analysis. The maximum of each sinusoidal term is reached when its argument is equal to $\pi/2 \pmod{\pi}$. Therefore, since $\epsilon \ll 1$:

- If $4C_1 \geq C_2$ (typical case), the maximum comes from the in–plane contribution. Maximization is achieved for $\cos\theta = \pm 1$, i.e. $\theta = 0$ or π. Then the out-of-plane contribution vanishes ($\sin\theta = 0$), and ψ is irrelevant.
- If $C_2 > 4C_1$ (rare configuration), the maximum comes from the out-of-plane contribution. Maximization is achieved for $\theta = \pi/2$ and $\psi = \pi/2 \pmod{\pi}$.

Result. The maximal projected Lense-Thirring apocenter displacement is reached for:

- $\boxed{\theta = 0 \pmod{\pi},\ \text{with arbitrary } \psi,\ \text{if } 4\big(1 - (\cos\omega \sin\iota)^2\big) > \sin^2\iota}$

This condition on ι and ω is met with most if not all of the currently known S-stars and presents the configuration where the projection on the sky of the LT in-plane precession is higher than the out-of-plane one. In terms of $i_\bullet$ and $\Omega_\bullet$, an example of values maximizing the quantity of interest is:

$$(i_\bullet, \Omega_\bullet) = \big(\iota,\ \Omega - \tfrac{\pi}{2}\big).$$

- $\boxed{\theta = \dfrac{\pi}{2},\ \psi = \dfrac{\pi}{2} \pmod{\pi},\ \text{if } 4\big(1 - (\cos\omega \sin\iota)^2\big) < \sin^2\iota}$

This condition on ι and ω presents the rare configuration where the orbit is close to being edge-on and its major axis close to being perpendicular to the line of sight. This leads to a projection on the sky of the LT in-plane precession that is smaller than the out-of-plane one. In terms of $i_\bullet$ and $\Omega_\bullet$, an example of values maximizing the quantity of interest in that case is:

$$i_\bullet = \arccos\big(\sin\iota\ \cos\omega\big), \qquad \Omega_\bullet = \Omega + \mathrm{atan2}\ \big(\cos\iota\ \cos\omega,\ -\sin\omega\big).$$

Orienting the black hole to minimize the projected total Lense-Thirring apocenter shift

According to chapter VII, the orientation of the black hole that minimizes the total secular apocenter shift is such that $\theta = \pi/2 \pmod{\pi}$ and $\psi = 0 \pmod{\pi}$, i.e., in the case of a polar orbit with a polar major axis. Let us verify if this still holds when we project the total apocenter displacement vector due to the Lense-Thirring effect onto the sky by explicitly finding the values of θ and ψ that minimize $V_{\mathrm{LT}//\mathrm{sky}}$.

From Eq. (21) we see that the minimum of each sinusoidal term is reached when its argument equals 0 (mod π). Therefore, since $\epsilon \ll 1$, the minimum is achieved for $\cos\theta = 0$, i.e. $\theta = \pi/2$ or $3\pi/2$ and $\sin\psi = 0$, i.e. $\psi = 0 \pmod{\pi}$.

Result. The minimal projected Lense-Thirring apocenter displacement is reached for:

$$\boxed{\theta = \frac{\pi}{2},\ \psi = 0 \pmod{\pi}}$$

This corresponds to a polar orbit with a polar major axis, consistent with the result obtained for the total secular apocenter shift. In terms of $i_\bullet$ and $\Omega_\bullet$, an example of values minimizing the quantity of interest is:

$$i_\bullet = \arccos\left(\sin\iota\,\sin\omega\right), \qquad \Omega_\bullet = \Omega + \mathrm{atan2}\left(\cos\iota\,\sin\omega,\ \cos\omega\right).$$

Orienting the black hole to get a intermediate projected total Lense-Thirring apocenter shift

$$V^2_{\mathrm{LT}//\mathrm{sky}} = 4r^2_{\mathrm{apo}}\left[C_1\,\sin^2\!\left(4\pi\epsilon^{3/2}\cos\theta\,\chi\right) + C_2\,\sin^2\!\left(2\pi\epsilon^{3/2}\sin\theta\sin\psi\,\chi\right)\right], \qquad (21)$$

Let us now determine the values of θ and ψ that yield an intermediate value of the projected LT shift on the sky, that is, halfway between its minimum and maximum possible values.

We know from earlier analysis that the minimum is achieved for $\theta = \pi/2$, $\psi = 0 \pmod{\pi}$, where $V^2_{\mathrm{LT}//\mathrm{sky,min}} = 0$. For most values of ι and ω, the maximum is achieved for $\theta = 0 \pmod{\pi}$, any ψ, where $V^2_{\mathrm{LT}//\mathrm{sky,max}} = 4r^2_{\mathrm{apo}}C_1\,\sin^2\!\left(4\pi\epsilon^{3/2}\,\chi\right)$.

We seek (θ, ψ) such that

$$V^2_{\mathrm{LT}//\mathrm{sky}} = \frac{1}{2}(V^2_{\mathrm{LT}//\mathrm{sky,min}} + V^2_{\mathrm{LT}//\mathrm{sky,max}}) = 2r^2_{\mathrm{apo}}\,C_1\,\sin^2\!\left(4\pi\epsilon^{3/2}\,\chi\right).$$

That is,

$$C_1 \sin^2\!\big(4\pi\epsilon^{3/2}\cos\theta\,\chi\big) + C_2 \sin^2\!\big(2\pi\epsilon^{3/2}\sin\theta\sin\psi\,\chi\big) = \frac{1}{2}C_1 \sin^2\!\big(4\pi\epsilon^{3/2}\,\chi\big). \quad (22)$$

Case 1: If we set $\psi = 0 \pmod{\pi}$, the second term vanishes and the condition reduces to

$$C_1 \sin^2\!\big(4\pi\epsilon^{3/2}\cos\theta\,\chi\big) = \tfrac{1}{2}C_1 \sin^2\!\big(4\pi\epsilon^{3/2}\,\chi\big).$$

For nonzero C_1, this requires

$$\sin^2\!\big(4\pi\epsilon^{3/2}\cos\theta\,\chi\big) = \tfrac{1}{2} \sin^2\!\big(4\pi\epsilon^{3/2}\,\chi\big).$$

A sufficient solution is obtained when

$$\cos\theta = \pm\tfrac{1}{\sqrt{2}} \quad \Longrightarrow \quad \theta = \tfrac{\pi}{4} \ \text{ or } \ \tfrac{3\pi}{4}.$$

Case 2: Alternatively, for $\theta = \pi/2$, the first term vanishes, giving

$$C_2 \sin^2\!\big(2\pi\epsilon^{3/2}\sin\psi\,\chi\big) = \tfrac{1}{2}C_1 \sin^2\!\big(4\pi\epsilon^{3/2}\,\chi\big).$$

This admits real solutions only if

$$C_1 \le 2C_2 \sin^2\!\big(4\pi\epsilon^{3/2}\,\chi\big) \simeq 2C_2,$$

in which case

$$\sin\psi = \pm\sqrt{\tfrac{C_1}{2C_2}} \quad \Longrightarrow \quad \psi = \arcsin\!\Big(\sqrt{\tfrac{C_1}{2C_2}}\Big) \ \text{ or } \ \pi - \arcsin\!\Big(\sqrt{\tfrac{C_1}{2C_2}}\Big).$$

Result: In most astrophysical situations where $C_1 > C_2$, the most natural intermediate solution is therefore

$$\boxed{\theta = \tfrac{\pi}{4}\left[\tfrac{\pi}{2}\right], \quad \psi = 0 \pmod{\pi}}$$

which corresponds to a black hole spin inclined by $\pi/4$ relative to the orbital plane. In terms of $i_\bullet$ and $\Omega_\bullet$, an example of values producing such an intermediate projected Lense–Thirring apocenter shift is:

$$i_\bullet = \arccos\!\left(\frac{\cos\iota + \sin\iota\,\sin\omega}{\sqrt{2}}\right), \qquad \Omega_\bullet = \Omega + \operatorname{atan2}\!\big(\sin\omega\cos\iota - \sin\iota,\ \cos\omega\big).$$

RÉSUMÉ

L'astrométrie et la spectroscopie des étoiles en orbite autour de Sgr A*, le trou noir de quatre millions de masses solaires au centre de la Galaxie, offrent une occasion unique de mettre en évidence des effets relativistes et de tester le théorème de la « calvitie » des trous noirs. Ces effets se manifestent par des précessions orbitales induites par le spin et le moment quadrupolaire du trou noir. Dans ce travail, nous caractérisons analytiquement et numériquement ces réorientations jusqu'à l'ordre post-newtonien 2PN, en utilisant la méthode à deux échelles de temps et en enrichissant les modèles de notre code pour inclure les termes de spin, les contributions quadrupolaires, les corrections de Schwarzschild d'ordre supérieur et l'impact du spin sur le décalage spectral. Nous comparons ces modèles à des simulations de tracé de rayons en relativité générale afin de préciser leur domaine de validité. Nous montrons aussi que le choix du système de coordonnées peut induire des écarts en ascension droite, déclinaison et vitesse radiale comparables à l'effet du spin, ce qui impose de spécifier clairement le système de coordonnées et le temps d'osculation. Côté observations, l'étoile récemment découverte S301 se révèle presque aussi sensible au spin que l'étoile hypothétique S2/10. Son suivi, combiné à celui d'étoiles aux orbites variées (S2, S29, S38, S55), permet de réduire les dégénérescences et d'accélérer la détection des paramètres du spin. Nos prévisions indiquent que sa magnitude pourra être contrainte avec une précision de 0,1 d'ici 2032, 0,05 en 2034 et 0,03 en 2036 si les autres paramètres sont fixés, avec des résultats comparables lorsque l'orientation du spin est également ajustée. L'astrométrie reste l'outil principal, mais la spectroscopie devient déterminante si la précision atteint environ 2 km/s, comme prévu avec MICADO. Dans l'ensemble, la détection du spin apparaît robuste pourvu que le suivi temporel soit suffisant et que les paramètres orbitaux soient bien connus. L'orientation du trou noir, combinée à des ajustements multi-étoiles et multi-instruments, constitue l'approche la plus prometteuse pour les prochaines décennies.

MOTS CLÉS

Physique des trous noirs – Gravitation – Centre galactique – Processus relativistes – Interférométrie

ABSTRACT

Measuring the astrometric and spectroscopic data of stars orbiting Sgr A*, the 4-million-solar-mass black hole at the Galactic Center, offers a unique opportunity to detect relativistic effects and test the no-hair theorem by monitoring spin- and quadrupole-induced orbital precessions. In this work, we analytically and numerically characterize these reorientations up to second post-Newtonian (2PN) order using the two-timescale method, extending dynamical models to include spin terms, quadrupole effects, higher-order Schwarzschild precession, and the spin contribution to redshift, and comparing them with full GR ray tracing to determine the regimes where each approximation is valid. Comparisons across coordinate systems reveal discrepancies in RA, DEC, and RV at the level of the spin effect, emphasizing the need to explicitly state the coordinate framework and osculation time when reporting orbital elements. Observationally, we show that the recently discovered S301 has spin sensitivity comparable to S2/10, and that combining its data with those of other stars of diverse orientations (S2, S29, S38, S55) reduces parameter degeneracies and accelerates spin detection. Quantitative forecasts indicate that the spin magnitude can be constrained to $\sigma_\chi \simeq 0.1$ by 2032, 0.05 by 2034, and 0.03 by 2036 when only fitting the spin magnitude χ, with comparable results when fitting all spin parameters. Astrometry provides the dominant leverage, while spectroscopy adds substantial value only if radial-velocity precision reaches 2 km/s, as expected with MICADO. Overall, spin detectability is robust given sufficient monitoring and knowledge of orbital parameters. The black hole orientation is a critical factor, along with multi-star, multi-instrument datasets, which together offer the most promising path forward.

KEYWORDS

Black hole physics – Gravitation – Galactic center – Relativistic processes - Interferometry